



DEVELOPMENT OF A RADAR-FREQUENCY METAMATERIAL
MEASUREMENT AND CHARACTERIZATION APPARATUS

THESIS

Stephen I. Faris, Captain, USAF

AFIT/GE/ENG/12-13

**DEPARTMENT OF THE AIR FORCE
AIR UNIVERSITY**

AIR FORCE INSTITUTE OF TECHNOLOGY

Wright-Patterson Air Force Base, Ohio

APPROVED FOR PUBLIC RELEASE; DISTRIBUTION IS UNLIMITED.

The views expressed in this thesis are those of the author and do not reflect the official policy or position of the United States Air Force, Department of Defense, or the United States Government.

This material is declared a work of the U.S. Government and is not subject to copyright protection in the United States.

DEVELOPMENT OF A RADAR-FREQUENCY METAMATERIAL
MEASUREMENT AND CHARACTERIZATION APPARATUS

THESIS

Presented to the Faculty
Department of Electrical Engineering
Graduate School of Engineering and Management
Air Force Institute of Technology
Air University
Air Education and Training Command
In Partial Fulfillment of the Requirements for the
Degree of Master of Science in Electrical Engineering

Stephen I. Faris, BS

Captain, USAF

March 2012

APPROVED FOR PUBLIC RELEASE; DISTRIBUTION IS UNLIMITED.

DEVELOPMENT OF A RADAR-FREQUENCY METAMATERIAL
MEASUREMENT AND CHARACTERIZATION APPARATUS

Stephen I. Faris, BS
Captain, USAF

Approved:

Peter J. Collins, PhD (Chairman) _____ Date _____

Ronald A. Coutu, Jr., PhD (Member) _____ Date _____

Milo Hyde, Maj, USAF (Member) _____ Date _____

Abstract

The purpose of this research was to design, build and test an apparatus for the measurement and characterization of radar-frequency metamaterials. Measurement and characterization is vital to metamaterial taxonomy and ultimately vital to metamaterial definitions. Thus, the current lack of clarity in metamaterial definitions has served as the primary motivation for pursuing a method for taxonomy and thus, this apparatus. The technical goal of this thesis was to aid understanding of a metamaterial's radar-frequency response by developing an apparatus that would take simple, yet significant measurements of a metamaterial's S-parameters and electric field distributions in near-field regions.

The apparatus under design became a hybridized form of the designs of three existing measurement systems: a focused-beam system housed in a moveable-plate, parallel-plate transmission line. Some of the system components were borrowed directly from the existing designs, whereas some components were designed from the examples of existing designs and some components were designed altogether new.

The culmination of this effort was a newly-built measurement device that upon inauguration provided the basic utility of measuring the radar-frequency responses of both traditional materials and metamaterials.

*To my wife,
Thanks for letting me stay at work so long... I still love you more.
To my baby,
Daddy is coming home to play now.*

Acknowledgments

I'd like to express sincere appreciation to Dr. Peter Collins for allowing me to take on such an attractive thesis. I am indebted to Charles McNeely for helping me wade through the ugly parts.

Stephen I. Faris, Capt, USAF

Table of Contents

	Page
Abstract	iv
Acknowledgments	v
List of Figures	viii
List of Tables	xv
I. Introduction	1
Background	1
Metamaterials Defined	2
Characterization and Measurement Overview	4
<i>Near-Field Measurements</i>	6
<i>Scattering Parameter Measurements</i>	7
<i>Design Inspirations and Issues</i>	8
Thesis organization	10
II. Literature Review	12
A Brief History of Metamaterials	12
Defining Metamaterials and Metamaterial Science	15
Technical Details from Design Inspirations	17
<i>BANTAM</i>	17
<i>GTRI Focused Beam System</i>	22
<i>Shelby Parallel-Plate Waveguide</i>	26
III. Methodology	31
Pre-existing Design Constraints	31
<i>BANTAM Chamber</i>	31
<i>Lens Material Constraints</i>	33
Hardware Design Data (Theories, Simulations, Specifications & Fabrication)	35
<i>Monopoles</i>	35
<i>Aluminum Sheets</i>	44
<i>Rolled Edge Framing</i>	57

<i>80/20 Plate Frames</i>	65
<i>Fiberglass Filler</i>	69
<i>Conductive Paint</i>	71
<i>Scissor Lift</i>	81
<i>Rexolite Lenses</i>	85
<i>Mode-Matching Components</i>	100
<i>Targets</i>	107
<i>BANTAM Reinforcements</i>	109
Assembly & Testing	111
<i>Mechanical Tuning</i>	111
<i>Basic Calibration</i>	116
IV. Results and Analysis	118
Chapter Overview	118
<i>Empty PPWG</i>	120
<i>Small Lenses in PPWG</i>	141
<i>Large Lenses in PPWG</i>	170
V. Conclusions and Recommendations	181
Conclusions	181
<i>Conclusions from Measurement Results and Analysis</i>	181
<i>Conclusions on Technical and Philosophical Significance</i>	182
Recommendations for Action and Research	183
<i>Component Recommendations</i>	183
<i>System Recommendations</i>	190
Appendix: Lens Optimization Spreadsheet	194
Bibliography	196

List of Figures

	Page
Figure 1: Conventional Near-Field and Far-Field Regions	7
Figure 2: Original Configuration of BANTAM.....	19
Figure 3: GTRI Free-Space Focused Beam System	23
Figure 4: CST Model of Shelby PPWG.....	28
Figure 5: CST Model of Shelby PPWG Operating at 8 GHz	29
Figure 6: CST Model of Shelby PPWG Evaluated Along Circular Path	30
Figure 7: CST Model of a Monopole.....	36
Figure 8: CST Monopole Cylindrical Wavefronts at 2 GHz	36
Figure 9: Quarter-Wave (red) and Half-Wave Monopole Elevation Pattern at 18 GHz ..	37
Figure 10: Quarter-Wave (red) and Half-Wave Monopole Azimuth Pattern at 18 GHz..	38
Figure 11: Three-Wavelength Monopole Elevation Pattern at 18 GHz	38
Figure 12: Three-Wavelength Monopole Azimuth Pattern at 18 GHz.....	39
Figure 13: Quarter-Wave, Eighth-Wave and 0.025-Wave (blue) Elevation at 2 GHz.....	40
Figure 14: Quarter-Wave, Eighth-Wave and 0.025-Wave (blue) Azimuth at 2 GHz	40
Figure 15: Half-inch Monopole (Tenth-Wavelength at 2 GHz) Radiation Patterns.....	41
Figure 16: Half-inch Monopole (Half-Wavelength at 10 GHz) Radiation Patterns	41
Figure 17: Half-inch Monopole (One-Wavelength at 18 GHz) Radiation Patterns	42
Figure 18: PPWG Monopole	43

Figure 19: Ray-Trace Diagram of Propagating Modes for 18 GHz in 2" PPWG	47
Figure 20: Circular Plate (12" Diameter) PPWG.....	49
Figure 21: Phase Animation in 12" Circular Plate PPWG for 2 GHz	49
Figure 22: Phase Animation in 12" Circular Plate PPWG for 4 GHz	50
Figure 23: Phase Animation in 12" Circular Plate PPWG for 18 GHz	50
Figure 24: Mag. Variation Along Evaluation Lines for Circ. Plate PPWG at 2 GHz	51
Figure 25: Phase Variation Along Evaluation Lines for Circ. Plate PPWG at 2 GHz	52
Figure 26: Mag. Variation Along Evaluation Lines for Circ. Plate PPWG at 4 GHz	52
Figure 27: Phase Variation Along Evaluation Lines for Circ. Plate PPWG at 4 GHz	53
Figure 28: Mag. Variation Along Evaluation Lines for Circ. Plate PPWG at 18 GHz	53
Figure 29: Phase Variation Along Evaluation Lines for Circ. Plate PPWG at 18 GHz ...	54
Figure 30: Flatness of Aluminum Sheets.....	57
Figure 31: Square Plate (12") PPWG	59
Figure 32: Phase Animation in 12" Square Plate PPWG for 2 GHz	60
Figure 33: Mag. Variation Along Evaluation Lines for Square Plate PPWG at 2 GHz ...	60
Figure 34: Phase Variation Along Evaluation Lines for Square Plate PPWG at 2 GHz..	61
Figure 35: Square Plate (12") PPWG with Rolled-Edge Frame	61
Figure 36: Phase Animation in 12" Square Plate PPWG with Rolled-Edges for 2 GHz .	62
Figure 37: Mag. Variation Along Eval. Lines for PPWG with Rolled-Edges.....	62
Figure 38: Phase Variation Along Eval. Lines for PPWG with Rolled-Edges.....	63
Figure 39: Machining PVC Pipe for PPWG Rolled-Edge Frame.....	65
Figure 40: Top Plate Frame (Ref. 12" Square Floor Tiles)	67
Figure 41: Bottom Plate Frame with PVC Pipes Installed	68

Figure 42: Top Plate Frame with Pipes and Aluminum Sheet Installed.....	68
Figure 43: Bottom Plate with Heavy-Weight Bondo Applied.....	70
Figure 44: Top Plate with Light-Weight Filler Applied	71
Figure 45: Top Plate with Primer Applied.....	73
Figure 46: Bottom Plate with Two Conductive Coats and Clear Top Coat Applied.....	74
Figure 47: Top Plate Under Repair to Remove Excess Primer	75
Figure 48: Paint Coupons.....	76
Figure 49: Fully Coated Vinyl Coupon at 10x Magnification.....	76
Figure 50: Coating Thickness on Aluminum Substrate.....	77
Figure 51: Coating Thickness on Vinyl Substrate	78
Figure 52: Sheet Resistance of Coatings on Al. Substrate.....	79
Figure 53: Sheet Resistance of Coatings on Vinyl Substrate	79
Figure 54: Using Lift to Install Top Plate (Raised)	83
Figure 55: Using Lift to Install Top Plate (Lowered)	83
Figure 56: Bottom Plate Installed on Scissor Lift.....	84
Figure 57: General Positioning of Scissor Lift and Bottom Plate	84
Figure 58: Focusing Factor of 2-D FBS Lenses	86
Figure 59: Beamwaists of 2-D FBS Lenses	87
Figure 60: Beam Radii at Aperture Planes of 2-D FBS Lenses.....	89
Figure 61: Amplitude Taper at Lens Aperture and Target Surface	90
Figure 62: Top Plate Scan Area for Sizing Small Lens	90
Figure 63: Large Lens Prior to Polishing.....	97
Figure 64: Bright Machine Marks in Profile Surface of Lens	98

Figure 65: Polishing Lens With Compound	99
Figure 66: Small Lenses on Bottom Plate.....	100
Figure 67: Small Mode-Matching Mesa	101
Figure 68: Small Mesa Effects on Overmoding	103
Figure 69: Large Mesa Effects on Overmoding	103
Figure 70: Mag. Variation Along Evaluation Lines for Small Mesa at 18 GHz	104
Figure 71: Phase Variation Along Evaluation Lines for Small Mesa at 18 GHz	104
Figure 72: Mag. Variation Along Evaluation Lines for Large Mesa at 18 GHz	105
Figure 73: Phase Variation Along Evaluation Lines for Large Mesa at 18 GHz	105
Figure 74: Targets for BANTAM 2-D FBS.....	109
Figure 75: Reinforcements on Short Axis Rail.....	110
Figure 76: Centering Bottom Plate of PPWG.....	112
Figure 77: Tripod for Stabilizing Bottom Plate	113
Figure 78: Lens Placement Tool.....	115
Figure 79: Positioning Targets in the PPWG.....	116
Figure 80: Measuring THRU for Two-Port Network Calibration	117
Figure 81: Empty PPWG Model.....	121
Figure 82: Empty PPWG with Magnitude and Phase Distributions.....	121
Figure 83: Measured vs. Simulated Near-Field Scans at 2 GHz	123
Figure 84: Measured vs. Simulated Near-Field Scans at 6 GHz	124
Figure 85: Measured vs. Simulated Near-Field Scans at 10 GHz	125
Figure 86: Measured Near-Field Scans at 18 GHz	126
Figure 87: Measured Left-to-Top S-Parameters (Mag.) (short focal)	128

Figure 88: Measured Left-to-Top S-Parameters (Phase) (short focal)	128
Figure 89: Measured Left-to-Top S-Parameters (Mag.) (long focal)	129
Figure 90: Measured Left-to-Top S-Parameters (Phase) (long focal)	129
Figure 91: Measured Left-to-Right S-Parameters (Mag.) (short focal)	131
Figure 92: Measured Left-to-Right S-Parameters (Phase) (short focal)	132
Figure 93: Measured Left-to-Right S-Parameters (Mag.) (long focal).....	132
Figure 94: Measured Left-to-Right S-Parameters (Phase) (long focal).....	133
Figure 95: Measured vs. Simulated Left-to-Right Reflection (short focal).....	135
Figure 96: Measured vs. Simulated Left-to-Right Transmission (short focal).....	135
Figure 97: Measured vs. Simulated Left-to-Right Reflection (long focal).....	136
Figure 98: Measured vs. Simulated Left-to-Right Transmission (long focal).....	136
Figure 99: Left-to-Right Reflection Error (short focal)	138
Figure 100: Left-to-Right Transmission Error (short focal)	139
Figure 101: Left-to-Right Reflection Error (long focal).....	139
Figure 102: Left-to-Right Transmission Error (long focal).....	140
Figure 103: PPWG Model with Small Lenses	142
Figure 104: PPWG with Small Lenses with Magnitude and Phase Distributions	142
Figure 105: Measured vs. Simulated Near-Field Scans at 2 GHz	143
Figure 106: Measured vs. Simulated Near-Field Scans at 6 GHz	144
Figure 107: Measured vs. Simulated Near-Field Scans at 10 GHz	145
Figure 108: Measured Near-Field Scans at 18 GHz	146
Figure 109: Difference Plot of Scan with Air Gap vs. No Air Gap at 2, 6, 10, 18 GHz	148
Figure 110: D-Ring Metamaterial Model and First-Look Scan.....	150

Figure 111: Measured Left-to-Top S-Parameters (Mag.)	152
Figure 112: Measured Left-to-Top S-Parameters (Phase)	152
Figure 113: Measured Left-to-Right S-Parameters (THRU) (Mag.)	153
Figure 114: Measured Left-to-Right S-Parameters (THRU) (Phase)	154
Figure 115: Measured vs. Simulated Left-to-Right Reflection (THRU)	155
Figure 116: Measured vs. Simulated Left-to-Right Transmission (THRU)	156
Figure 117: Left-to-Right Reflection Error (THRU)	157
Figure 118: Left-to-Right Transmission Error (THRU)	157
Figure 119: Measured Left-to-Right S-Parameters (SHORT) (Mag.)	158
Figure 120: Measured Left-to-Right S-Parameters (SHORT) (Phase)	159
Figure 121: Measured vs. Simulated Left-to-Right Reflection (SHORT)	160
Figure 122: Measured vs. Simulated Left-to-Right Transmission (SHORT)	160
Figure 123: Left-to-Right Reflection Error (SHORT)	161
Figure 124: Left-to-Right Transmission Error (SHORT)	161
Figure 125: Measured Left-to-Right S-Parameters (Acrylic) (Mag.)	162
Figure 126: Measured Left-to-Right S-Parameters (Acrylic) (Phase)	163
Figure 127: Measured vs. Simulated Left-to-Right Reflection (Acrylic)	163
Figure 128: Measured vs. Simulated Left-to-Right Transmission (Acrylic)	164
Figure 129: Left-to-Right Reflection Error (Acrylic)	165
Figure 130: Left-to-Right Transmission Error (Acrylic)	165
Figure 131: Measured Left-to-Right S-Parameters (D-Ring) (Mag.)	166
Figure 132: Measured Left-to-Right S-Parameters (D-Ring) (Phase)	167
Figure 133: Measured vs. Simulated Left-to-Right Reflection (D-Ring)	167

Figure 134: Measured vs. Simulated Left-to-Right Transmission (D-Ring)	168
Figure 135: Left-to-Right Reflection Error (D-Ring)	169
Figure 136: Left-to-Right Transmission Error (D-Ring)	169
Figure 137: PPWG Model with Large Lenses	170
Figure 138: PPWG with Large Lenses with Magnitude and Phase Distributions	170
Figure 139: Measured Left-to-Right S-Parameters (THRU) (Mag.)	171
Figure 140: Measured Left-to-Right S-Parameters (THRU) (Phase)	172
Figure 141: Measured vs. Simulated Left-to-Right Reflection (THRU)	173
Figure 142: Measured vs. Simulated Left-to-Right Transmission (THRU)	173
Figure 143: Left-to-Right Reflection Error (THRU)	175
Figure 144: Left-to-Right Transmission Error (THRU)	175
Figure 145: Measured Left-to-Right S-Parameters (SHORT) (Mag.)	176
Figure 146: Measured Left-to-Right S-Parameters (SHORT) (Phase)	177
Figure 147: Measured Left-to-Right S-Parameters (Acrylic) (Mag.)	178
Figure 148: Measured Left-to-Right S-Parameters (Acrylic) (Phase)	178
Figure 149: Measured Left-to-Right S-Parameters (D-Ring) (Mag.)	180
Figure 150: Measured Left-to-Right S-Parameters (D-Ring) (Phase)	180
Figure 151: Small Lens Optimization Sheet	194
Figure 152: Large Lens Optimization Sheet	195

List of Tables

	Page
Table 1: Higher-Order Modes in 2" PPWG.....	45
Table 2: Angles of Incidence for Propagating Higher-Order Modes	46
Table 3: Thickness of Conductive Coatings	78
Table 4: Sheet Resistance of Conductive Coatings	80
Table 5: BANTAM 2-D FBS Test Matrix.....	119

DEVELOPMENT OF A RADAR-FREQUENCY METAMATERIAL
MEASUREMENT AND CHARACTERIZATION APPARATUS

I. Introduction

Background

Within the Radio Frequency electromagnetic spectrum, the Institute of Electrical and Electronics Engineers has standardized the S-band (2-4 GHz), C-band (4-8 GHz), X-band (8-12 GHz), Ku-band (12-18 GHz) and K-band (18-27 GHz) as designator bands for characterizing frequency-dependent radar applications [1]. The materials used in these radar applications play a key role in manipulating electromagnetic phenomena for practical use. The study and development of these materials has been an area of interest in materials science, solid-state physics, and electrical and electronics engineering for decades [2]. Recently, the vast catalog of radar-frequency materials has been expanding to include what are popularly referred to as metamaterials. Radar-frequency metamaterials, as an alternative or complement to traditional radar-frequency materials, is a maturing area of study. Development of

an apparatus for measurement and characterization of metamaterial performance in the S-band through Ku-band (2-18 GHz) is the focus of this thesis.

Metamaterials Defined

In growing maturity, the exact nature of metamaterials and the benefits they provide can be defined in many different ways. Definitions vary with potential technical applications and performance expectations. In short, by the definition of the prefix, *meta-*, a metamaterial is a conceptual extension of another common material. The conceptual extension may apply to either the physical characteristics of the material or the application of the material. Determining the conceptual extension is the foundation of the metamaterial definition.

Outright, this thesis recognizes the inherent ambiguity and deficiency in generally defining a metamaterial. However, given a specific class of applications such as radar-frequency applications, definitions can become much more accurate. For use in this thesis, the definition of a radar-frequency metamaterial is that of a bulk material which exhibits a response to radar-frequencies which it would not otherwise exhibit in its classical component form. In general, engineering the properties of radar-frequency metamaterials can lead to responses that are unique and possibly superior to those of conceptually adjacent, i.e. traditional, materials. Theoretically, metamaterial responses may be so unique that the response cannot be, or has yet to be, observed in nature.

Chapter 2 of this thesis will briefly discuss the broad idea of metamaterial definitions. However, care must be taken in managing expectations of metamaterial performance relative to a particular definition. This caution is due to the lack of community consensus towards a particular definition and the common misinterpretation of the prefix, *meta-* which implies that a metamaterial is akin to a supernatural material. A famous and enlightening example of this linguistic faux pas is in interpreting the title of Aristotle's work, *Metaphysics*. By the proper interpretation, the treatises of *Metaphysics* are simply Aristotle's writings following his treatises of *Physics*. *Physics* dealt with physical phenomena and *Metaphysics*, logically, dealt with consciousness, thought, existence of self and of God [3]. The two writings are conceptually adjacent in that they both function in the context of man's attempt to understand the universe, not that *Metaphysics* is a science book of supernaturally physical phenomena. In like manner, a metamaterial, properly interpreted, is that concept of a material which logically follows another common concept. By misinterpretation, a metamaterial would seem to possess supernaturally physical characteristics.

In conducting research for this thesis, misinterpretations have been noticed in technical publications, some hardly obvious, but some quite exaggerated. Chapter 2 will not attempt to discredit any metamaterial concept or author of such, but instead, by revealing the degree of the tendency of metamaterial definitions to be ambiguous and misguided, this chapter will attempt to justify the importance of systematic measurement and characterization of actual metamaterial performance. It is anticipated that ongoing measurement and characterization will lead to an accepted

metamaterial taxonomy which would better shape a metamaterial definition within a specific application. It should be noted that at the writing of this thesis, there is no common, coherent, community-accepted definition for a metamaterial.

It is hoped that this thesis can provide something of intellectual value that will not only further the technical development of radar-frequency metamaterials, but also guide metamaterial philosophies in general. The intent behind the design of a measurement and characterization apparatus is not to prove or disprove metamaterial concepts, but to provide an additional tool to the taxonomy toolkit.

Characterization and Measurement Overview

This thesis will address development of a measurement and characterization apparatus for radar-frequency metamaterials in the S-band through Ku-band. Accepted techniques for measuring and characterizing electromagnetic properties of traditional materials will be applied. Chapter 2 of this thesis will discuss in detail several techniques that form the basis for the apparatus under design. Though many measurement techniques are available and many have been applied to metamaterials already, this thesis will focus primarily on developing an apparatus that takes direct field measurements in the near-field region of a metamaterial sample. Secondarily, this thesis will focus on developing, in physical combination with the primary apparatus, an apparatus that takes measurements of metamaterial scattering parameters in a 2-dimensional configuration. In order to obtain these functions in physical combination, the proper component devices must be designed and built.

According to AFIT professor, Dr. Peter Collins, who can be credited for the original design concepts and subsequent design guidance, the final product of this thesis will be a patentable design for a near-field and S-parameter measurement device that can be applied to both metamaterials and traditional radar-frequency materials [4].

The efforts of this thesis will be scoped such that the measurements provided by the apparatus under design will be limited to near-field measurements and 2-D scattering parameters. Any discussion of other measurement types or techniques will be presented for reference only. There will be allowance for general comparison of different techniques, but there will be no measurements taken by these other techniques. The resultant raw measurements will be used to effectively rate the utility of the apparatus under design, but they will not be used to immediately characterize a particular material. It is anticipated that the apparatus will deliver all the necessary raw measurements of sufficient quality such that material characterization could be performed at any time.

All design parameters of the apparatus components will be simulated in Computer Simulation Technology Microwave Studio (CST-MWS) Transient Domain Solver prior to the components being fabricated. Full system simulations will be generated to the extent possible and comparisons will be made with the actual system performance. When the apparatus is built and completed, actual measurements of material and metamaterial samples will be compared to simulated measurements.

Near-Field Measurements.

Near-field electric field measurements are relevant to the cause of characterizing metamaterials as they help to define the overall performance of the metamaterial in the wave-material interaction. Conventionally, measurements of an electromagnetic scattering target are taken in the far-field of the target where spherical, cylindrical, asymmetrical, or otherwise non-planar wavefronts have propagated far enough to be considered planar and uniform by a measuring device. The near-field measurement becomes relevant under the assumption that understanding the wave-material interaction near the surface of the target is more valuable than understanding the wave-target interaction at a distance. Particular advantages of near-field over far-field measurements are 1) many measurements and many types of measurements can be obtained with standard lab equipment due to the proximity of the measurement probe to the target; 2) near-field imaging of field distributions can provide diagnostic tools for analyzing a material's spatial elements; 3) near-field measurements not only supplement far-field measurements but can be used to predict and validate far-field measurements [5]. For use in this thesis, the definition of the near-field region will follow the convention shown in Figure 1 and as given in [6].

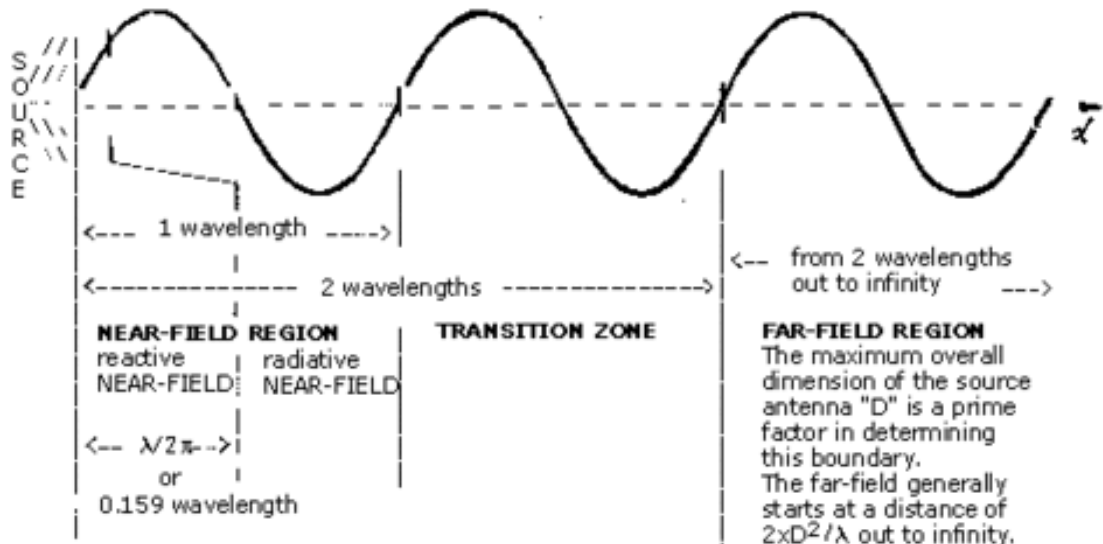


Figure 1: Conventional Near-Field and Far-Field Regions

Scattering Parameter Measurements.

In like manner, measuring S-parameters is relevant to the cause of characterizing metamaterials. The S-parameters of the wave-material interaction consist of electromagnetic wave reflections from the metamaterial surfaces and electromagnetic wave transmissions through the metamaterial surfaces. Measuring these reflections and transmissions and comparing them to the incident electromagnetic wave will result in derived values of the metamaterial's constituent parameters of permittivity and permeability. These constituent parameters can then be used to further characterize the bulk metamaterial.

Design Inspirations and Issues.

Design inspiration for the near-field measurement function comes from the AFIT Broadband Antenna Near-Field Test and Measurement Range (BANTAM). In brief, the BANTAM is a compact (large enough for a single technician to work comfortably), shielded, anechoic chamber with two linear translation rails capable of scanning a probe from side to side and from front to back within the chamber. An antenna under test is placed on a rotary pedestal in the BANTAM floor. The height difference between the probe and the antenna is adjustable by either lowering the translation rails or by raising the antenna on the pedestal [5].

The BANTAM chamber, to include the current configuration of anechoic absorber, will be used to house the apparatus under design. The translation rails, the current control software and the current network analyzer will be used to direct the probe's scanning motion and data collection. The BANTAM will be described further in Chapter 2.

In general, the most important issues in taking near-field measurements are characterizing the measurement probe and correcting for probe-target interaction. Ideally, the measurement probe should not interact with the target, the probe should have an isotropic radiation pattern, the probe should have a dual polarization capability, and the probe should have a frequency-independent response [7]. In designing the near-field measurement function for this apparatus, it is assumed for simplicity that the initial measurement probe will be metallic, it will interact with metamaterial samples over the desired set of radar frequencies and it will utilize a single polarization. As a limitation in scope, the issues of probe characterization and

probe-target interaction will not be addressed in this thesis. It is intended that the apparatus under design will be open to modification for different types of probes in the future.

Design inspiration for the scattering parameter measurement function comes from the Georgia Tech Research Institute (GTRI) Focused Beam System (FBS) and the parallel-plate waveguide (PPWG) apparatus of R. A. Shelby et als' (2001), *Experimental Verification of a Negative Index of Refraction* [8][9]. In brief, the GTRI Focused Beam System simulates plane-wave illumination of a material sample in free-space by using lenses to focus microwave energy as radiated from horn antennas - the system is symmetric such that S-parameters can be obtained. Shelby's parallel-plate waveguide apparatus consists of a radiating antenna and a material sample sandwiched between two conductive plates. At the end of the waveguide near the material sample, a detector can be circumferentially positioned around the sample to gather angularly-dependent S-parameter measurements.

Conceptually, the apparatus under design will implement a 2-dimensional focused beam system housed in a parallel-plate waveguide for S-parameter measurements. The GTRI and Shelby systems will be described further in Chapter 2.

In general, the most important issue in developing the scattering parameter measurement function is designing the layout of the apparatus within the BANTAM chamber. The BANTAM chamber must house two parallel plates that sandwich an excitation source, a lens, a material sample, another lens, and a detector. In addition, the BANTAM chamber must house any necessary support and control structure. In particular, the most important issue is that the pre-existing size and shape of the

BANTAM chamber will dictate the allowable electrical path length between source and detector. The allowable path length must be segmented into focal lengths and material lengths respectively which must be optimized electrically as well as geometrically. Simultaneously, the entire apparatus must be physically combined with the BANTAM's linear translation rails to provide the capability of the near-field measurement function without degrading the performance of the S-parameter measurement function. Conceptually, the near-field measurements will be achieved by scanning the top plate over the bottom plate with the top plate serving as the mounting point for the scanning probe.

The apparatus under design will be hereafter referred to as the BANTAM 2-D Focused Beam System. The details behind the design and construction methodology of the BANTAM 2-D Focused Beam System will be discussed in Chapter 3.

Thesis organization

The remainder of this thesis is divided into several chapters. Chapter 2 is a literature review that addresses metamaterial history and the issues involving metamaterial definitions – this is the primary motivation behind development of the BANTAM 2-D Focused Beam System. Technical details of the original BANTAM, the GTRI FBS and the Shelby PPWG will be discussed further with design advantages and disadvantages as they relate to the design of the BANTAM 2-D FBS. Chapter 3 will present detailed theories, simulations, specifications, and fabrication techniques as they were applied to the design of the BANTAM 2-D FBS components.

Chapter 4 will attempt to analyze the initial performance of the BANTAM 2-D FBS by comparing material measurements taken by the physical to material measurements taken by a simulated system. Chapter 5 will use the results of Chapter 4 to rate the utility of the BANTAM 2-D FBS as a measurement device and reach conclusions that are pertinent to the technical and philosophical significance of metamaterial measurement. Chapter 5 will also provide recommendations for future actions and future research necessary for the continued success of the BANTAM 2-D FBS.

II. Literature Review

This chapter presents the background information necessary to thoroughly understand the motivation and goals of this thesis. In brief, this chapter provides an overview of the history of metamaterials, followed by, more importantly, how a metamaterial is popularly defined and how metamaterial performance is popularly characterized. Following this discussion, three accepted techniques for measuring and characterizing electromagnetic properties of materials will be introduced as they provide design inspiration to this thesis.

A Brief History of Metamaterials

In conducting research for this thesis, popular metamaterial literature had been pored over to determine what key topics and events had contributed to the making of the metamaterial subject. Reviewing commonly cited literature was one avenue to discover the subject's rich history. Another avenue was randomly reviewing literature simply because it contained the word, *metamaterial* in the body of the text. Another avenue still was to follow the work of metamaterial intellectual giants in hope that their progress and insights would reveal the historical big picture. The most meaningful avenue was reviewing a formal record of metamaterial history and its forerunners. This formal record seemed to hold the most applicability and authority on the subject.

Shamonina and Solymar's, *Metamaterials: How the Subject Started* is number seven of the top-10 cited articles of the past five years from the peer-reviewed scientific journal, *Metamaterials* [10]. According to Shamonina and Solymar, there are four seminal papers that have established the initial momentum in the birth of the subject of metamaterials [11]. The four papers are Viktor Veselago's (1968), *The Electrodynamics of Substances with Simultaneously Negative Values of ϵ and μ* , David R. Smith et als' (2000), *Composite Medium with Simultaneously Negative Permeability and Permittivity*, R. A. Shelby et als' (2001), *Experimental Verification of a Negative Index of Refraction*, and J. B. Pendry's (2001), *Negative Refraction Makes a Perfect Lens*.

Shamonina and Solymar assert that Veselago's speculation on negative ϵ and μ , though it should have grabbed headlines at the time, remained dormant until uncovered by Smith et al. Smith et al validated Veselago's speculation by publishing an experimentally verified design for an artificial material which produced both negative permeability and negative permittivity in the same frequency band. Later, Shelby et al (to include Smith) published their experimental observations of the negative index of refraction in an artificial material. It was finally Pendry's publication, which, in providing the new theory with the practical application of a perfect lens, opened the scientific floodgates.

Though these four papers are considered pivotal for launching the subject of metamaterials, Shamonina and Solymar also enumerate those forerunning topics which were alive and flourishing at the time of the metamaterial upsurge. Accordingly, there also have been a large number of springboard topics which continue to sustain interest and development in the subject. The forerunners of the metamaterials subject include:

1. Effective Medium Theory (beginning 1850)
2. Negative permittivity (beginning 1929)
3. Negative permeability (beginning 1955)
4. Plasmon polaritons (beginning 1969)
5. Backward waves (beginning 1904)
6. Theory of Periodic Structures (beginning 1892)
7. Resonant elements small relative to the wavelength (beginning 1939)
8. Frequency filters made of periodically arranged resonant elements
(beginning 1965)
9. Slow-wave structures (beginning 1960)
10. Super-directivity, super-resolution, sub-wavelength focusing and imaging
(beginning 1922)
11. Inverse scattering (beginning 1970)
12. Bi-anisotropy (beginning 1992)
13. Photonic band-gap materials (beginning 1987)
14. Waves on nano-particles (beginning 1998)

Using the forerunners as the historical foundation, Shamonina and Solymar explain that the four seminal papers taken together served as a catalyst for creating a new field of study.

Papers started to pour in. The subject had not had a name as yet but everyone knew which the fundamental papers were. People agreed and disagreed. The large majority agreed with a few dissenting voices... The beauty of this new field was that it had so many different aspects and a very low barrier to entry. Reading the four seminal papers anyone doing research (or just having an interest) in any of the topics mentioned must have been tempted to become a Metamaterialist... Scores of people entered the field, contributions poured in

leading to an exponential increase in the usual measures of research activities (scientific papers and books, number of groups involved, number of citations, grants received, articles in popular science journals, etc.) bringing forth the necessity of baptism. [11]

Defining Metamaterials and Metamaterial Science

Despite the sense of history, it is important to note that to date there is neither a formal definition for a metamaterial nor for metamaterial science. According to Shamonina and Solymar, “*By now there is a consensus that all the phenomena associated somehow with wave propagation on resonant elements and with negative refraction should be known under the generic term of metamaterials.*”

Ari Sihvola, in the journal, *Metamaterials*, introduces the critical difficulty of defining a metamaterial. “*Metamaterials are hard to define and classify... What do all the concepts mean that are being used in discussions on material electromagnetics?... And what are all those abbreviations?*” [12]

Sihvola analyzes some of the most visible definitions of metamaterials to include those from Wikipedia, the Metamorphose Network of Excellence (European Union), the DARPA Technology Thrust program on metamaterials, and researchers Pendry and Smith. With no universal consistency, Sihvola’s concern is that in the great activity of research and in the high rate of publications on metamaterials, the number of different definitions will overwhelm any complete understanding of the term.

However, within the many definitions, certain salient characteristics can be distinguished. Specifically, metamaterials are popularly expected to exhibit properties that are neither observed in the separate constituent materials nor observed in nature.

Secondary to these, the scale (physical dimensions) and periodicity (the order of the structure) of a metamaterial is also deemed to be important. In some definitions, these secondary characteristics may either be present or absent, so Sihvola questions if the emphasis for scale and periodicity is essential or if the emphasis is just a side-effect of holding unproven expectations.

Sihvola further demonstrates that attempting to classify any material in general is very difficult. Sihvola assumes two extremes of material type: that which possesses global properties qualitatively different than its constituents and that which possesses global properties quantitatively averaged by its constituents. Starting with one extreme and working towards the other, Sihvola quickly concludes that definitions are sometimes too restrictive and problematic, sometimes too inclusive and contradictory, or otherwise inconsistent with common characterizations. Of particular concern is how difficult it is to find unambiguous language altogether.

Sihvola concludes that perhaps the trouble with metamaterial definitions is due to attempts to qualitatively distinguish the metamaterial mixture from the metamaterial ingredients. In the expectations for emergent global properties there is no popular expectation of the mixture to directly inherit properties of the ingredients. Actually, the expectation is for the mixture to exhibit traits not present in any ingredient. The difficulty then, is, anticipating what the global properties will be without any indication of where or how they will originate.

By comparing metamaterial science to chemistry, Sihvola ponders whether a reductionist approach is an appropriate way to define a metamaterial. The reductionist approach says that higher-level phenomena are explainable by deeper disciplines, i.e. all

chemical phenomena can be predicted by the principles of quantum physics. However, the popular expectations of metamaterial science imply the opposite in that the higher-level phenomena of the mixture cannot be readily predicted by the lower-level phenomena of the ingredients.

Therefore, in quoting the paleontologist Stephen Gould, “*Taxonomy (the science of classification) is often undervalued as a glorified form of filing... but taxonomy is a fundamental and dynamic science...*,” Sivhola implies that defining metamaterials cannot be a simple, rote and reductionist task. Rather, it can involve extensive amounts of creativity and familiarity with metamaterial ingredients and mixtures that are tirelessly measured, characterized and sorted.

Technical Details from Design Inspirations

In support of the aforementioned need for taxonomy, the BANTAM 2-D FBS implements a hybridized form of three accepted techniques for measuring and characterizing electromagnetic properties of materials. Technical details of these design inspirations are introduced below and are discussed throughout the methodology of Chapter 3.

BANTAM

The BANTAM was originally constructed to supplement the far-field measurement capability of the Air Force Research Laboratory (AFRL) Radiation and Scattering Compact Antenna Laboratory (RASCAL). The BANTAM validated and

predicted RASCAL far-field measurements through a large dynamic range of near-field measurements [5]. Full technical detail can be found in C. M. Shaffe's (2004), *Air Force Research Laboratory: BANTAM*.

BANTAM Chamber

The BANTAM chamber is rectangular and constructed of aluminum beams manufactured by 80/20 Inc. The chamber is roughly 8.5' wide, 6' deep, and 6' tall. The front wall contains three side-by-side access doors and the ceiling contains two side-by-side access panels. The floor is divided into nine removable panels of honey-combed aluminum. A rotary pedestal is mounted to the central floor panel. The BANTAM chamber stands on four legs with the BANTAM floor 11" above the laboratory floor.

Linear Translation Rails

The BANTAM's linear translation rails are manufactured by THK Co., Ltd. The rail running from side-to-side is designated the *long axis* and the rail running from front-to-back is designated the *short axis*. The long axis is mounted with linear bearings to the 80/20 wall studs of the chamber. The short axis is mounted to the underside of the long axis, but the short axis does not mount directly to the chamber frame. The moment load rating for the free-hanging ends of the short axis, significant to the methodology of Chapter 3, is 160.48 ft-lbs. Together, the two rails can be raised or lowered on the linear bearings.

Absorber

The anechoic absorber is manufactured by Cuming Microwave. Each piece of absorber is approximately 2' by 2', but each piece has been custom trimmed to ensure the best fit within the chamber. The absorber on the floor is the 12" pyramid style. The absorber on the ceiling and the top two feet of each wall is the 8" pyramid style. The absorber on the bottom four feet of each wall is the 8" wedge style. The reflectivity of the absorber at normal incidence is approximately 30-50% from 2-18 GHz. Figure 2 depicts the original configuration of the BANTAM.



Figure 2: Original Configuration of BANTAM

Control Hardware

All BANTAM functions are controlled by a single computer. The primary BANTAM functions are RF measurement and motion control. RF measurements are taken through an HP8720C (50 MHz – 20 GHz) network analyzer. Motion control is maintained by a Computroller 6k4 motion controller. The network analyzer is connected to the antenna under test and the near-field probe with RF cable leading through the floor and the left BANTAM wall. The motion controller is connected to three stepper motor drives on each of the long, short and rotary axes. Each axis has magnetic limit switches to prevent over-reach during scanning and a home switch to give an absolute position reference at power-up.

Control Software

The BANTAM control software was written by Charles McNeely (AFIT/ENG staff collaborator for thesis detailed design) in LabVIEW. The LabVIEW control software offered tremendous flexibility for incorporating the BANTAM 2-D FBS. There are three software pages to be viewed: the HP8720 Setup Page, the Data Collection Page and the Motion Control Page.

The HP8720 Setup Page has seven main controls: Scan Type Selector (full area scan, single-axis scan or single-position scan); Frequency List (frequency start, stop and increment); Scan Channel (S11, S12, S21 or S22); Number of Averages (2^n , n=0...8); Power Level (dBm); Step/Ramp Mode; Polarization (vertical or horizontal).

The Data Collection Page has two main controls: acquire data and save data.

During data acquisition, a coordinate display allows the user to monitor the progress of the scan. Saved data is readable in ASCII format and consists of a series of three-axis, frequency, and real/imaginary field data points.

The Motion Control Page provides software limit switches, acceleration and speed control, and scan-position control (start, stop and increment) for each axis. The Motion Control Page can be useful to test-drive the scan area prior to taking measurements.

Additional Information

The appendices in [5] provide standard measurement procedures, drawings and parts lists for the motion control box, diagrams for the network analyzer interconnects, functional diagrams of the LabVIEW software, and other hardware documentation. Of immediate importance to the BANTAM 2-D FBS are the specifications of the absorber, the stepper motors, the limit switches, and the linear rails. These will be considered in the methodology of Chapter 3.

Advantages and Disadvantages to Thesis Design

The BANTAM offers many design advantages to this thesis. Foremost is the pre-existing near-field scanning capability. Other advantages, not in priority order, are: 1) the pre-fabricated and dedicated anechoic chamber; 2) the developed software and controls; 3) the full documentation of all hardware and software; 4) the plug-and-play nature of the chamber.

The primary disadvantage is the size of the BANTAM chamber. The BANTAM 2-D FBS, being housed within the chamber, must be built to pre-defined dimensions. Other potential disadvantages arise from using the pre-existing hardware. For example, the top plate of the PPWG is expected to be much heavier than the current near-field probe, so static and dynamic limits of both the stepper motors and the linear rails must be investigated and components must be replaced or reinforced as necessary. Mitigation of these disadvantages is addressed by design and detailed in Chapter 3.

GTRI Focused Beam System

The intent behind the design of the GTRI FBS was to compliment the S-parameter measurement capabilities of common transmission-line systems such as waveguides, coaxial lines and resonant cavities. Transmission-line fixtures are designed for homogeneous, low-loss material samples and suffer from inaccuracies caused by inhomogeneities, sample conductivity, and air gaps between the sample and transmission line. The primary advantage of the free-space focused-beam system over a transmission line is broadband coverage, easy sample preparation, use of varying incidence angles, and elimination of air gap errors (no physical contact with sample). The free-space method is often more appropriate for characterizing inhomogeneous, lossy and anisotropic materials as well. Full technical detail can be found in GTRC's (2007), *Users Guide: Theory and Operation of the GTRI Focused Beam System* [8].

The standard GTRI FBS was derived from the Naval Research Laboratory Arch and uses lenses to focus microwave energy onto a sample. This focusing simulates plane wave illumination of the sample while minimizing illumination of a sample's edges (a

source of measurement error caused by diffraction). The GTRI FBS uses HP/Agilent Network Analyzers and Octave/MATLAB[©] data processing for S-parameter measurements. The system is shown in Figure 3.

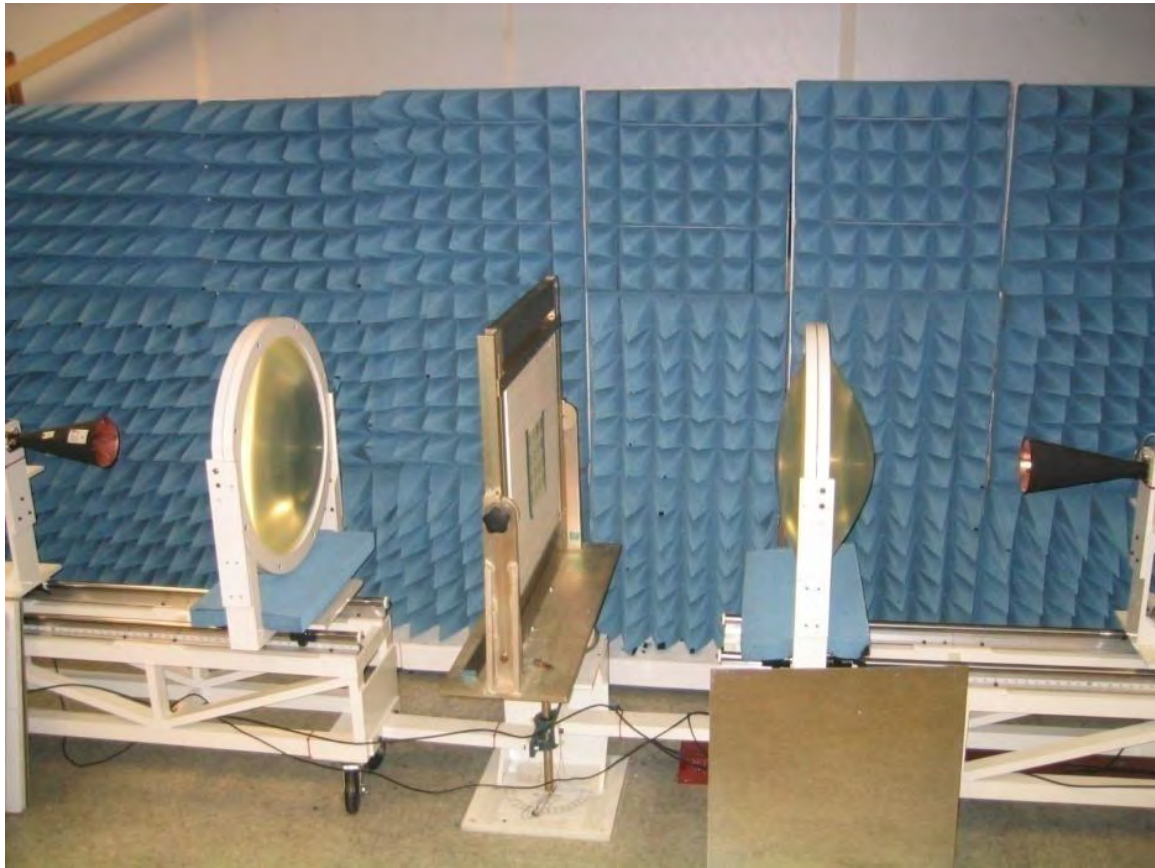


Figure 3: GTRI Free-Space Focused Beam System

Theory and Design of GTRI FBS

The GTRI FBS is modular in design such that it can be used for monostatic and a variety of bistatic configurations. The system has two arms, each supporting an antenna and a Rexolite ® lens. The sample holder, residing between the arms, can be turned by a

computer. The position of the antennas and lenses on the arms can be varied along translation rails for varying focus.

The system is usable in bandwidths from 2-110 GHz per antenna performance. Optimally positioning the antennas and lenses results in an assumed plane wave on the target with all energy assumed to be interacting with the target. These assumptions require a minimum sample size to eliminate illumination of the sample edges. Absorber carts surround the system to reduce spurious emissions and reflections from other laboratory equipment. A parts list is included in [8].

GTRI derives many equations in [8] that result in the design of the lens' physical profiles. Parameters under consideration include the excitation antenna's radiation pattern, desired lens focal lengths, lens material index of refraction, desired Gaussian beamwaist and position, sample size, etc. Each lens is considered as having a collimating half and a focusing half. In designing the profile for the collimating half, geometrical optics was used, and in designing the profile for the focusing half, Gaussian optics was used. In their document, GTRI provides many rules of thumb when considering focusing limit constraints, amplitude taper on lens and target, phase change within the beam, etc.

Calibration and Data Processing

As detailed in [8], the GTRI FBS uses response and response/isolation calibration methods for S-parameter measurements. Each method solves for and corrects a different set of systematic errors. Such errors include directivity (E_{df}), reflection tracking (E_{rf}), transmission tracking (E_{tf}) and isolation (E_{xf}) errors

In response calibration, the GTRI FBS uses one calibration standard (a *thru* for transmission paths and a *short* or *open* for reflection paths) to measure the signal path frequency response exclusive of source/load match and directivity/isolation effects. With this style of calibration, the transmission coefficient of a sample is simply

$$S_{21} = \frac{S_{21}^{measured}}{S_{21}^{RESPONSE}} \quad (1.1)$$

where $S_{21}^{RESPONSE}$ is the measurement of the standard and $S_{21}^{measured}$ is the measurement of the sample. The reflection coefficient of a sample is then,

$$S_{11} = -\frac{S_{11}^{measured}}{S_{11}^{RESPONSE}} \quad (1.2)$$

In response/isolation calibration the GTRI FBS uses two calibration standards (thru, short, open, or load) for transmission and reflection measurements. In response/isolation calibration, more accuracy is expected than in response calibration because response/isolation calibration accounts for more error sources. The coefficients for transmission and reflection are respectively,

$$S_{21} = \frac{S_{21}^{measured} - S_{21}^{isolation}}{S_{21}^{RESPONSE} - S_{21}^{isolation}} \quad (1.3)$$

$$S_{11} = -\frac{S_{11}^{measured} - S_{11}^{isolation}}{S_{11}^{RESPONSE} - S_{11}^{isolation}} \quad (1.4)$$

In each calibration method, GTRI advises on the criticality of precise use of the calibration planes to measurement accuracy. Shifting the sample from the calibration plane will introduce phase shifts in the electrical path and defocusing in the beam.

Further, GTRI discusses appropriate techniques for gating and windowing measurement signals for optimum data extraction.

Advantages and Disadvantages to Thesis Design

The GTRI FBS offers many design advantages to this thesis. Primarily, the lens design process is readily applicable and covers the frequency band of interest. It is anticipated that the BANTAM 2-D FBS will also inherit easy sample preparation and plane wave illumination with minimized sample edge effects. Further advantages are, not in priority order: 1) the availability of the GTRI FBS for study, use and practice; 2) near-identical maintenance expectations for lenses; 3) analogous calibration methods and kits; 4) similar target positioning options (normal vs. oblique incidence); 5) similar measurement and data-processing techniques.

The primary disadvantages of the GTRI FBS are the potential for external noise and clutter interference (despite the absorber carts) and the frequency-driven shift of the horn antennas' phase center. These disadvantages are respectively mitigated by the BANTAM anechoic chamber and use of monopole antennas as described in Chapter 3.

Shelby Parallel-Plate Waveguide

The intent behind Shelby's PPWG was to study microwave scattering (8-12 GHz) of a structured metamaterial that exhibits a negative effective index of refraction. Full technical details can be found in R. A. Shelby et als' (2001), *Experimental Verification of a Negative Index of Refraction* [9].

The Shelby PPWG was used to measure the scattering angle of waves transmitted through a metamaterial prism. The illumination was transverse magnetic polarization (electric field perpendicular to the parallel plates) with the excitation fed into the PPWG through a coaxial cable (effectively a monopole) one meter from the prism. The waves were confined above and below by metal plates and laterally by flat anechoic absorber. The waves, after propagating down the rectangular plates and being refracted by the prism, were measured by a waveguide detector that swung around the circular plates in 1.5 degree steps. This detector measured the exit angle of the waves for the subject metamaterial prism and a Teflon prism used as an experimental control.

A Shelby PPWG model was recreated in CST for use in this thesis and is shown in Figure 4. In the model, the dimensions of the rectangular plates are approximately 100 cm long by 30 cm wide. The circular plates are 30 cm in diameter. The space between the plates is 1.2 cm. The type of absorber used in the experiment had not been defined in the document, so Eccosorb LS-30 was used arbitrarily in the model. The space between the absorber is 9.3 cm and the width of the absorber was estimated to be about 9 cm. The angle between the two prism faces was defined as 18.43 degrees. In the model, the prism was Teflon.



Figure 4: CST Model of Shelby PPWG

For referencing in this thesis, CST was used to model the propagation of 8-12 GHz waves through the Teflon prism. This is shown in Figure 5 for 8 GHz. In this figure, the waveguide is clearly over-moded between the absorber. The presence of over-moding would seem to spread the exiting beam as the numerous modes approach the prism from different incident angles, but nothing is mentioned in the article to this effect.

CST fields were then evaluated along a circular path around the prism to determine the exit angle of the waves. This evaluation is shown in Figure 6 for 8, 10 and 12 GHz. At approximately 11-13 cm around a 24 cm diameter evaluation circle, the peak amplitude corresponds to an exit angle of approximately 30 degrees off the normal of the prism's second face. This is in close agreement to the 27-degree refraction angle published in the experiment.

Advantages and Disadvantages to Thesis Design

The Shelby PPWG offers one distinct design advantage to this thesis - a simple structure to excite and guide waves towards a material sample. This advantage presumes the ideal operation of the waveguide, i.e. operation in the fundamental mode only (even

though the Shelby PPWG does not operate this way). This advantage also relies on the use of monopoles, having a common phase center for all frequencies.

The primary disadvantage of the Shelby PPWG is the method of confining the illumination beam in the transverse direction. The use of flat anechoic absorber confines the beam to the area of the first prism face, but it also appears to be the cause of the over-moding, i.e. what should be a PPWG is behaving more like a rectangular waveguide with heavy loss in the side walls. Confining the beam in this way eliminates edge illumination of the prism, but it is accomplished at the expense of introducing higher-order modes. In order to use differently sized targets, it is assumed that the absorber would have to be custom packed around each target, changing the mode structure each time.

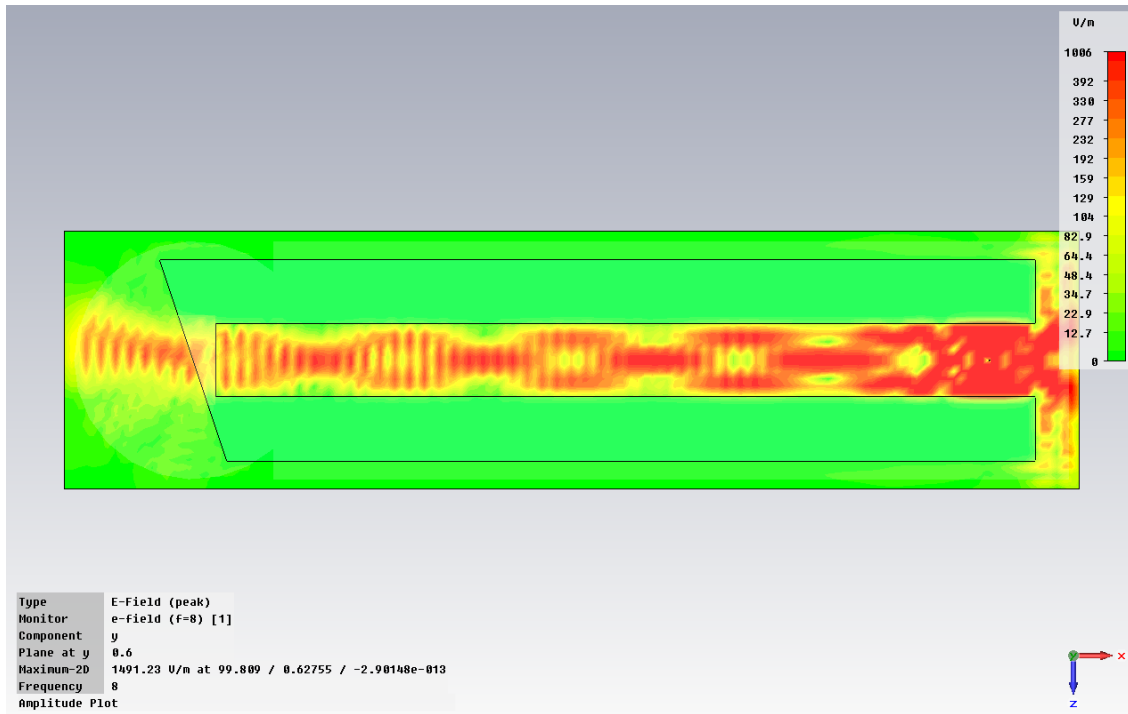


Figure 5: CST Model of Shelby PPWG Operating at 8 GHz

In designing the BANTAM 2-D FBS, this disadvantage will be addressed by maintaining a true PPWG. The incident beam will be confined to the interior of the target by the focusing action of the lenses. The targets can then be fabricated to a standard length in the transverse direction.

Minor disadvantages of the Shelby PPWG are the small gap between the plates (1.2 cm or 0.47") and the design frequency of 8-12 GHz. The small gap would allow 8-12 GHz to propagate in the fundamental mode only but it leads to small targets heights by necessity. The BANTAM 2-D FBS will be designed for 2-18 GHz, propagating as near the fundamental mode as possible, and will allow targets up to 2" tall.

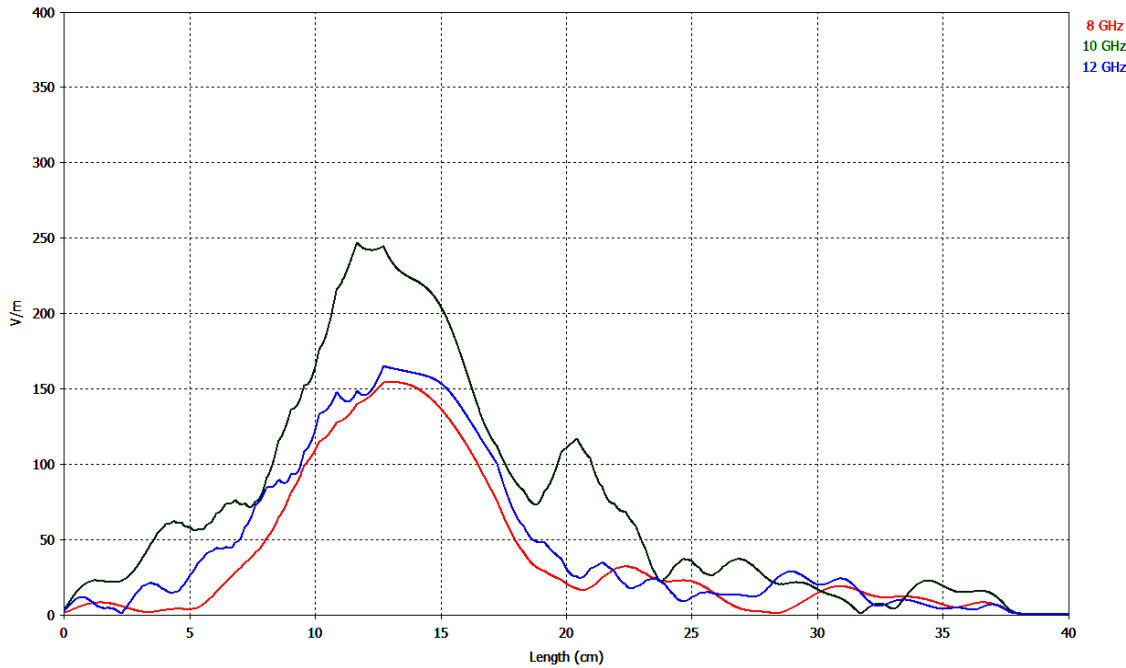


Figure 6: CST Model of Shelby PPWG Evaluated Along Circular Path

III. Methodology

This chapter presents the methodology of designing, fabricating, building and tuning the BANTAM 2-D FBS. The first section highlights the pre-existing design constraints placed on the BANTAM 2-D FBS by the original BANTAM design and by the lens material - the lens material was already on-hand at the commencement of this thesis. The second section highlights the geometrical and electrical design theory of the individual hardware components, presenting the component design information in the form of theory, simulation and material specification. Following each component's design data, the details behind fabrication are discussed. The third section highlights building the components, including the pre-existing software and control components, into the final system architecture and discusses mechanical tuning and basic electrical calibration. This final section will lead to the results of Chapter 4 where the BANTAM 2-D FBS is characterized and raw material measurements made by the physical system will be compared to raw material measurements made by the simulated system.

Pre-existing Design Constraints

BANTAM Chamber

The primary design constraint for the BANTAM 2-D FBS was the physical size of the BANTAM chamber. With anechoic absorber in place, the usable space within the chamber measures approximately 76" from side to side and approximately 52" from front

to back. Without the 12" pyramidal absorber on the floor, the maximum usable vertical space measures approximately 50" from the floor to the underside of the short axis. If necessary, the floor panels could be removed to gain the additional 11" to the laboratory floor.

Given these dimensions, the largest expected size of the parallel-plate waveguide is approximately 76" x 52". In the vertical direction, placement of the top plate is constrained by the position of the translation rails. Though adjustable, the current position of the rail system, approximately 50" above the BANTAM floor, will be a constraint due to the difficulty in properly lowering, leveling and squaring it relative to the rest of the chamber. Vertical placement of the bottom plate is constrained by the optimum spacing between the two plates and the distance to the BANTAM floor. Outright, this constraint is addressed by using a scissor lift, placed on the BANTAM floor, to raise the bottom plate into position below the top plate.

The translation rail system provides a further constraint in its mounting fixtures. The ends of the long axis are mounted to the 80/20 wall studs of the chamber, but the short axis is mounted to the underside of the long axis at a central point. The constraint is in the moment loads that can be placed on the ends of the short axis as the top plate scans. This rating is 160.48 ft-lbs. This means that at an arbitrary forward or reverse scan distance of 12", the top plate must weigh no more than 160 lbs. This rating does not indicate how the axis rail will flex under the load, so to be safe, an arbitrary weight buffer of 25% indicates that the top plate must weigh no more than 120 lbs. For ideal scanning performance (to maintain plates in parallel), an unknown amount and type of rail flexing indicates that the short axis rail should be reinforced with a structure that ties it securely

to the BANTAM frame. The reinforcements will allow the short axis to travel the length of the long axis, but the ends of the short axis will no longer hang free of the BANTAM frame. The specifications of the reinforcements will be described later. The same load concern could be addressed in the performance of the stepper motors as well – fortunately, the weights involved do not approach the motor load ratings as closely.

For translation of the top plate over the bottom plate, the perimeter of the BANTAM chamber puts a constraint on the size of the top plate, i.e. the top plate must be small enough to move over a meaningful scan area within the confines of the chamber. The size of the top plate is also inversely constrained by the size of the components that will be sandwiched between the parallel plates. The top plate must be large enough to cover all components and maintain a quality waveguide structure while scanning.

Finally, the BANTAM floor provides the constraint of static weight. While there is no specific rating published, the weight of the bottom plate and an appropriately sized scissor lift must be considered. It would be reasonable to assume that the combined weight of these components should not exceed that of several men (400-500 lbs).

Lens Material Constraints

To achieve similarity with the GTRI FBS lenses, Rexolite was provided for the BANTAM 2-D FBS lenses prior to the commencement of this thesis.

Rexolite is advertised as a unique, cross-linked polystyrene microwave plastic with outstanding dielectric properties. The dielectric constant is maintained at 2.53 (index of refraction is 1.59) through 500 GHz with extremely low dissipation factors. Rexolite is able to withstand high voltages and has been proven superior to acrylics,

epoxies, urethanes and other plastics for electrical resistance applications. Rexolite castings are stress-free and do not permanently deform under normal loading. Optical transmission is approximately equal to acrylic and acoustical impedance is close to that of water. Rexolite handles well in all machining operations and handles well with water, alkalis, alcohols, and aliphatic hydrocarbons (aromatic and chlorinated hydrocarbons will cause swelling and should be avoided). Rexolite is 15% lighter than acrylic and less than half the weight of Teflon. Rexolite adhesives and copper claddings are commercially available [13].

The Rexolite on-hand at AFIT was in the form of a 48" x 24" slab approximately 2" thick. Practical and timely machining constrained the thickness of the lenses to the slab thickness of 2" and thus constrained the spacing of the waveguide to 2".

At a 2" spacing, higher-order propagating modes will be supported in the PPWG over the 2-18 GHz band. Traditionally, it is desirable to operate a waveguide such that it only supports the dominant mode for all frequencies, but in this case, to achieve propagation of only the fundamental (dominant) mode for all frequencies, the spacing of the plates must be less than 0.328", or, less than a half-wavelength at 18 GHz. The 2" spacing constraint given by the lens material thus introduces a 600% increase in spacing and thus, allows the support of six higher-order propagating modes at 18 GHz. Allowing the excitation of these modes into the PPWG will cause undesirable phase variations and interference in the vertical direction between the plates and thus, over the face of a target. Exciting the higher-order modes will also cause phase variations and interference in the propagation direction as each mode simultaneously propagates down the waveguide at

different velocities. The nature of the higher-order mode structure will be detailed later alongside a design for a component that should mitigate these effects.

Hardware Design Data (Theories, Simulations, Specifications & Fabrication)

Monopoles

Theory and Simulation

A monopole is an obvious choice to excite the BANTAM 2-D FBS as it is the best candidate to represent a point source that emanates cylindrical wavefronts having a common phase center for all frequencies. As the GTRI FBS lenses are designed to reformat spherical wavefronts emanating from horn antennas, the BANTAM 2-D FBS lenses will be designed to reformat cylindrical wavefronts emanating from monopoles.

Monopoles were simulated in CST-MWS to determine the proper length of the monopole beyond the surface of the PPWG plates. The monopole was modeled as a coaxial line with its outer conductor and internal dielectric mating flush with the inside surface of a ground plane. The inner conductor extends to a given length beyond the surface. The model dimensions were based on the coaxial line available in the laboratory. This model is shown in Figure 7. An example of the cylindrical wavefronts within a PPWG for 2 GHz (a snapshot of a CST phase animation) is shown in Figure 8.



Figure 7: CST Model of a Monopole

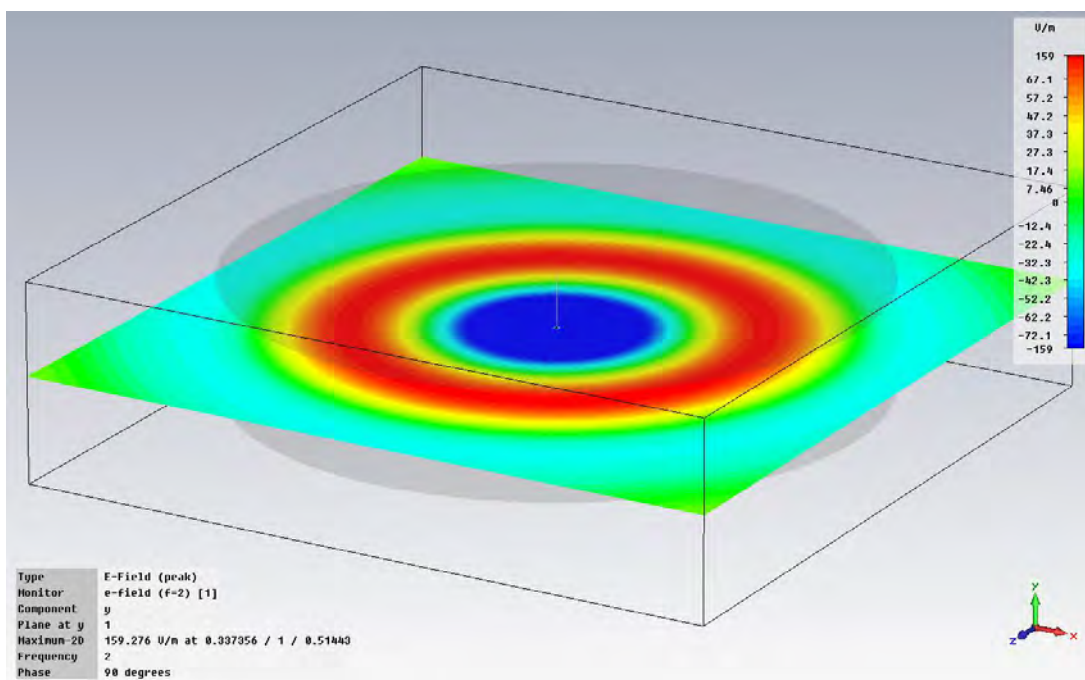


Figure 8: CST Monopole Cylindrical Wavefronts at 2 GHz

A parametric study was conducted in CST to determine if there was an optimum monopole length. For a particular frequency, a monopole on a single ground plane will be most directive in the radial direction (under far-field considerations) if its height is approximately one-quarter wavelength to one-half wavelength. This is illustrated in Figure 9 (elevation) and Figure 10 (azimuth) for a quarter-wavelength (0.164") and half-wavelength (0.328") monopole operating at 18 GHz.

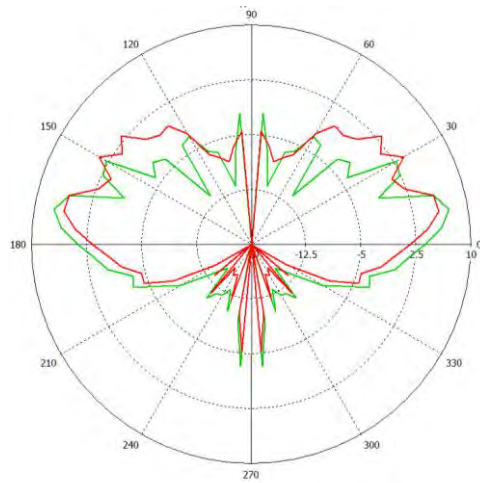


Figure 9: Quarter-Wave (red) and Half-Wave Monopole Elevation Pattern at 18 GHz

As the height of the monopole increases, the radiation pattern becomes lobed for this particular frequency and less directive and less powerful in the radial direction. This is illustrated in Figure 11 (elevation) and Figure 12 (azimuth) for a 3-wavelength (1.969") monopole operating at 18 GHz. A monopole of this height, at this frequency, and with this lobe structure, will directly excite higher-order modes into the 2" PPWG at the relative strengths as indicated in the figure and as indicated in upcoming discussion.

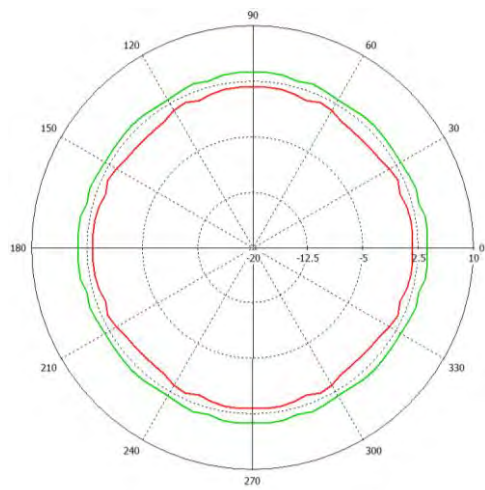


Figure 10: Quarter-Wave (red) and Half-Wave Monopole Azimuth Pattern at 18 GHz

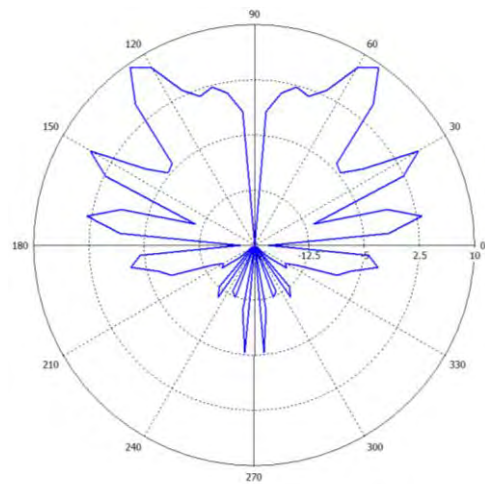


Figure 11: Three-Wavelength Monopole Elevation Pattern at 18 GHz

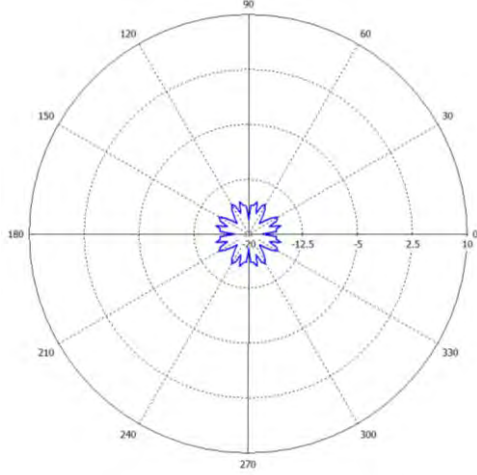


Figure 12: Three-Wavelength Monopole Azimuth Pattern at 18 GHz

As the height of the monopole decreases below a quarter-wavelength for a particular frequency, both the radiation pattern and the radial power stays consistent down to approximately an eighth-wavelength. Below an eighth-wavelength, the radiation pattern becomes directed primarily at 45 degrees of elevation and the radial power decreases. This is illustrated in Figure 13 (elevation) and Figure 14 (azimuth) for a 0.025-wavelength (0.148"), eighth-wavelength (0.738") and a quarter-wavelength (1.48") monopole operating at 2 GHz.

Based on these far-field considerations, for operating over frequencies between 2-18 GHz, the monopole's optimum length should be between 0.328" (half-wavelength at 18 GHz) and 0.738" (eighth-wavelength at 2 GHz). The number halfway between these values (0.533") corresponds roughly to a half-wavelength at 10 GHz which is the midband frequency. Operation of an antenna of this length would give the radiation patterns for a tenth-wavelength monopole for 2 GHz, a half-wavelength monopole for 10 GHz, and approximately a one-wavelength monopole for 18 GHz as shown in Figure 15,

Figure 16, and Figure 17. Of course, this optimization is bound to a single monopole operating over 2-18 GHz, rather than, ideally, several monopoles of various heights operating over frequency octaves.

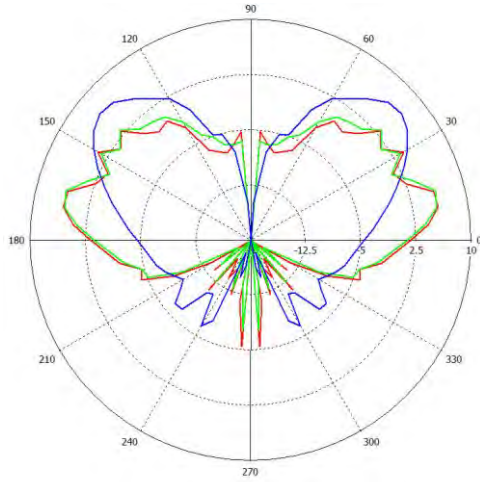


Figure 13: Quarter-Wave, Eighth-Wave and 0.025-Wave (blue) Elevation at 2 GHz

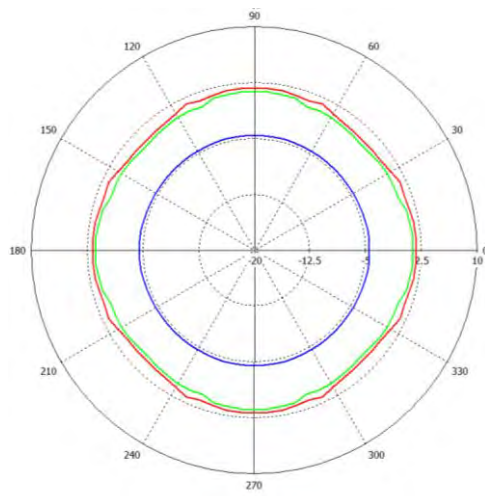


Figure 14: Quarter-Wave, Eighth-Wave and 0.025-Wave (blue) Azimuth at 2 GHz

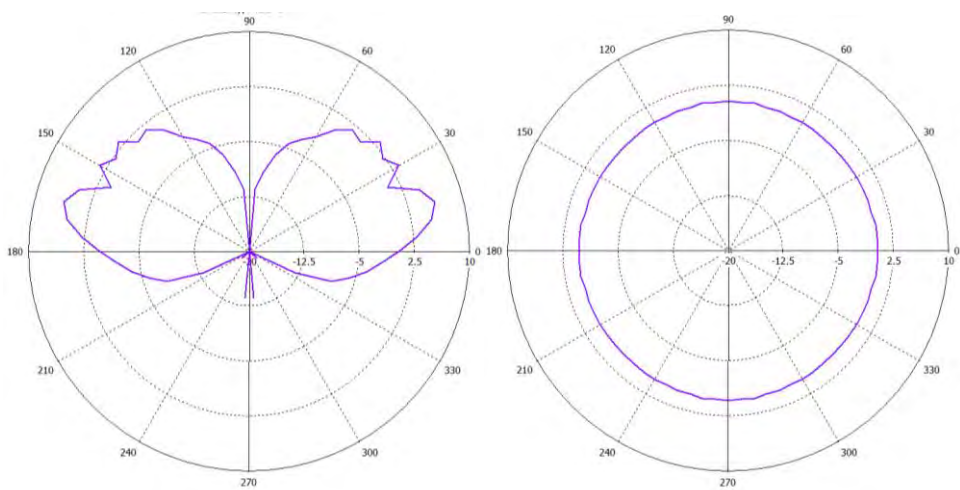


Figure 15: Half-inch Monopole (Tenth-Wavelength at 2 GHz) Radiation Patterns

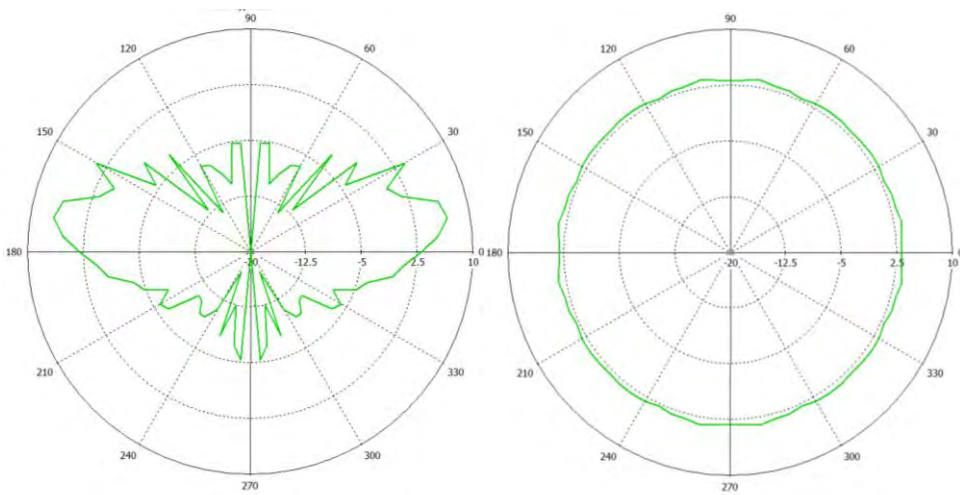


Figure 16: Half-inch Monopole (Half-Wavelength at 10 GHz) Radiation Patterns

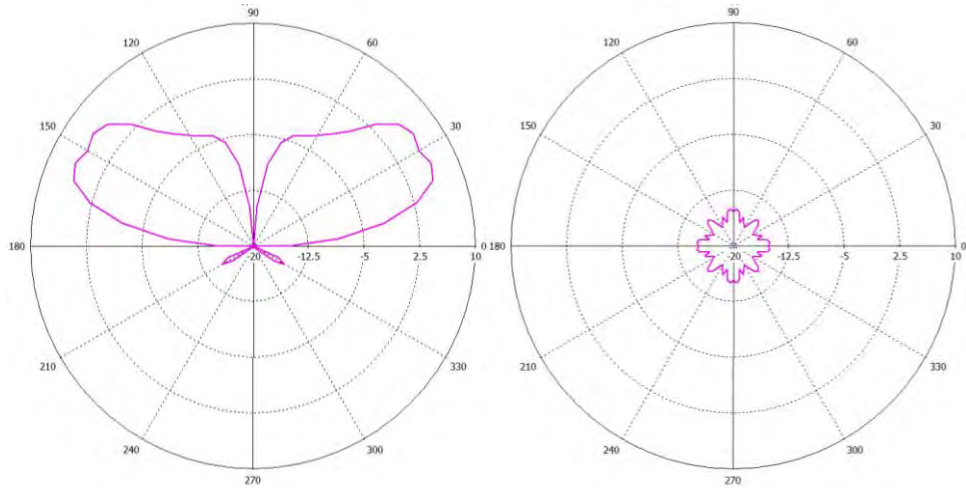


Figure 17: Half-inch Monopole (One-Wavelength at 18 GHz) Radiation Patterns

Specification

Independent of the height study, it was determined that the length of the scanning probe (also a monopole) should be approximately 2" just as the lens height and the plate spacing is 2". Spanning 2" achieves the best coupling between the scanning monopole and the energy in the gap between the plates. If the scanning monopole were as short as the optimum monopole length, coupling with all the available energy between the plates would be reduced. Based on the coupling requirement, and for similarity, the excitation monopoles on the bottom plate will be approximately 2" as well.

The actual length of the monopoles will be such that a small gap exists between the tip of the monopole and the opposite plate. Introducing this gap during the fabrication process brought the average monopole length to 1.916".

A final consideration on the use of a monopole in the PPWG is that with omnidirectional radiation, the system will waste radiated energy to all directions but the forward direction of each monopole. However, the energy waste is a worthy trade-off to

maintaining a point source representation. Upcoming component design will address how to manage this wasted energy.

Fabrication

Figure 18 shows the actual monopole to be used in the PPWG. The average length beyond the plate surface is approximately 1.916". The collar (outer conductor) of the coaxial adapter was ground flush with the internal dielectric. The monopole rod was stripped from a separate coaxial line (inner conductor) and is removable from the coaxial adapter. The monopole is installed into the PPWG by threading the coaxial adapter into the plate from the outside surface, ensuring a flush fit, and inserting the monopole rod. Of the three monopoles used in the BANTAM 2-D FBS, a left-side and right-side monopole on the bottom plate is used for the S-parameter measurements. A monopole extending downward from the surface of the top plate is used in conjunction with the left-side or right-side monopole for near-field scanning. All three monopoles are similar except that the scanning monopole is upside-down.



Figure 18: PPWG Monopole

Aluminum Sheets

Theory and Simulation

For a monopole with waves traveling in the radial direction, the waves' variation in that direction is represented by either Hankel function, $H_m^{(1)}$ or $H_m^{(2)}$. Such radial waves possess equiphases that are constant radius planes. The PPWG of the BANTAM 2-D FBS is a structure that supports radial waves and for the monopoles being used, the TM^z modes (electric field perpendicular to plates) are considered.

For the given analysis in [14], applying the boundary conditions of the PPWG to the magnetic vector potential function A_z results in

$$A_z(\rho, \phi, z) = [C_1 H_m^{(1)}(\beta_\rho \rho) + D_1 H_m^{(2)}(\beta_\rho \rho)] [C_2 \cos(m\phi) + D_2 \sin(m\phi)] \times [C_3 \cos(\beta_z z)] \quad (1.5)$$

where

$$\begin{aligned} E_\rho(0 \leq \rho \leq \infty, 0 \leq \phi \leq 2\pi, z = 0) &= E_\rho(0 \leq \rho \leq \infty, 0 \leq \phi \leq 2\pi, z = h) = 0 \\ E_\phi(0 \leq \rho \leq \infty, 0 \leq \phi \leq 2\pi, z = 0) &= E_\phi(0 \leq \rho \leq \infty, 0 \leq \phi \leq 2\pi, z = h) = 0 \end{aligned} \quad (1.6)$$

Based on the boundary conditions,

$$\begin{aligned} \beta_\rho^2 + \beta_z^2 = \beta^2 \Rightarrow \beta_\rho &= \pm \sqrt{\beta^2 - \beta_z^2} = \pm \sqrt{\beta^2 - \left(\frac{n\pi}{h}\right)^2} \\ n &= 0, 1, 2, \dots \\ m &= 0, 1, 2, \dots \text{ (because of periodicity of the fields in } \phi) \end{aligned} \quad (1.7)$$

and the cutoff frequencies of the PPWG can be shown to be

$$(f_c)_n^{TM^z} = \frac{n}{2h\sqrt{\mu\epsilon}} \quad n = 0, 1, 2, \dots \quad (1.8)$$

Further,

$$\beta_\rho = \begin{cases} \sqrt{\beta^2 - \left(\frac{n\pi}{h}\right)^2} = \beta \sqrt{1 - \left(\frac{f_c}{f}\right)^2} & f > f_c \\ 0 & f = f_c \\ -j \sqrt{\left(\frac{n\pi}{h}\right)^2 - \beta^2} = -j\beta \sqrt{\left(\frac{f_c}{f}\right)^2 - 1} = -j\alpha & f < f_c \end{cases} \quad (1.9)$$

and

$$\begin{aligned} Z_w^{+\rho} \left(TM_n^z \right) &= \frac{E_z^+}{-H_\phi^+} = -j \frac{\beta_\rho}{\omega\epsilon} \frac{H_m^{(2)}(\beta_\rho\rho)}{H_m^{(2)*}(\beta_\rho\rho)} \\ Z_w^{+\rho} \left(TM_n^z \right) \Big|_{f < f_c} &= j \frac{\alpha}{\omega\epsilon} \frac{K_m(\alpha\rho)}{d(\alpha\rho) [K_m(\alpha\rho)]} \end{aligned} \quad (1.10)$$

where $K_m(\alpha\rho)$ is the modified Bessel function of the second kind. For the wave impedance it can be shown that below the cutoff frequency for each mode, the wave impedance is capacitive and the modes are evanescent, i.e. the waveguide behaves as a capacitive storage element.

Table 1 displays f_c for each mode in the 2" PPWG. Note that the seventh mode is not supported when operating over 2-18 GHz.

Table 1: Higher-Order Modes in 2" PPWG

Mode	0	1	2	3	4	5	6	7
f_c (GHz)	0.000	2.951	5.901	8.852	11.803	14.754	17.704	20.655

By ray-tracing, the angle of incidence for the travel of each mode between the plates for a particular frequency can be reviewed. The incidence angle is defined by

$$\psi = \begin{cases} 0^\circ & \text{for } f = \infty \\ \cos^{-1} \left[\sqrt{1 - \left(\frac{f_c}{f} \right)^2} \right] & \text{for } f_c \leq f < \infty \\ 90^\circ & \text{for } f = f_c \end{cases} \quad (1.11)$$

Table 2 displays the angles of incidence for each mode of 2, 4, 8, 12 and 18 GHz. A dashed entry indicates an evanescent mode. Note that for each particular angle of incidence, as a mode reflects off of the top plate, a mirror wave is simultaneously being reflected from the bottom plate.

Table 2: Angles of Incidence for Propagating Higher-Order Modes

f (GHz)	2	4	8	12	18
Tsi-0 (deg.)	0.000	0.000	0.000	0.000	0.000
Tsi-1 (deg.)	-	47.535	21.644	14.235	9.435
Tsi-2 (deg.)	-	-	47.535	29.458	19.139
Tsi-3 (deg.)	-	-	-	47.535	29.458
Tsi-4 (deg.)	-	-	-	79.603	40.974
Tsi-5 (deg.)	-	-	-	-	55.050
Tsi-6 (deg.)	-	-	-	-	79.603

From these angles, the propagation path of each mode can be visualized. Figure 19 depicts a ray trace diagram of half of the mirrored propagating modes for 18 GHz. This serves as a basic guide to show where and how phase variations and interference will occur within the waveguide. The propagation path of each mode is depicted in order from the fundamental mode path to the sixth-order mode path followed by the overlaying

of all mode paths. Figure 19 does not indicate the relative power excited into each mode so the actual degree of interference cannot be visualized here.

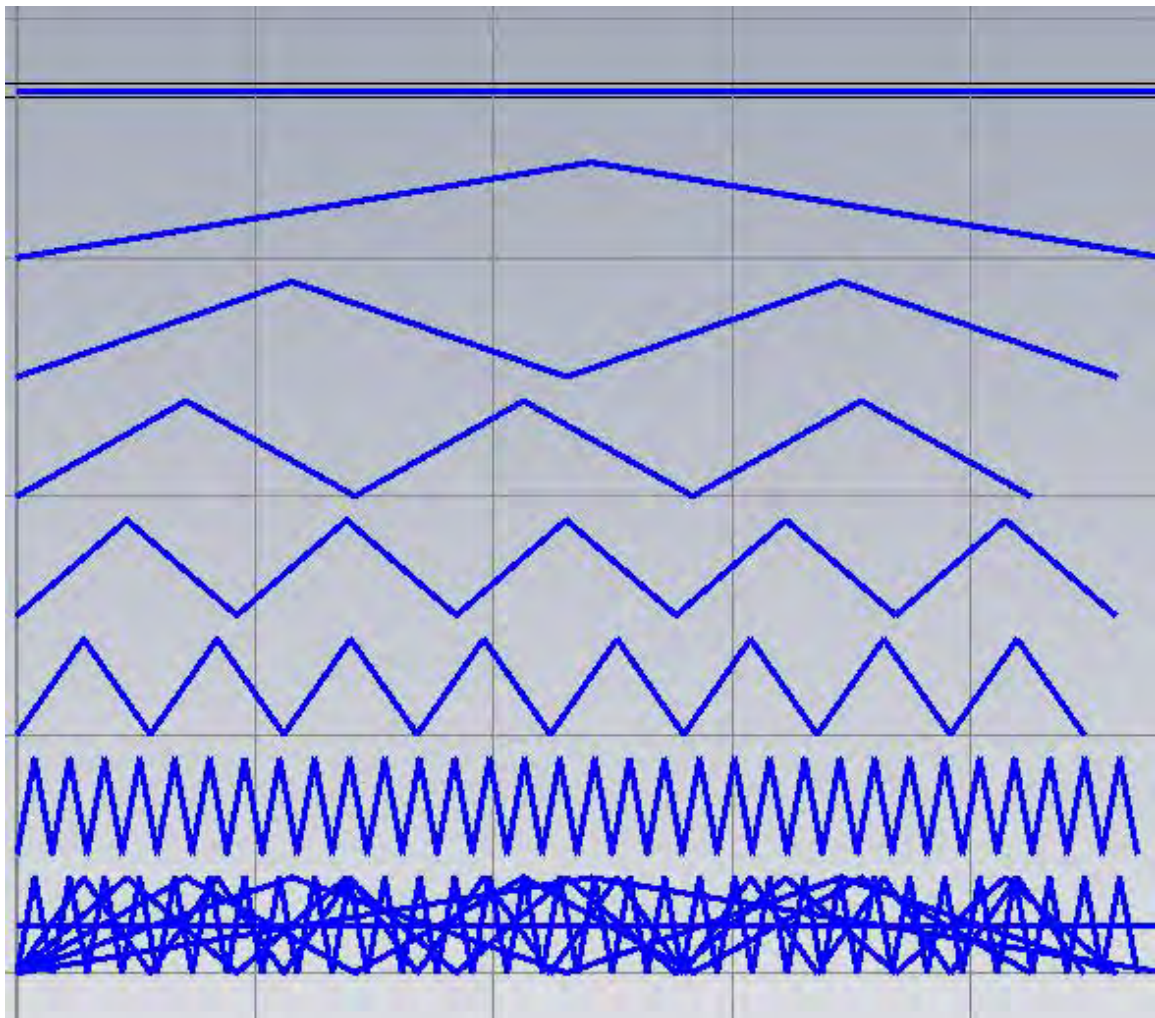


Figure 19: Ray-Trace Diagram of Propagating Modes for 18 GHz in 2" PPWG

However, the radiation pattern of a 3-wavelength monopole operating at 18 GHz (Figure 11) will aid the visualization. Referring back to Figure 11, it is apparent that the fundamental mode (propagating at zero degrees of elevation) will be excited the least.

The relative power of Mode 1, Mode 3 and Mode 5, propagating at the angles indicated in Table 2, correspond to the tips of the first, second and third elevated lobes of Figure 11. The relative power of Mode 2 and Mode 4 correspond to the first and second elevated nulls of Figure 11. The relative power of Mode 6 corresponds to the area slightly prior to the deep null at the monopole's zenith. From this visualization, it is apparent that a 3-wavelength monopole, operating at 18 GHz, will more readily excite, in order, Mode 5, Mode 3, Mode 1, Mode 6, Mode 4, Mode 2, then Mode 0.

Initially, the PPWG was modeled in CST as a small (12" diameter) circular-plate PPWG to study the qualitative aspects of the higher order mode propagation. Figure 20 shows the model. The excitation source is a coaxial monopole as describe above. The plates are modeled as perfect electrical conductors (PEC) of zero thickness for simplicity. The blue lines between the plates are field evaluation lines, along which, magnitude and phase variations can be plotted. For the overall qualitative effect, Figure 21, Figure 22, and Figure 23 each show a snapshot of phase animation in the radial direction for 2 GHz, 4 GHz, and 18 GHz. For these frequencies, 2 GHz is below the first-order cutoff so the figure shows only a propagating fundamental mode (planar wavefronts). For 4 GHz, the first-order mode has been excited so the figure shows the combined effects of a propagating fundamental mode and a propagating first-order mode. For 18 GHz, all higher-order modes that are supported by the spacing of the PPWG have been excited and the effects are apparent.

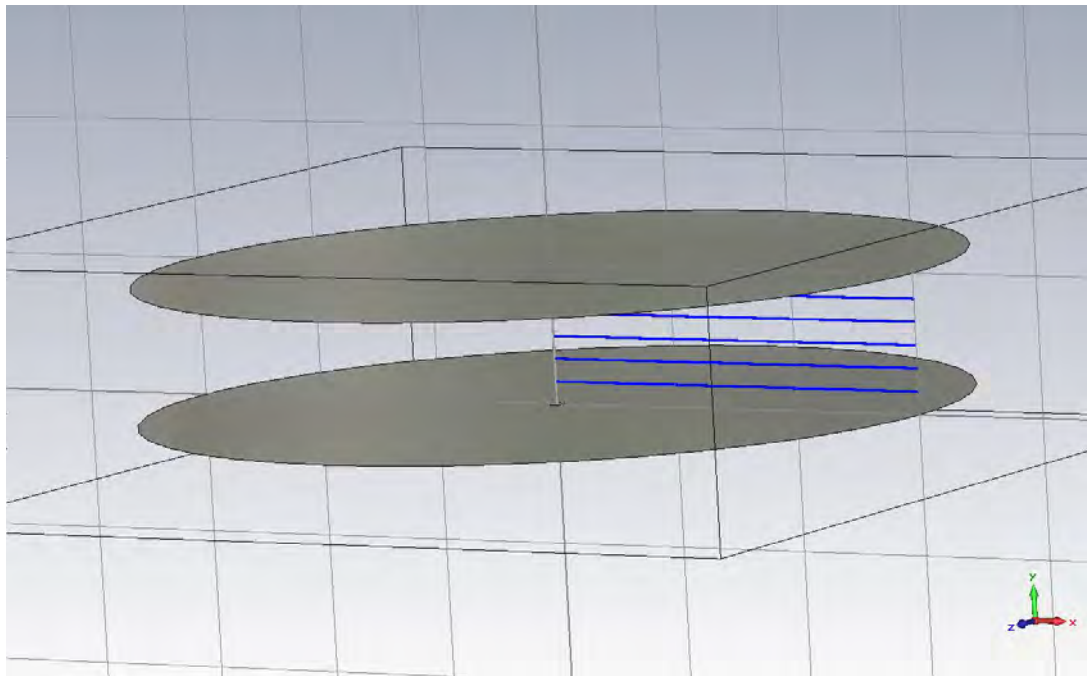


Figure 20: Circular Plate (12" Diameter) PPWG

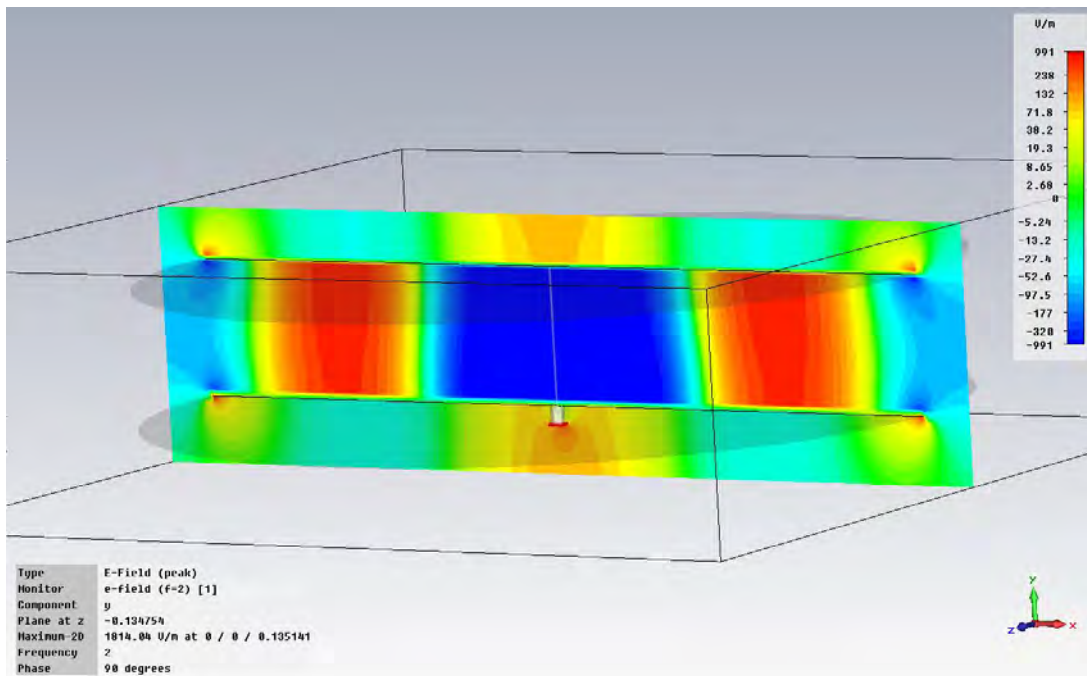


Figure 21: Phase Animation in 12" Circular Plate PPWG for 2 GHz

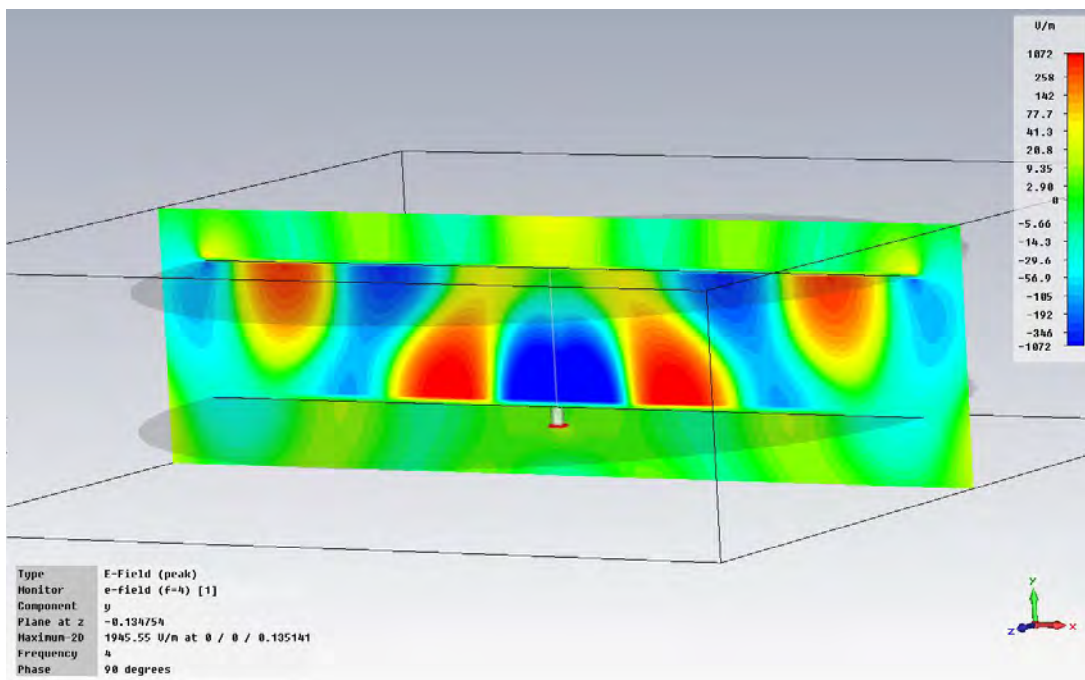


Figure 22: Phase Animation in 12" Circular Plate PPWG for 4 GHz

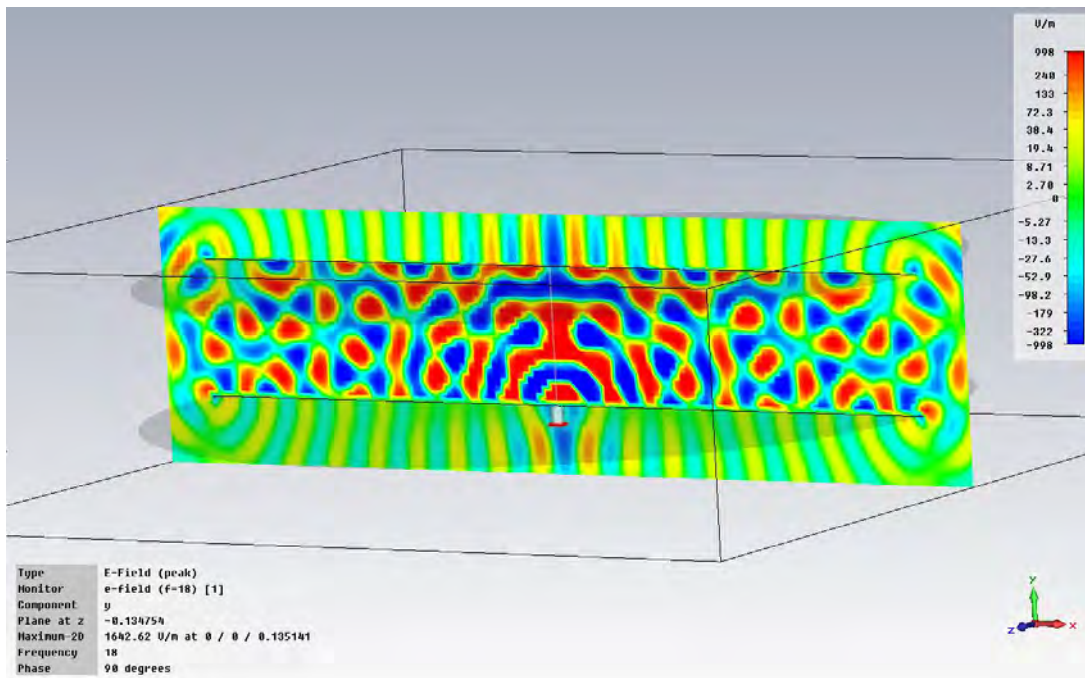


Figure 23: Phase Animation in 12" Circular Plate PPWG for 18 GHz

Figure 24 and Figure 25 show the forward-directed magnitude and phase variations along the various evaluation lines for 2 GHz. Overlaying the plots for the individual evaluation lines depicts the magnitude and phase variation in the vertical direction as well. It can be seen that for 2 GHz, away from the monopole antenna, magnitude and phase values converge to a narrow band, i.e. only propagation of the fundamental mode is established. Figure 26 and Figure 27 show the same information for 4 GHz and Figure 28 and Figure 29 show this for 18 GHz, but as expected, there is no convergence of magnitude or phase values. This data will be considered again when designing a component to mitigate the higher-order mode effects.

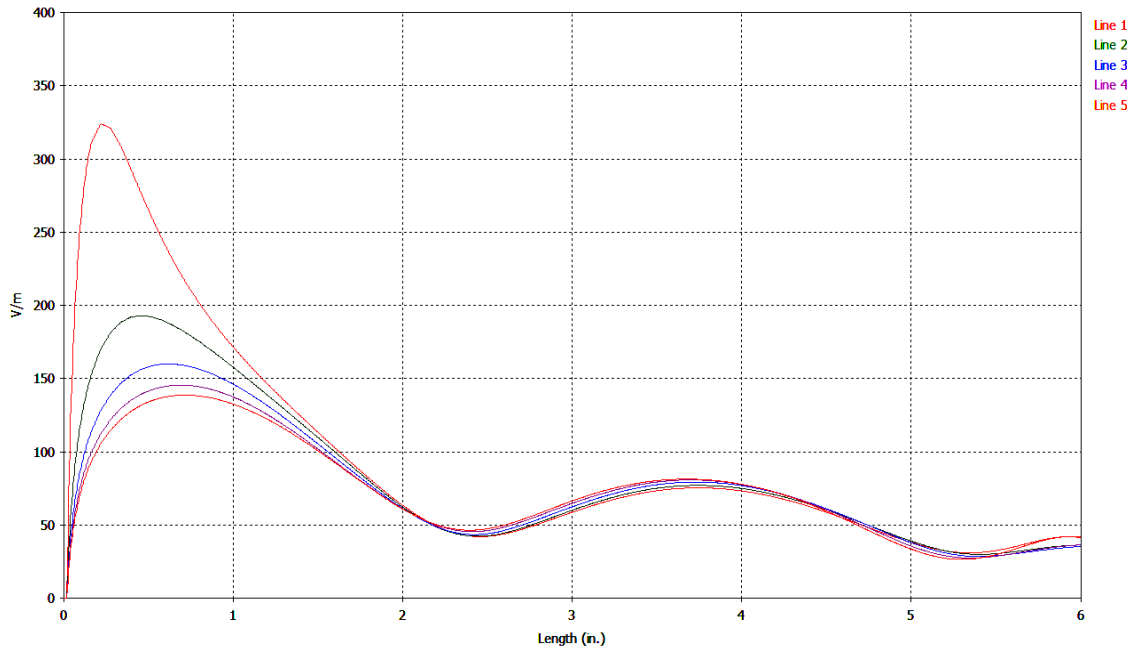


Figure 24: Mag. Variation Along Evaluation Lines for Circ. Plate PPWG at 2 GHz

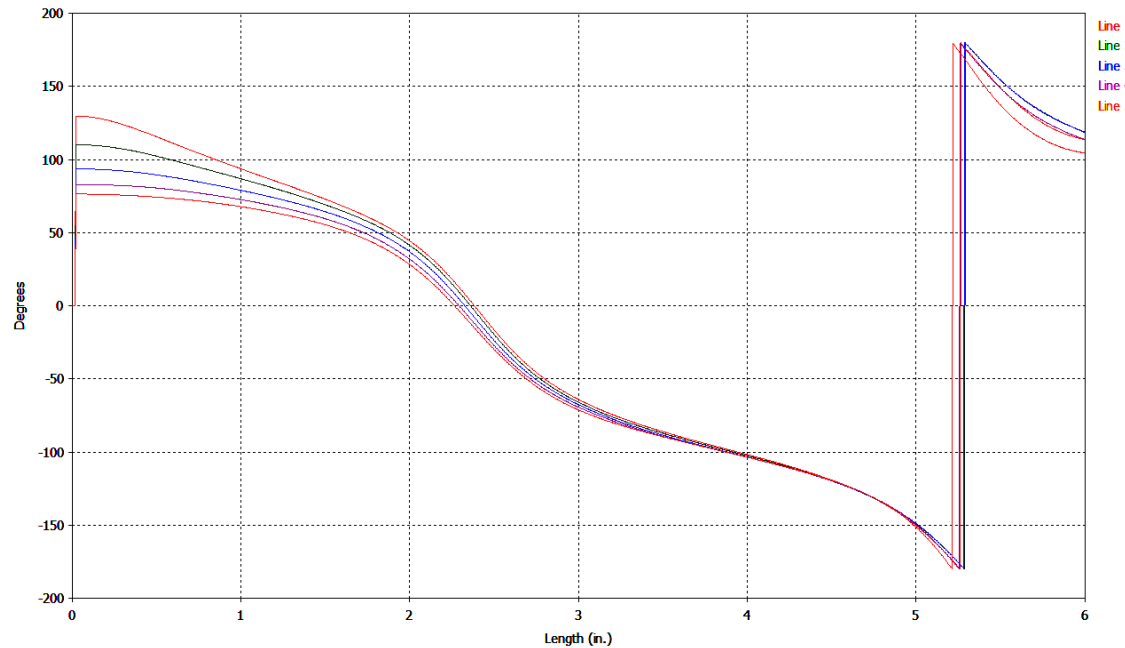


Figure 25: Phase Variation Along Evaluation Lines for Circ. Plate PPWG at 2 GHz

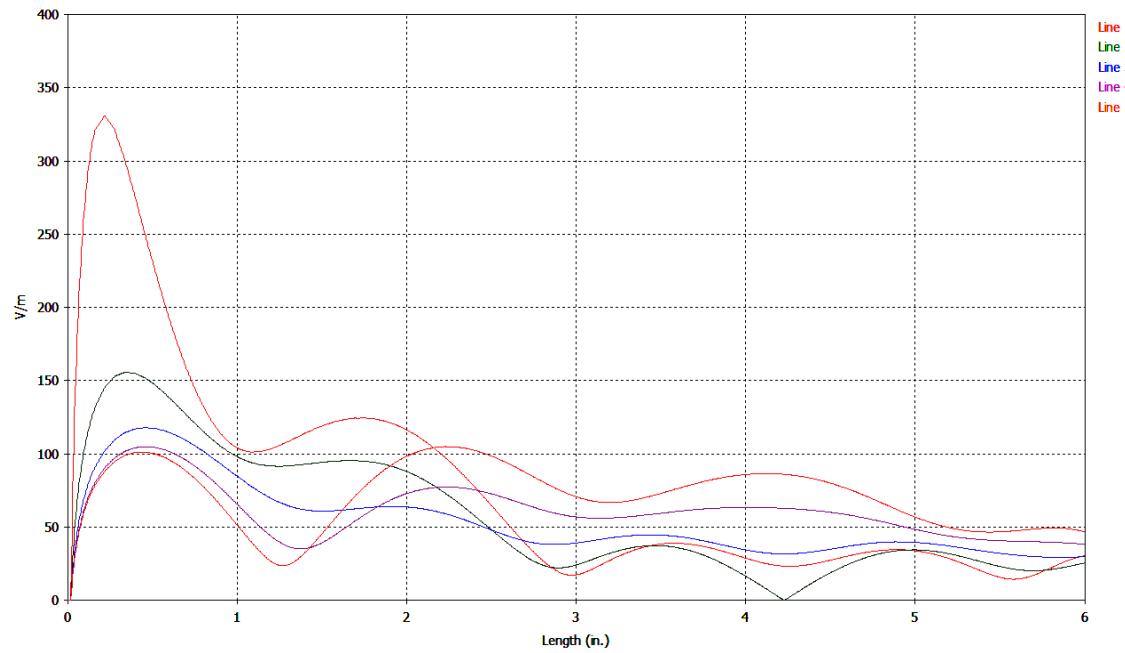


Figure 26: Mag. Variation Along Evaluation Lines for Circ. Plate PPWG at 4 GHz

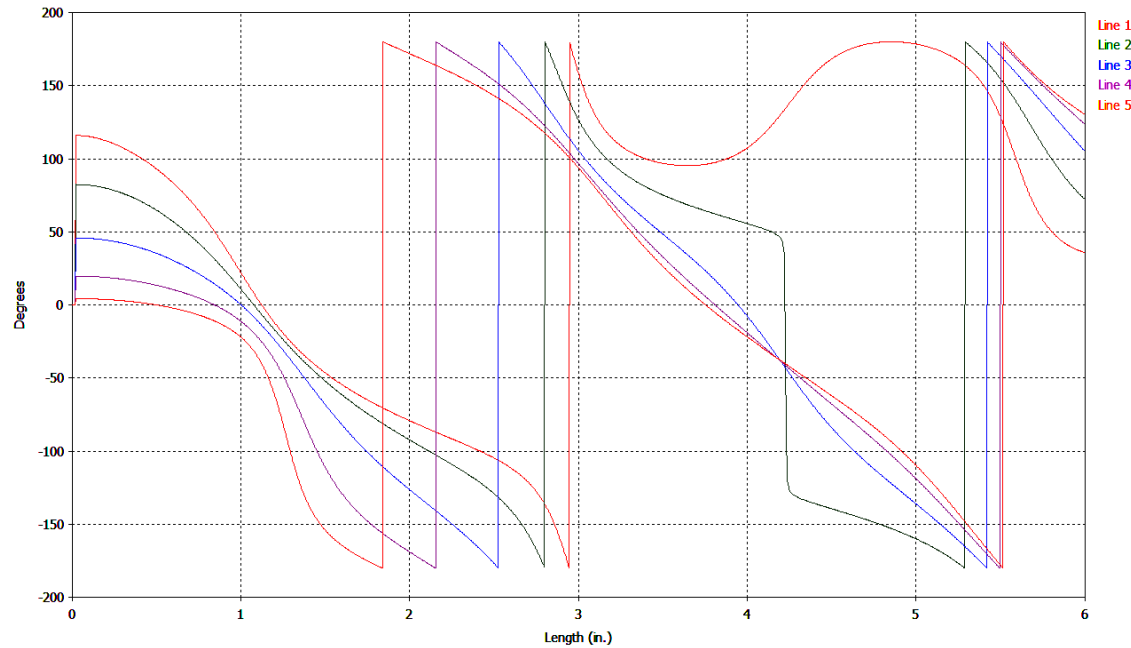


Figure 27: Phase Variation Along Evaluation Lines for Circ. Plate PPWG at 4 GHz

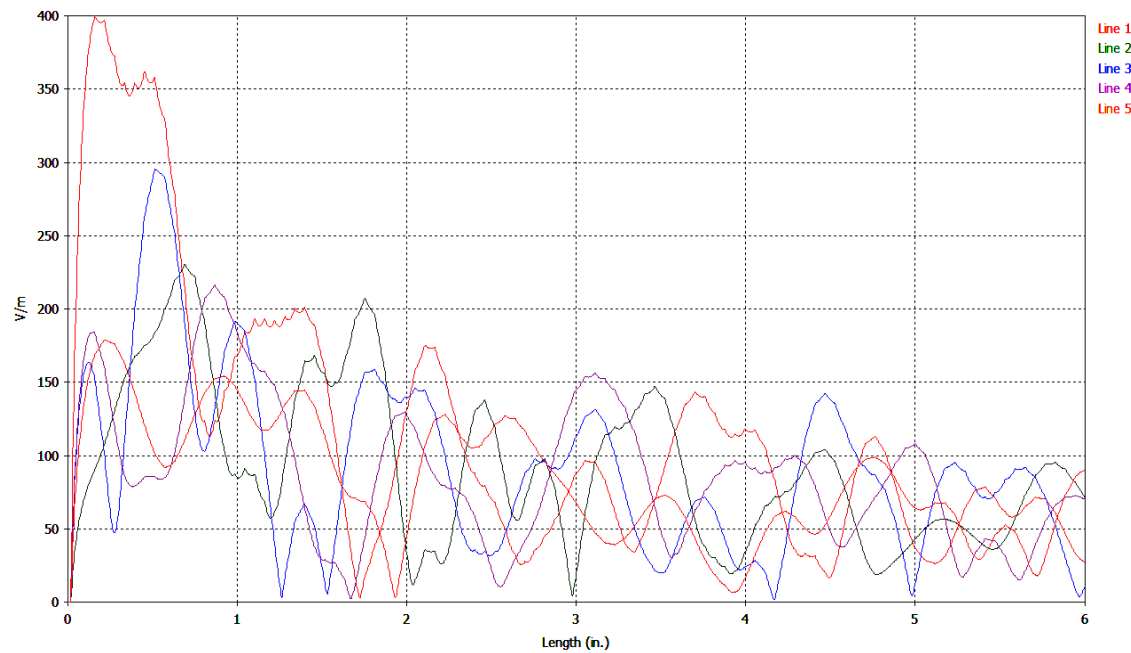


Figure 28: Mag. Variation Along Evaluation Lines for Circ. Plate PPWG at 18 GHz

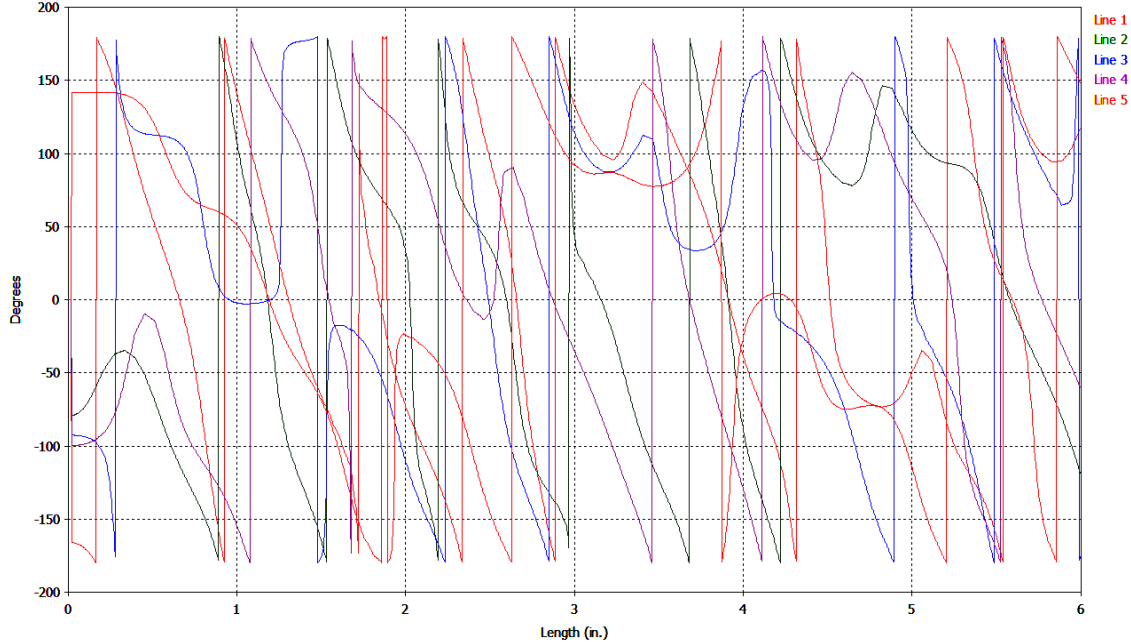


Figure 29: Phase Variation Along Evaluation Lines for Circ. Plate PPWG at 18 GHz

Finally, the total propagating power in the PPWG is distributed among the existing modes. The radially-directed power density can be written as

$$\left(\bar{S}_\rho \right)_{mn} = \hat{\rho} \frac{1}{2} \operatorname{Re} \left[-E_z H_\phi^* \right] \quad (1.12)$$

where the electric and magnetic field components can be determined from A_z .

The associated power is obtained by integrating over a cross-section of the guide

$$P_{mn} = \int_0^h \int_0^\phi S_\rho \rho d\phi dz \quad (1.13)$$

where h is the spacing between the plates and ϕ is an angular span (azimuth) of radiation. The usable fraction of power is in the forward section of the monopole's radiation and the wasted fraction of power is everywhere else. The azimuth of usable

power can be defined by the angle formed by the monopole and the two tips of the adjacent lens. The total power is equal to the sum of all power components associated with each mode,

$$P_{total} = \sum_{m,n} P_{mn}^{TM^2} \quad (1.14)$$

By completing this power analysis, a more exact contribution of each mode to the total power in the PPWG could be determined. This information could be used to guide steps towards mitigating the effects of each mode in a priority order (similar to the visualization technique above).

The mathematical analysis is left incomplete for the purpose of proposing a general solution to the mitigation of higher-order mode effects. This solution is the design of a basic mode-matching component that introduces a miniature PPWG inside the BANTAM PPWG. The miniature PPWG would be suitably spaced for supporting only the fundamental mode of 18 GHz (less than 0.328" as indicated earlier). Transitioning from the miniature PPWG to the BANTAM PPWG should favorably affect the overall mode structure within the 2" spacing. The technical details of the mode-matching component will be discussed later.

Specification

The BANTAM chamber allowed for a bottom plate size of 76" x 52". The plates were constructed using three sheets of aluminum that were on-hand at AFIT. The sheets were approximately 72" x 48" with a thickness of 0.1915". In anticipation of diffraction effects related to the blunt edges of the aluminum, the sheets would have to be framed

with rolled edges. To make room for the rolled-edge framing, the sheet for the bottom plate was sized to 66.8" x 42.8". The technical details of the rolled-edge framing will be discussed later, but with the framing, it was expected that the bottom plate would span 75.625" x 51.625" leaving a perimeter of only 0.375" wide between the bottom plate and the tips of the wall absorber.

Similarly, the aluminum sheet for the top plate was sized to 52.3" x 27.8". With the same rolled-edge framing, the top plate would span 61.125" x 36.625". Derivation of the top sheet dimensions will be included in the technical details of the lens design since the top plate is further constrained by the size of the components that will be housed between the two plates.

For the given size of the top plate relative to the bottom plate, a maximum (approximate) scan area of 14.5" x 15" over the center of the bottom plate is expected. The maximum scan area dimensions are only approximated as they relate to the recommended positions of the interior components and the outer limits of top-plate travel due to software limit switches, hardware limit switches and the tips of the wall absorber. The recommended maximum scan area is 14.25" x 14.25".

The top and bottom sheets are expected to weigh approximately 60 lbs and 80 lbs respectively. The degree of sheet flatness went undetermined, but by Figure 30 it can be seen that a very slight bend can be expected in both.

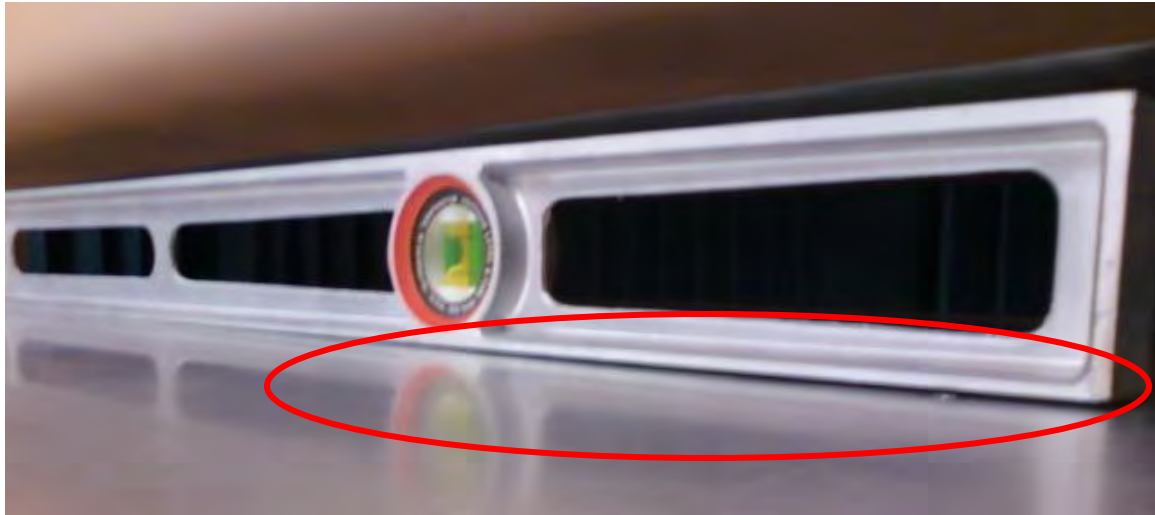


Figure 30: Flatness of Aluminum Sheets

Fabrication

The on-hand aluminum sheets were cut to size by the AFIT Model & Fabrication Shop. A series of thru holes were drilled and tapped into each for mounting the monopoles and for mounting the sheets onto their respective plate frames.

Rolled Edge Framing

Theory and Simulation

For the monopoles of the BANTAM PPWG, energy is radiated omni-directionally within the plates with a fraction of that energy being put to use and a fraction being wasted. Of the fraction being wasted, energy will either be expelled from the sides and ends of the PPWG or it will ring throughout the PPWG. The energy expelled from the PPWG will be directed into the wall absorber directly across from the PPWG openings. It is assumed for simplicity that the absorber will attenuate this energy completely and that nothing will be reflected back into the PPWG openings. The energy available for

ringing will come from the energy being expelled as that energy crosses over the joint formed by the top surface of the aluminum sheet and the side surface of the blunt aluminum edge. The same effect occurs at the corners of the sheet where three orthogonal surfaces meet. These slope diffraction effects are described in full detail in [15] where a line source illuminates the edge of a half-plane.

It is desirable to minimize the opportunity for diffraction since ringing energy can go back and forth throughout the PPWG and interfere with the monopole's usable energy. To soften the diffraction effects, the bluntness of the joint of the sheets' surface and edges can be transitioned in a way to smoothly guide more energy out of the PPWG. This transition will blend the top surface of an aluminum sheet (with radius of curvature = ∞) with the surface of a rolled-edge frame (with radius of curvature $\neq \infty$) and bypass altogether the orthogonal surface of the edges (also with radius of curvature = ∞). These effects of diffraction and the joining of two surfaces with different radii of curvature are described in full detail in [15] where energy coupling between a source and observer is considered on and off a variety of curved surfaces.

For modeling diffraction effects, an 12" square-plate PPWG was simulated in CST. This model can be seen in Figure 31. A snapshot of the phase animation at 2 GHz is used to qualitatively review the diffraction effects. This is shown in Figure 32. It can be seen how the fields are immediately altered by the presence of edges and corners when compared to the circular-plate PPWG of Figure 20. Similar to the circular-plate PPWG, field evaluation lines are used to quantitatively review magnitude and phase due to diffraction effects at 2 GHz. This data is shown in Figure 33 and Figure 34. When overlaid with the data of Figure 24 and Figure 25 for the circular-plate PPWG, it can be

seen how the square edges affect both magnitude and phase. The asterisks in the legend of Figure 33 and Figure 34 represent the newest (square PPWG) plots.

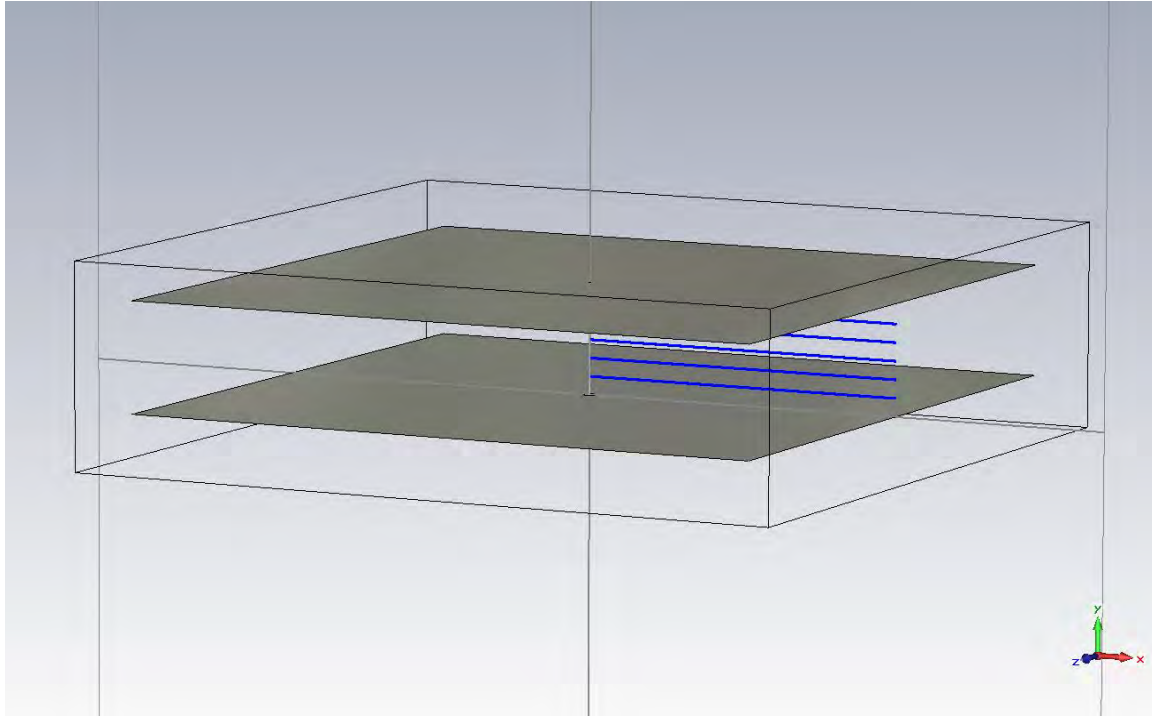


Figure 31: Square Plate (12") PPWG

The model for a 12" square-plate PPWG with rolled-edge framing is shown in Figure 35. The rolled-edge framing was designed with a diameter of 6.625" - the significance of this diameter will be revealed later. A snapshot of the phase animation at 2 GHz is used to qualitatively review the effects of the rolled edges. This is shown in Figure 36. The field evaluation lines are re-evaluated and are overlaid with those of the original square PPWG in Figure 37 and Figure 38. The asterisks in the legend represent the newest (rolled edge) data. In all these figures, it can be seen that the rolled edges heavily reduce the effects of diffraction.

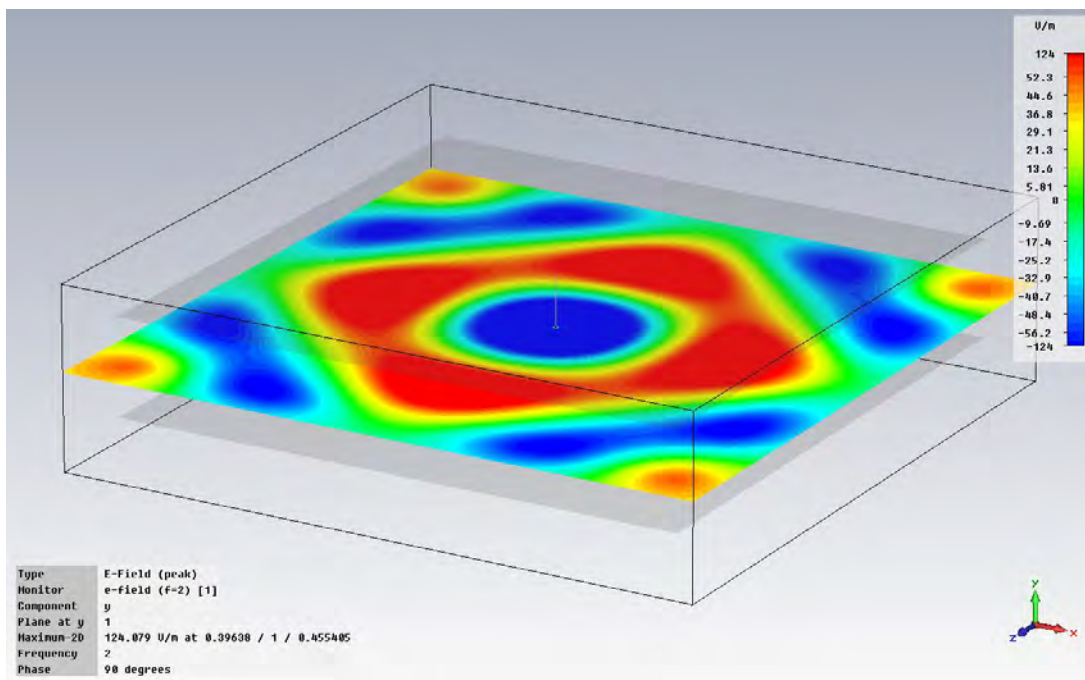


Figure 32: Phase Animation in 12" Square Plate PPWG for 2 GHz

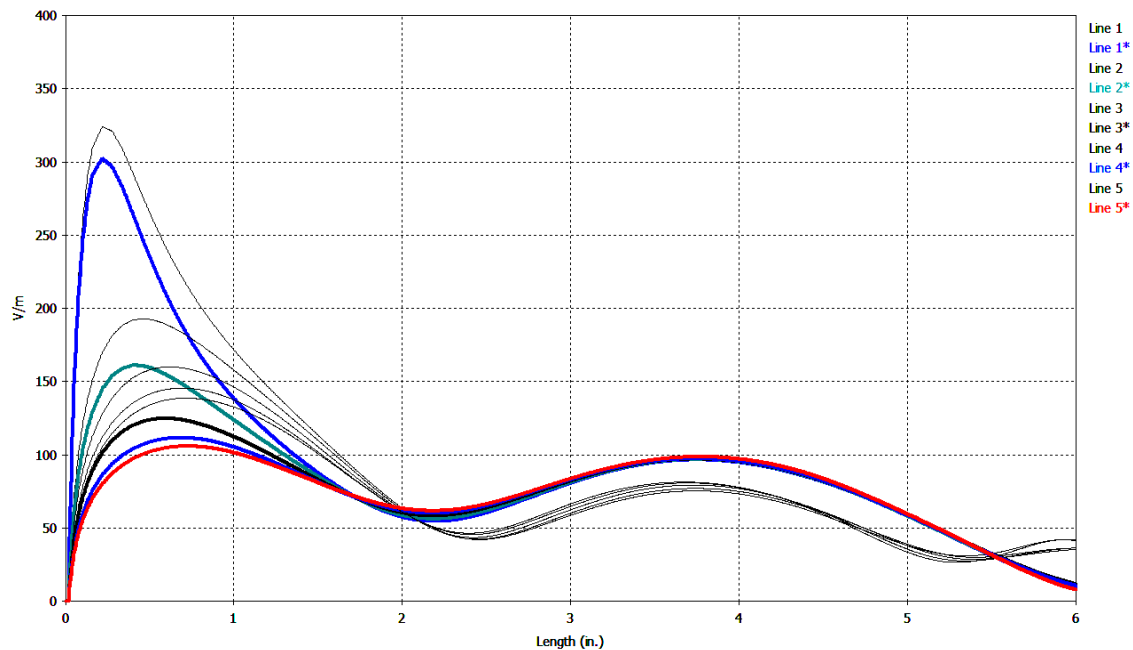


Figure 33: Mag. Variation Along Evaluation Lines for Square Plate PPWG at 2 GHz

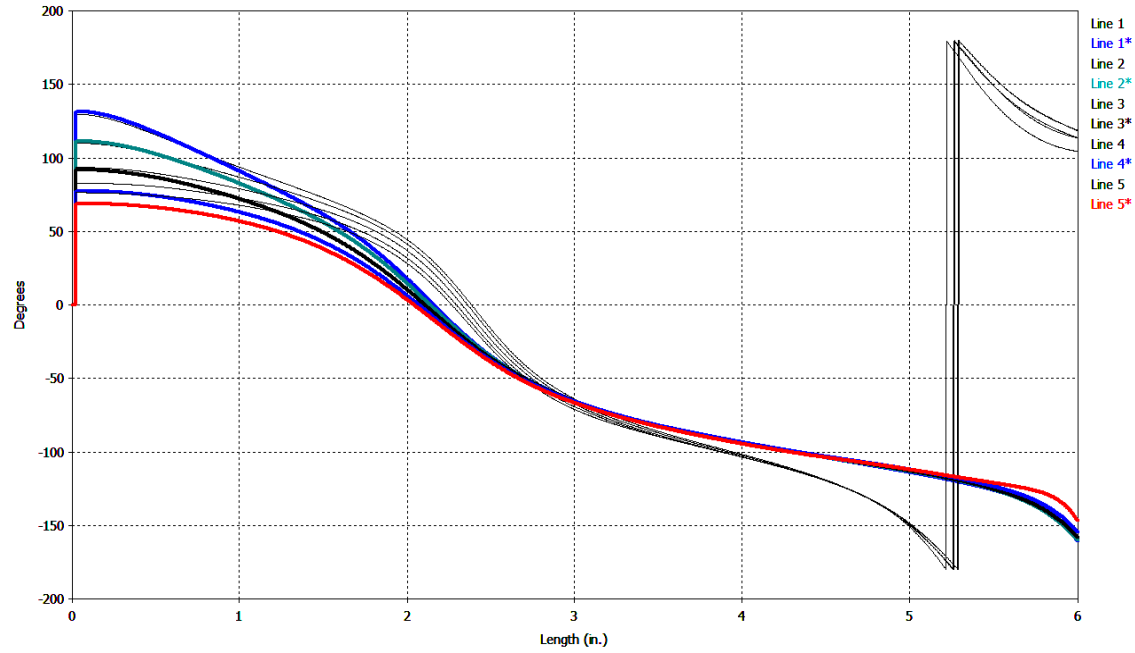


Figure 34: Phase Variation Along Evaluation Lines for Square Plate PPWG at 2 GHz

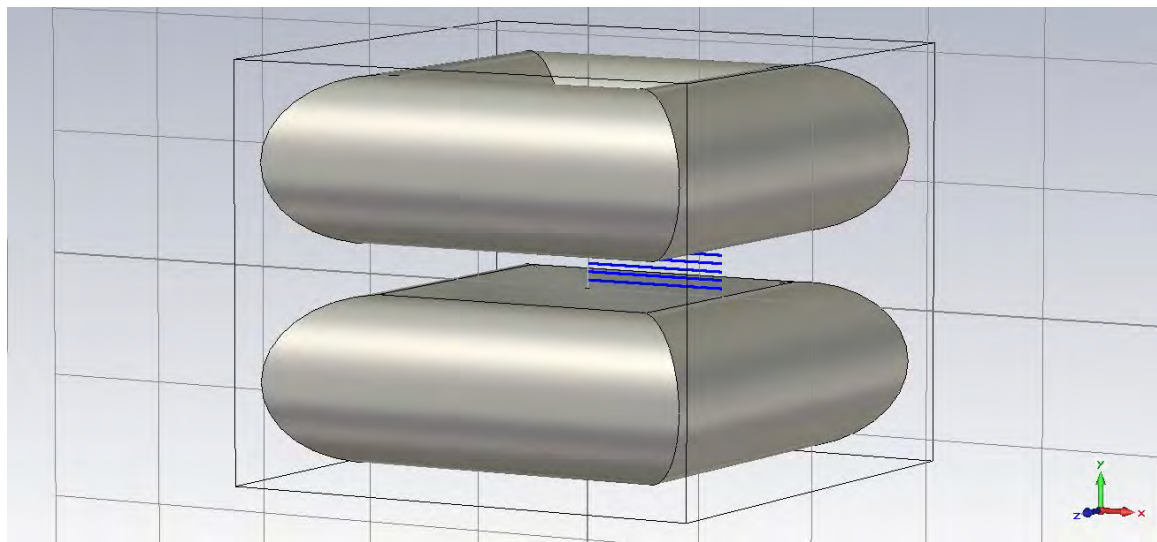


Figure 35: Square Plate (12") PPWG with Rolled-Edge Frame

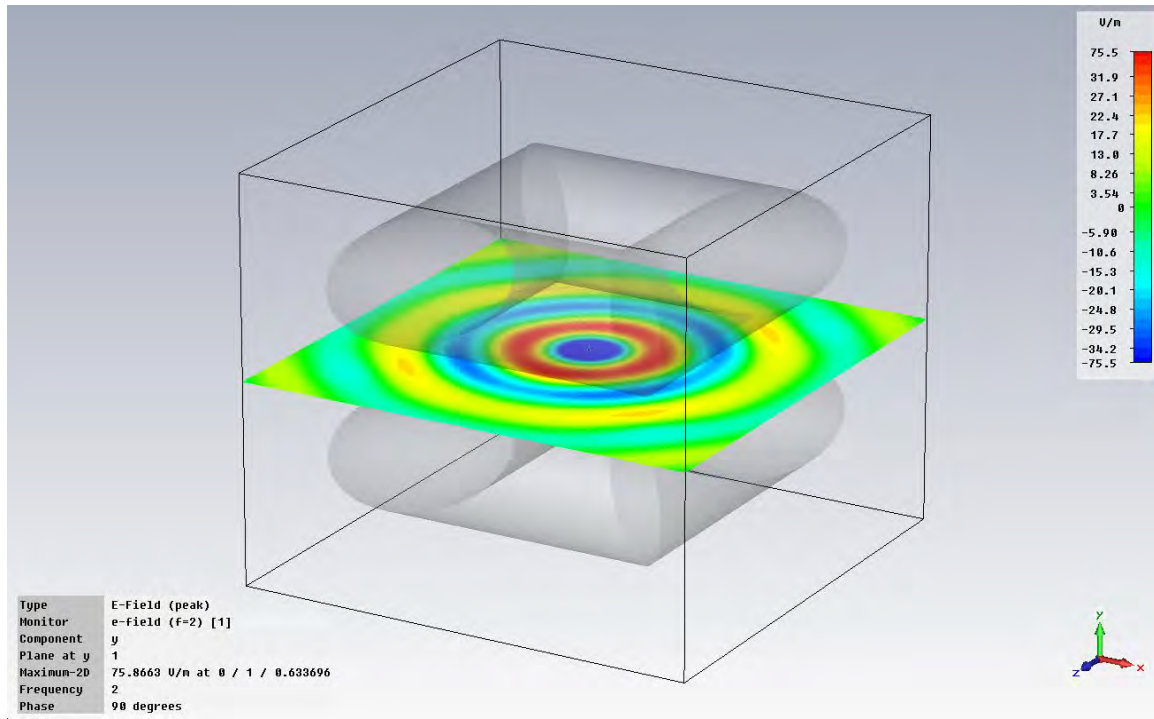


Figure 36: Phase Animation in 12" Square Plate PPWG with Rolled-Edges for 2 GHz

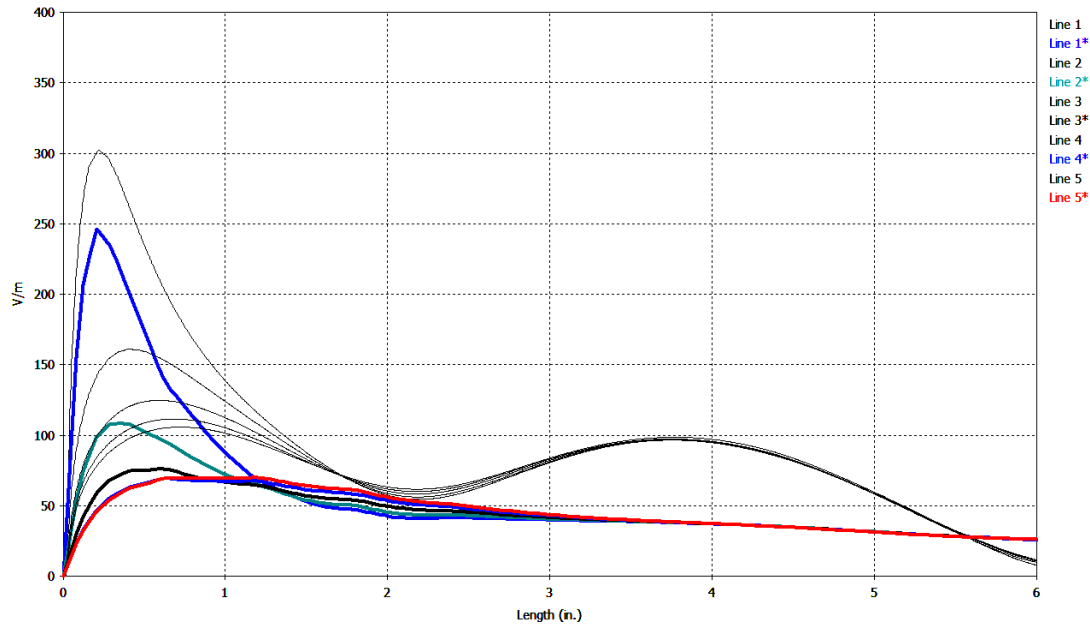


Figure 37: Mag. Variation Along Eval. Lines for PPWG with Rolled-Edges

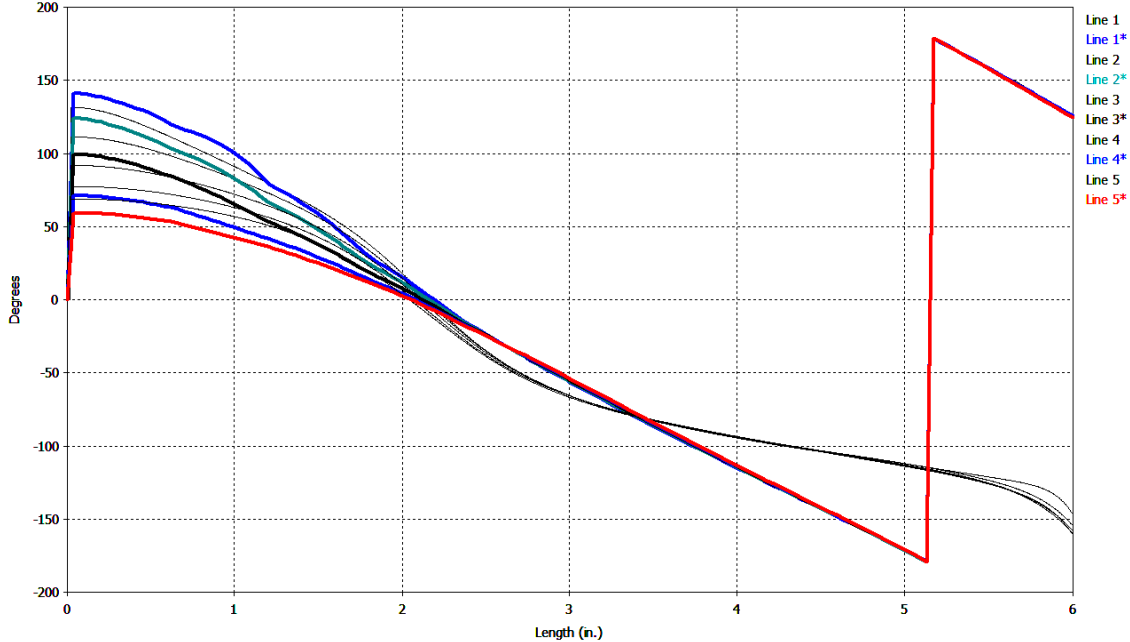


Figure 38: Phase Variation Along Eval. Lines for PPWG with Rolled-Edges

Specifications

The radius of curvature for the rolled-edge frame for both the CST modeling and the BANTAM PPWG is 3.3125" (slightly greater than $0.5\lambda_{2GHz}$). While it would be helpful to simulate a parametric study to examine the effects of different radii of curvature, it is intuitive that a larger radius will soften diffraction effects more than a smaller radius. Thus, it is clear that a rolled-edge frame should be designed to have the longest, practical radius of curvature relative to the longest wavelength of operation. The radius of 3.3125" comes from the first convenient, practical, machinable, and available material found. The material is 6.625"-diameter PVC drain, waste and sewer pipe from Lowe's.

The PVC pipe was purchased in 10' lengths and had to be cut to length to fit the edges of the top and bottom aluminum sheets and their respective plate frames. The corners of the pipe were designed with a miter to join each other at 45°. With the given diameter of the PVC pipe, the bottom sheet with rolled-edge frame occupies the entire space available within the BANTAM chamber. During scanning, at the extreme outside positions, the outside tangents of the top plate run plumb with the outside tangents of the bottom plate. The diameter of the PVC is also the height of the fully assembled top and bottom plates, which as a new design constraint, must be considered when designing the plate frames and when designing the interface of the top plate with the translation axis and the interface of the bottom plate with the scissor lift.

Fabrication

The 10' PVC pipes were cut to length and mitered by hand using a custom designed miter box. The miter box was made of 80/20 aluminum extrusion and included clamps to prevent the pipe from moving along its length and rotation axes. Pilot holes were designed into the 80/20 miter box so that drilling holes for mounting the pipe to the plate frames could be accomplished alongside cutting. Figure 39 depicts the machining process.



Figure 39: Machining PVC Pipe for PPWG Rolled-Edge Frame

80/20 Plate Frames

Theory and Simulation

The plate frames were not modeled for the purpose of simulation. However, since CST offers many file formats for drawings, the design of the plate frames took place in CST. The basic intent for the plate frames is to provide a mounting structure for the aluminum sheets and the PVC pipe so that each plate can be considered as a single unit. Each plate frame resembles a small table with many legs.

Specification

The complete technical specifications of the top and bottom plate frames will be made available at a later date.

Fabrication

The plate frames were designed in collaboration with a product specialist from Voelker Controls, a vendor of 80/20 material. Upon receipt of the material, the frames were simply assembled to specification. The frame pieces consisted of various lengths of 1.5" x 1.5" T-slotted aluminum extrusion. The legs on each side of each frame were designed pre-drilled to match the holes placed in the PVC pipe. A long, rectangular washer was included in the design of the frame to assist in mounting the pipes securely.

The bottom frame included two adjustable cross-members used to mount the frame to the scissor lift. The adjustable cross members were prepositioned and tightened prior to installing the aluminum sheets and PVC pipe. The scissor lift, described shortly, was fitted with three beams of 80/20 that run orthogonally to the adjustable cross members.

The top frame, intended to hang upside-down, included four vertical posts that slide along linear bearings. The bearing pads were made of a self-lubricating, low friction ultra-high molecular weight polyethylene. The bearings were mounted to the short axis by a 12" x 12" aluminum adapter plate. The linear bearings give the top plate approximately 1.5" of vertical play as it hangs.

Figure 40 shows a picture of one of the completed frames. Figure 41 shows a frame after the installation of the PVC pipe. The long, rectangular washer runs the length

of each pipe and is hidden inside. Figure 42 shows a frame with pipes after the installation of the aluminum sheet. The aluminum sheet straddles the frame like a tabletop and a series of bolts are used to fasten the sheet to the frame. At this point in the construction, the holes for the monopoles are small pilot holes. There is also a 1.1" wide perimeter gap between each edge of each sheet and the top tangent of each pipe. This perimeter gap was to be filled with a fiberglass filler to smooth the transition from the aluminum sheet to the PVC pipe.

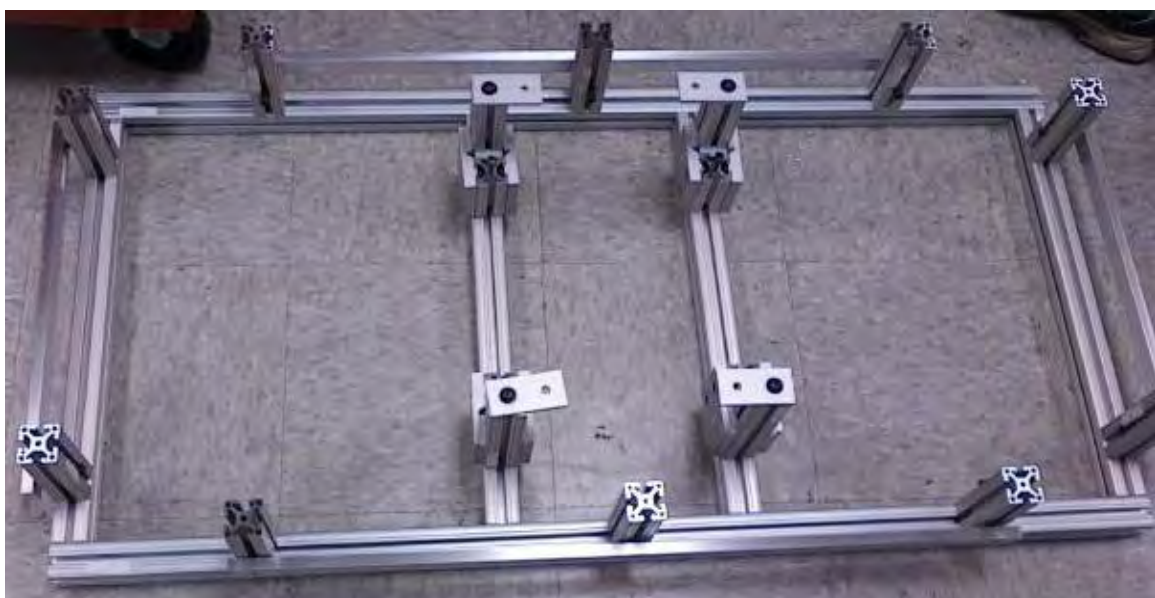


Figure 40: Top Plate Frame (Ref. 12" Square Floor Tiles)



Figure 41: Bottom Plate Frame with PVC Pipes Installed

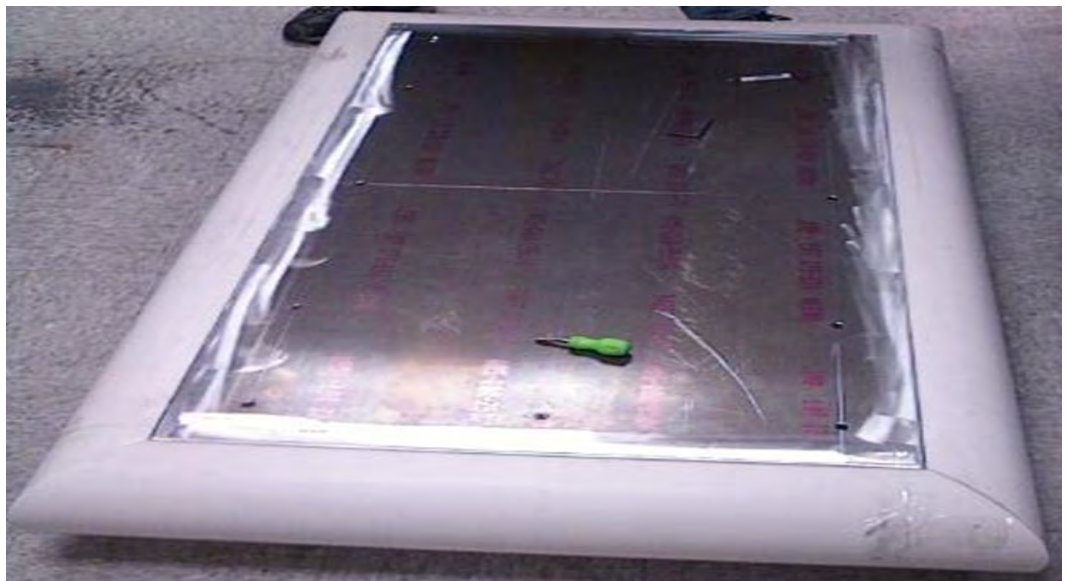


Figure 42: Top Plate Frame with Pipes and Aluminum Sheet Installed

Fiberglass Filler

Theory and Simulation

The fiberglass filler was a practical and acceptable gap filler to smooth the transition from the aluminum sheets to the PVC pipe. It also was used to fill the heads of the sunken fasteners that hold the aluminum sheets to the frames. There was no simulation of the fiberglass filler.

Specification

The fiberglass filler came in two brands: 3M Bondo 272 heavy-weight filler and Evercoat light-weight filler. The heavy-weight filler was used to fill the primary perimeter gap. The light-weight filler was used to fill any remaining minor gaps, air bubbles, and grooves between the aluminum and PVC surfaces.

Fabrication

The aluminum and PVC surfaces had to be prepared to receive the heavy-weight Bondo. This entailed a surface sanding with medium-grit sandpaper. The PVC was sanded from the PVC-aluminum joint to approximately 270 degrees around the pipe. The aluminum was sanded in a perimeter approximately 6" wide. Sanding these extended areas prepared each surface for paint as well. The interior of the aluminum was sanded to a much finer level to give a slightly polished appearance.

After sanding the surfaces, heavy-weight Bondo was applied to the perimeter gap of both plates. A cure time of at least two hours was required for the Bondo to set. After setting, the heavy-weight Bondo was sanded flat and the light-weight filler was applied.

The light-weight filler was applied to a much wider area than the heavy-weight Bondo to further smoothen the aluminum-to-PVC transition. In turn, the light-weight filler was sanded flat to prepare the surface for paint. Figure 43 shows a plate after the heavy-weight Bondo application. Figure 44 shows a plate after the light-weight filler application.



Figure 43: Bottom Plate with Heavy-Weight Bondo Applied

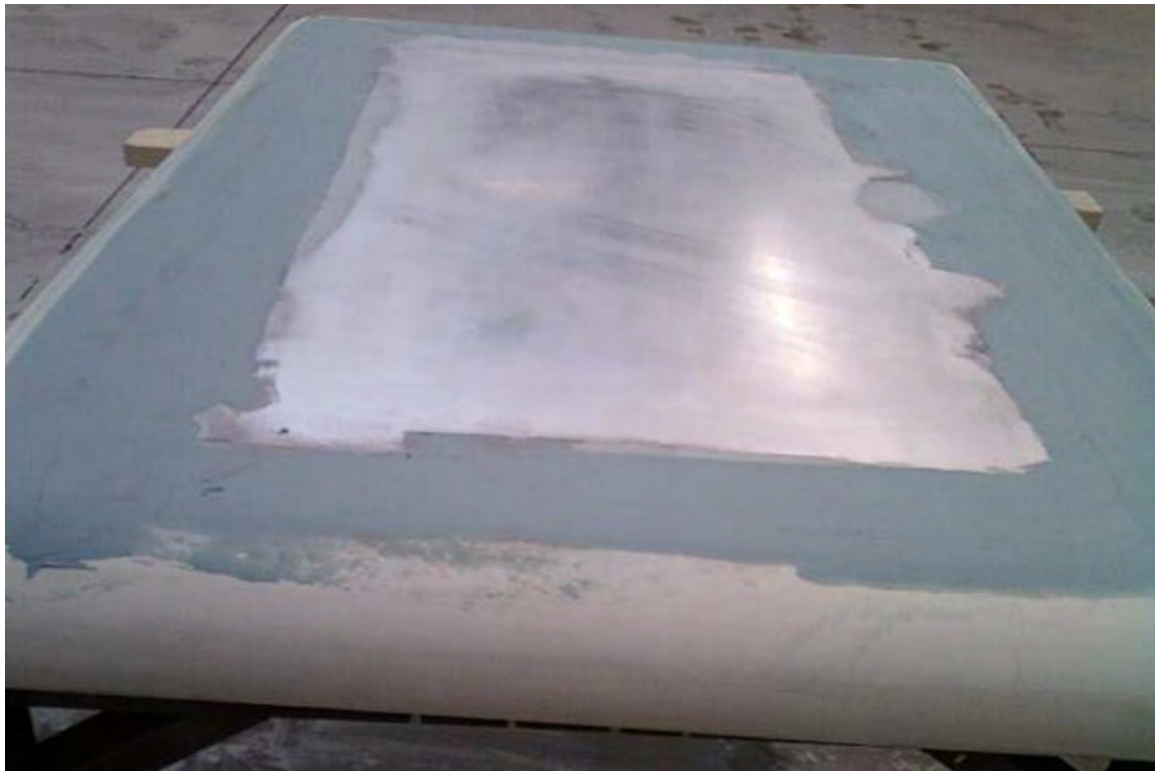


Figure 44: Top Plate with Light-Weight Filler Applied

Conductive Paint

Theory and Simulation

As the filler and PVC pipes provide a smooth geometrical transition to the plates, a conductive coating applied to the filler and pipes provide a smooth electrical transition as well. Conductive paint will complete the rolled-edge frame and soften the diffraction effects of radiation as it exits the PPWG openings.

CST simulations were not performed for the conductive paint, but it could have been characterized to determine how well it is electrically matched with the aluminum sheets. Characterization would have also allowed the application process to be optimized in that a desired resistivity could have been reached by applying a predetermined number

of coats. For use in this thesis, the conductive paint was used for its ballpark effectiveness in matching the rolled edges to the aluminum sheets.

Specifications

All the coatings used were manufactured by SprayLat Corporation and supplied by Sherwin Williams. These coatings included a zinc-chromate primer for the aluminum surfaces, a conductive silver-coated copper paint, and a clear top coat.

The conductive paint is a sprayable form of silver-coated copper that is typically used on plastic substrates. The paint was advertised to possess effective shielding at less than 1.0 mil (25 microns) dry film thickness (dB levels not immediately available). The dried conductive film is supposed to be extremely hard, tough and durable with excellent adhesion. Sheet resistance was advertised at less than $0.015 \frac{\Omega}{square}$ per 1.0 mil dry film.

The clear top coat is a talc-based coating that protects the copper in the paint from mineral salts, moisture and oxidation. This is mainly used to preserve the appearance of the painted portions of the PPWG.

Fabrication

Following the final preparation of the filled surfaces, the plates were painted. Final filling, sanding and painting was accomplished by L&M Dry Wall, a local company, because they had the properly-sized facilities to perform the paint job while the AFIT Model & Fabrication Shop did not. The cure time between the conductive coats and the top coat was approximately 24 hours. The cure time following application of the

top coat was approximately 48 hours. Figure 45 shows a plate following the application of zinc-chromate primer. Figure 46 shows a plate following the application of two coats of conductive paint and the clear top coat.

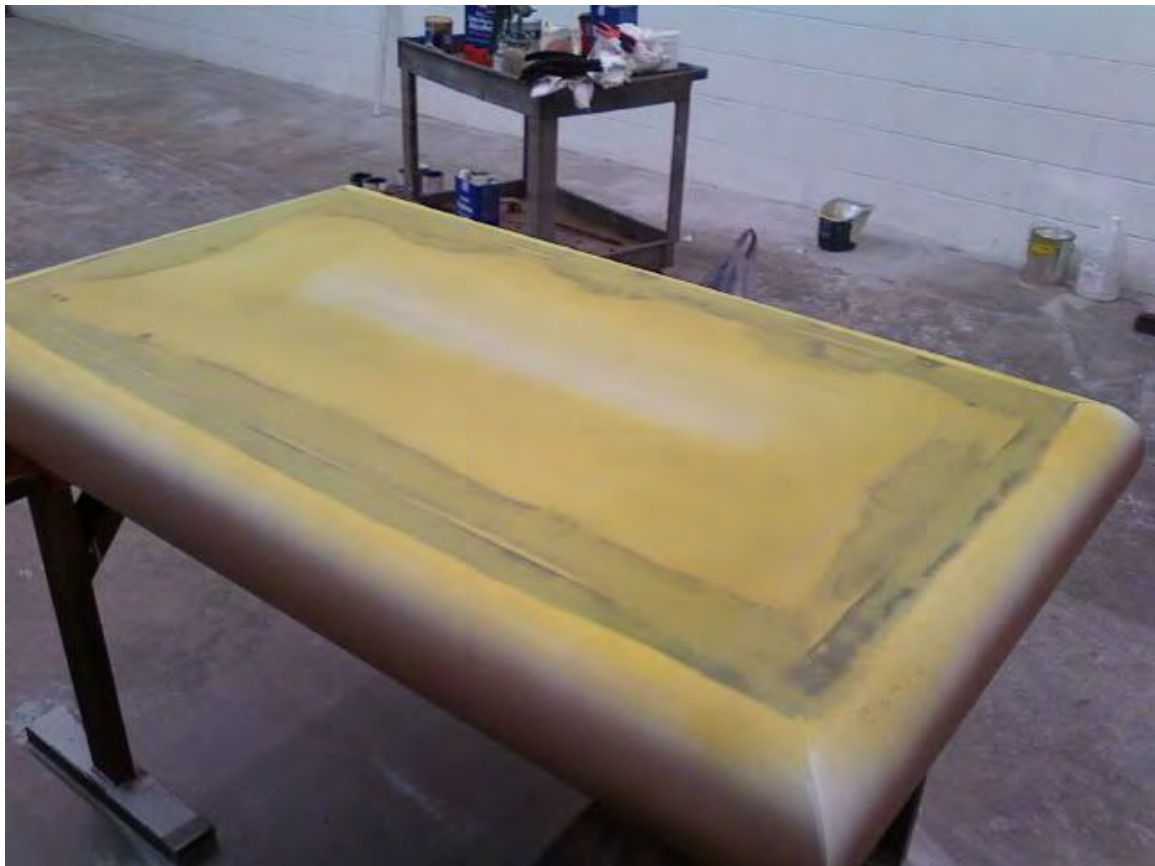


Figure 45: Top Plate with Primer Applied



Figure 46: Bottom Plate with Two Conductive Coats and Clear Top Coat Applied

A miscommunication with L&M Drywall on how much aluminum was to be painted resulted in the over-spraying of the primer on most of the aluminum. The aluminum wasn't to be fully painted, but left bare over much of the plates' center to ensure reliable conductivity. If the paint were to flake off, and the non-conductive primer layer was exposed, the conductivity of the flat portion of the plate would be degraded. Albeit, if the paint flecked off of the PVC, the conductivity would be degraded there also, but since the vital components (antennas, lenses and material samples) are on the flat portion, it is best to rely on the conductivity of the aluminum. Figure 47 shows a plate under the repair process of removing the primer from the central metal area. Both plates

had to be repaired in this way. The bare-metal area of both plates is surrounded by approximately a 6" wide paint perimeter.



Figure 47: Top Plate Under Repair to Remove Excess Primer

To examine the effectiveness of the conductive paint, small vinyl and aluminum coupons were painted alongside the plates. Half of each coupon was taped off so that the thickness of each layer could be measured by a surface profiler. A sheet resistance meter (direct-current, four-point probe) was used to measure the sheet resistance of each coupon as well. The coupons are displayed in Figure 48. They represent respectively, from left to right, bare vinyl and aluminum, primed aluminum, the addition of a single

coat of paint, the addition of a second coat of paint, and the addition of the clear top coat.

The overall number of coats of paint was limited to two based on cost.



Figure 48: Paint Coupons

Figure 49 shows the texture of the vinyl coupon with two coats of paint and a clear top coat. The magnification is 10x.

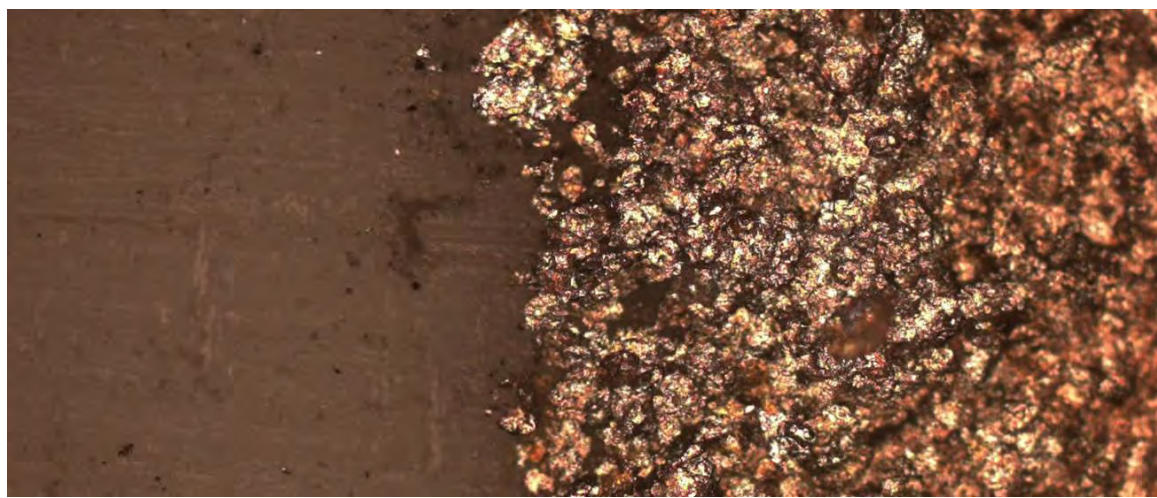


Figure 49: Fully Coated Vinyl Coupon at 10x Magnification

Paint thickness and sheet resistance measurements were taken to determine the representative quality of the paint. For the future, these measurements should assist in determining 1) how many coats would be necessary to achieve the appropriate sheet resistance; 2) how many coats were optimum from a cost perspective; 3) how uniformly the paint coatings can be applied. Figure 50 and Figure 51 show the thickness measurements for each coating. Figure 52 and Figure 53 show the sheet resistance measurements. Note that the sheet resistance of the primer and top coat were too resistive to measure. Table 3 and Table 4, with means and standard deviations, accompany the figures.

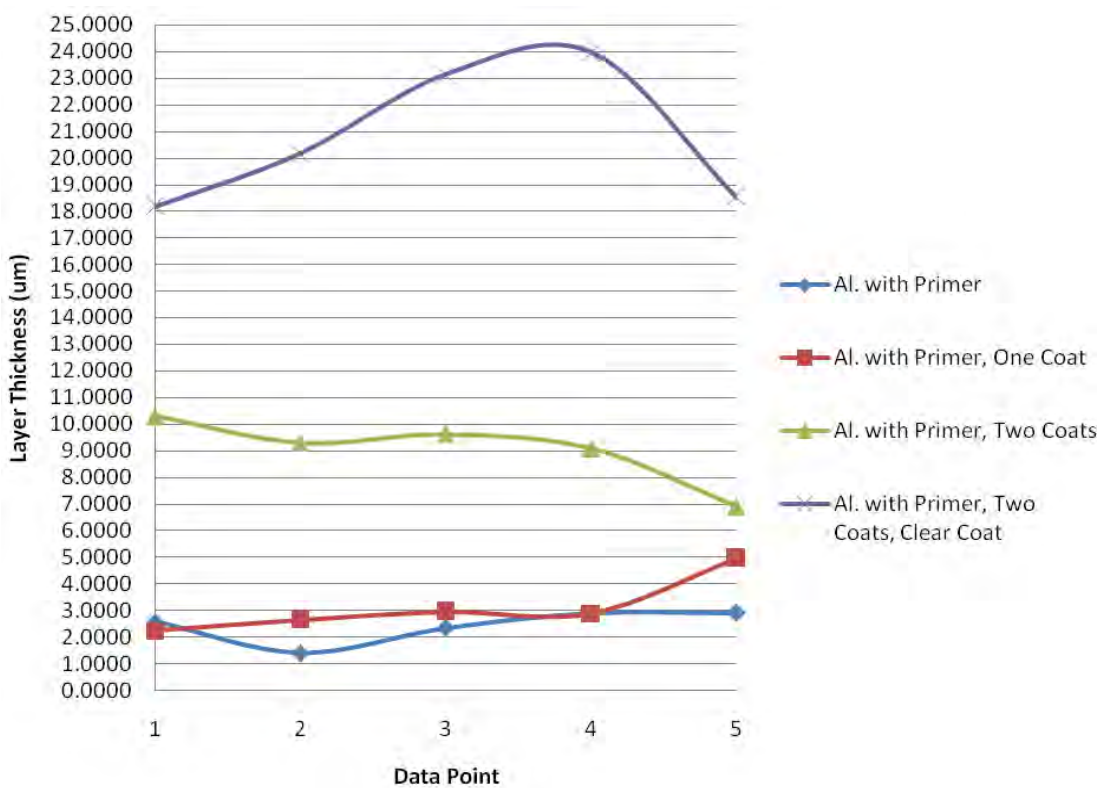


Figure 50: Coating Thickness on Aluminum Substrate

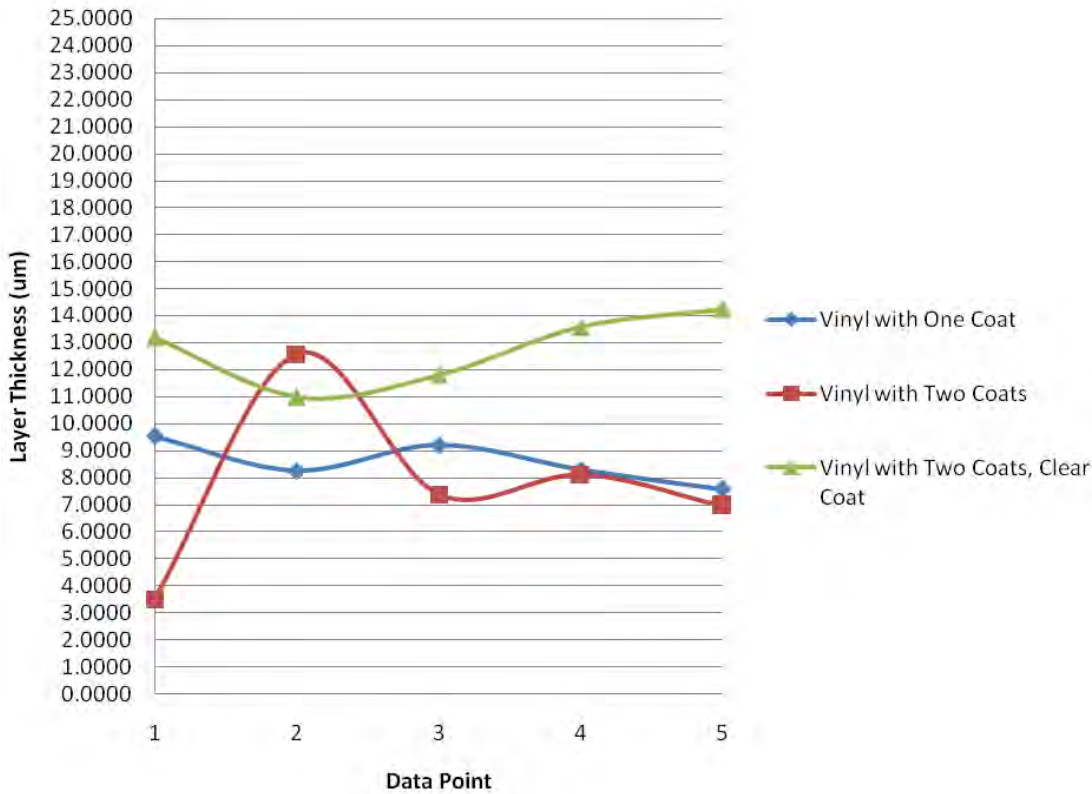


Figure 51: Coating Thickness on Vinyl Substrate

Table 3: Thickness of Conductive Coatings

		Paint Thickness (um) Data Points					Average	Std. Dev.
		1	2	3	4	5		
Aluminum	Primer	2.5777	1.3906	2.3383	2.8928	2.8978	2.4194	0.6211
	Primer & One Coat	2.2240	2.6533	2.9532	2.8890	4.9460	3.1331	1.0530
	Primer & Two Coats	10.2990	9.2985	9.6222	9.0812	6.8992	9.0400	1.2821
	Primer, Two Coats, & Top Coat	18.1740	20.1560	23.1160	23.9580	18.5080	20.7824	2.6410
Vinyl	One Coat	9.5296	8.2555	9.2113	8.2984	7.5811	8.5752	0.7878
	Two Coats	3.4968	12.5690	7.3814	8.1178	6.9603	7.7051	3.2480
	Two Coats & Top Coat	13.2050	10.9890	11.8080	13.5760	14.2350	12.7626	1.3306

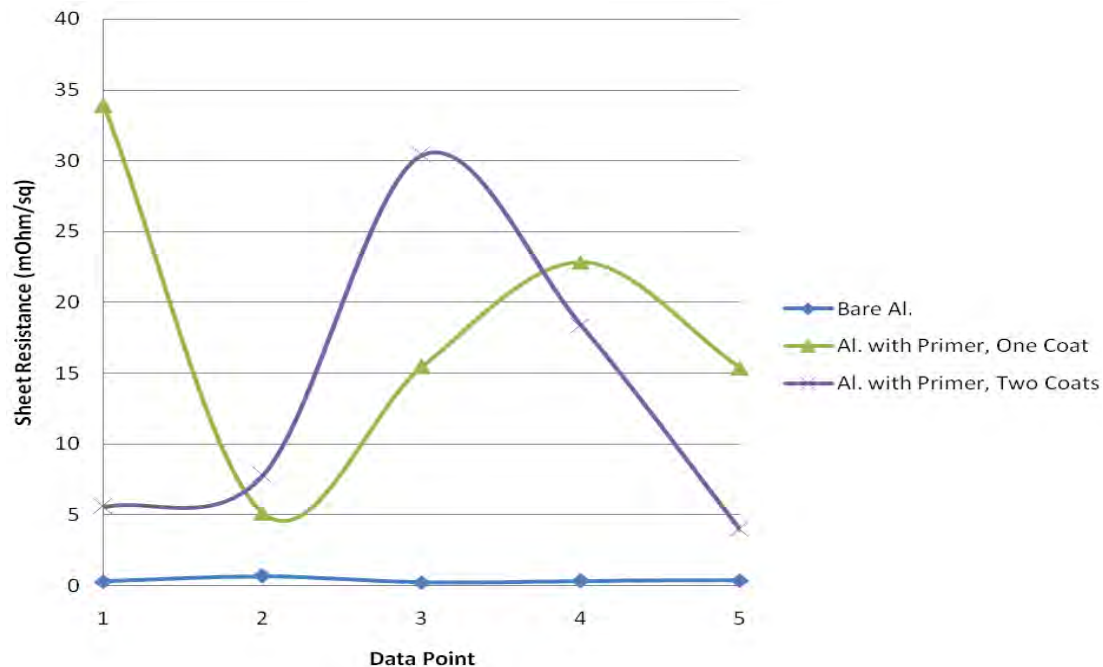


Figure 52: Sheet Resistance of Coatings on Al. Substrate

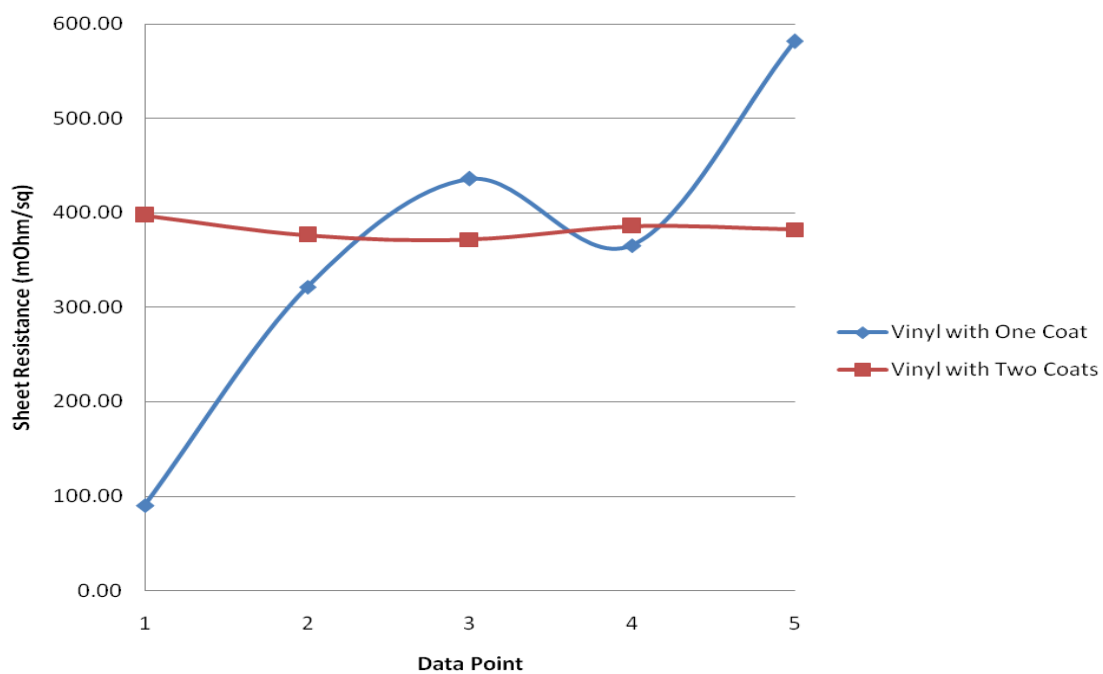


Figure 53: Sheet Resistance of Coatings on Vinyl Substrate

Table 4: Sheet Resistance of Conductive Coatings

		Sheet Resistance (mOhms/sq) Data Points						
		1	2	3	4	5	Average	Std. Dev
Aluminum	Primer	Too Resistive to Measure						
	Primer & One Coat	33.87	5.10	15.45	22.83	15.36	18.52	10.65
	Primer & Two Coats	5.54	7.78	30.39	18.35	3.95	13.20	11.13
	Primer, Two Coats, & Top Coat	Too Resistive to Measure						
Vinyl	One Coat	90.19	321.48	436.20	365.36	581.39	358.92	179.67
	Two Coats	397.40	376.18	371.60	385.59	382.27	382.61	9.88
	Two Coats & Top Coat	Too Resistive to Measure						

Based on the average values of coating thickness and sheet resistance, values for DC conductivity can be derived. DC conductivity is derived by

$$\sigma = \frac{1}{RS \cdot t} \quad (1.15)$$

where RS is sheet resistance and t is thickness.

For bare aluminum, CST gives a DC conductivity value of $3.56e7$ S/m. The derived DC conductivity of primed aluminum and top coated substrates is zero S/m. The derived conductivity of the first and second coat of paint on aluminum is $1.72e7$ S/m and $0.84e7$ S/m respectively. The derived conductivity of both the first and second coat of paint on vinyl is $0.03e7$ S/m.

Concerning this data, coating thickness was very sporadic across all data points for all coatings. For example, on average, two coats on vinyl was thinner than one coat on vinyl! Sheet resistance values also varied wildly across all data points for most coatings. However, there is consistency in that the paint on aluminum is about 40 times more conductive than the paint on PVC. On average, conductivity went down with a second coat on aluminum because, on average, the thickness went up dramatically. Conductivity was consistent on painted PVC as both thickness and sheet resistance

average values were similar. As can be inferred from these figures, without consistent measurements, it may be impossible to tell how many coats would be needed to achieve the paint's specified sheet resistance ($0.015 \frac{m\Omega}{square}$) and bring the conductivity of the painted PVC to the closest match with the aluminum. Of course, consistent measurements depend heavily on a consistent application process.

Scissor Lift

Theory and Simulation

Based on the constraints of the original BANTAM design, specifically the vertical position of the linear translation rails, it became necessary to provide a lift mechanism to bring the bottom plate into position with the hanging top plate.

For the chosen lift, with the bottom plate installed and in the lowered position, the surface of the bottom plate could be conveniently utilized as a work surface to prepare the antennas, lenses and material samples. In the upper position, all the cabling below the bottom plate could be easily accessed. The lift was also a convenient tool for installing the top plate.

Specification

The scissor lift is a part of a Low Boy dog grooming table from Ascot Products. The lift came with leveling legs and an up/down foot pedal. The starting height is 6" and the maximum height is 42". The jackscrew that moves the lift is equipped with a protective clutch and prevents continued motion at the maximum and minimum limits.

The maximum weight capacity for the lift is 250 lbs. The weight of the lift was not indicated in the product sheet.

The lift requires very little routine maintenance. The frame articulation points (scissor joints) should be lubricated periodically with a spray lubricant. The bearing races must remain free of dirt and debris and should not be lubricated. The threads of the jackscrew can be lubricated with automotive grease if operation of the lift becomes louder.

Fabrication

The lift was initially used as a tool for mounting the top plate onto the short axis rail. This procedure is illustrated in Figure 54 and Figure 55 with the lift raised and lowered respectively.

Three beams of 80/20 extrusion were fastened to the lift in preparation for the bottom plate. The three beams orthogonally span three cross members of the bottom plate's 80/20 frame. The two outer cross members of the bottom frame were adjustable such that a rubber mallet could be used to position them on the beams of the lift. Once in position, all fasteners could be tightened. This arrangement is shown in Figure 56. The lift had to be generally prepositioned in the BANTAM chamber prior to installing the bottom plate. The general positioning is depicted in Figure 57. Details for exact positioning follow in the section on mechanical tuning.



Figure 54: Using Lift to Install Top Plate (Raised)



Figure 55: Using Lift to Install Top Plate (Lowered)



Figure 56: Bottom Plate Installed on Scissor Lift



Figure 57: General Positioning of Scissor Lift and Bottom Plate

Rexolite Lenses

Theory and Simulation

The Rexolite lenses were designed by following the example set by GTRI for their 3-D FBS. However, the design steps were re-arranged. GTRI has designed their lenses for quadridge horn antennas which have a specific forward beam pattern whereas the BANTAM 2-D FBS will use an omni-directional monopole. Furthermore, being a free-space FBS, GTRI did not have any apparent spatial constraints along the propagation direction whereas the BANTAM 2-D FBS will be confined within two plates and a chamber of restricted volume.

There are multiple design parameters in the 2-D FBS lenses which facilitate trade-offs. The goal is plane-wave like illumination on a material sample (while minimizing sample edge effects) so that plane-wave models can be applied to calculate permittivity and permeability from reflection and transmission coefficients. The material illumination is based on Gaussian optics but differences between Gaussian and plane-wave illumination can lead to errors in calculating permittivity and permeability. The error will largely depend upon the size of the beamwaist produced by the lenses. Error should decrease with increasing $k_0 w_0$ (focusing factor) and increase with increasing lens thickness. Gaussian illumination can be approximated as plane-wave illumination with less than 1% error (in freespace) if beams have waists such that $k_0 w_0 \geq 10$. A design rule-of-thumb on the lower limit of the focusing factor is a beamwaist approximately one wavelength in diameter or $k_0 w_0 = \pi$ [8]. The relationship between beamwaist and wavelength is

$$k_0 w_0 = \frac{2\pi w_0}{\lambda} \quad (1.16)$$

where beamwaist on the left side of the equation is part of the desired focus factor.

The design for the BANTAM 2-D FBS lenses will begin with this lower focusing limit applied near the lower frequency side of 2-18 GHz. The actual design-to frequency for focusing factor is 2.574 GHz as this frequency translated directly to the optimum lens size. As shown in Figure 58, focusing factor improves with frequency and approaches a value of 10 as recommended for minimizing error.

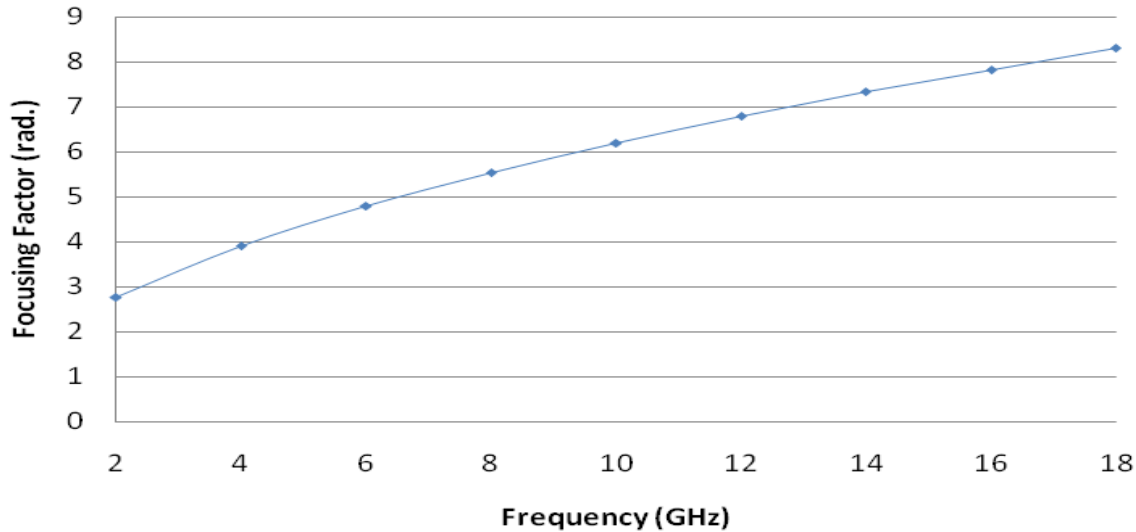


Figure 58: Focusing Factor of 2-D FBS Lenses

The relationship between beamwaist and frequency shows that the desired beamwaist for 2.574 GHz is 2.294". Beamwaist is then plotted against frequency for the BANTAM 2-D FBS lenses in Figure 59.

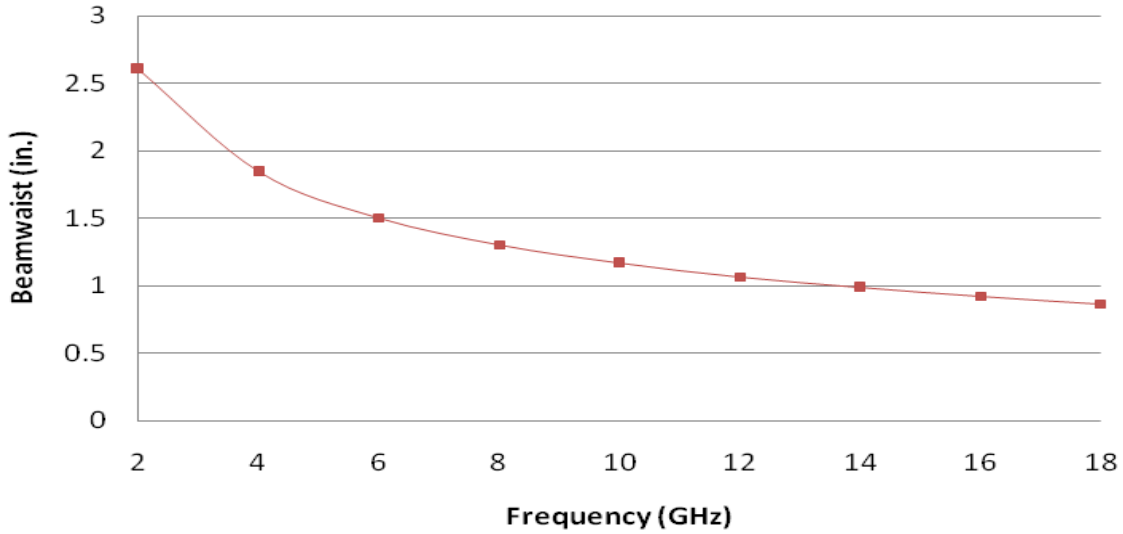


Figure 59: Beamwaists of 2-D FBS Lenses

Following the GTRI example, a value for amplitude taper at the lens aperture (the tip-to-tip plane through the two lens halves) and at the edge of illumination on the sample material was chosen to be

$$T_{\text{lens edge}} = 0.01, \text{ or } -20\text{dB}$$

$$T_t = 0.01, \text{ or } -20\text{dB}$$

From the beamwaist and taper values presented thus far, the minimum size of the sample material can be determined for 2.574 GHz in the following relationship.

$$r_i = \sqrt{\frac{w_0^2 \ln(T_t)}{-2}} \quad (1.17)$$

For 2.574 GHz, the minimum [radius] size of 3.481" can be applied to all frequencies 2.574-18 GHz. For $2-2.574\text{ GHz}$ the minimum size will be slightly larger. The minimum size is only that size of a target that will fit in the beam and receive the

required amplitude taper. The actual targets will be longer such that their edges do not cause significant diffraction effects in the beam.

Similar to the beam's radius at its waist, the beam's radius can be defined at other points along the beam. By knowing the beam's radius at the lens aperture plane, the lens design can progress into defining where to place the target relative to the beamwaist to achieve the desired taper. With the desired value of amplitude taper at the aperture plane, the beam radius at the aperture plane can be derived from

$$w_L = \sqrt{\frac{-2r_{lens}^2}{\ln(T_{lens\ edge})}} \quad (1.18)$$

where r_{lens} is the lens tip-to-tip radius and is defined by the BANTAM constraints. This results in a target placement of

$$z = \frac{\pi w_0^2}{\lambda} \left(\sqrt{\frac{w_L^2}{w_0^2} - 1} \right) \quad (1.19)$$

relative to the beamwaist where the position of the beamwaist is defined by the focusing focal length of the design-to frequency.

It is at this point in the lens design that two lens sizes will be presented. One size, the smaller, will be optimized for the near-field scanning function of the BANTAM - it will be useful in measuring S-parameters as well. The other size, the larger, will be optimized for S-parameters - it will likely not be useful for near-field scanning since its elongated electrical lengths (lens thicknesses, focal lengths, etc.) will elongate the component layout in long axis and prevent a meaningful scan area. For the final design of both lens sizes, the beam radius at the lens aperture plane can be seen in Figure 60.

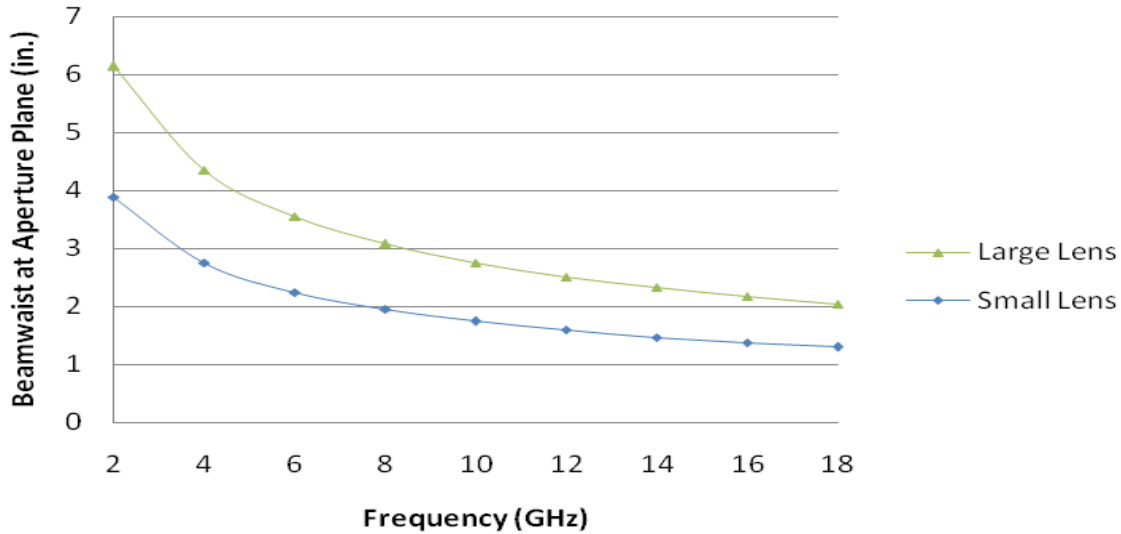


Figure 60: Beam Radii at Aperture Planes of 2-D FBS Lenses

Further, for target placement relative to the beamwaist,

$$z = 7.701"$$

for the large lens and

$$z = 3.999"$$

for the small lens, each using the design-to frequency of 2.574 GHz. By placing the target in this position for all frequencies in the 2-18 GHz band, the amplitude taper at the lens aperture (for both lenses) and at the target surface takes on the trend shown in Figure 61.

For the smaller lens, r_{lens} (the lens tip-to-tip radius) is limited by the forward/reverse scanning motion of the top plate over the bottom plate. The top plate must be wide enough (front-to-back) to scan over a meaningful area without disrupting the waveguide's physical structure or the beam within the waveguide. This is illustrated in the top and bottom frame of Figure 62.

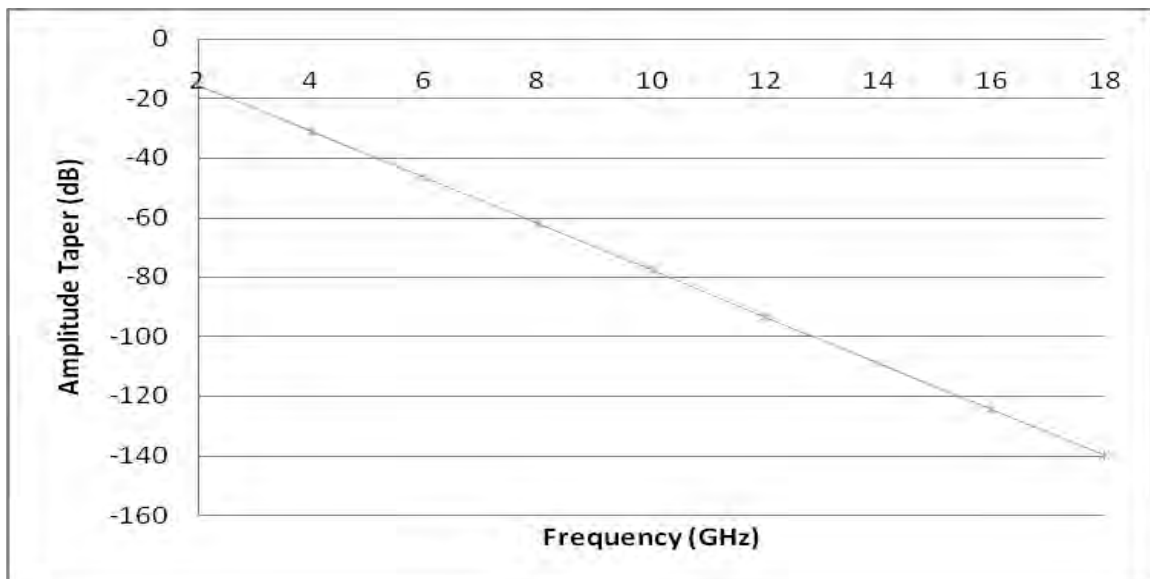


Figure 61: Amplitude Taper at Lens Aperture and Target Surface

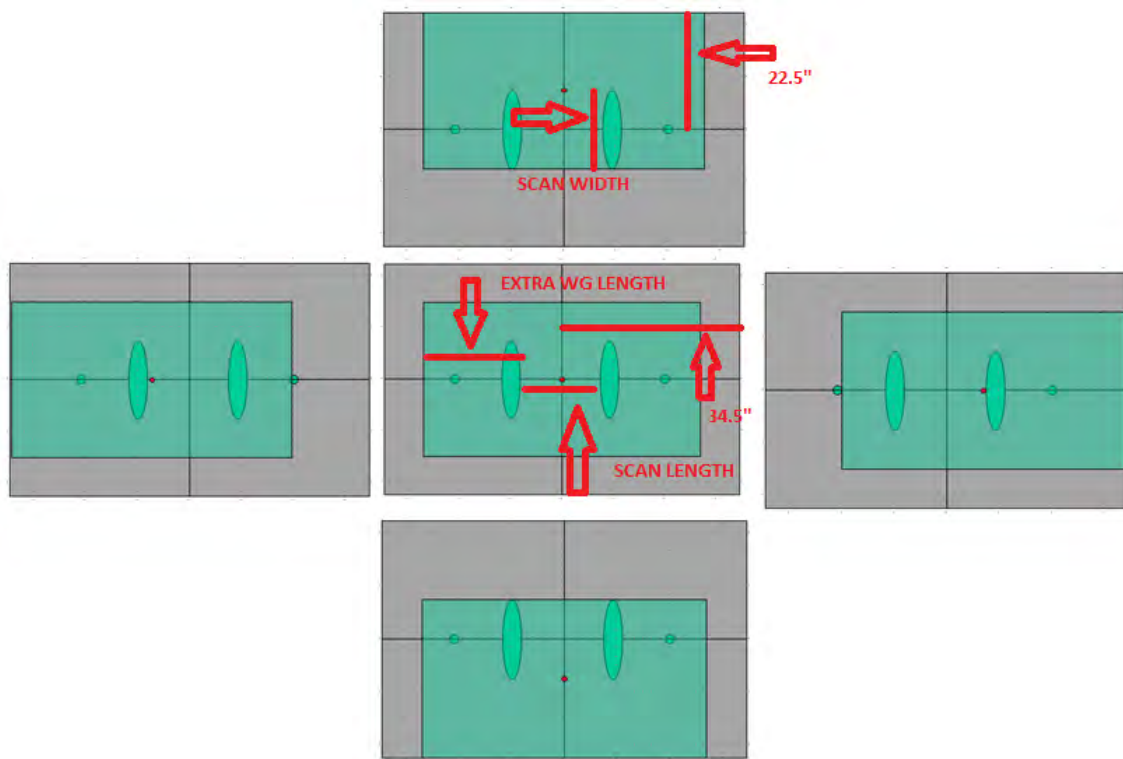


Figure 62: Top Plate Scan Area for Sizing Small Lens

In order to keep the contents (antennas and lenses, particularly, but target generally) of the PPWG covered by the top plate, the width of the top plate must be twice the width of the desired scan area. However, the maximum width of the top plate is constrained by the width of the BANTAM chamber, or more appropriately, the half-width of the bottom plate (22.5" at the aluminum, Bondo, and PVC joint). Due to symmetry, the half-width of the bottom plate is equivalent to one-and-a-half times the maximum width of the desired scan area. This means that

$$\text{max scan width} = \frac{22.5''}{1.5} = 15''$$

If the width of the maximum meaningful scan area was defined from tip-to-tip of the small lens, then

$$r_{\text{lens}} \leq 7.5''$$

As this maximum radius relates to the top plate, the tips of the small lens will contact the tangent (aluminum, Bondo, and PVC joint) of the front and back rolled edges at the extreme positions in the forward and reverse scans. For the large lens, r_{lens} was designed such that in a scan (though it wasn't designed explicitly for scanning) the lens tips would be exposed somewhat at these extremes.

For each lens, r_{lens} is related to the collimating lens focal length, the thickness of the collimating lens, the focusing lens focal length and the thickness of the focusing lens. This relationship is

$$t_i = \frac{-f_i + \sqrt{f_i^2 + \left(\frac{n+1}{n-1}\right)r_{\text{lens}}^2}}{n+1} \quad (1.20)$$

$$t_0 = \frac{-f_0 + \sqrt{f_0^2 + \left(\frac{n+1}{n-1}\right)r_{lens}^2}}{n+1} \quad (1.21)$$

where

f_i = an optimization input for the collimating focal length

t_i = thickness of collimating lens

n = index of refraction of Rexolite

and

$$f_0 = z \left(1 + \left[\frac{\pi w_0^2}{\lambda z} \right]^2 \right) \quad (1.22)$$

where

z, w_0, λ are given according to the design-to frequency

and where

t_0 = thickness of focusing lens

In this trade space, the available electrical path length between monopoles and the available scan space in the BANTAM length provide additional constraints. The top plate must be long enough to scan over the entire length of the area between the lenses without hitting the lenses with the scanning probe or otherwise disrupting the waveguide structure. This can be seen in the side frames of Figure 62. This means that the length of the top plate must be twice the combined distances of the scan length and the remaining length necessary to maintain the waveguide, i.e. the length that still provides coverage of the monopole. However, the maximum length of the top plate is constrained by the length of the BANTAM chamber, or more appropriately, the half-length of the bottom

plate (34.5" at the aluminum, Bondo, and PVC joint). Due to asymmetry, the half-length of the bottom plate is equivalent to one-and-a-half times the maximum length of the desired scan area plus the length required to maintain the waveguide structure. This means that

$$1.5 \cdot ScanLength + ExtraWaveGuideLength \leq 34.5"$$

and

$$Length_{top\ plate} = 2(ExtraWaveguideLength + ScanLength)$$

The *ExtraWaveguideLength* can be interpreted as

$$MonopoleM \arg in + f_i + t_i + t_0$$

and the *ScanLength* can be interpreted as

$$2 * f_0 \text{ (the space between the lenses)}$$

Then,

$$\begin{aligned} & 1.5 \cdot ScanLength + ExtraWaveGuideLength \\ &= MonopoleM \arg in + f_i + t_i + t_0 + 1.5 \cdot 2 \cdot f_0 \leq 34.5" \end{aligned}$$

and

$$Length_{top\ plate} = 2(MonopoleM \arg in + f_i + t_i + t_0 + 2 * f_0)$$

Each of these length variables ($r_{lens}, f_i, t_i, t_0, f_0, MonoM \arg in$) were put into a spreadsheet to optimize each for the given length constraints. For both lens sizes, the collimating focal length was used as an input to the optimization program. The

optimization program was Microsoft Excel's Goal Seek. The value for r_{lens} , and thus, the remaining length variables were based on the optimum relationship between r_{lens} and the collimating focal length, i.e. the collimating $f\#$, as shown by

$$f\# = \frac{f_i}{2 \cdot r_{lens}} \quad (1.23)$$

One optimization solution was discovered when the $f\# = 0.25$, or when r_{lens} was twice the length of the collimating focal length. The results of the optimization allowed the curvature profile of each lens, collimating and focusing halves respectively, to be determined by

$$t(r) = t_i + \frac{f_i - \sqrt{f_i^2 + \left(\frac{n+1}{n-1}\right)r^2}}{n+1} \quad (1.24)$$

$$t(r) = t_0 + \frac{f_0 - \sqrt{f_0^2 + \left(\frac{n+1}{n-1}\right)r^2}}{n+1} \quad (1.25)$$

where the optimum lengths are, for the small and large lenses respectively,

$$f_i = 2.600" \text{ and } 4.107"$$

$$t_i = 3.306" \text{ and } 5.222"$$

$$r_{lens} = 5.200" \text{ and } 8.214"$$

$$t_0 = 2.243" \text{ and } 3.924"$$

$$f_0 = 7.246" \text{ and } 9.387"$$

and

MonoM arg in = 4.614" (roughly one wavelength of 2.574 GHz).

$$Length_{top\ plate} = 54.5"$$

$$Width_{top\ plate} = 30"$$

The optimization spreadsheet for each lens is shown in the appendix of this document. The optimization program for each of these spreadsheets was designed to 2.574 GHz. The expected values for each parameter for the even frequencies from 2-18 GHz are tabulated alongside 2.574 GHz. The entries highlighted in red are inputs to the program. Simulation of the lenses will be presented with the final system architecture.

Specifications

As described above, the lenses will be 2" tall cut from a Rexolite slab having an index of refraction of 1.594. There will be two small lenses and two large lenses cut from the slab. The collimating profile of the small lens will be defined by

$$t(r) = 3.306 + \frac{2.600 - \sqrt{2.600^2 + \left(\frac{1.594+1}{1.594-1}\right)r^2}}{1.594+1} \quad (-5.2 \leq r \leq 5.2)$$

and the focusing profile will be defined by

$$t(r) = 2.243 + \frac{7.246 - \sqrt{7.246^2 + \left(\frac{1.594+1}{1.594-1}\right)r^2}}{1.594+1} \quad (-5.2 \leq r \leq 5.2)$$

The collimating profile of the large lens will be defined by

$$t(r) = 5.222 + \frac{4.107 - \sqrt{4.107^2 + \left(\frac{1.594+1}{1.594-1}\right)r^2}}{1.594+1} \quad (-8.214 \leq r \leq 8.214)$$

and the focusing profile will be defined by

$$t(r) = 3.924 + \frac{9.387 - \sqrt{9.387^2 + \left(\frac{1.594+1}{1.594-1}\right)r^2}}{1.594+1} \quad (-8.214 \leq r \leq 8.214)$$

The weight of a small lens is approximately 2.5 pounds and the weight of a large lens is approximately 6 pounds. The approximate coefficient of static friction of a finished lens on the aluminum sheet is 0.5 based on the equation:

$$\mu_s = \frac{f}{F_n} \approx \frac{1.32}{2.5} \quad (1.26)$$

where f was the laterally applied force that initiated lens movement along the aluminum surface. The coefficient of dynamic friction was not determined. Given the friction coefficient and scanning tests that showed the top plate was capable of dragging the lenses across the bottom plate, the lenses will be held in place on the bottom plate by double-sided conductive tape 0.003" thick.

Fabrication

Each lens was rough cut from the Rexolite slab using a high-powered water jet. The cutting was performed at the AFIT Model and Fabrication Shop. Following the rough cut, the lenses were precision machined to tolerances as low as $\pm 0.0018"$ on each profile face and each flat face. Figure 63 shows one of the large lenses immediately after machining.

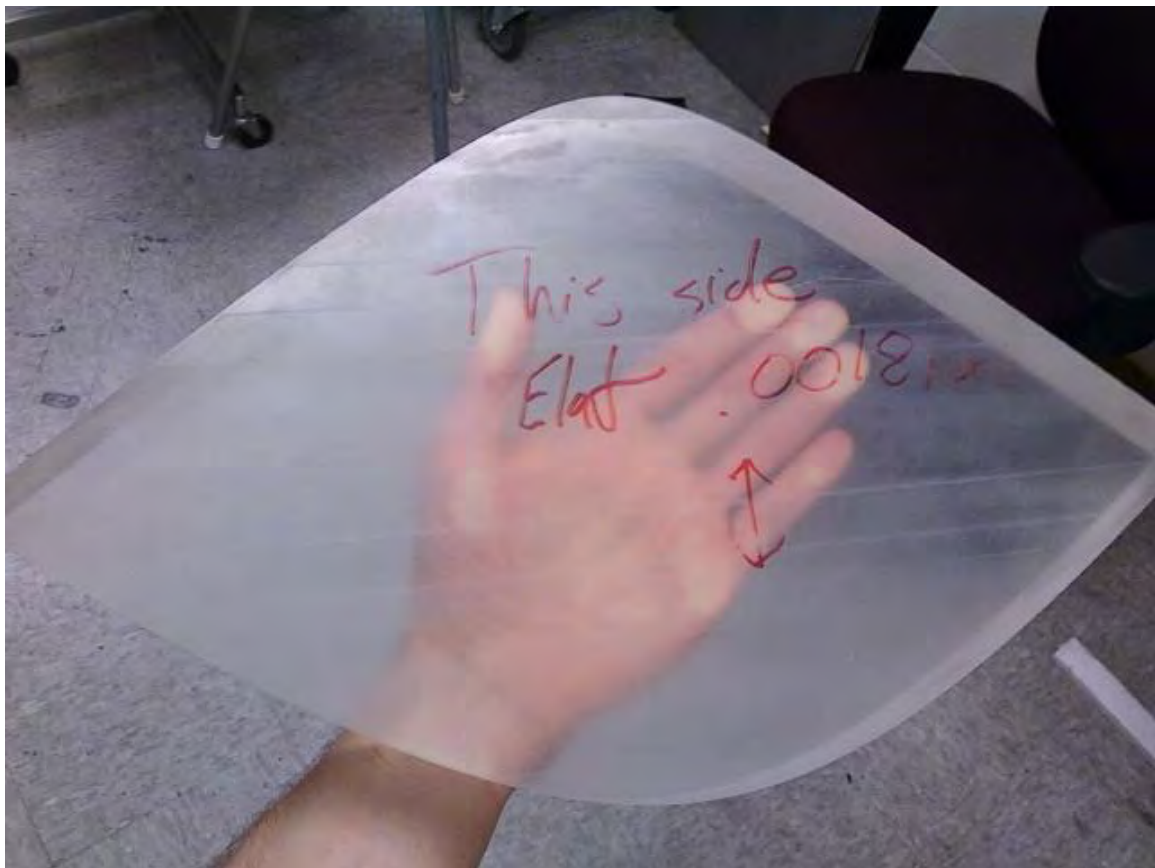


Figure 63: Large Lens Prior to Polishing

Each face of each lens had to be polished. It was never determined to what degree polishing must be achieved, but enough polishing was accomplished to remove all machining marks and bring the faces to fullest transparency.

The profile faces were polished much longer than the flat faces. Polishing occurred by taping a sheet of 1,000-grit sandpaper to a precision flat plate and simultaneously pulling and rolling the lens over the sandpaper. Progress was indicated by the diminishing brightness of the machining marks as viewed through one of the flat faces. This is shown in Figure 64.



Figure 64: Bright Machine Marks in Profile Surface of Lens

Use of the 1,000-grit sandpaper lasted for approximately 800 strokes or until the bright machining marks were removed. Approximately 200 strokes on 1,500-grit sandpaper reduced the surface roughness further. The backside of a piece of sandpaper was then used to apply Turtle Wax and then Meguiar's Polishing Compound to the profile faces. This is shown in Figure 65. A final pair of lenses, after polishing for approximately 8 hours, is shown resting on the bottom plate of the PPWG in Figure 66.



Figure 65: Polishing Lens With Compound



Figure 66: Small Lenses on Bottom Plate

Mode-Matching Components

Theory and Simulation

Mode-matching components have been referred to throughout this document as a component for mitigating the higher-order mode effects (undesirable phase variation along the propagation and vertical directions) caused by the height of the lenses. These components will not be addressed by mathematical mode-matching techniques, but will rather be designed and simulated in CST based off of intuition alone.

The over-moding in the PPWG is due to the fact that all frequencies above the first-order cutoff (2.951 GHz) are excited directly into the 2" PPWG spacing. In the design of the mode-matching component, all these frequencies will be excited directly into a PPWG of a much smaller spacing (0.166", or equivalent to a quarter-wavelength of 18 GHz) allowing only the fundamental mode for 2-18 GHz to propagate. Then, the geometry of the small PPWG will be transitioned as smoothly as practical to the

geometry of the 2" PPWG. This transition, if accomplished smoothly enough, could prevent the excitation and propagation of the higher-order modes from the monopole to a large degree. However, this spacing still supports higher-order modes and they may in fact be excited by introducing a target into the space. Overall, the exact degree of higher-order mode suppression would have to be determined mathematically.

To verify the effect of the mode-matching component, CST simulations of a PPWG containing the component will be reviewed and compared qualitatively to the over-moded circular-plate PPWG of Figure 23 operating at 18GHz. The CST model for one of these components is shown in Figure 67. The component will be referred to as a mode-matching mesa due to its resemblance to a flat-topped pyramid.

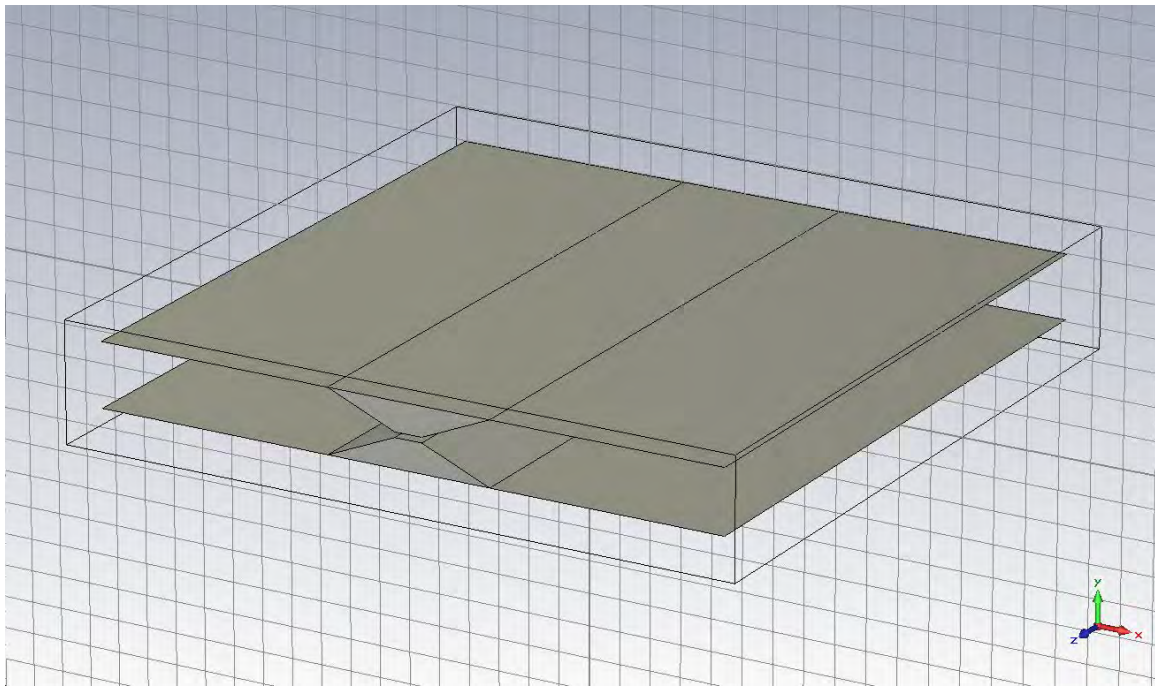


Figure 67: Small Mode-Matching Mesa

In the CST model, a coaxial line is fed through the center of the 10" long bottom mesa. The coaxial adapter and the internal dielectric are joined flush to the flat-top of the bottom mesa with the inner conductor (monopole) rising 0.166" to the flat-top surface of the top mesa. The width of the mesa's base will be constrained by the required distance between the monopole and the adjacent lens. Since the distance between the monopole and the lens is the collimating focal length, the mesa's base will be twice that length. For each lens size, there will be an associated mesa size. Figure 68 and Figure 69 shows the qualitative effect of the small mesa and the large mesa on the mode structure within the PPWG. The only noticeable difference between the two sizes is the patch of interference (likely caused by diffraction from the mesa's long edges) shortly outside of the small mesa. The large mesa develops the same interference patch, but at a longer distance. The monopole's cylindrical wavefronts are maintained in both arrangements.

Figure 70 and Figure 71 show the forward-directed magnitude and phase variations for 18 GHz along various evaluation lines extending from the small mesa. Figure 72 and Figure 73 are overlays of the large mesa data on the small mesa data. Asterisks in the legend indicate the newest (large mesa) information.

The primary characteristic of these figures is how cleanly the magnitude and phase varies in the propagation direction. This is in complete contrast to Figure 28 and Figure 29 for the over-moded circular-plate PPWG. Another noticeable characteristic is the peak of the magnitude plots. In Figure 28, the peak of the magnitude plot is at 400 V/m. With either of the mesas installed, the peak of the magnitude plot is near 1,600 V/m. This suggests that energy that would have been distributed among several higher-order modes is now distributed among much fewer higher-order modes.

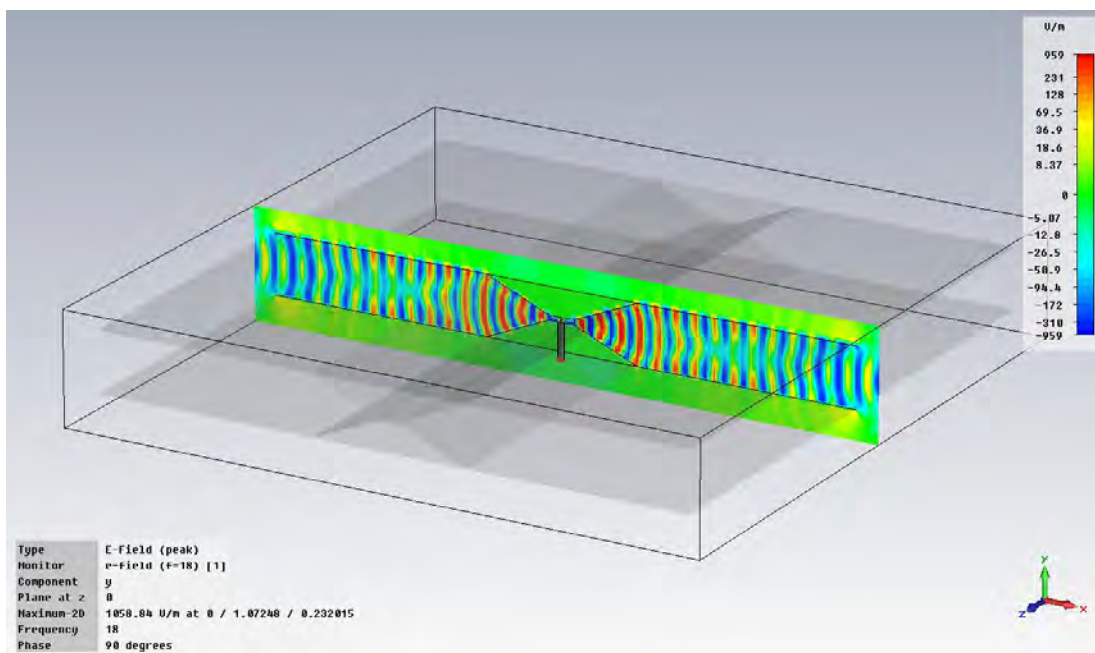


Figure 68: Small Mesa Effects on Overmoding

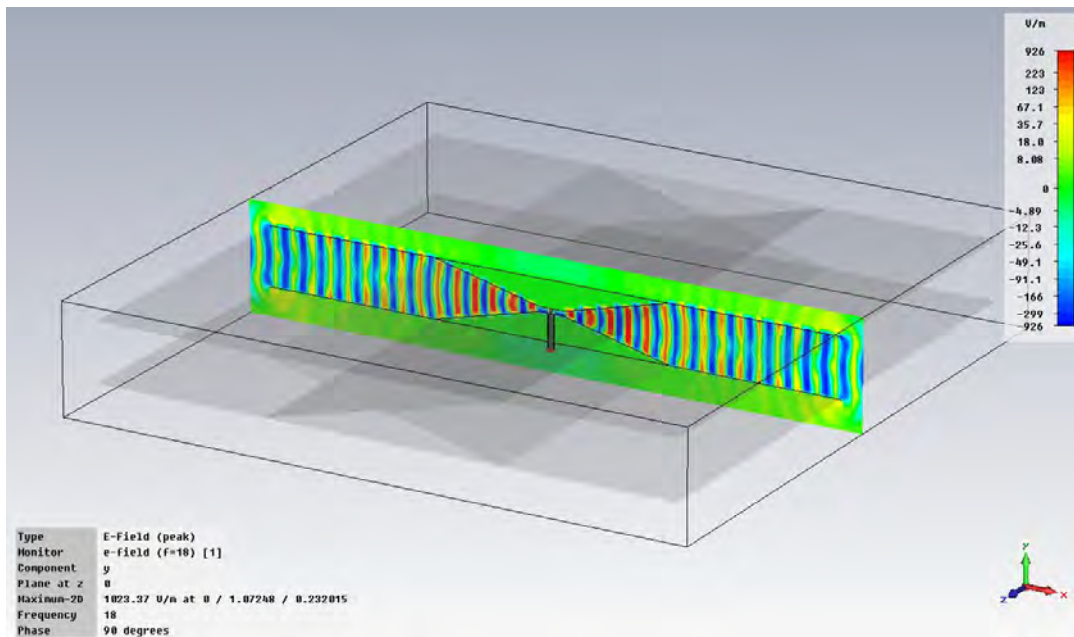


Figure 69: Large Mesa Effects on Overmoding

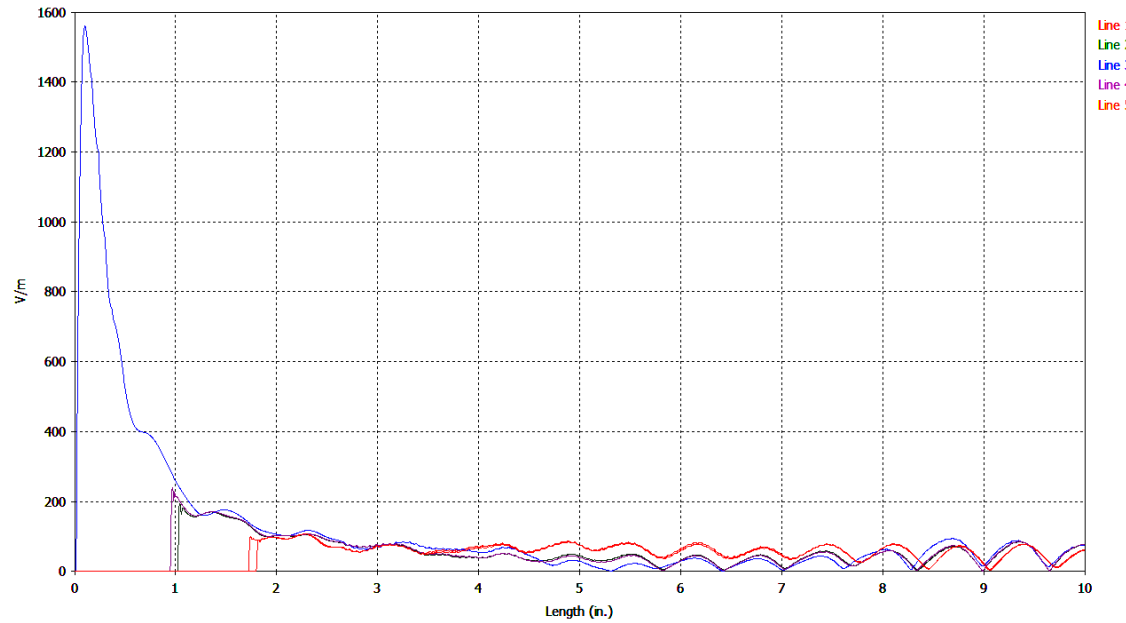


Figure 70: Mag. Variation Along Evaluation Lines for Small Mesa at 18 GHz

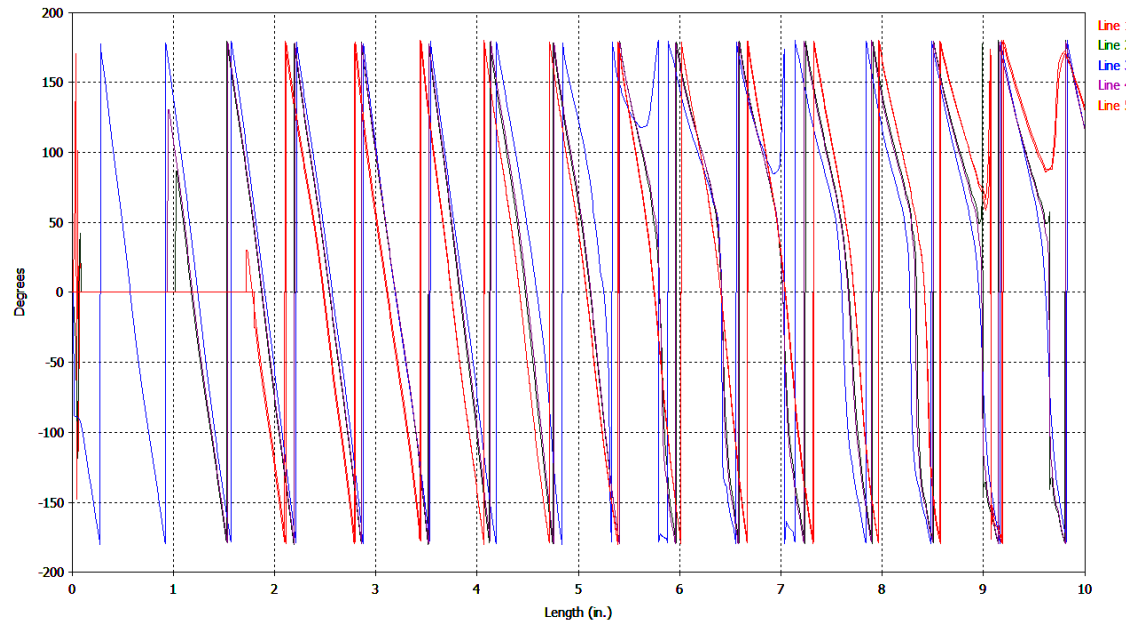


Figure 71: Phase Variation Along Evaluation Lines for Small Mesa at 18 GHz

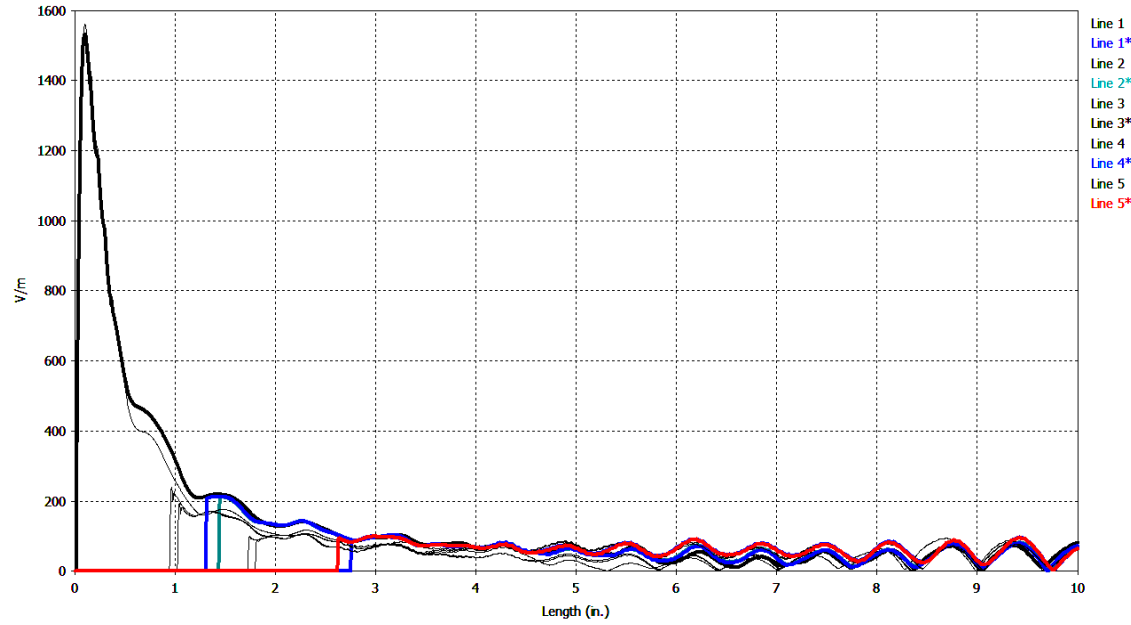


Figure 72: Mag. Variation Along Evaluation Lines for Large Mesa at 18 GHz

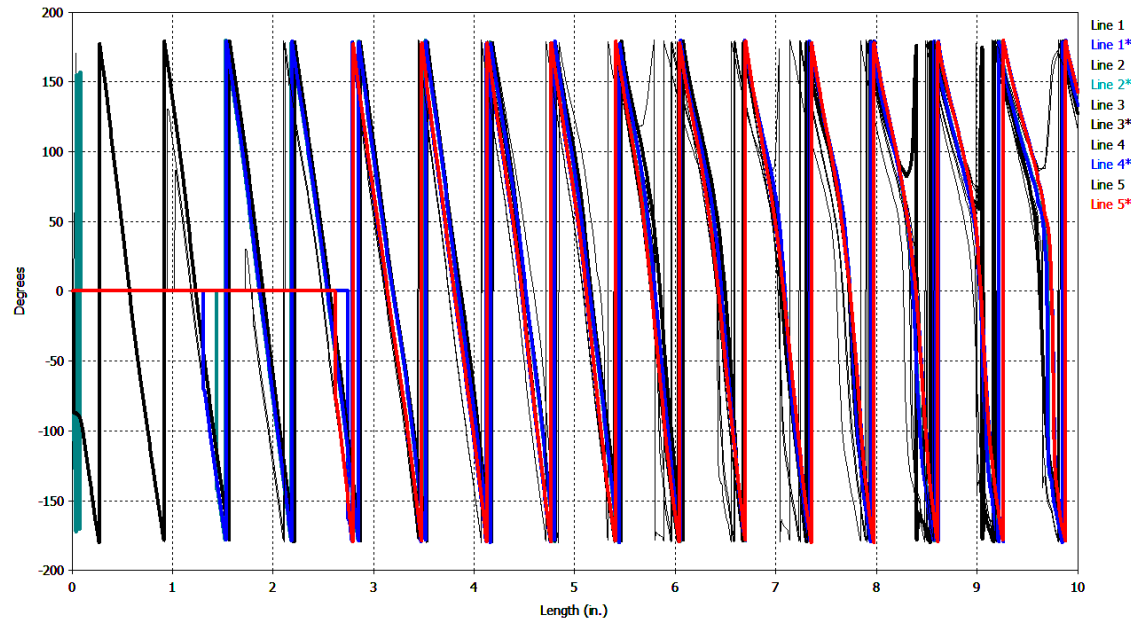


Figure 73: Phase Variation Along Evaluation Lines for Large Mesa at 18 GHz

The phase plots suggest that the phase variation in the vertical direction is brought under much tighter control. The vertical phase variation of Figure 29 varies as widely as 360° from bottom plate to top plate. In Figure 73, the vertical phase variation seems to be approximately 30° from bottom plate to top plate except in the area of the interference patches. It could even be suggested that with the mode-matching mesas, the phase variations of 18 GHz are cleaner than the first-order phase variations of 4 GHz (Figure 27). This would suggest that the mode-matching mesas are capable of correcting the six-higher-order mode structure to below first-order levels.

Specification

Utilizing the small and large mode-matching mesas is the quickest way to effectively address the over-moding of the 2" PPWG. As indicated, the base width of each mesa should be determined by the collimating focal length of the respective lens. The height of each mesa should be such that a PPWG of less than 0.328" spacing could be formed between them. In the simulations, the spacing was arbitrarily set at 0.166", or the equivalent of one-quarter wavelength at 18 GHz. This made the height of each mesa 0.917". Of course, this design is bound to a single spacing and monopole operating over 2-18 GHz, rather than, ideally, several mesa designs of various spacing and various monopole heights operating over frequency octaves.

The width of the mesa's flat top should be wide enough such that the vertical magnitude and phase variation in the small PPWG at 18 GHz has time to converge to a tight band of values as does the 2" PPWG operating at 2 GHz (Figure 24 and Figure 25).

For the mesa simulation, the flat top was 0.866" across to accommodate the diameter of a coaxial adapter and the equivalent of a half-wavelength of 18 GHz on either side.

The length of the mesa should be the longest practical length usable by the BANTAM PPWG. The exact length will coincide with the width of the bare-metal area on the bottom plate. This bare-metal area will accept a mesa 32" long.

Fabrication

Due to time constraints, the mode-matching mesas were not fabricated for this thesis. It is recommended that final designing and fabricating be an immediate future action.

Targets

Theory and Simulation

Upon assembly of the BANTAM 2-D FBS, several targets were evaluated. The target set consisted of an aluminum target, an acrylic target, and a metamaterial D-ring target. The aluminum target was expected to behave analogously to the calibration short used in the GTRI FBS. The acrylic target and the D-ring target served as an unknown target. However, each target is not completely unknown as the S-parameters of the D-ring target have been measured by the GTRI FBS in the past and measurements of acrylic targets are well documented. For measurement by the GTRI FBS, the D-ring target was a 4x4 array (8" x 8" panel) of D-rings. For measurement by the BANTAM 2-D FBS, the D-ring target was a 1x16 array (2" x 32" strip) of D-rings.

Each target was simulated in the full system architecture in CST. The appropriate S-parameters and field distributions will be compared to the physical measurements in the results of Chapter 4.

Specification

The aluminum, acrylic, and D-ring targets are each 32" long by 2" wide. The aluminum is 0.1915" thick, the acrylic is 0.1975" thick, and the D-ring target is 0.0345" thick. As shown in Figure 74, the D-rings are 1" in diameter and their centers are spaced 2" apart. The trace width is 0.04" (1 mm) and the trace thickness is 0.0014" (0.035 mm). The vertical gap is 0.157" (4 mm) and the horizontal gap is 0.079" (2 mm).

Fabrication

The aluminum and acrylic was cut to specification at the AFIT Model & Fabrication Shop. The GTRI D-ring target was cut into strips in the microwave laboratory and taped end-to-end.

Installing each of the targets in the BANTAM PPWG for measurement was an uncertain process due to a yet-to-be-designed target mounting fixture. For simplicity, in both simulation and measurement, the targets were placed approximately half-way between the lenses (focusing focal point) rather than at the recommended target position relative to the beamwaist. There is general uncertainty in the side-to-side position, the forward-reverse position, the degree of rotation on the bottom plate, the degree of tilt, the degree of bowing, and the degree of placement repeatability for each target. The targets are shown in Figure 74.

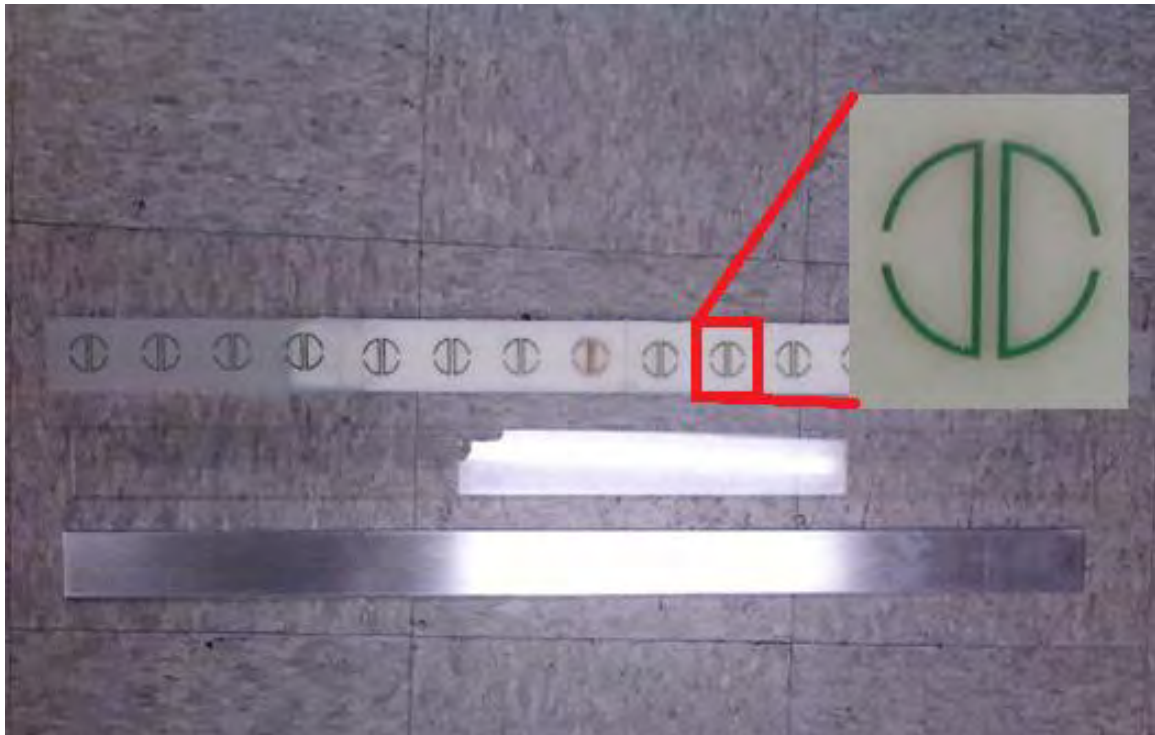


Figure 74: Targets for BANTAM 2-D FBS

BANTAM Reinforcements

Theory and Simulation

The final component for the BANTAM 2-D FBS is the reinforcement kit used to fasten the short axis rail to the BANTAM chamber. As discussed previously, the reinforcements will prevent the top plate from overloading the short axis as the top plate scans to its extreme forward and reverse positions.

Specification

The reinforcement kit consists of two horizontal 80/20 rails that span the length of the chamber and fasten to the wall studs. The reinforcement rails are positioned slightly above the short axis rail. An assembly of 80/20 resembling a hanger is fastened to each

end of the short axis rail. The hook of each hanger fastens over a horizontal rail and is free to move side-to-side via linear bearings.

Fabrication

The reinforcement kit was designed in collaboration with a product specialist at Voelker Controls. The pre-fabricated pieces were assembled directly into the BANTAM chamber. These reinforcements are shown in Figure 75.

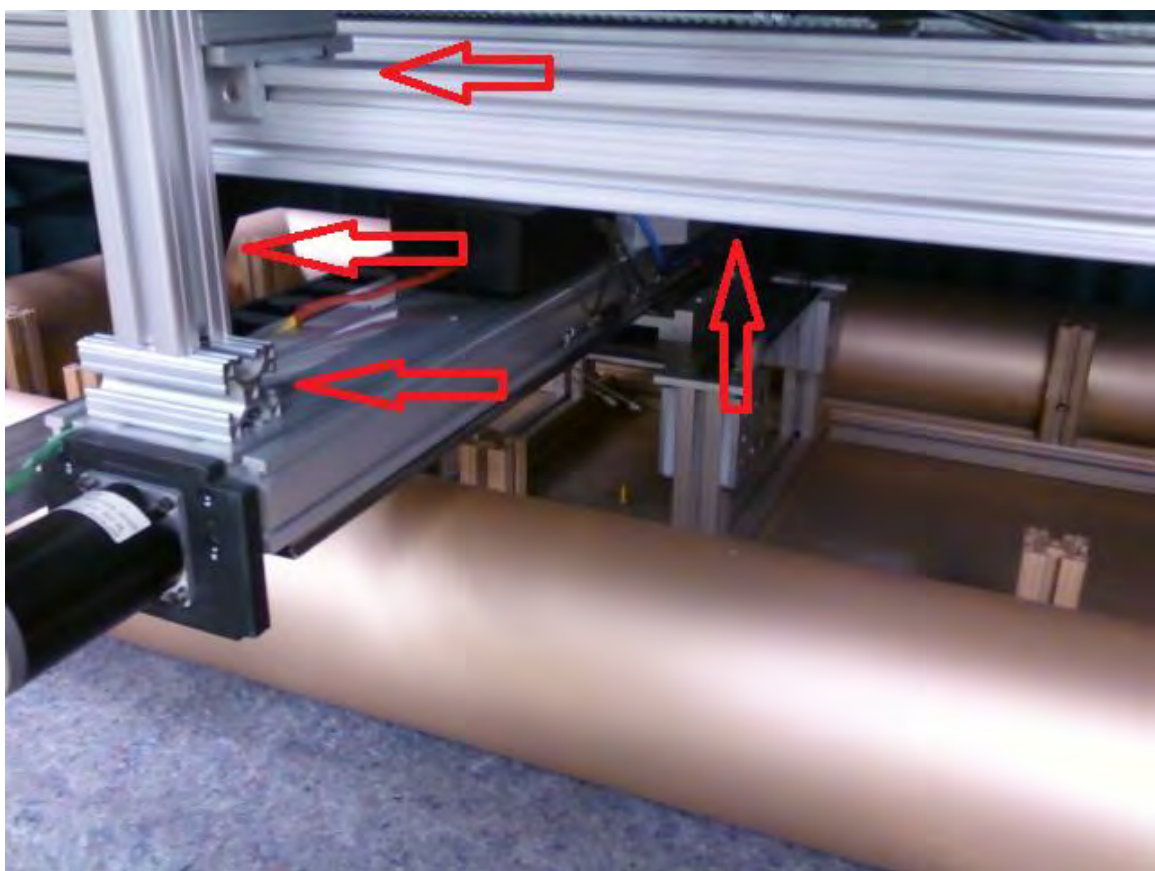


Figure 75: Reinforcements on Short Axis Rail

Assembly & Testing

Upon fabrication, the system components were brought together into the final system architecture. Each plate was assembled with an 80/20 frame, an aluminum sheet, PVC rolled edges, fiberglass filler and conductive paint. The bottom plate was installed on the scissor lift and the top plate was installed on the short axis rail alongside the reinforcement kit. Prior to use, the system had to be precisely tuned and calibrated. These procedures are discussed below. The general use procedures for the BANTAM 2-D FBS follow the original BANTAM use procedures detailed in the appendices of [5].

Mechanical Tuning

Immediately upon installation, each plate had to be leveled and centered. The top plate was centered automatically by its position on the linear translation rails. The top plate was leveled by inserting aluminum shims into the area of vertical play given by each of the four vertical linear bearings.

The bottom plate was roughly centered under the top plate by pushing or pulling the scissor lift into position. Precise centering was accomplished by moving the scissor lift fractions of an inch with a crowbar. Centering was verified by two methods: using the plumb indicator in a hand level and using a plumb line. The plumb line verified the centering when the top plate was in its home position. The plumb indicator of the hand level verified the centering when the top plate was in an extreme scan position (the two rolled edges should line up on the plumb line). These procedures are illustrated in Figure 76. The bottom plate was leveled by adjusting the leveling legs of the scissor lift.

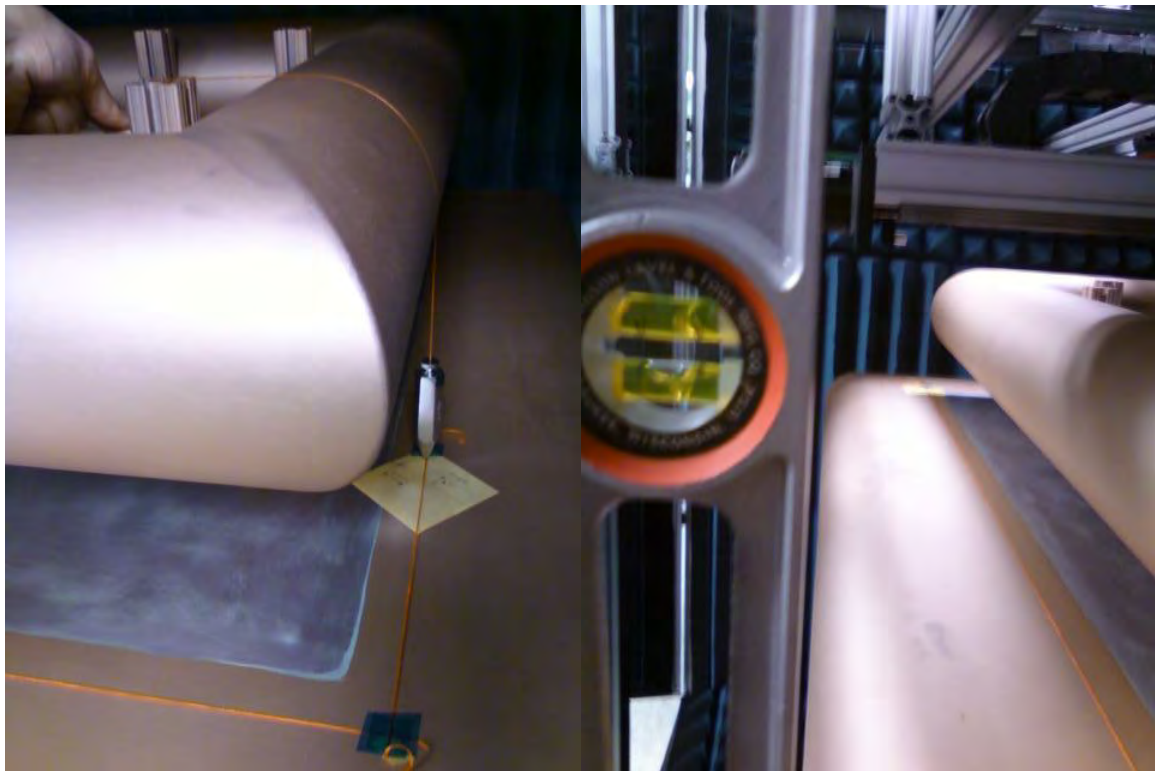


Figure 76: Centering Bottom Plate of PPWG

For the first scan test, the small lenses were placed on the bottom plate and the bottom plate was lifted to the top plate. The lenses connected with the top plate and actually lifted the top plate slightly - this was intended to make a true 2" PPWG. During scanning, at the extreme long axis positions, the top plate tended to pivot over the edge of the nearer lens and lift off the surface of the farther lens. At the extreme short axis positions, the top plate tended to pivot over the nearest lens tips and lift off of both lens surfaces. During the pivoting, the weight of the top plate was transferred through the lens(es) to the bottom plate and to the lift. In reaction to the pivoting, the bottom plate tended to lean with the top plate, re-establishing (to some degree) a parallel plate structure, but at the expense of strain in the scissor lift joints. This effect was mitigated

by reducing the height the lenses lifted the top plate and by introducing a tripod underneath the bottom plate at both ends. This tripod arrangement is only required when operating the scanning function. The tripods must be removed for any lowering of the bottom plate. The tripod arrangement is shown in Figure 77.



Figure 77: Tripod for Stabilizing Bottom Plate

Also during scanning, as the top plate moved over the lenses, the top plate would drag the lenses. This problem was eliminated by applying double-sided conductive tape to the bottoms of the lenses. With the tape applied, the dynamic friction between the top plate and the lenses resulted in a jerking motion during scanning. This effect was mitigated by reducing the scan velocity and by applying a Teflon lubricant to the bare aluminum of the top plate and to the top surface of the lenses.

The monopoles were tuned to an acceptable length by conducting a trial scan and iteratively trimming them as the top plate made physical contact. As previously shown in Figure 30, the plates are not exactly flat, so one portion of the plate may pass over the monopole while another portion drags over the monopole. The three monopoles were trimmed to an average height of 1.916". Since the monopole rod was somewhat flexible, the monopole had to be straightened as well.

The lenses were positioned on the bottom plate with a custom-made lens positioning tool. The tool was pinned to the bottom plate using the two monopole coaxial adaptors on either end of the plate (short focal point and long focal point together). The lens was placed into the profile of the tool, with double-sided tape already applied, and the tool was removed. For the small lens, the tool is a single piece. For the large lens, the tool is in two pieces. This procedure is illustrated in Figure 78 for positioning the large lens.

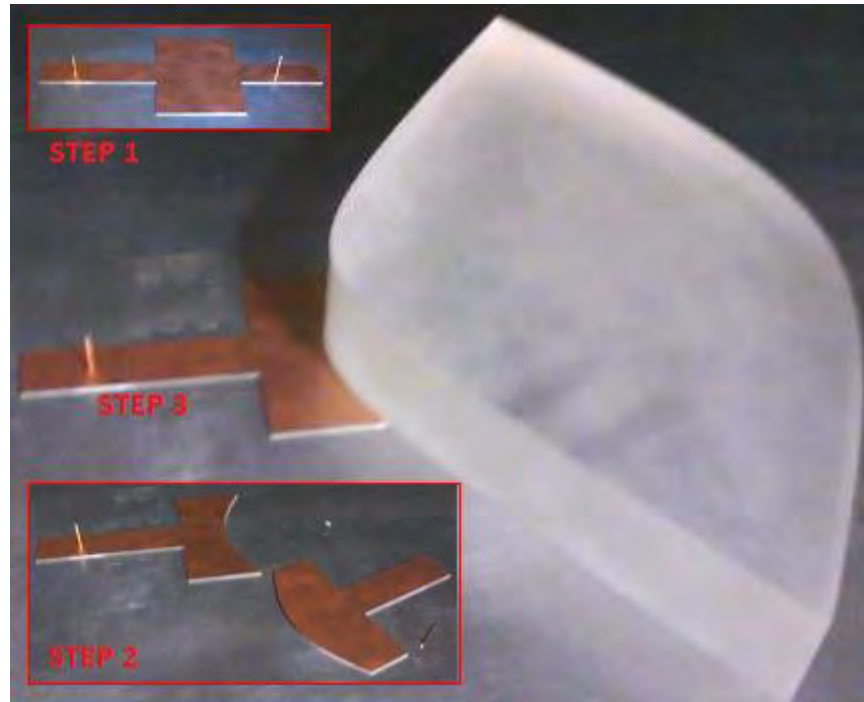


Figure 78: Lens Placement Tool

Positioning the targets was the least precise operation of the system tuning. To be precise, this procedure requires the design and fabrication of a target fixture. In general, the front face of each target was assumed to be placed at the focusing focal length of the left lens. Due to varying thicknesses among the targets, the rear faces were assumed to be forward of the focusing focal length towards the right lens. The targets were positioned and aligned by sight and straightened with the assistance of two identical, flat-laying, surplus targets. With the three pieces positioned together on the bottom plate, the bottom plate was raised to the top plate until the target was slightly compressed. The two surplus targets were then removed. This procedure is illustrated in Figure 79.

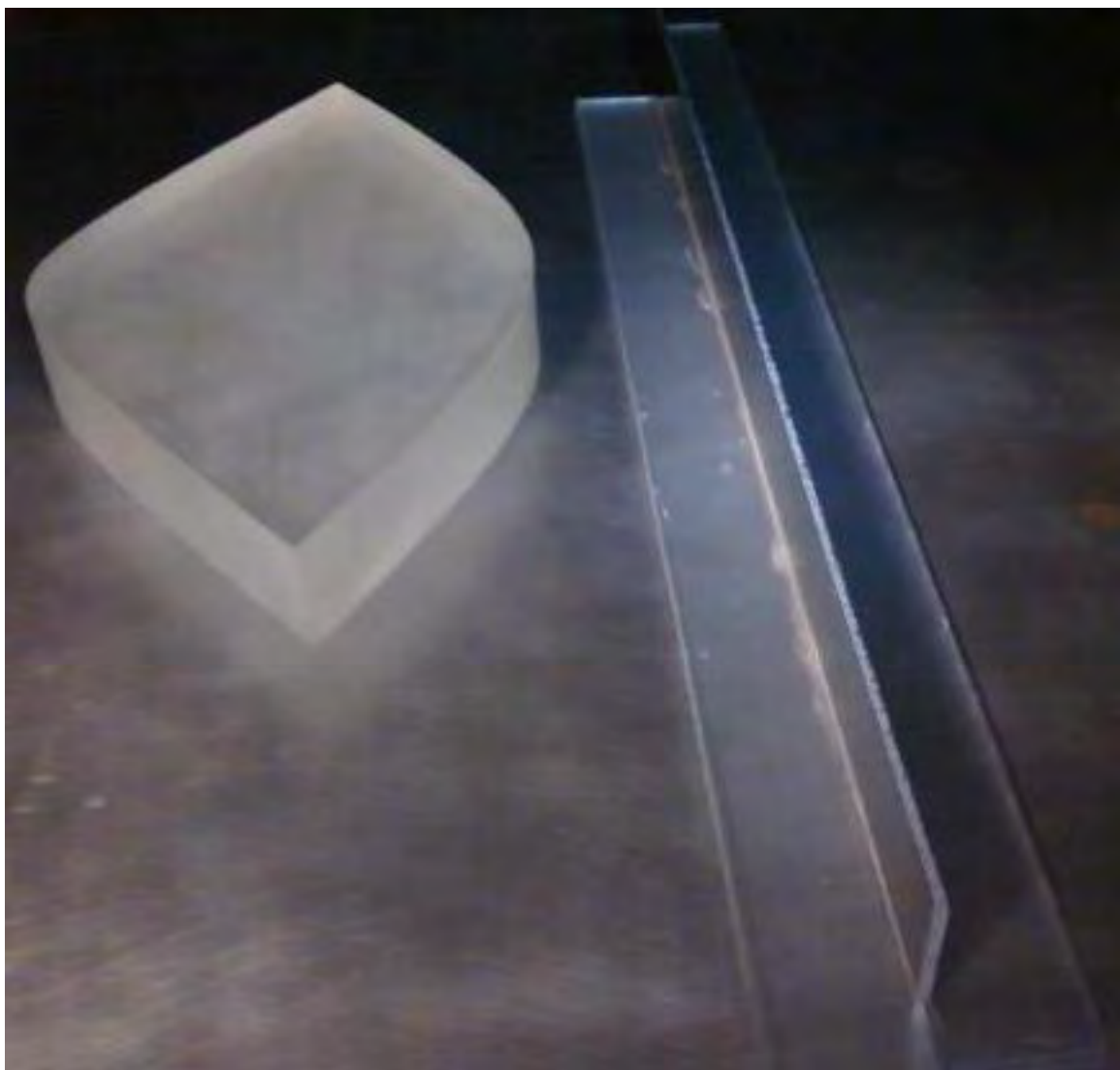


Figure 79: Positioning Targets in the PPWG

Basic Calibration

The extent of calibrating the BANTAM 2-D FBS for this thesis involved only a two-port network calibration. The two-port calibration would correct for the systematic errors up to the point of the coaxial adaptors.

Calibration has to be performed for three different two-port scenarios: 1) S-parameter measurements via left monopole and right monopole; 2) near-field scans via top probe with excitation by left monopole; 3) near-field scans via top probe with excitation by right monopole. The two-port network calibration is performed by measuring calibration standards at the extreme ends of each port's cabling (this includes the coaxial elbows). The standards include a short, an open, a broadband load, and a thru. Measuring the thru for the top probe and left monopole is shown in Figure 80.

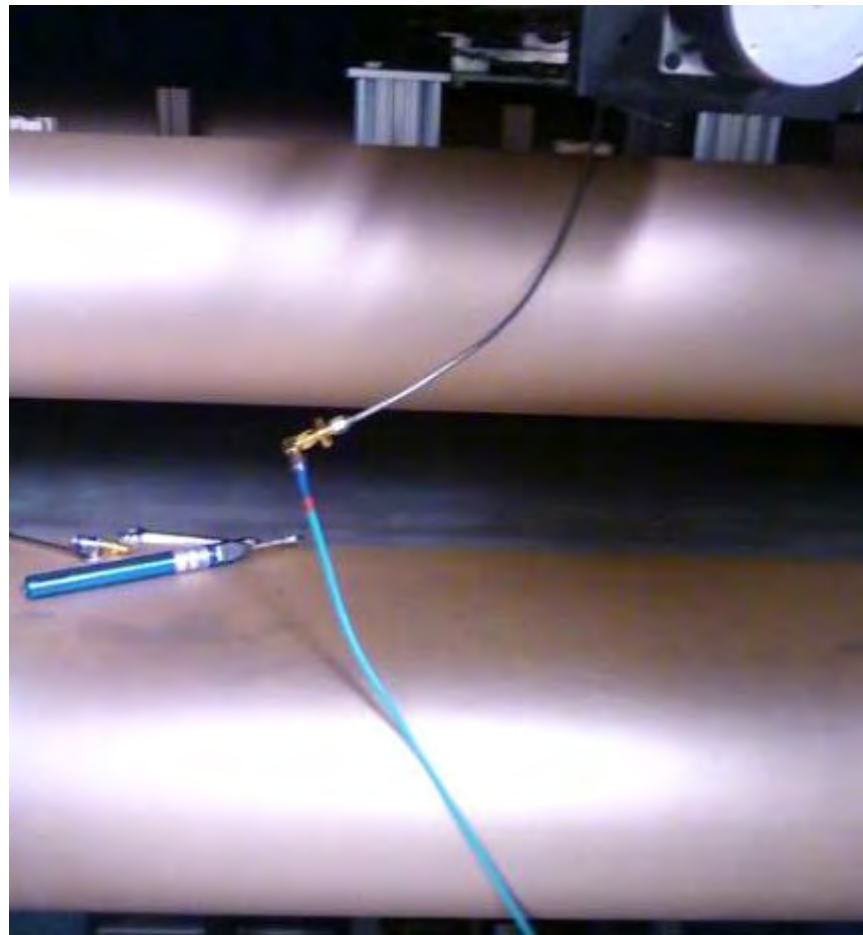


Figure 80: Measuring THRU for Two-Port Network Calibration

IV. Results and Analysis

Chapter Overview

This chapter presents the results of raw measurements made by the newly built BANTAM 2-D FBS and compares them to the results of raw measurements made by simulating the system in CST. The approach to analyzing these results is such that basic measurement phenomena can be highlighted, though not thoroughly and rigorously accounted for as would be necessary for a quality system assessment. The amount of simulation, measurement and analysis required to draw solid conclusions about the actual performance of the BANTAM 2-D FBS is assumed to be quite lengthy, so a rigorous characterization of the system will have to be postponed until a later date. The introductory test matrix, shown in Table 5, is the extent of the tests performed for this thesis, and it is only a small portion of the measurements required. The measurement data provided in this chapter should be of sufficient quality to render a derivation of permittivity and permeability for the acrylic target, but such derivation will not be performed here.

Table 5: BANTAM 2-D FBS Test Matrix

Test Point	Configuration	Function	Description
1	Empty PPWG	Near-Field Scan	Left monopole (short focal)
2		S-Parameters	Left-to-top (short focal)
3			Left-to-top (long focal)
4			Left-to-right (short focal)
5			Left-to-right (long focal)
6	Small Lenses in PPWG	Near-Field Scan	Left monopole
7			Left monopole (air gap)
8			Left monopole (D-Ring)
9		S-Parameters	Left-to-top (short focal)
10			Left-to-right (THRU)
11			Left-to-right (SHORT)
12			Left-to-right (Acrylic)
13			Left-to-right (D-Ring)
14	Large Lenses in PPWG	S-Parameters	Left-to-right (THRU)
15			Left-to-right (SHORT)
16			Left-to-right (Acrylic)
17			Left-to-right (D-Ring)

In CST, the full system architecture was simulated to the best practical representation. All conductive surfaces (except for the traces of the metamaterial D-rings) were modeled as perfect electrical conductors. The system accuracy was set to -40 dB. Port symmetry and geometrical symmetry were used whenever possible.

The rolled edges were not included in the simulations due to the massive mesh they imposed on CST. For example, with one-fold geometrical symmetry (only applicable along the long axis), the mesh size was reduced by 50% to approximately *two-billion* mesh cells for 12.6 GHz. Above 12.6 GHz, CST failed to generate a mesh. The timeliest simulation of the empty rolled-edged PPWG took five hours for 0-4 GHz, but these narrow results were simply too inadequate to be useful.

Simulating with no rolled edges from 0-18 GHz presented a different problem where field data simply did not exist in the farthest reaches of the model geometry. The issue was discussed with the CST specialists at Sonnet Software, but it was never resolved. It was rumored that perhaps the model was too electrically large, i.e. the longest dimension, being greater than 60 wavelengths at 18 GHz, triggered an internal error. Reducing the frequency to 10 GHz brought the model to less than 60 wavelengths and allowed field values everywhere within the model geometry, but it was never confirmed that 10 GHz was the true upper limit of the model.

The final set of simulations did not have rolled edges, they were run from 0-10 GHz rather than 0-18 GHz, and only excitation of the left monopole was considered for comparison with the physical system. The left-side-only simulations followed left-side-only measurements (as shown in the test matrix) mainly due to the time constraints of recalibrating and re-measuring from the right side of the physical system. The time constraint of the physical system was in the 14 hours required to accomplish a single scan at a meaningful spatial resolution.

Empty PPWG

The simulation model for the empty PPWG is shown in Figure 81. The magnitude and phase distributions throughout the waveguide, as excited by the left monopole, can be arbitrarily visualized in Figure 82.

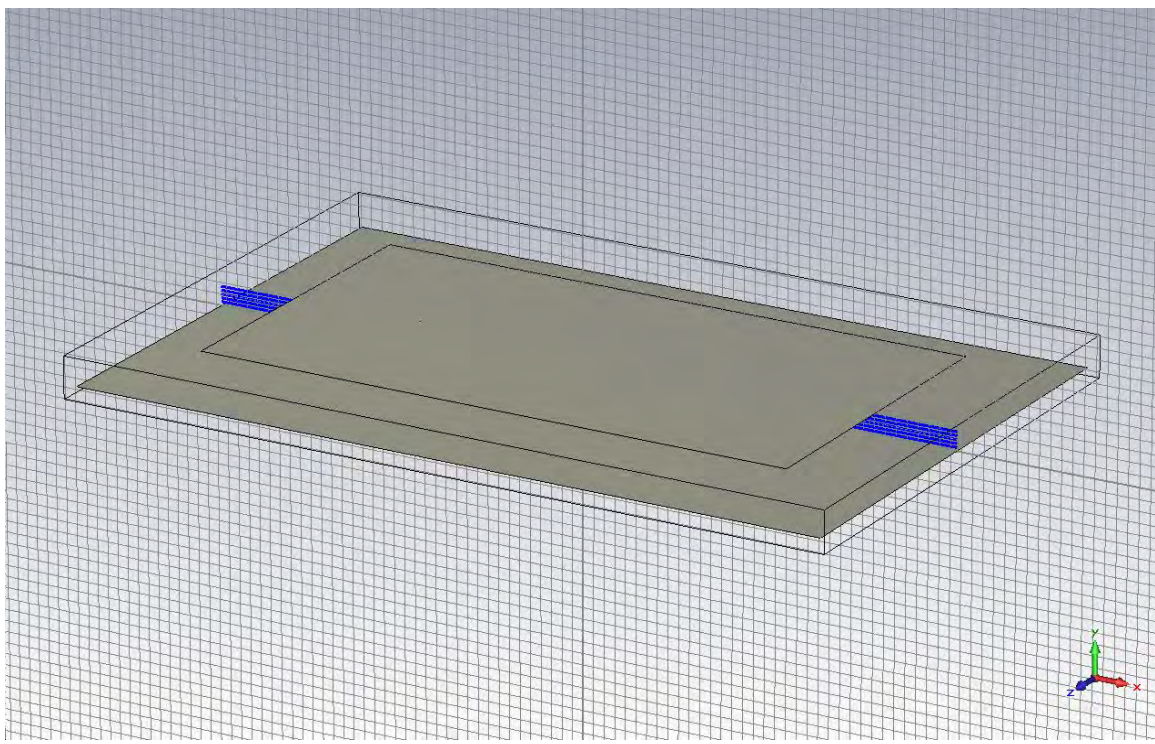


Figure 81: Empty PPWG Model

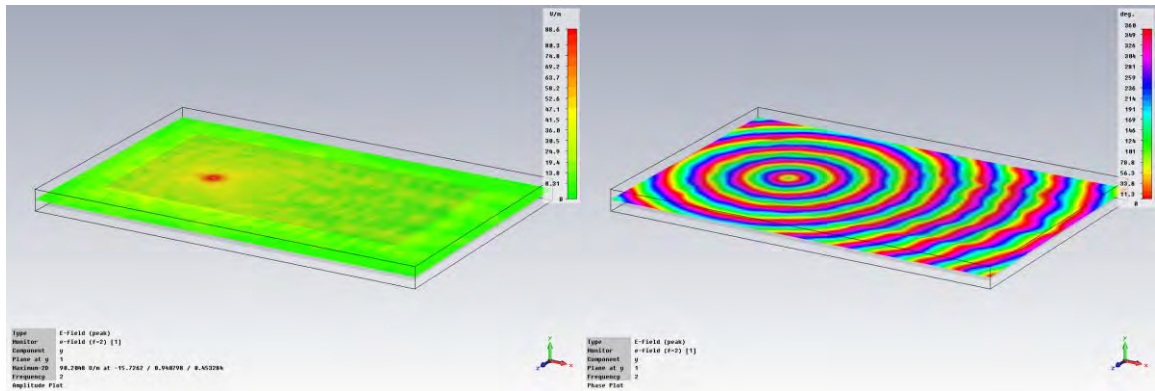


Figure 82: Empty PPWG with Magnitude and Phase Distributions

Near-Field Scans (Test Point 1)

Near-field scans were conducted over the center of the bottom plate in an area of 14.25" x 14.25" with a spatial resolution of 0.25" (3,364 points). The frequency resolution was 20 MHz from 2-18 GHz (801 points).

Figure 83, Figure 84, and Figure 85 show the measured and simulated scans with the left monopole at the short focal length for 2 GHz, 6 GHz and 10 GHz respectively. Figure 86 shows the measured scan for 18 GHz. The nature of the measured patterns are due to the physical integration of the x- y- and z-components of the electric fields over the probe's length. For true comparison, the simulated fields should be integrated over the 2" gap. However, for simplicity, a single planar cut, corresponding to the tip of the probe, using only the y-component of the electric fields, was taken from the simulated data and used for a qualitative comparison.

For the 2 GHz fields, the main difference is in the magnitude plot. The difference is assumed to be due to the lack of integrating all components of the simulated fields. In the phase, the ripple in the simulation is assumed to be due to the lack of rolled edges. Qualitatively, the measured and simulated scans are in agreement. They each show the magnitude plot weakening as waves propagate from the left side and down the long axis. Also, in the phase, they each show a cylindrical wave, with a wavelength approximately 6", propagating from the same phase center to the left of the scan area.

For the 6 GHz fields, the main difference is also in the magnitude plot. The difference is assumed to be due to the lack of integrating all components of the simulated fields, but it is also assumed that the difference highlights the presence of the higher-order modes in this particular planar cut. The higher-order modes are indicated by the

periodic nulls in the simulated scan. Had the integration occurred, it is assumed that the modes would have been considered collectively. In the phase, the ripple of the 2 GHz simulation has been nearly eliminated. Qualitatively, the measured and simulated scans are in agreement. They each show the magnitude plot weakening as waves propagate from the left side and down the long axis. Also, in the phase, they each show a cylindrical wave, with a wavelength approximately 2", propagating from the same phase center to the left of the scan area.

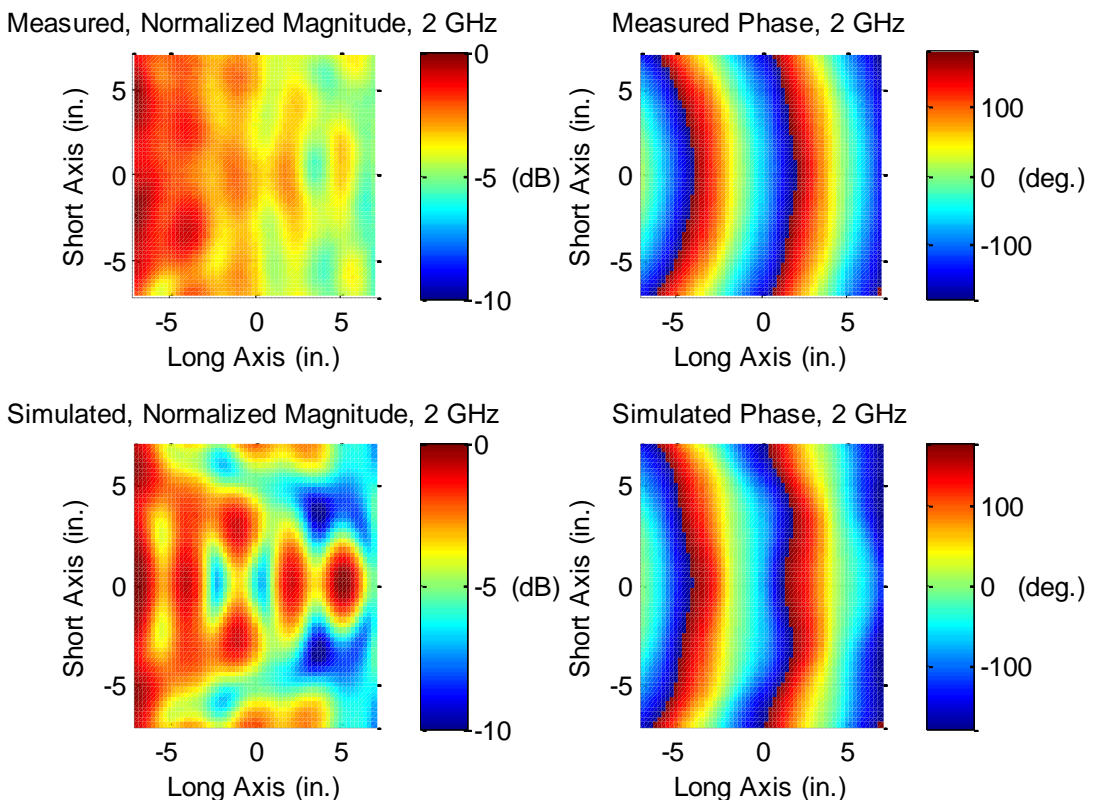


Figure 83: Measured vs. Simulated Near-Field Scans at 2 GHz

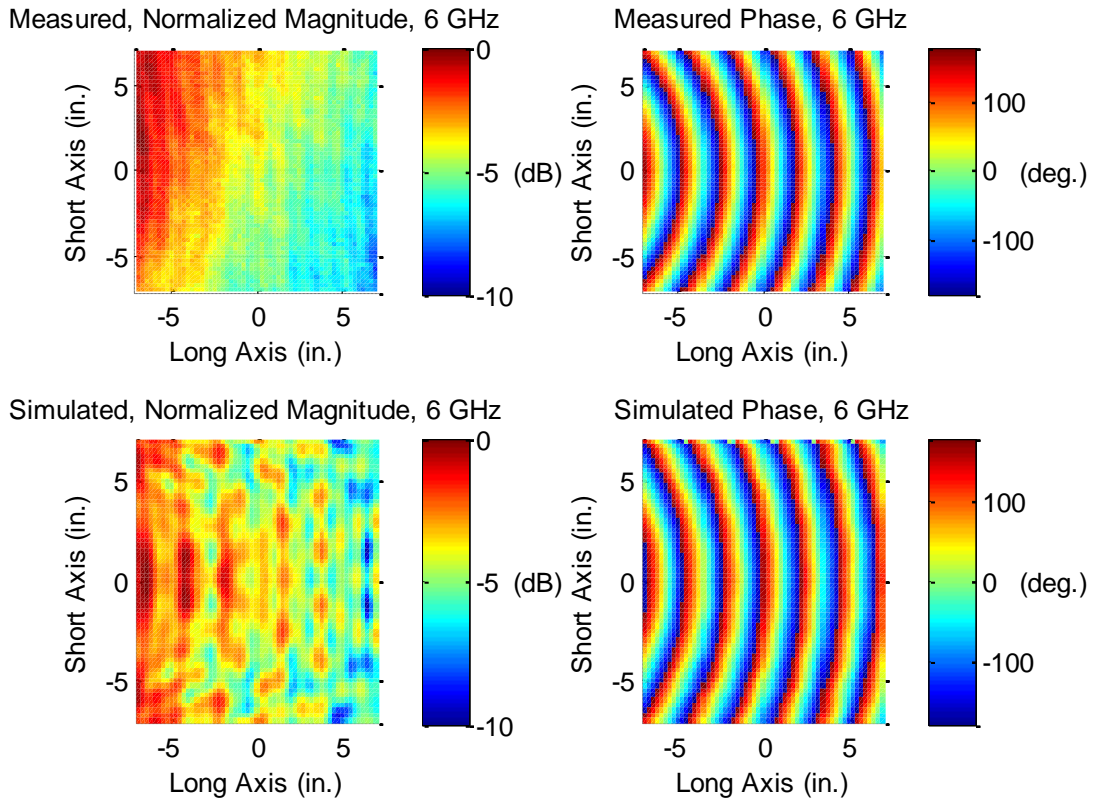


Figure 84: Measured vs. Simulated Near-Field Scans at 6 GHz

For the 10 GHz fields, the main difference is again in the magnitude plot. The difference is again assumed to be due to the lack of integrating all components of the simulated fields and due to the presence of higher-order modes in this particular planar cut. In the phase, the distortion common to both measurement and simulation is assumed to be due to the spatial sampling resolution. The resolution of each plot is 0.25" which is approximately one-quarter wavelength for 10 GHz. Qualitatively, the measured and simulated scans are in agreement. They each show the magnitude plot weakening as waves propagate from the left side and down the long axis. Also, in the phase, they each

show a cylindrical wave, with a wavelength approximately 1", propagating from nearly the same phase center to the left of the scan area.

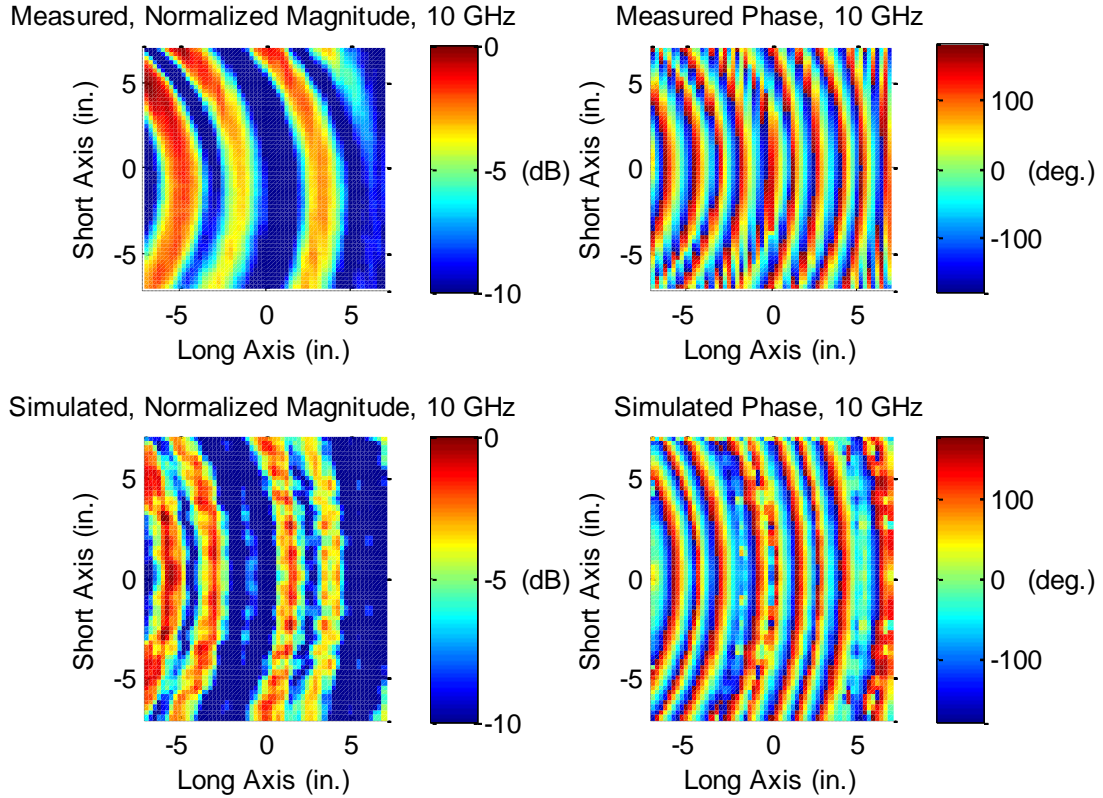


Figure 85: Measured vs. Simulated Near-Field Scans at 10 GHz

For the 18 GHz fields, there was no simulation to make comparisons with. Qualitatively, the behavior shown in the magnitude plot agrees with the previous plots for lower frequencies. The magnitude is weakening along the propagation direction and the nulls are caused by interference of all the modes. In the phase, the distortion is more apparent since the spatial sampling resolution is approaching the Nyquist limit for aliasing. With finer sampling, the phase plot should indicate the presence of cylindrical

wavefronts with a wavelength approximately 0.6", propagating from the phase center to the left of the scan area.

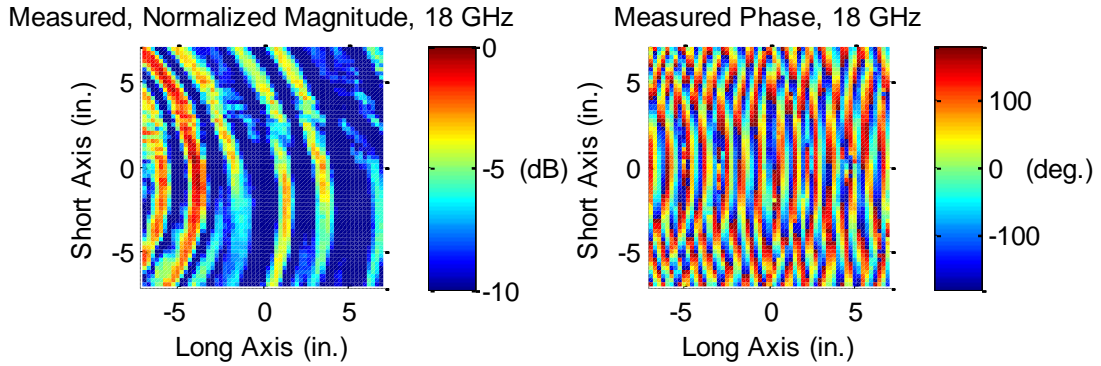


Figure 86: Measured Near-Field Scans at 18 GHz

S-Parameters (Test Points 2-5)

S-parameters were measured from the left monopole to the top probe and from the left monopole to the right monopole. Each set of S-parameters was measured with the monopoles at the short focal lengths and then at the long focal lengths. The frequency resolution was 20 MHz from 2-18 GHz (801 points).

Figure 87 through Figure 94 show these measurements for magnitude and phase. Figure 95 through Figure 98 compares the measurements to simulations. A basic percent-error plot is shown in Figure 99 through Figure 102 for these comparisons. The percent-error plots follow the traditional

$$\%Error = 100 \frac{\text{Theoretical} - \text{Measured}}{\text{Theoretical}} \quad (1.27)$$

where the theoretical solution comes from CST, but this error analysis will be of limited validity since there are no rolled edges in the simulation.

Qualitatively, for these left-to-top magnitude plots, there is general agreement between S11 and S22 for the monopole at both the short and long focal lengths. In each plot, S11 (top probe) reveals a higher-frequency harmonic at frequencies above 10 GHz for the short focal length and above 12 GHz for the long focal length whereas S22 (left monopole) does not. Also, at the nulls, S22 tends to be deeper than S11 and S22 exhibits a shift to lower frequencies beyond 10 GHz, relative to S11. Finally, S11 exhibits a noise pattern around 5 GHz whereas S22 does not.

Generally speaking, each reflection response contains six peaks corresponding to the six cut-off frequencies of the PPWG (approximately every 2.95 GHz) and five nulls corresponding to frequency increments of approximately 3.08 GHz. These null increments are assumed to be due to the height of the monopole (average height was 1.916") which corresponds to a half-wavelength of 3.08 GHz.

The higher-frequency harmonic and the 5 GHz noise pattern in the top probe may be due to poor connections along the cabling. Physically, it was difficult to access the cabling for the top probe, so it is possible that connections were not fully tightened. Tightening, calibration and measurement should be re-accomplished to verify this as a source of error.

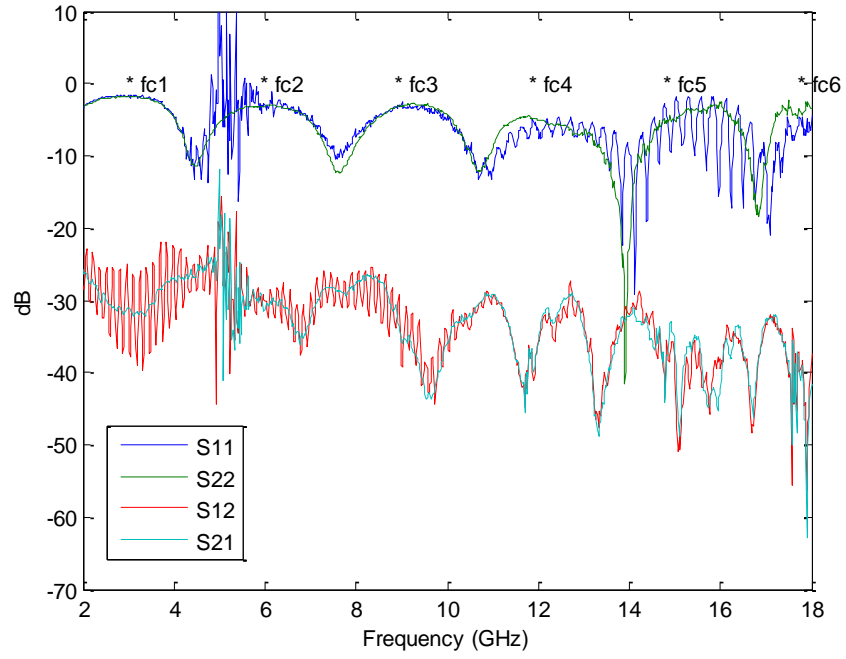


Figure 87: Measured Left-to-Top S-Parameters (Mag.) (short focal)

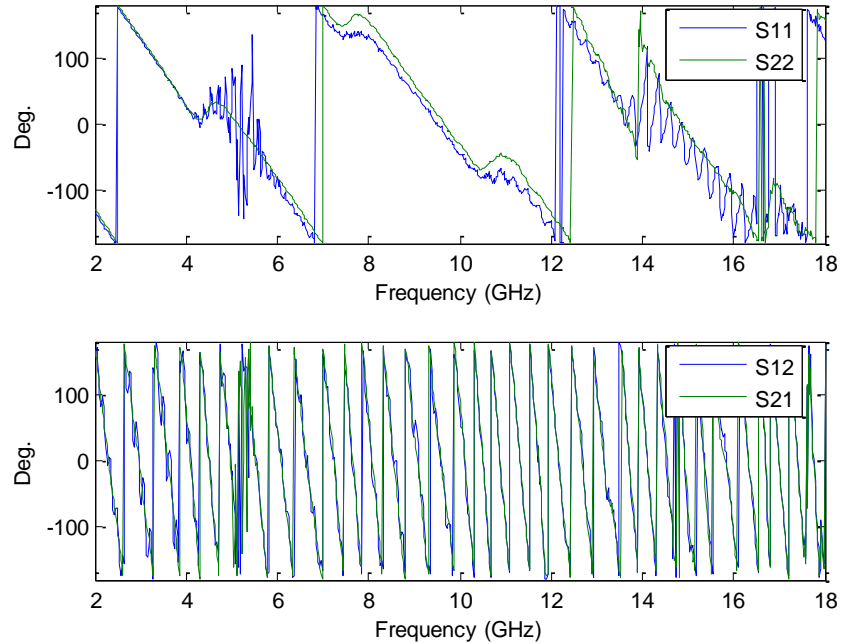


Figure 88: Measured Left-to-Top S-Parameters (Phase) (short focal)

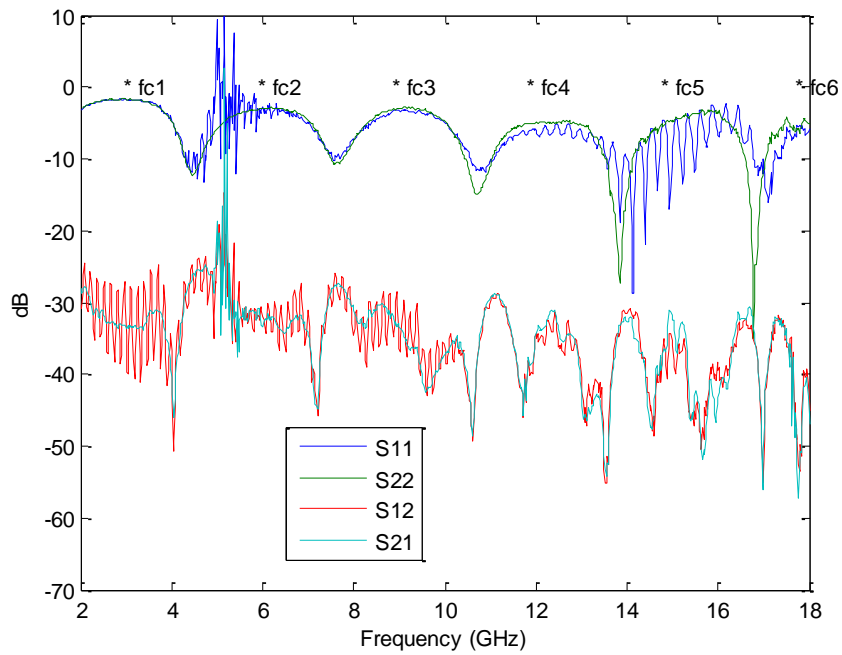


Figure 89: Measured Left-to-Top S-Parameters (Mag.) (long focal)

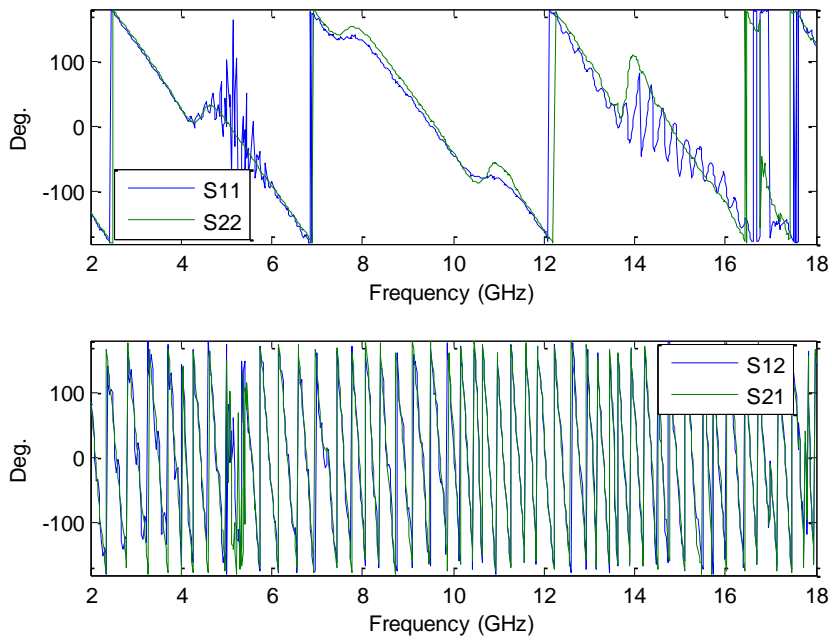


Figure 90: Measured Left-to-Top S-Parameters (Phase) (long focal)

The depth and shift of the S22 nulls relative to the S11 nulls are assumed to be due to the position of the left monopole relative to the position of the top probe. The top probe was centered within the PPWG whereas the monopole was off-center at the short focal length, then at the long focal length. The deeper nulls in S22 are assumed to be due to more destructive interference caused by diffraction at the rolled edges. Based on proximity to the rolled edges alone, S11, buried deeper in the PPWG, would experience less destructive interference. The shift of the S22 nulls (consistently about -0.2 GHz after 10 GHz) can be most likely attributed to the difference in exact length of the left monopole relative to the exact length of the top probe. For example, a height increase of the left monopole of 0.02" would result in a shift of the nulls by -0.16 GHz. However, attributing this shift to antenna height cannot be verified for certain unless the frequency resolution of the measurements is adjusted below 20 MHz. It has not been determined why the shift occurs after 10 GHz.

Qualitatively, for these left-to-top magnitude plots, there is general agreement between S12 and S21 for the monopole at both short and long focal lengths. In each plot, S12 (signal received in top probe from left monopole) reveals a higher-frequency harmonic at all frequencies whereas S21 does not. Both S12 and S21 exhibit a similar noise pattern around 5 GHz. Generally speaking, each transmission response should be in very close agreement due to reciprocity along the transmission path.

All sets of left-to-top phase plots are in general agreement and they each reveal the same issues found in the magnitude plots where the nulls of the magnitude plots correspond to either a swing or a discontinuity in the trend of the phase plots. For both of these test points, S22 (left) tends to occur about 15 degrees later in phase than S11 (top)

after about 6 GHz. Why this delay occurs has not yet been determined, but it can be assumed that the reflection path of the left monopole is slightly longer than the reflection path of the top probe.

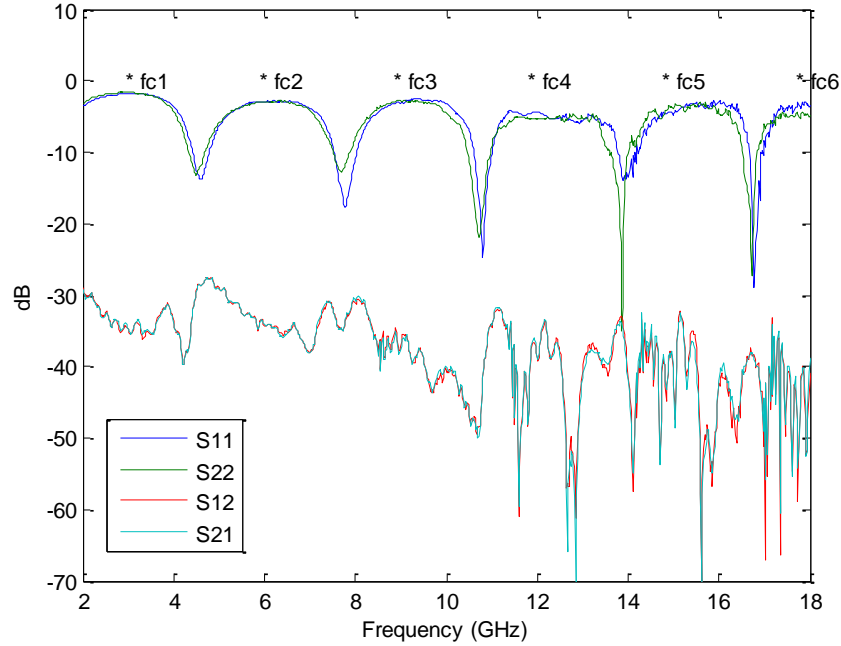


Figure 91: Measured Left-to-Right S-Parameters (Mag.) (short focal)

Qualitatively, for these left-to-right magnitude plots, there is general agreement between S11 (left) and S22 (right) for the monopoles at both short and long focal lengths. At the nulls, S11 tends to be deeper than S22 for the short focal length (except for the null near 14 GHz) and S22 tends to be deeper than S11 for the long focal length. There is no general shifting of these S-parameters relative to each other as previously discussed. Finally, the noise pattern and higher-frequency harmonics exhibited by the left-to-top reflection responses are not present. The noise and harmonics seem to be characteristic of the top probe only.

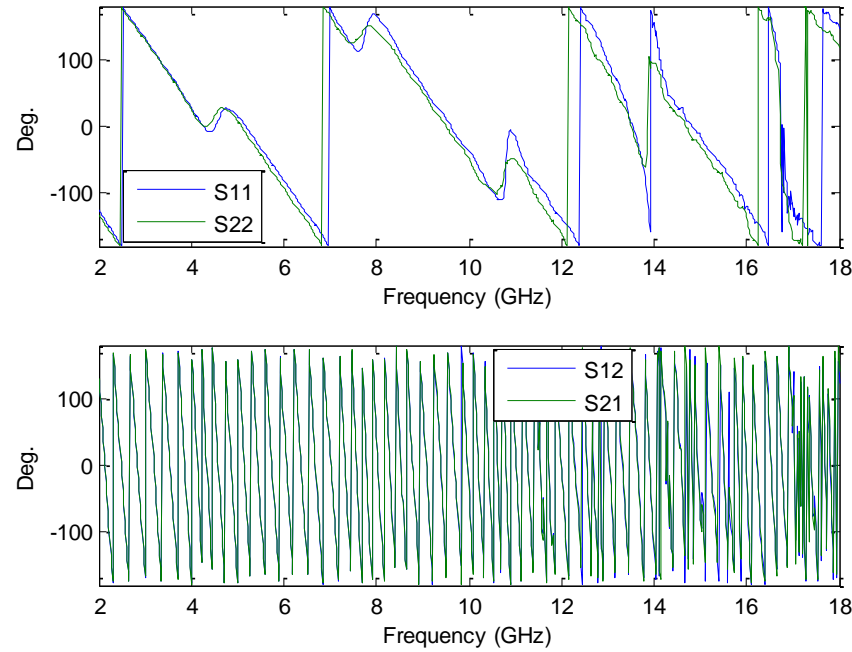


Figure 92: Measured Left-to-Right S-Parameters (Phase) (short focal)

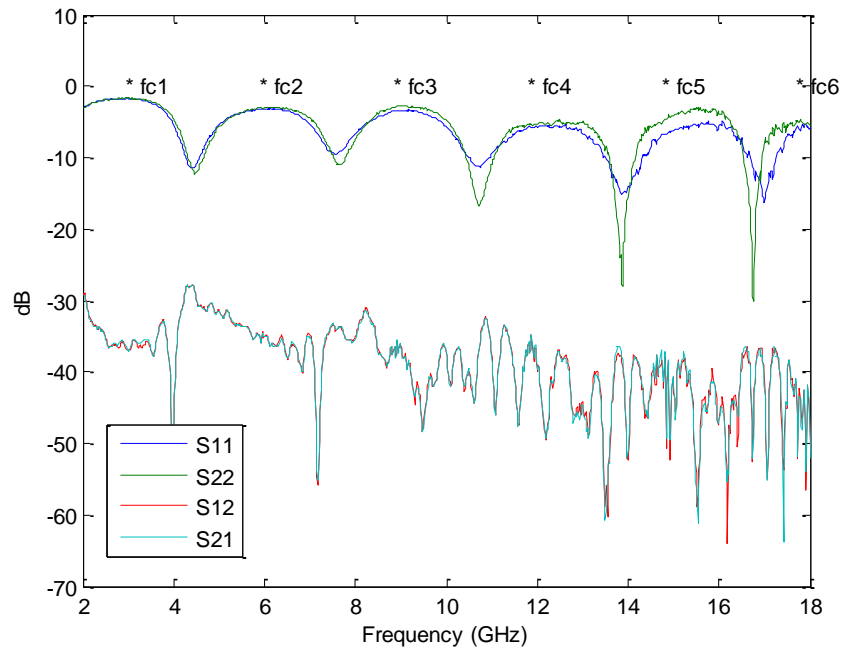


Figure 93: Measured Left-to-Right S-Parameters (Mag.) (long focal)

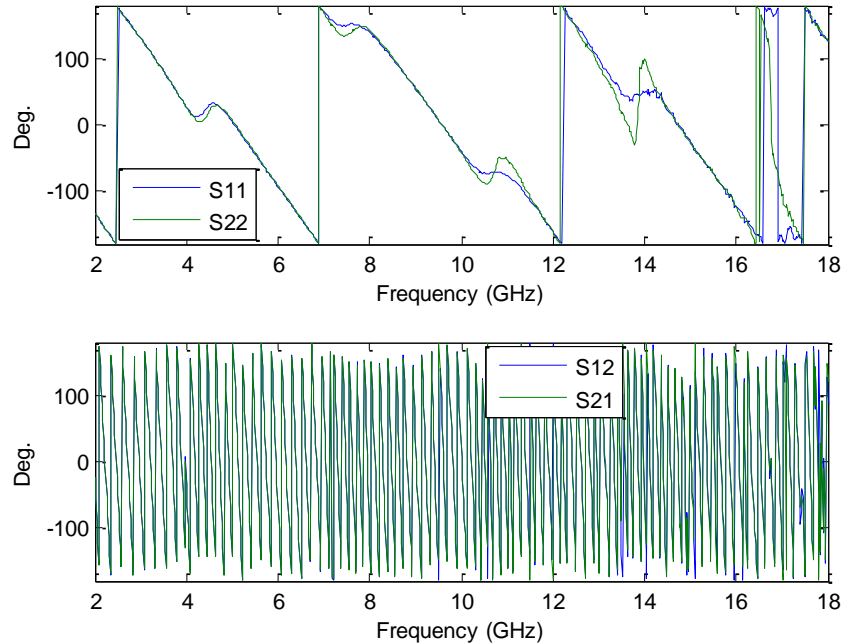


Figure 94: Measured Left-to-Right S-Parameters (Phase) (long focal)

The depth of the S11 nulls relative to the depth of the S22 nulls are again assumed to be due to the position of the left monopole relative to the position of the right monopole. Each monopole was in the mirror-image position of the other, so ideally, S11 and S22 should be identical. The exact depth and position of the nulls in each are assumed to be due to the combined effects of the exact features of the monopole, the aluminum surface, the painted surface, the rolled surface, the surrounding chamber, etc. as seen by the left or right monopole at the short or long focal position.

Qualitatively, for these left-to-right magnitude plots, there is general agreement between S12 and S21 for the monopoles at both short and long focal lengths. Again, generally speaking, each transmission response should be in very close agreement due to reciprocity along the transmission path.

All sets of left-to-right phase plots are in general agreement and they each reveal the same issues found in the magnitude plots. Again, the nulls of the magnitude plots correspond to either a swing or a discontinuity in the trend of the phase plots. For the short focal length, S11 (left) tends to occur about 15 degrees later in phase than S22 (right), just as S22 (left) was delayed relative to S11 (top) in the left-to-top measurement. However, in this case, the delay is apparent as low as 4 GHz rather than 6 GHz. For the long focal length, the only relative phase delays are near the swings, whereas in the left-to-top measurement, S22 (left) was delayed relative to S11 (top) throughout the plot after 6 GHz. Why these delays occur has not yet been determined, but it can be assumed that the reflection path of the left monopole is slightly longer than the reflection path of the right monopole when they are both at the short focal length. When they are both at the long focal length, it can be assumed that the two reflection paths are closer to the same length.

In comparing measured S-parameters to simulated S-parameters, only 0-10 GHz can be reviewed. Qualitatively, there is general agreement between each measured and simulated S11 and each measured and simulated S22. The main difference is that in the peaks of the reflection responses, the measurements seem to shift to higher frequencies relative to the simulations. The same shift is apparent in the nulls as well. Also, the magnitudes of the peaks of the simulation are noticeably decreasing whereas those in the measurements are decreasing much more gradually.

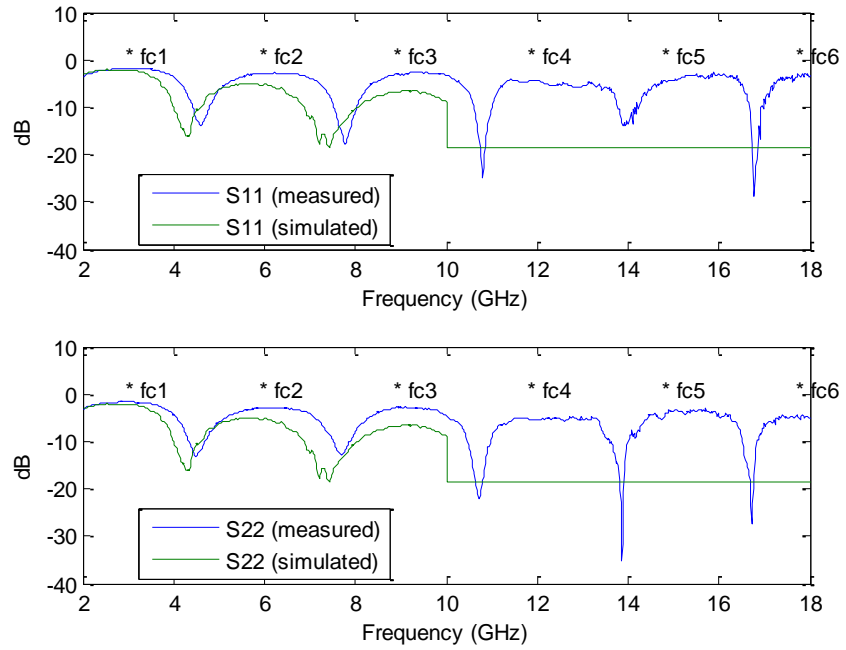


Figure 95: Measured vs. Simulated Left-to-Right Reflection (short focal)

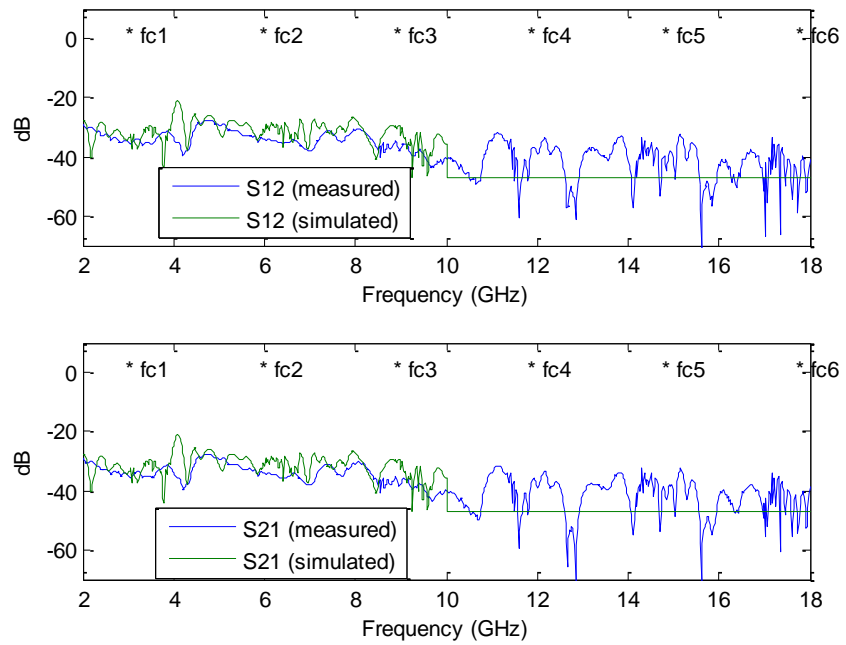


Figure 96: Measured vs. Simulated Left-to-Right Transmission (short focal)

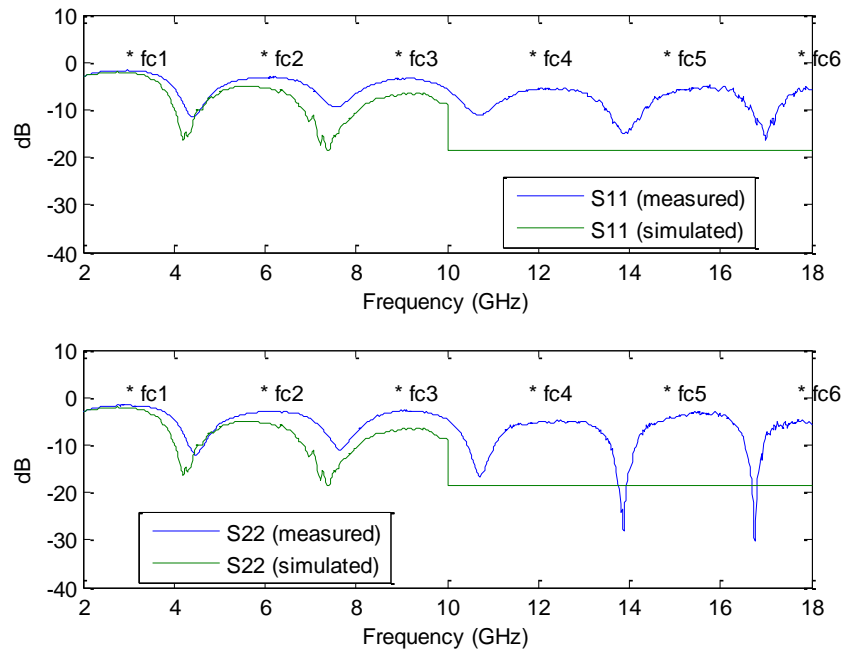


Figure 97: Measured vs. Simulated Left-to-Right Reflection (long focal)

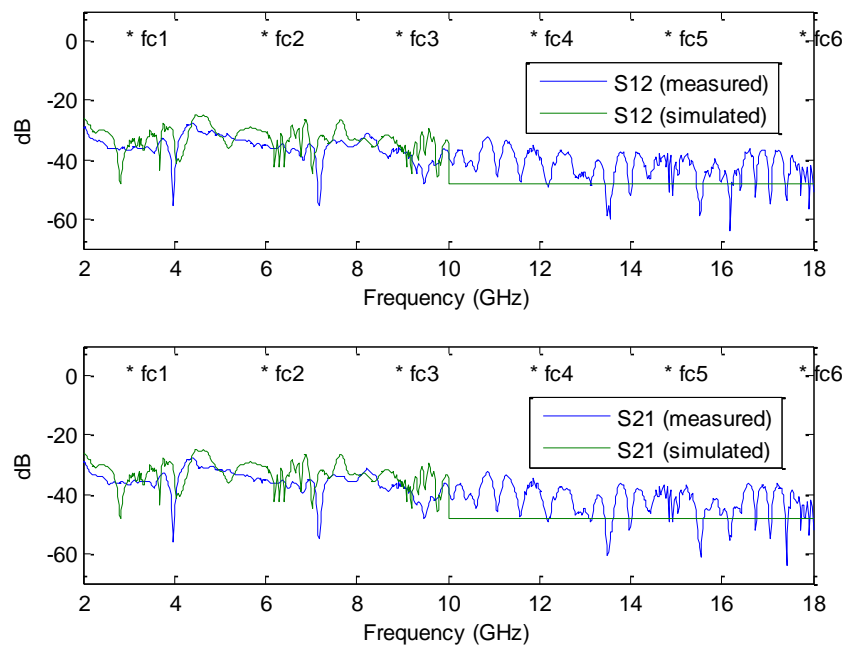


Figure 98: Measured vs. Simulated Left-to-Right Transmission (long focal)

For each cut-off frequency of the PPWG, a tag was placed in each plot to measure the position of the peaks relative to the cut-off frequency. Generally speaking, the peaks of the simulations are always fixed relative to the cut-off frequencies, so it is apparent that the peaks of the measurements are shifting away from the theoretical cut-off frequencies. The degree of each shift can be used to make assumptions about the spacing between the PPWG plates. For example, for a 2" PPWG, the third cutoff frequency is 8.852 GHz, but if the corresponding peak of the measured S11 has shifted by approximately 0.2 GHz, it can be said that the spacing between the plates at some point(s) is not exactly 2" but 1.956". The same procedure can be followed for all cut-off frequencies to determine the variation in the plate spacing as seen by the monopole at the left or right side and at the short or long focal point.

The shifting in the nulls can be assumed to be caused by the varying heights of the monopoles as previously discussed. However, in these measurements, both the shifting peaks and shifting nulls should be re-evaluated with a frequency sampling that is finer than 20 MHz. It is unknown whether frequency shifting is a general combination of monopole heights and PPWG spacing or if it is due to strictly one parameter or the other.

The degree of decreasing magnitudes in the simulations relative to the measurements is assumed to be due to the lack of rolled edges in the simulation. With more interference due to stronger diffraction effects, it can be assumed that magnitudes in the simulation will decrease more quickly than magnitudes in the measurement. It has not been determined why the fourth, fifth and sixth peak of the measurements are flattened.

Qualitatively, there is less general agreement between each measured and simulated S12 and S21 than there was for the reflection responses. The main difference for each focal length is that the simulated transmission response has more peaks and nulls than the measured, but each follows the same trend. It is assumed that the lack of rolled edges in the simulation caused this effect.

In these basic percent-error plots, each measurement was evaluated with respect to each simulation up to 10 GHz. The percent-error for the reflection responses follow the same near-linear trend with error increasing from around 2 GHz (about 5%) to repeated maximums (about 50%-60%) at the positions of the magnitude nulls. The percent-error plots for the transmission responses follow the same general trend with the highest error at the positions of the nulls. As stated previously, these percent-error plots are of limited validity since the simulation did not have rolled edges.

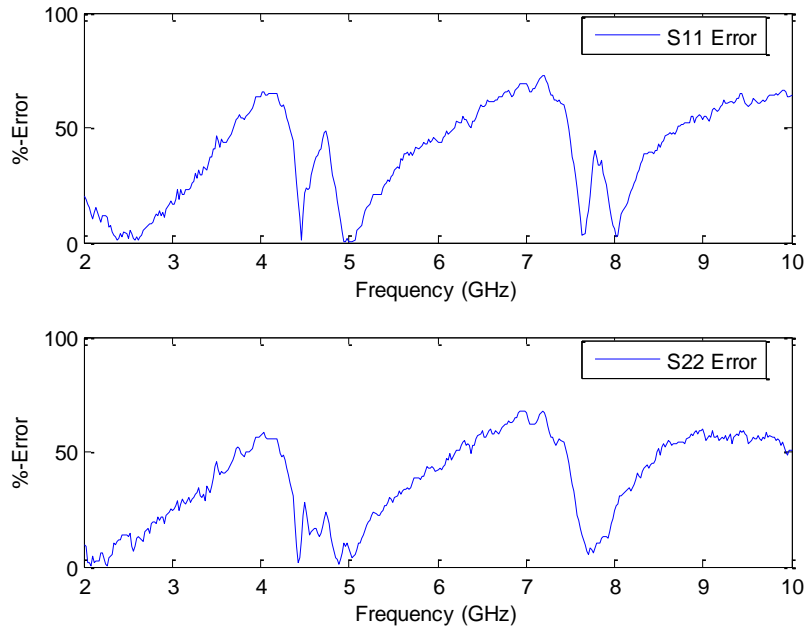


Figure 99: Left-to-Right Reflection Error (short focal)

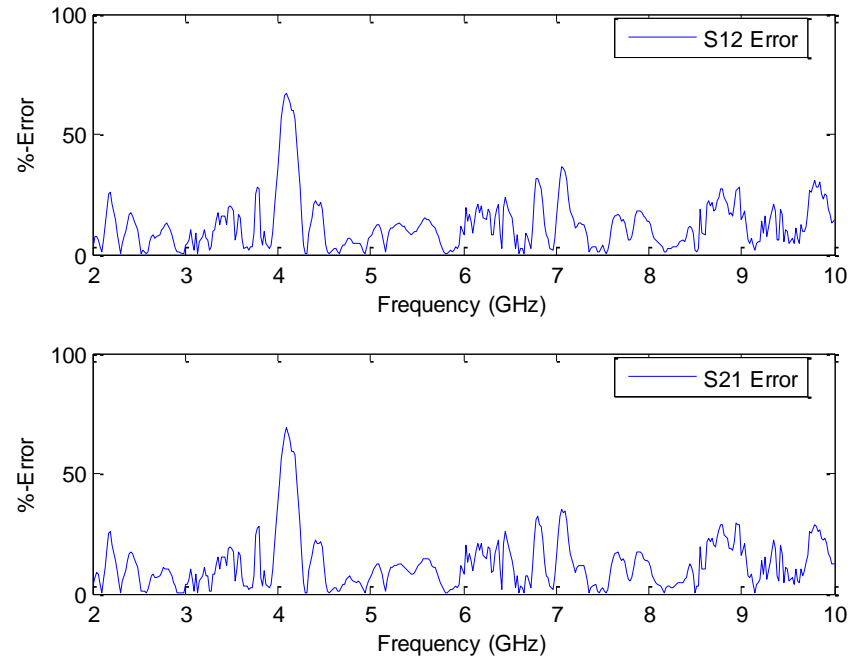


Figure 100: Left-to-Right Transmission Error (short focal)

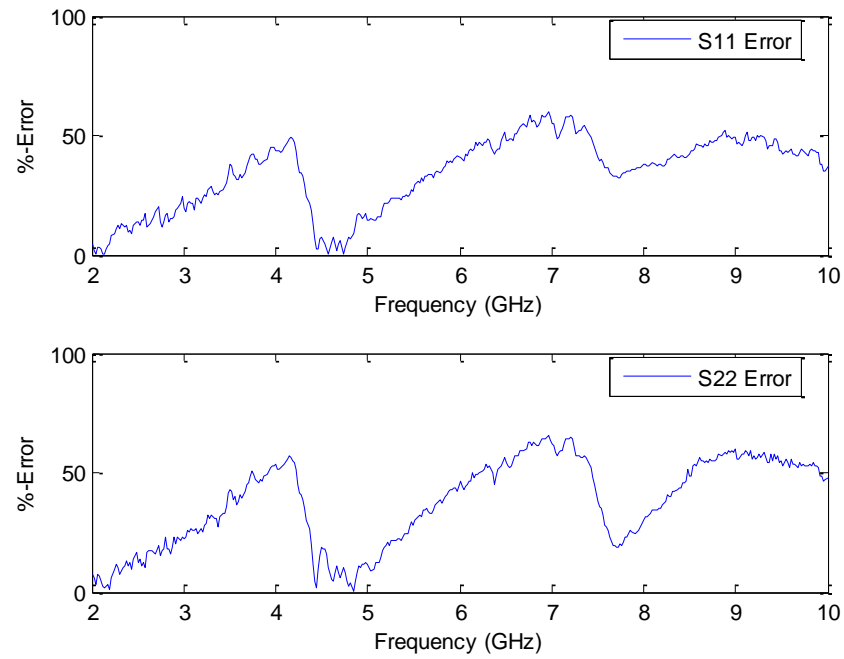


Figure 101: Left-to-Right Reflection Error (long focal)

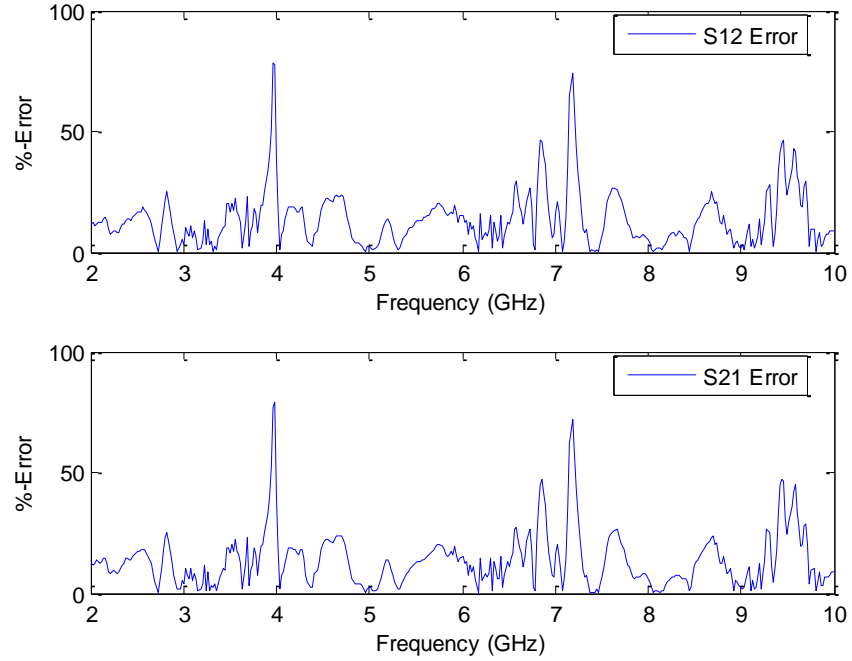


Figure 102: Left-to-Right Transmission Error (long focal)

To conclude the basic analysis for the empty PPWG, the highlighted measurement phenomena were 1) attenuated cylindrical wavefronts of the appropriate wavelength crossing over the scan area from a common phase center; 2) visibility of higher-order mode effects (nulls) throughout the scan area; 3) effects of spatial under-sampling; 4) general agreement between S11 and S22 measurements; 5) general agreement between S12 and S21 measurements; 6) general agreement between measurements and simulations despite an incomplete simulation model; 7) higher-frequency harmonics and noise presumably due to the top probe; 8) relative depth of nulls in each reflection response; 9) consistency in position or relative shift of nulls in each reflection response; 10) peaks of each reflection response shifted from the cut-off frequencies; 11) nulls of each reflection response at frequency increments related to the monopole height; 12)

effects of frequency under-sampling; 13) phase delays between ports in reflection responses.

It was assumed throughout the analysis that some physical component or some combination of components in the empty PPWG was accountable for each phenomenon. However, this assumed accountability is not a thorough enough accounting to be conclusive about the performance of the system altogether. The assumptions carry only so far as to create a baseline of phenomena that can be expected when performing measurements with the lenses and targets. That stated, the aforementioned phenomena will be excluded from the observations and analyses of the remaining tests and new phenomena specific to the lenses and targets will be highlighted.

Small Lenses in PPWG

The simulation model for the PPWG with small lenses is shown in Figure 103. The magnitude and phase distributions throughout the waveguide, as excited by the left monopole, can be arbitrarily visualized in Figure 104.

Near-Field Scans (Test Points 6-8)

The near-field scans were conducted over the center of the bottom plate, between the lenses, in an area of 14.25" x 14.25" with a spatial resolution of 0.25" (3,364 points). The frequency resolution was 20 MHz from 2-18 GHz (801 points).

Figure 105, Figure 106, and Figure 107 shows the measured and simulated scans for 2 GHz, 6 GHz and 10 GHz respectively. Figure 108 shows the measured scan for 18 GHz. Again, the nature of these measured patterns is due to the integration of the x- y-

and z-components of the electric fields over the probe's length. For true comparison, the simulated fields should be integrated over the 2" gap. However, for simplicity, a single planar cut, corresponding to the tip of the probe, using only the y-component of the electric fields, was taken from the simulated data and used for a qualitative comparison.

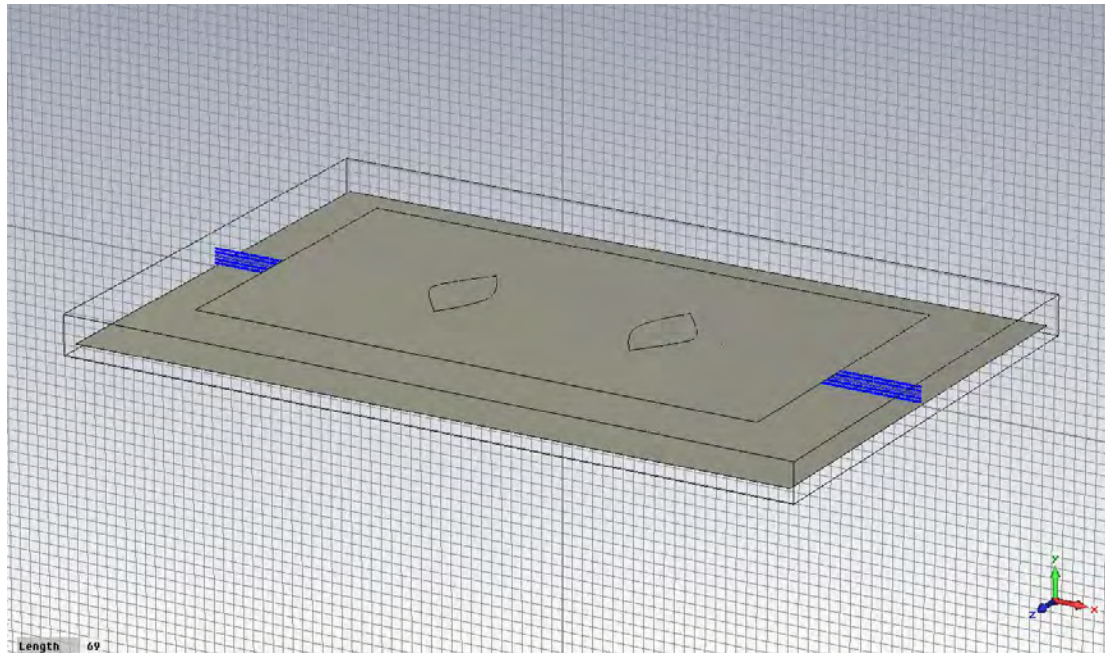


Figure 103: PPWG Model with Small Lenses

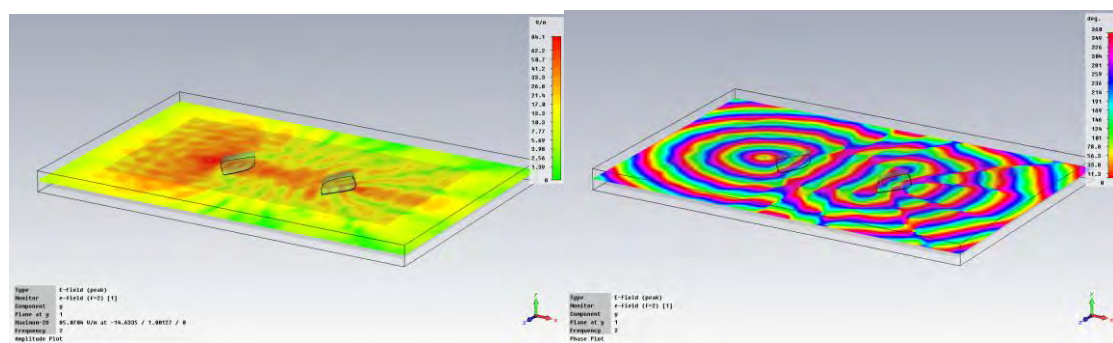


Figure 104: PPWG with Small Lenses with Magnitude and Phase Distributions

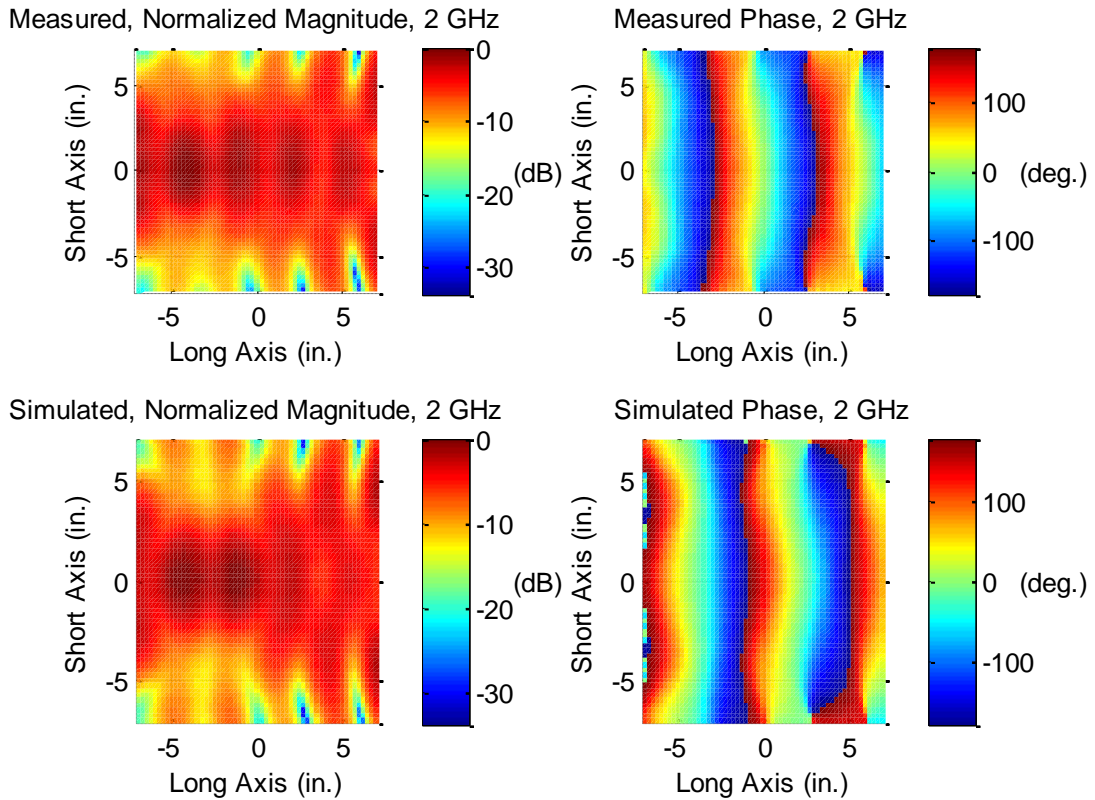


Figure 105: Measured vs. Simulated Near-Field Scans at 2 GHz

For the 2 GHz fields, there is not much difference between either the measured or simulated magnitude and phase plots. Qualitatively, the measured and simulated scans are in agreement except for an apparent 90 degree shift in phase. The reason for this shift went undetermined. The differences in magnitude are assumed to be due to the lack of integrating all components of the simulated fields. In the magnitude plots, the general shape of the beam is consistent having a beam radius of approximately 2.6" at an offset of approximately 4" from the geometric focus. The normalized taper over the minimum target radius of 3.5" at this position in the beam is approximately -15 dB. The dark lobes in the beam are assumed to be caused by a standing wave between the lenses. In the

phase plots, the general shape of the wavefronts are consistent with inverted cylindrical wavefronts converging to, then diverging from planar wavefronts at the beamwaist. The excess ripple in the simulated phase plot is still assumed to be due to the lack of rolled edges in the simulation.

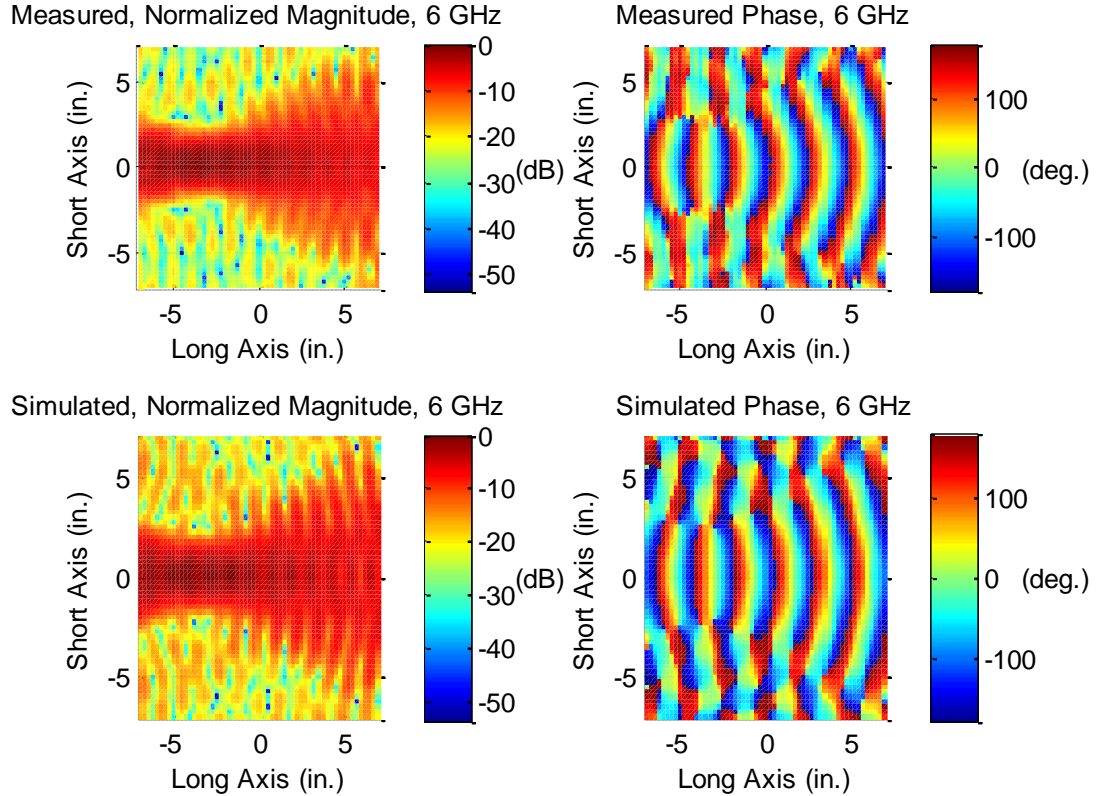


Figure 106: Measured vs. Simulated Near-Field Scans at 6 GHz

For the 6 GHz fields, there is not much difference between either the measured or simulated magnitude and phase plots. Qualitatively, the measured and simulated scans are in excellent agreement except for an apparent 90 degree shift in phase. The differences are assumed to be due to the lack of integrating all components of the simulated fields, but it is also assumed that the difference is in part due to the presence of

higher-order modes however unapparent. In the magnitude plots, the general shape of the beam is consistent having a beam radius of approximately 1" - 1.5" at an offset of approximately 4" from the geometric focus. The normalized taper over the minimum target radius of 3.5" at this position in the beam is approximately -30 dB. The dark lobes in the beam are assumed to be caused by a standing wave between the lenses. In the phase plots, the general shape of the wavefronts are consistent with inverted cylindrical wavefronts converging to, then diverging from planar wavefronts at the beamwaist.

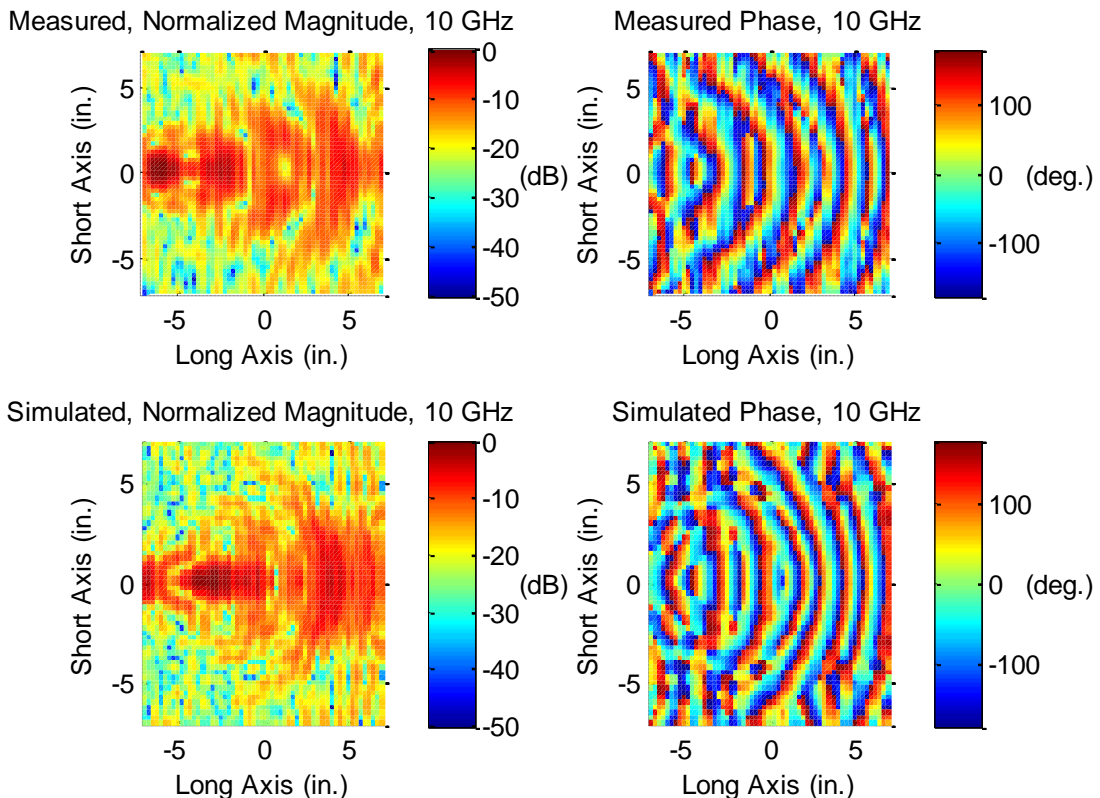


Figure 107: Measured vs. Simulated Near-Field Scans at 10 GHz

For the 10 GHz fields, there is not much difference between either the measured or simulated magnitude and phase plots. Qualitatively, the measured and simulated scans

are in agreement. Due to spatial sampling distortion, it is not apparent if there is a 90 degree phase shift in these plots as there was previously. Overall, the differences are assumed to be due to the lack of integrating all components of the simulated fields and due to the presence of higher-order modes. In the magnitude plots, the general shape of the beam is consistent having a beam radius of approximately 1" at an offset of approximately 6" from the geometric focus. The normalized taper over the minimum target radius of 3.5" at this position in the beam is approximately -40 dB. In the phase plots, the general shape of the wavefronts are consistent, but distortion makes it difficult to visualize.

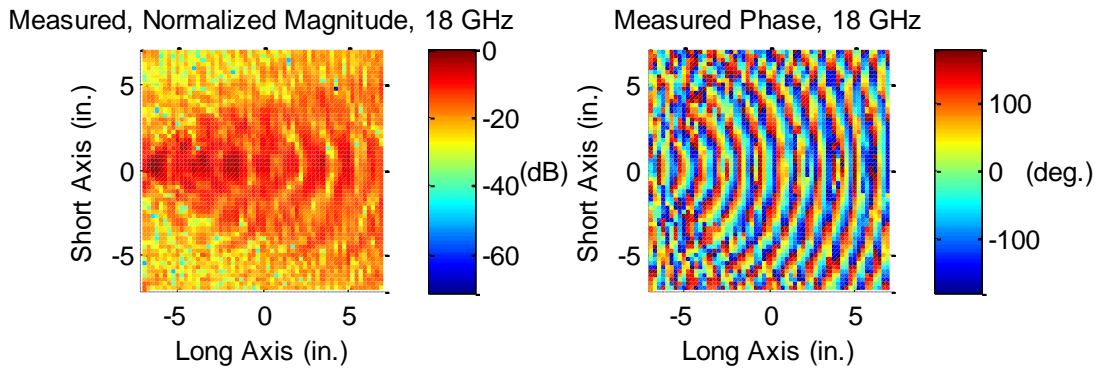


Figure 108: Measured Near-Field Scans at 18 GHz

For the 18 GHz fields, there was no simulation to make comparisons with. Qualitatively, the behavior shown in the magnitude plot agrees with the previous plots for lower frequencies. The general shape of the beam is consistent having a beam radius of approximately 0.5" - 1" at an offset of approximately 6.5" from the geometric focus. The normalized taper over the minimum target radius of 3.5" at this position in the beam is

approximately -40 dB. In the phase plots, the distortion is more apparent than in previous plots since the spatial sampling resolution is approaching the Nyquist limit for aliasing. With finer sampling, the phase plot should indicate the appropriate phase patterns for 18 GHz.

Figure 109 shows the measured difference between performing a scan with an air gap between the lenses and the top plate (approximately 0.0625") and performing a scan without an air gap. This is shown for 2 GHz, 6 GHz, 10 GHz and 18 GHz respectively. This air-gap scan was performed to determine if there were any electrical vs. mechanical trade-offs in the scanning function. At its worst, the mechanical aspects of the scanning function involved the top plate heavily dragging itself over the lenses. If a trade-off were necessary, it would be the mechanical preservation of the lenses at the expense of overall electrical performance.

In each of these plots, the color axis ranges from the minimum difference to the maximum difference created by the air gap. It is apparent that operating the scanning function with an 0.0625" air gap above the lenses produces greater variation in both magnitude and phase as the frequency rises. The magnitude profile for 2 GHz is hardly altered except in the areas near the face of the receiving lens and the phase profile contains few, sharp unexplainable spikes. The magnitude and phase profiles for 6 GHz is more apparently changed with variations throughout as high as +/- 20 dB and +/- 200deg. The changes in the magnitude and phase profiles for 10 GHz and 18 GHz are more apparent still with variations throughout as high as +/- 40 dB and +/- 200deg.

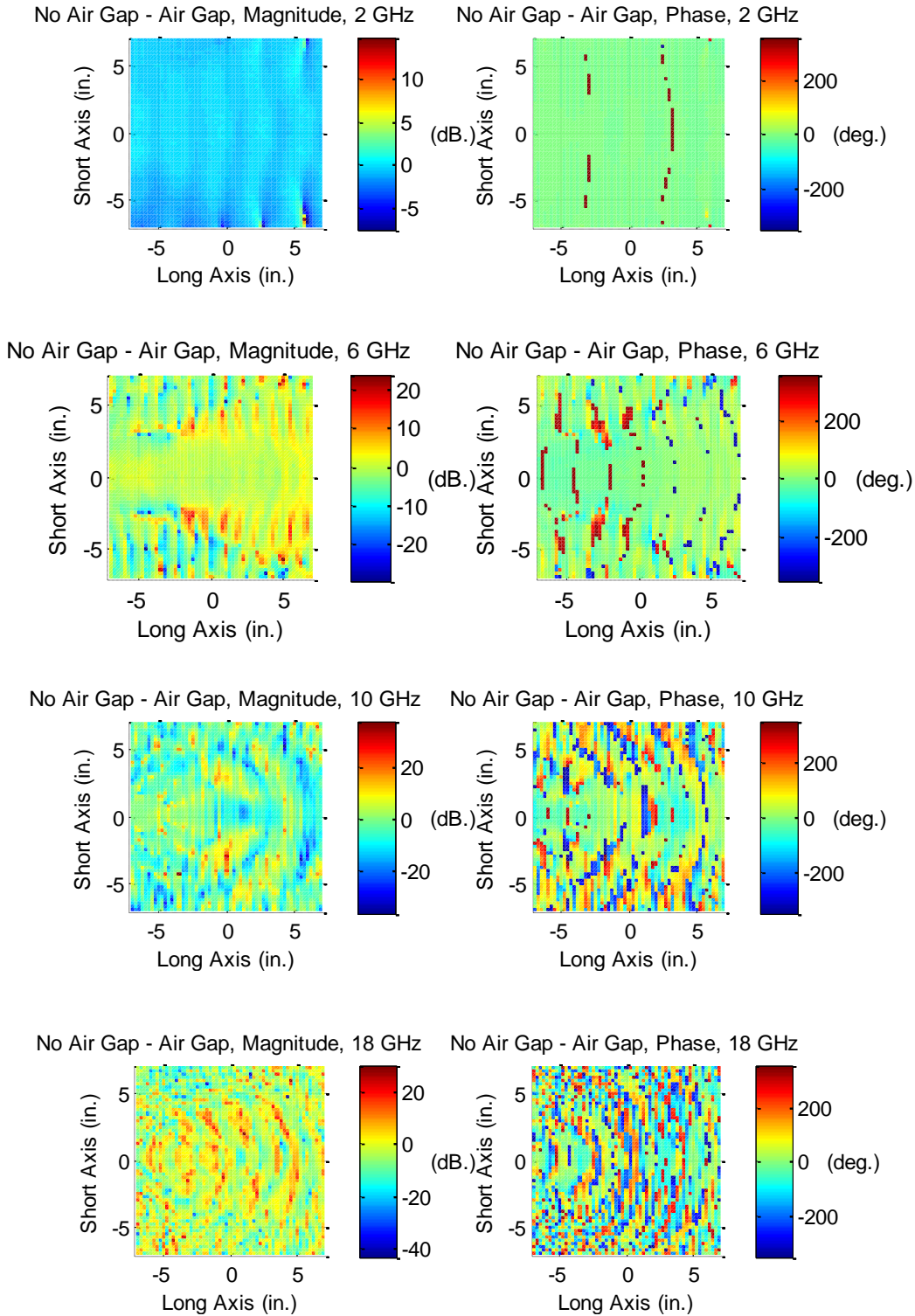


Figure 109: Difference Plot of Scan with Air Gap vs. No Air Gap at 2, 6, 10, 18 GHz

All of these variations are assumed to be caused by higher-frequency diffraction from off the upper edges of the lenses and by the new mode structure caused by introducing the air gap. Due to the extent of these variations and due to the degree of lens wear exhibited thus far, it does not seem necessary that the scan should be performed with an air gap.

The final scanning test point is a measurement-only first-look at the BANTAM 2-D FBS's near-field scanning capabilities for a metamaterial. The measurement was simulated in CST, but due to an untimely CST license expiration, the simulated results were not available for comparison.

As described early on in this document, true near-field scanning of a metamaterial will explore regions of the metamaterial at distances up to one wavelength away from its surface. For 2-18 GHz, this means scanning up to 0.656" - 5.9" from the surface. For the metamaterial D-rings, the scan was limited to 0.2" from the incident surface (the side with copper traces) in an area of 6" x 0.2" with a 0.02" spatial resolution (3,311 points). Favorably, this scan was performed deep into the near-field region, but it should be noted that the scan was limited in both dimensions due to the time required to collect a meaningful number of data points. The spatial resolution was chosen to be half the minimum D-ring dimension, or half the trace width of 0.04". Equivalent measurements were not taken for the opposite D-ring surface, i.e. the transmission side.

The D-ring sample was measured at the position of the geometric focus of the left lens, or, with the front face halfway between the lenses. As will be reviewed in S-parameter measurements, the D-rings exhibit a sharp resonance at 2 GHz, so this was the frequency chosen for the scan. As shown in Figure 110, in response to the beam, the D-

rings seem to re-radiate energy back into the beam with the given pattern. In the magnitude plot, each three-lobed structure represents the spatial presence of a 2" wide D-ring. In the phase plot, the D-rings have created sharply contrasting phase regions distributed orthogonally to the phase regions of the beam.

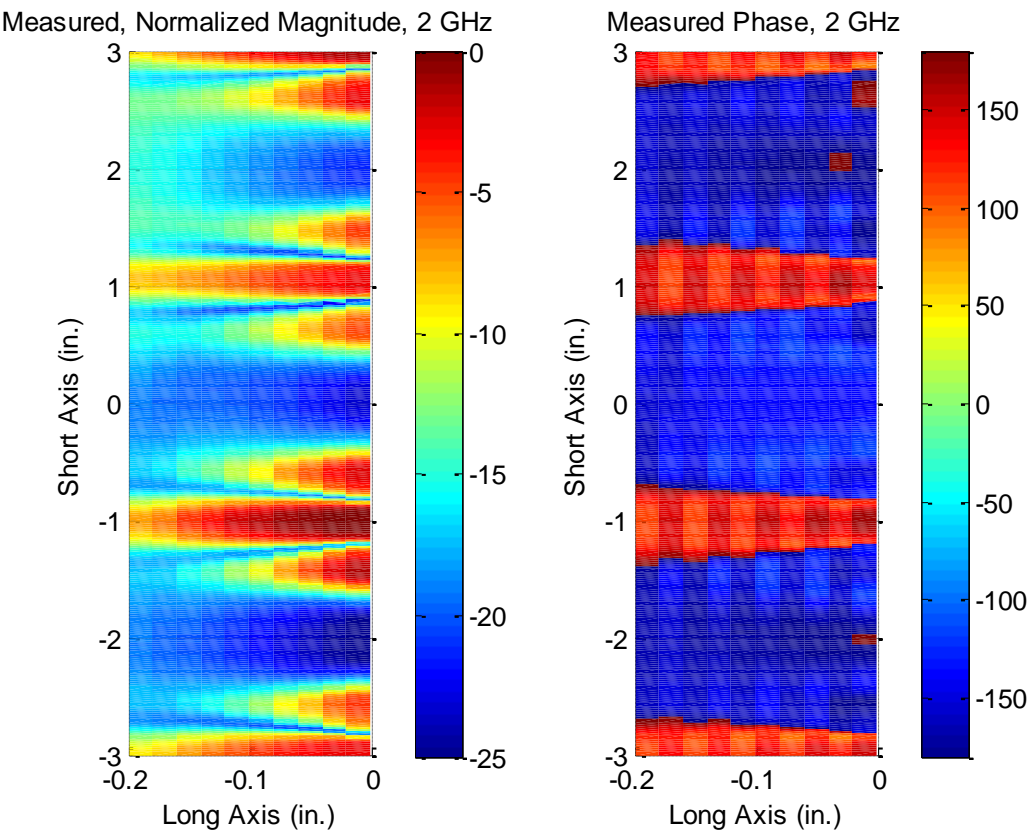


Figure 110: D-Ring Metamaterial Model and First-Look Scan

S-Parameters (Test Points 9-13)

S-parameters were measured from the left monopole to the top probe (a single measurement) and from the left monopole to the right monopole for each target. Each set

of S-parameters was measured with the monopole at the short focal length. The frequency resolution was 20 MHz from 2-18 GHz (801 points).

Figure 111 and Figure 112 shows these measurements for the left-to-top magnitude and phase. Figure 113 and Figure 114 shows these measurements for the left-to-right THRU magnitude and phase. Figure 115 and Figure 116 compares the THRU measurements to simulations. A basic percent-error plot for THRU is shown in Figure 117 and Figure 118 for these comparisons.

Qualitatively, for these left-to-top magnitude plots, there is general agreement between S11 and S22. Compared to the baseline of the empty PPWG, the only difference made by the presence of the lenses is that the deep null at 14 GHz has been reduced. There are no indicators as to why the 14 GHz null was affected.

There is also general agreement between S12 and S21. When compared to the empty PPWG, the transmission responses with the lenses are not only unique but 5 dB higher in magnitude. The magnitude increase is assumed to be due to the focusing action of the lenses.

The left-to-top phase plots are in general agreement and as compared to those of the empty PPWG, there is no discernable change aside from the softened null at 14 GHz.

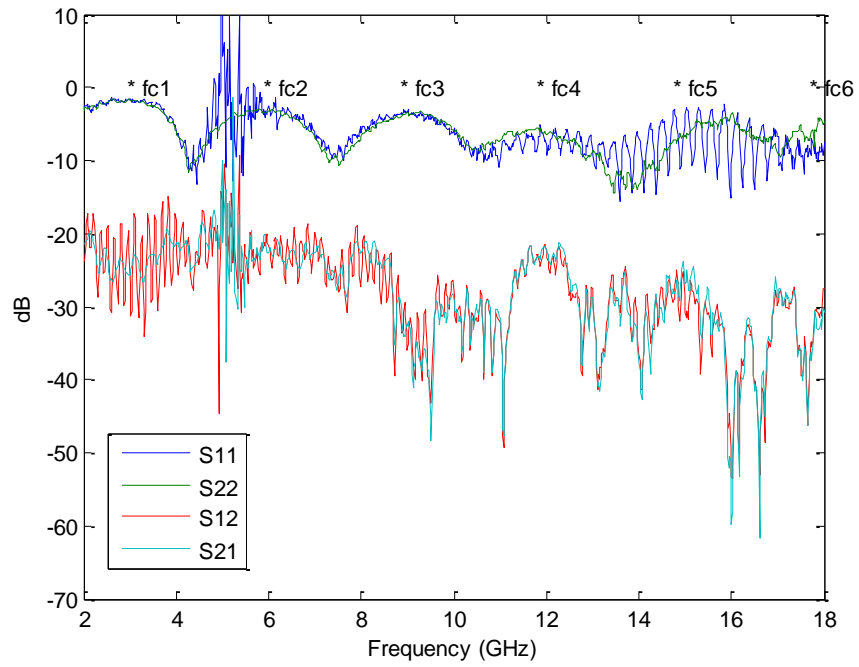


Figure 111: Measured Left-to-Top S-Parameters (Mag.)

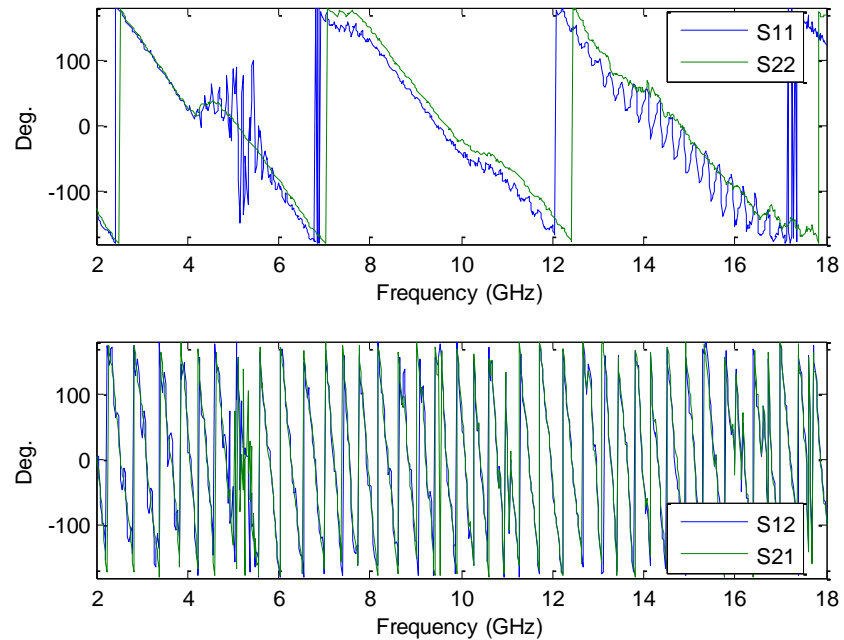


Figure 112: Measured Left-to-Top S-Parameters (Phase)

Qualitatively, for the left-to-right magnitude plots, there is general agreement between S11 and S22. Compared to the baseline of the empty PPWG, the main difference is in the depth of the nulls. The presence of the small lenses seems to have softened the effects of prior interference, but it is unknown how this has occurred.

There is also general agreement between S12 and S21. When compared to the empty PPWG, the transmission responses with the lenses are not only unique but 10 dB higher in magnitude. The magnitude increase is assumed to be due to the focusing action of the lenses.

The left-to-right phase plots are in general agreement and as compared to those of the empty PPWG, there is no discernable change aside from the softened nulls throughout, but especially at 14 GHz.

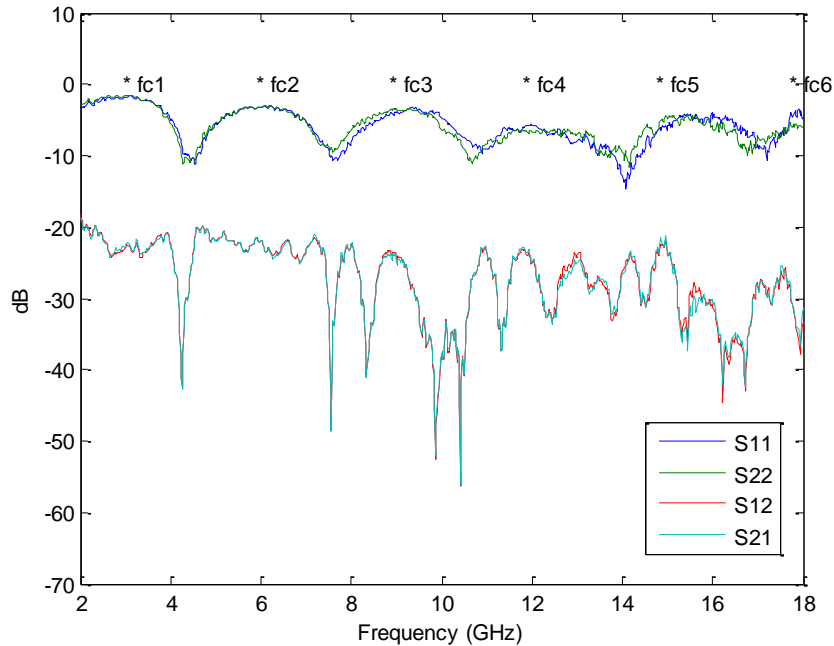


Figure 113: Measured Left-to-Right S-Parameters (THRU) (Mag.)

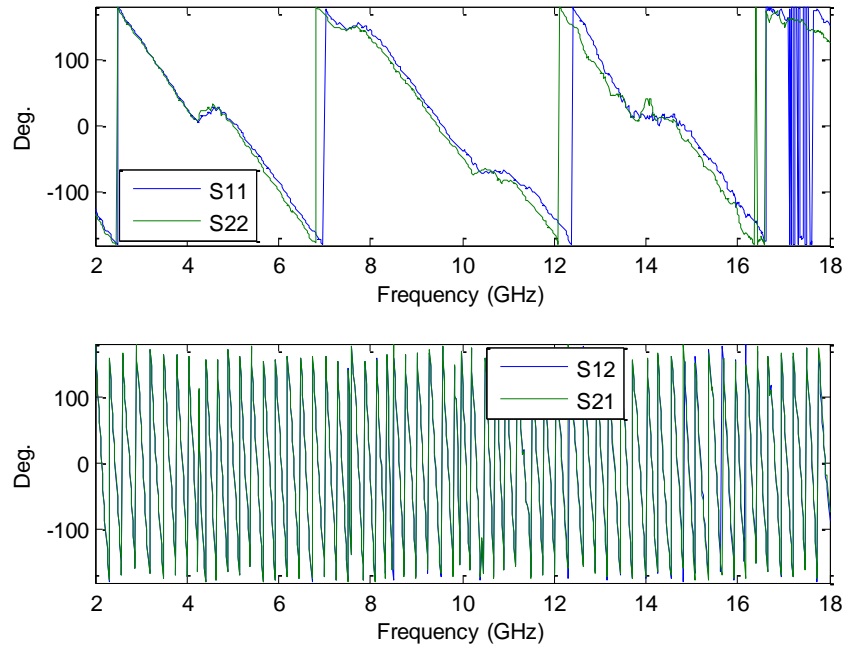


Figure 114: Measured Left-to-Right S-Parameters (THRU) (Phase)

In comparing measured S-parameters to simulated S-parameters, only 0-10 GHz can be reviewed. Qualitatively, there is general agreement between the measured and simulated S11 and S22. As was the case for the empty PPWG, the main difference with the lenses is still that the peaks and nulls of the reflection responses are shifted to higher frequencies relative to the simulations. It is not immediately discernable if there is a difference in the simulated reflection responses with or without the lenses.

There is very close agreement between the measured and simulated S12 and S21 with the small lenses. The only real difference is that the measured and simulated responses diverge from 9-10 GHz. The reason for this is unknown. The very close agreement between the measured and simulated transmission responses with the lenses is in sharp contrast to the less general agreement between the measured and simulated

transmission responses of the empty PPWG. It was assumed previously that the lack of rolled edges in the empty PPWG simulation led to less agreement in those transmission responses. Based on the very close agreement just observed with the lenses, it is assumed that the focusing action of the lenses has made the diffraction effects of the empty PPWG simulation negligible.

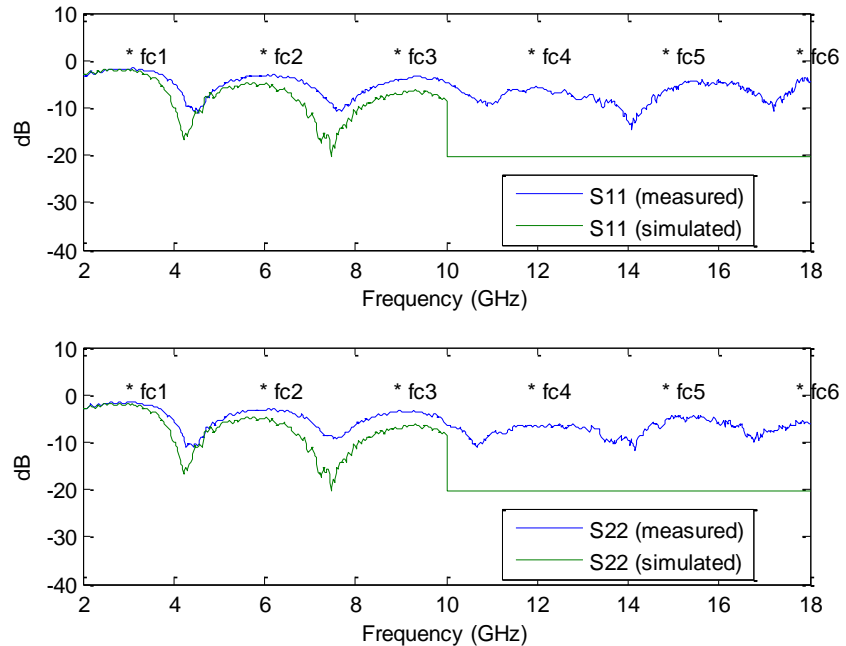


Figure 115: Measured vs. Simulated Left-to-Right Reflection (THRU)

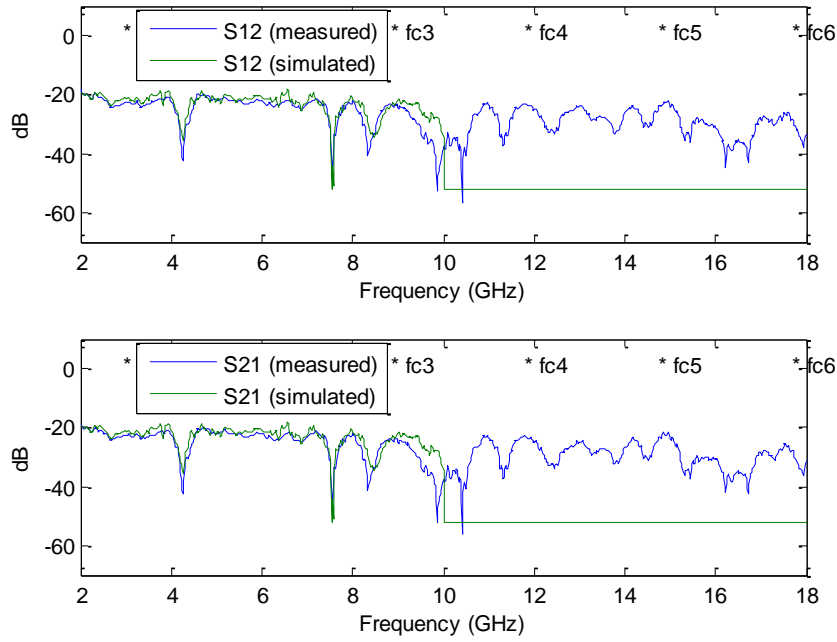


Figure 116: Measured vs. Simulated Left-to-Right Transmission (THRU)

The percent-error for the reflection responses follow the previous near-linear trends with error increasing from around 2 GHz (about 5%) to repeated maximums (about 50%-60%) at the positions of the magnitude nulls. The percent-error plots for the transmission responses follow the same general trend with the error peaks loosely corresponding to the positions of the nulls. The greatest transmission error is where the measured and simulated signals diverge from 9-10 GHz. As compared to the empty PPWG, the reflection response errors are similar, but with the lenses, there appears to be more point-to-point fluctuation in the error. As compared to the empty PPWG, the transmission response errors are also similar, but with the lenses, there appears to be less error overall as the measured and simulated responses are more closely aligned.

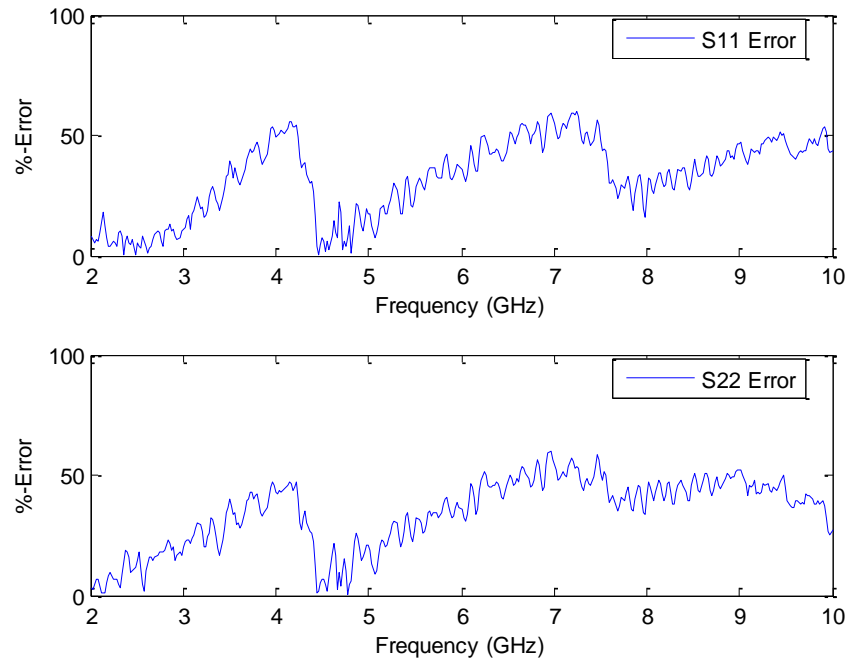


Figure 117: Left-to-Right Reflection Error (THRU)

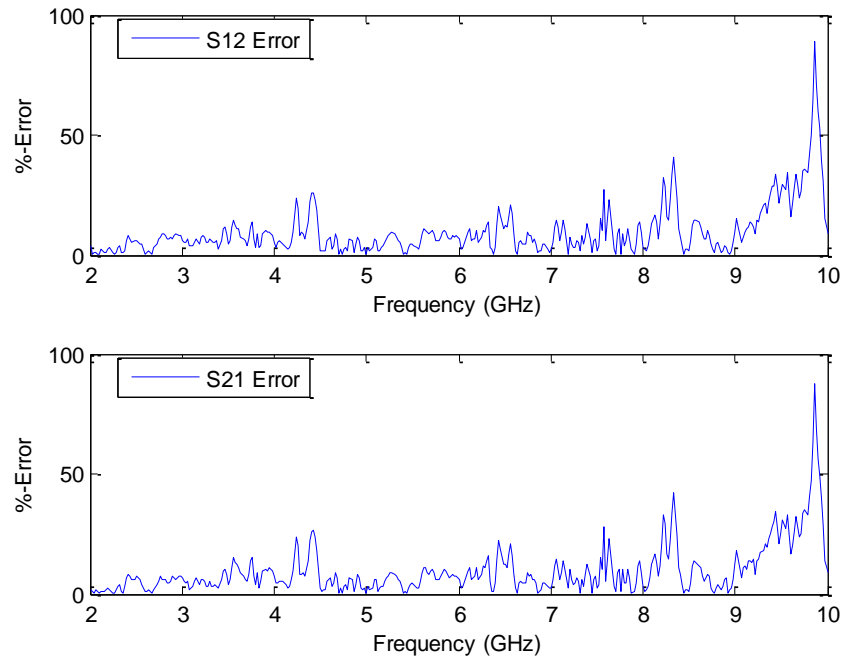


Figure 118: Left-to-Right Transmission Error (THRU)

For the SHORT measurement, Figure 119 and Figure 120 show the S-parameter magnitude and phase. Figure 121 and Figure 122 compares the measurements to simulations. A basic percent-error plot is shown in Figure 123 and Figure 124 for these comparisons.

Qualitatively, for these left-to-right magnitude plots, there is general agreement between S11 and S22. The nulls have deepened relative to the THRU measurement and a higher-frequency harmonic has been introduced throughout each response.

There is general agreement between S12 and S21 as well. Relative to the THRU measurement, the initial magnitude for the SHORT measurement is down 20 dB and there is a higher-frequency harmonic.

In the phase plots, the SHORT reflection responses exhibit sharpened discontinuities at the magnitude nulls and one sharp discontinuity at 14 GHz.

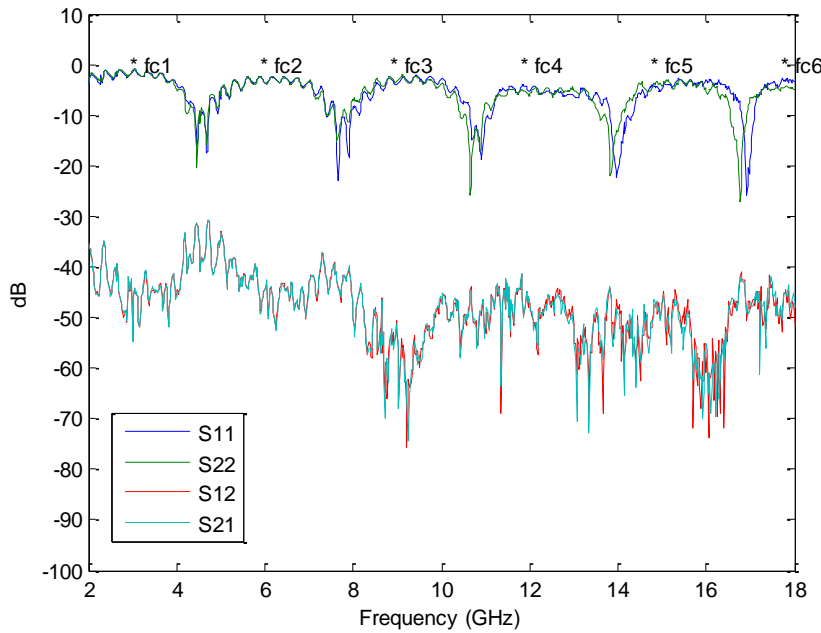


Figure 119: Measured Left-to-Right S-Parameters (SHORT) (Mag.)

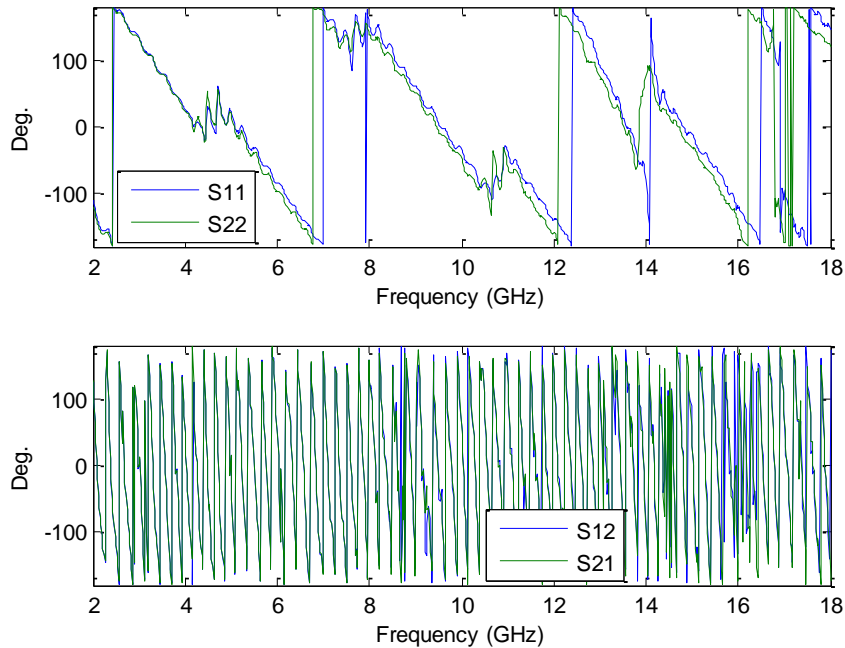


Figure 120: Measured Left-to-Right S-Parameters (SHORT) (Phase)

There is general agreement between the measured and simulated S11 and S22 for the SHORT measurement.

There is little agreement between the measured and simulated S12 and S21 for the SHORT measurement. The measured response is consistently 30 dB higher than the simulated response and the forms of each response are not similar. It is unknown why this has occurred.

The percent-error plots for the SHORT reflection responses follow the same near-linear trends as before except for the higher-frequency harmonics and the occasional spike. The percent-error plots for the transmission responses do not follow any of the trends presented thus far.

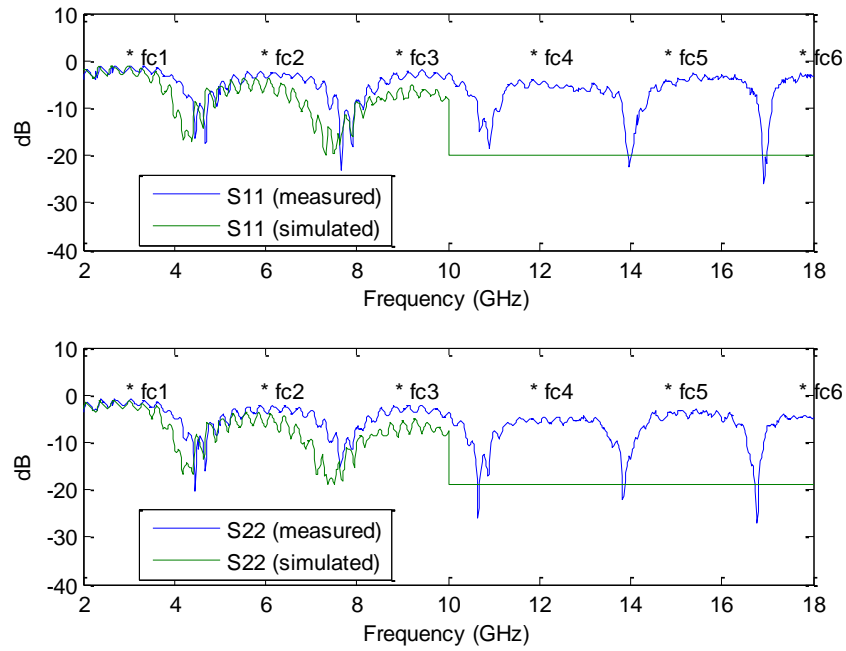


Figure 121: Measured vs. Simulated Left-to-Right Reflection (SHORT)

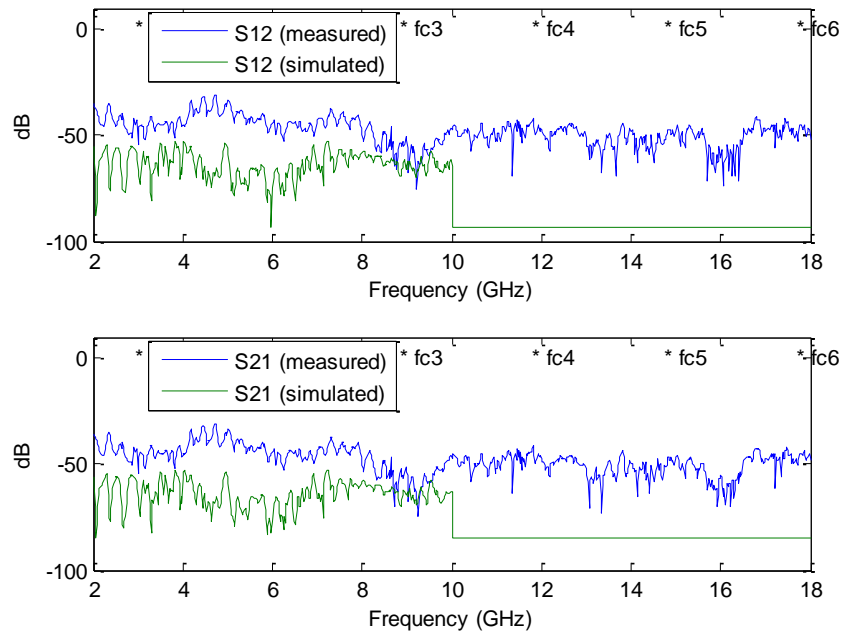


Figure 122: Measured vs. Simulated Left-to-Right Transmission (SHORT)

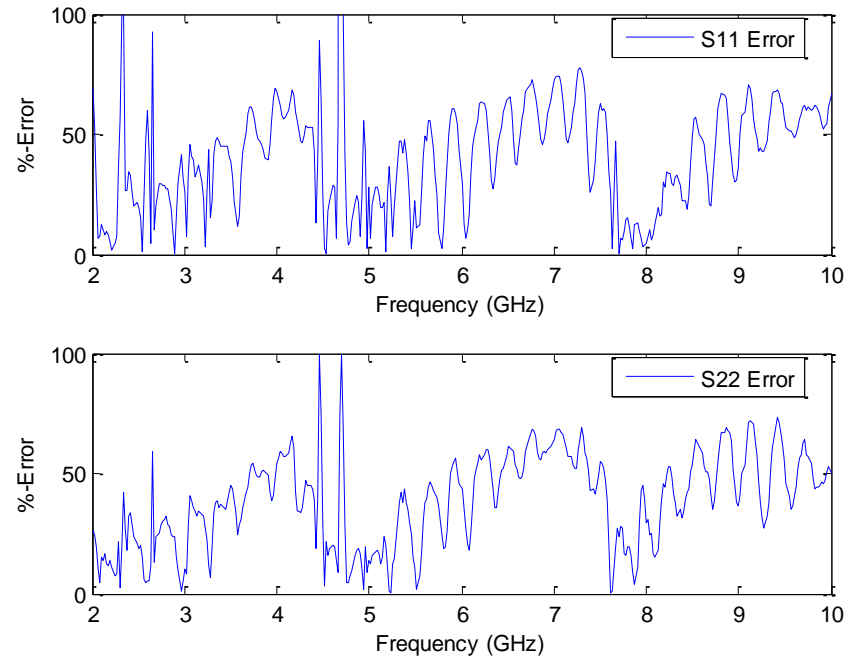


Figure 123: Left-to-Right Reflection Error (SHORT)

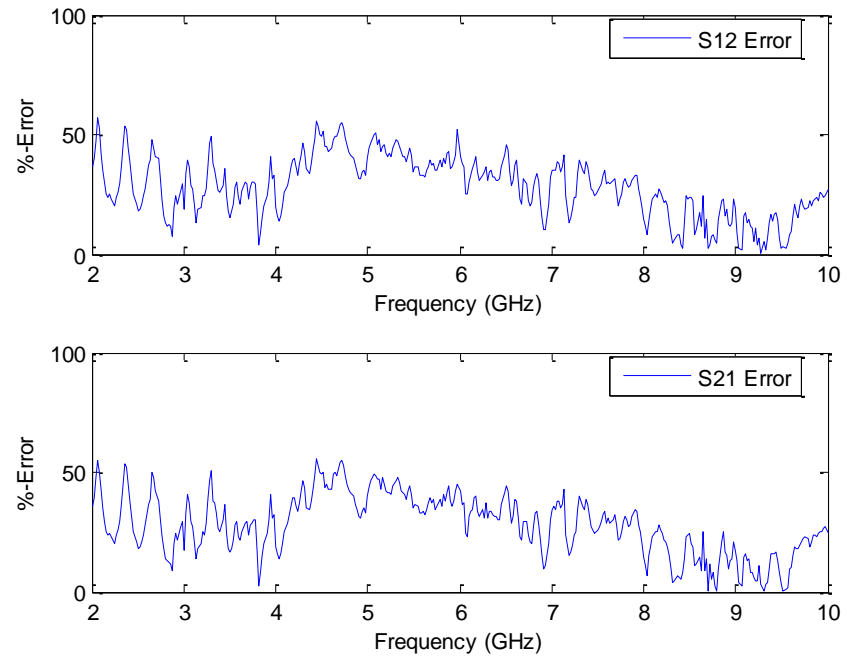


Figure 124: Left-to-Right Transmission Error (SHORT)

For the acrylic measurement, Figure 125 and Figure 126 show the S-parameter magnitude and phase. Figure 127 and Figure 128 compares the measurements to simulations. A basic percent-error plot is shown in Figure 129 and Figure 130 for these comparisons. In the CST simulations, the permittivity of acrylic was set 3.6 by default.

Qualitatively, for these left-to-right magnitude plots, there is general agreement between S11 and S22. The main difference between the acrylic and the THRU measurement is that the peaks of the acrylic measurement are higher, and that the higher-frequency nulls have deepened.

There is general agreement between S12 and S21 for acrylic. Relative to the THRU measurement, the initial magnitude for the acrylic measurement has not changed.

In the phase plots, the acrylic reflection responses behave similarly to the THRU reflection responses aside from the discontinuity at 14 GHz.

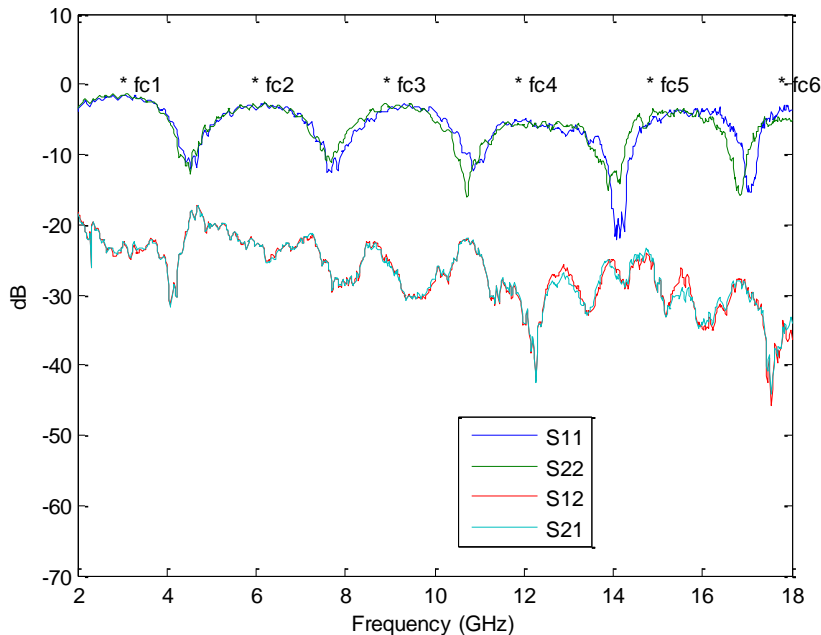


Figure 125: Measured Left-to-Right S-Parameters (Acrylic) (Mag.)

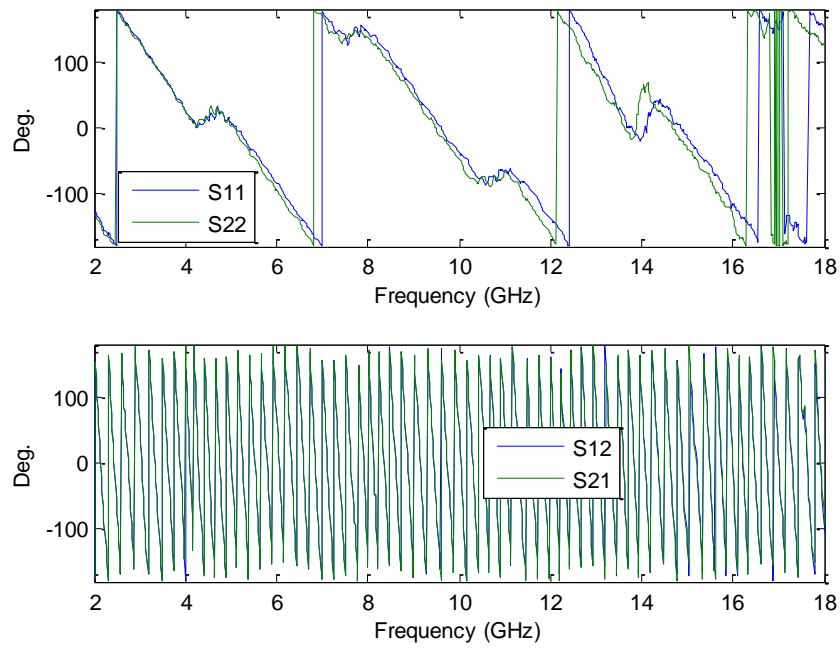


Figure 126: Measured Left-to-Right S-Parameters (Acrylic) (Phase)

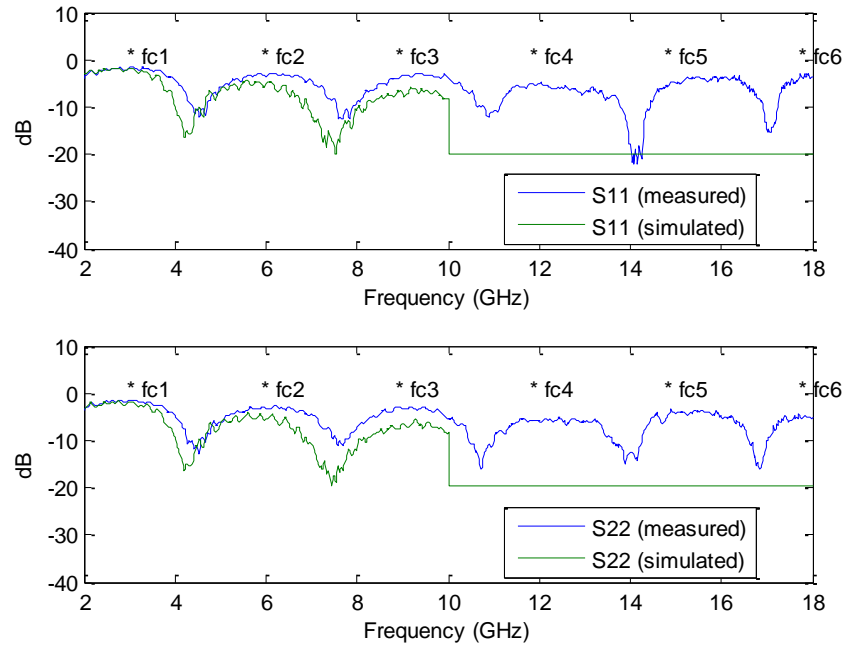


Figure 127: Measured vs. Simulated Left-to-Right Reflection (Acrylic)

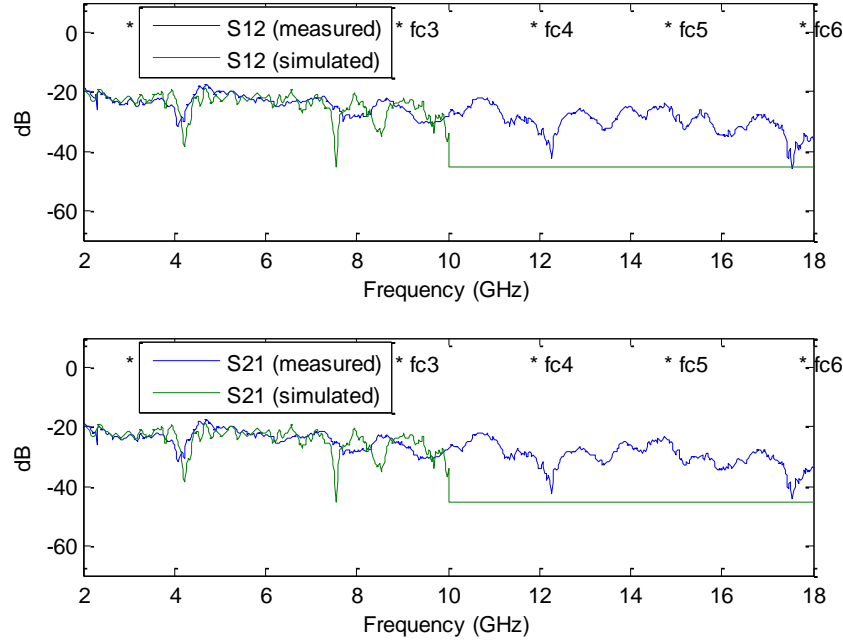


Figure 128: Measured vs. Simulated Left-to-Right Transmission (Acrylic)

There is general agreement between the measured and simulated S11 and S22 for the acrylic measurement. There is also general agreement between the measured and simulated S12 and S21. For S12 and S21, the main difference is in the nulls that occur near 7.5 GHz and 8.5 GHz. The difference is assumed to be related to either the CST permittivity value of 3.6 as compared to the actual, unknown permittivity of the acrylic target, or the lack of precision in the construction and placement of the target.

These percent-error plots for the acrylic reflection responses follow the same near-linear trend as seen in most of the measurement and simulation comparisons. The percent-error plots for the transmission responses could be generally described as following the trends for the THRU measurement but without the large error at 9-10 GHz.

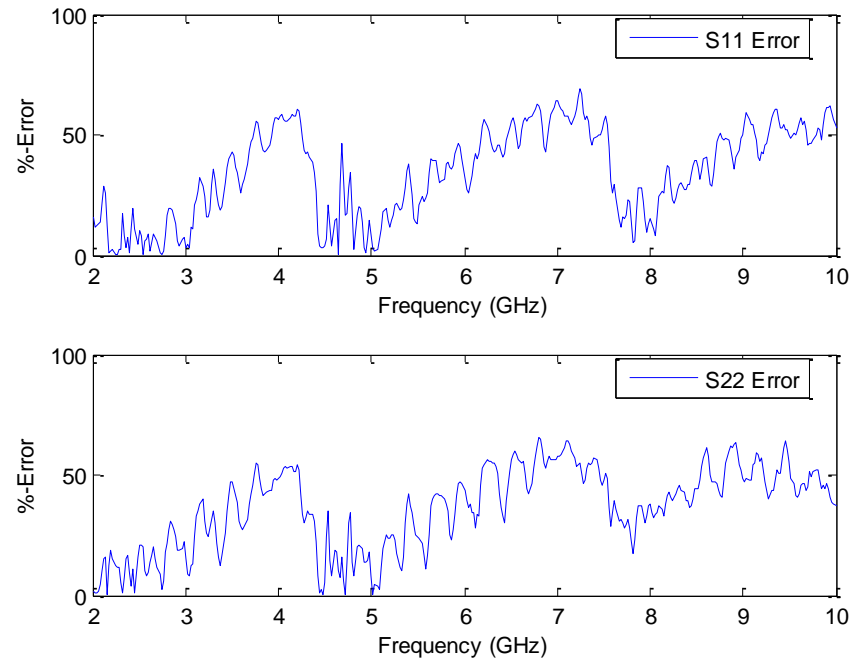


Figure 129: Left-to-Right Reflection Error (Acrylic)

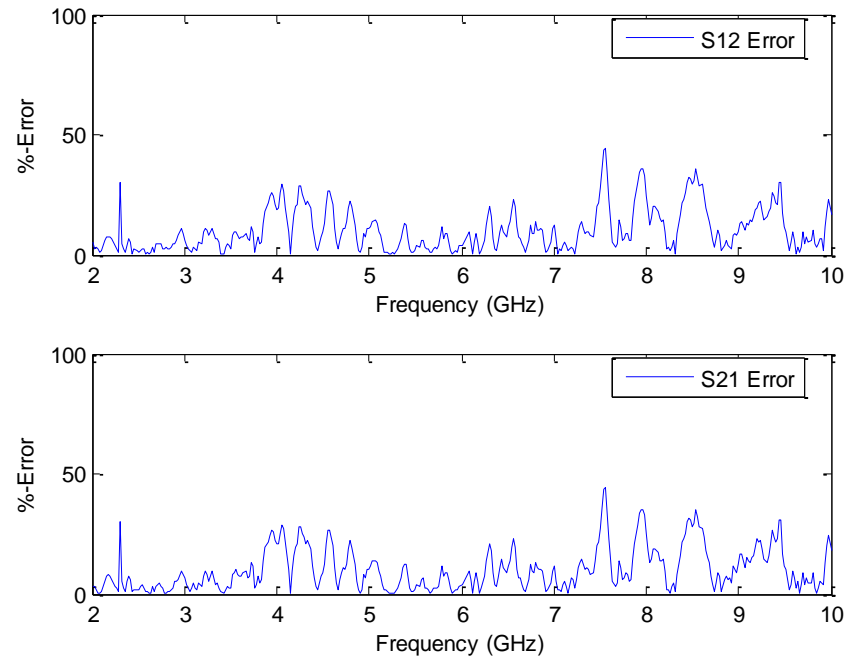


Figure 130: Left-to-Right Transmission Error (Acrylic)

For the D-ring measurement, Figure 131 and Figure 132 shows the S-parameter magnitude and phase. Figure 133 and Figure 134 compares the measurements to simulation. A basic percent-error plot is shown in Figure 135 and Figure 136 for these comparisons.

Qualitatively, for these left-to-right magnitude plots, there is general agreement between S11 and S22. The main difference between the D-Ring and the THRU measurement is that the higher-frequency nulls have deepened.

There is general agreement between S12 and S21 for the D-Rings. Relative to the THRU measurement, the initial magnitude for the D-ring measurement has dropped by nearly 20 dB, but has resumed to THRU magnitude levels after a narrow resonance band.

In the phase plots, the D-ring reflection responses behave similarly to the THRU reflection responses, varying only in sharpness at the positions of the magnitude nulls.

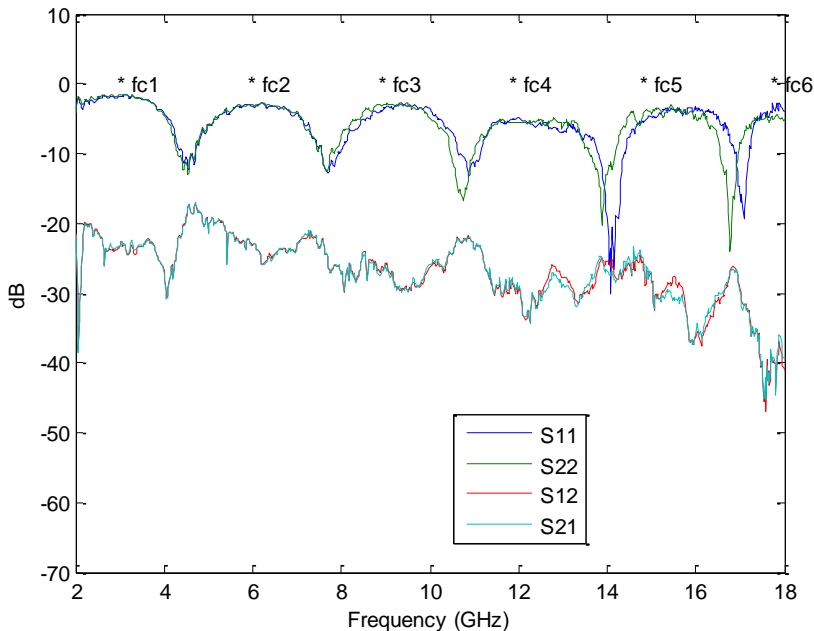


Figure 131: Measured Left-to-Right S-Parameters (D-Ring) (Mag.)

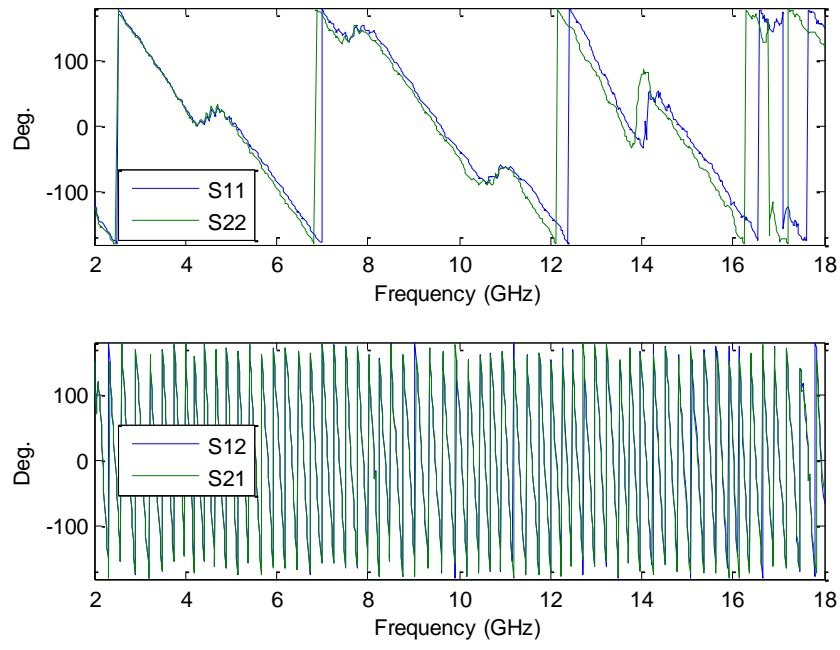


Figure 132: Measured Left-to-Right S-Parameters (D-Ring) (Phase)

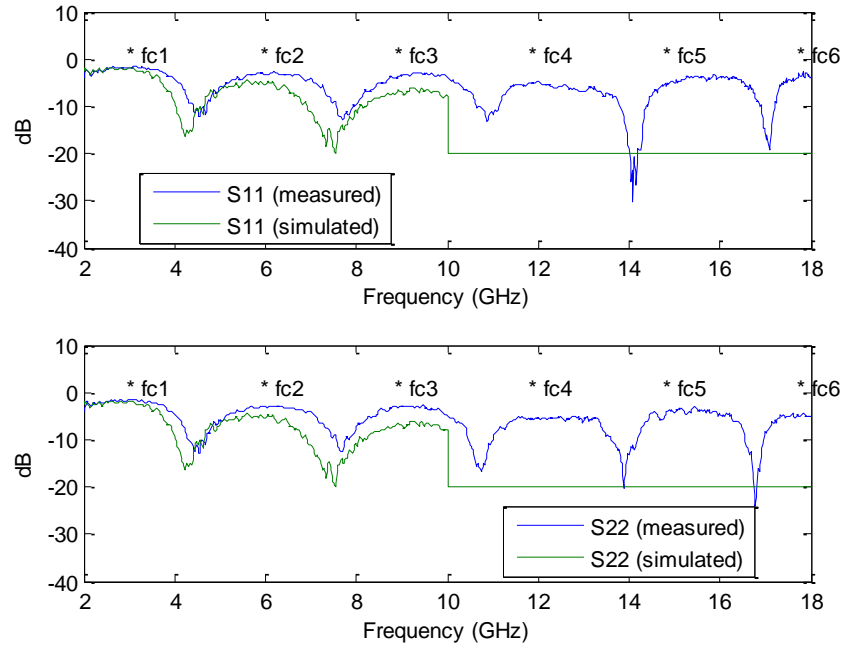


Figure 133: Measured vs. Simulated Left-to-Right Reflection (D-Ring)

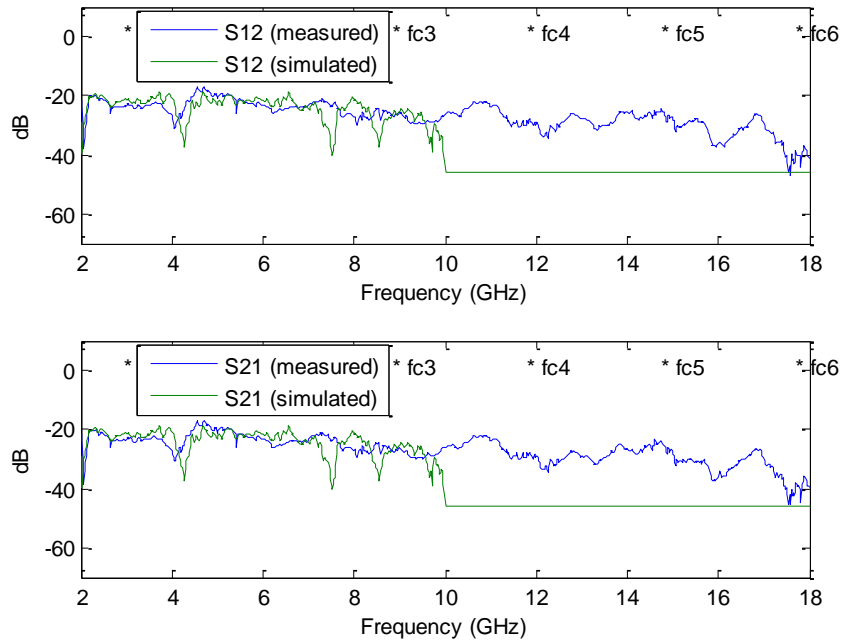


Figure 134: Measured vs. Simulated Left-to-Right Transmission (D-Ring)

There is general agreement between the measured and simulated S11 and S22 for the D-ring measurement. There is also general agreement between the measured and simulated S12 and S21. For S12 and S21, the main difference is in the nulls that occur near 7.5 GHz and 8.5 GHz, just as in the acrylic measurement. The cause of this difference is unknown.

These percent-error plots for the D-ring reflection responses follow the same near-linear trend as seen in most of the measurement and simulation comparisons. The percent-error plots for the transmission responses could be generally described as following the trends for the THRU and acrylic measurements.

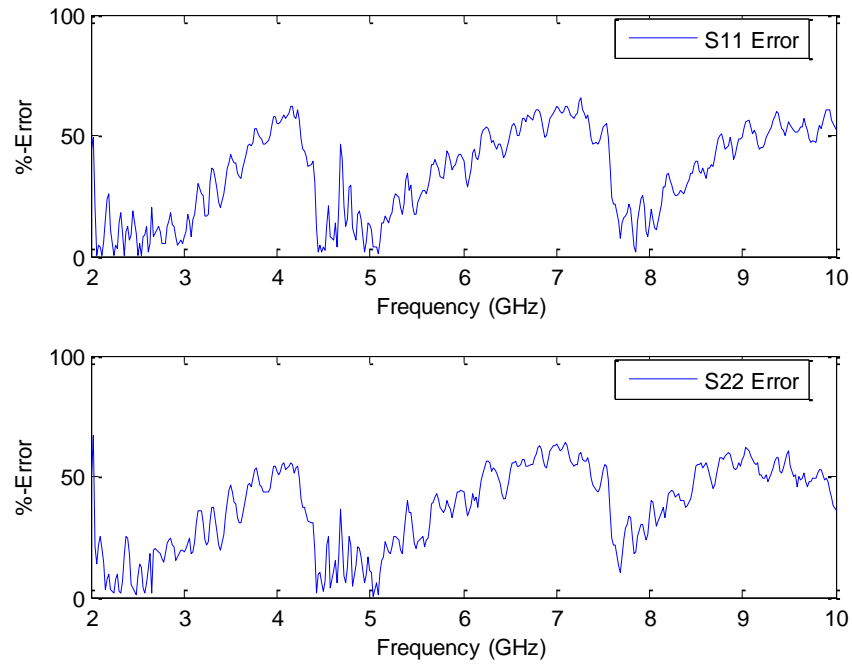


Figure 135: Left-to-Right Reflection Error (D-Ring)

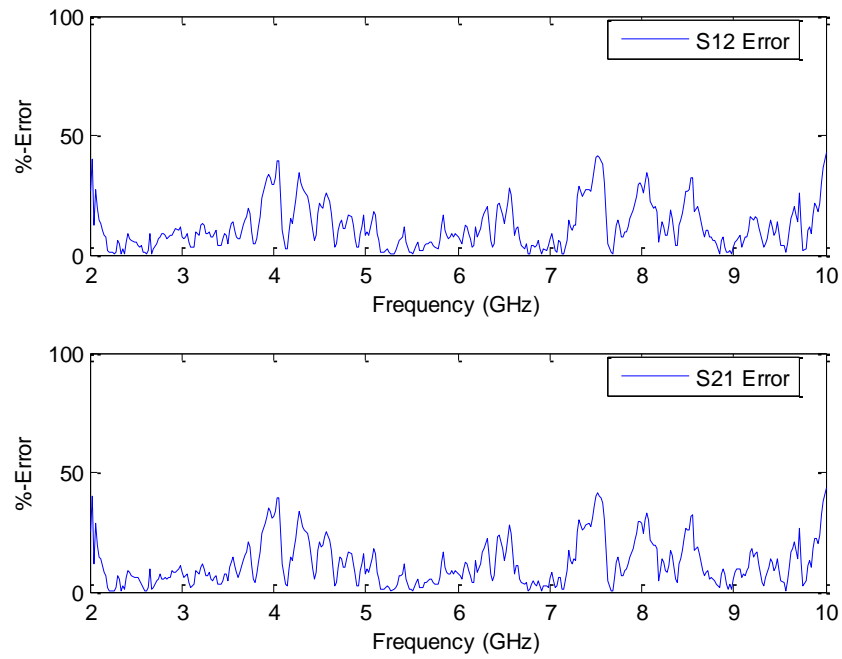


Figure 136: Left-to-Right Transmission Error (D-Ring)

Large Lenses in PPWG

The simulation model for the PPWG with large lenses is shown in Figure 137.

The magnitude and phase distributions throughout the waveguide, as excited by the left monopole, can be arbitrarily visualized in Figure 138.

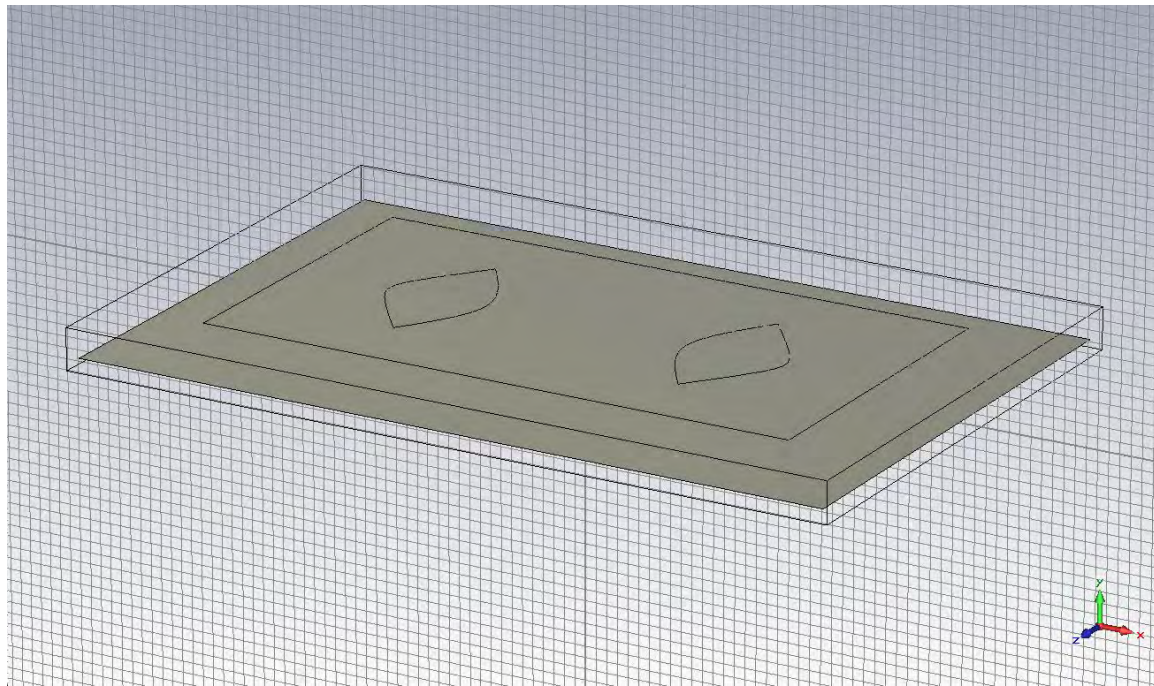


Figure 137: PPWG Model with Large Lenses

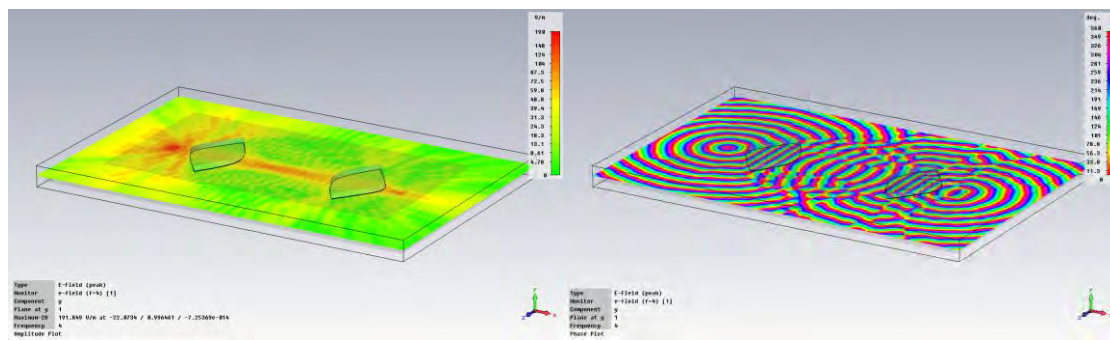


Figure 138: PPWG with Large Lenses with Magnitude and Phase Distributions

Near-Field Scans

There are no near-field scans with the large lenses.

S-Parameters (Test Points 14-17)

S-parameters were measured from the left monopole to the right monopole (each at the long focal length) for the THRU configuration and for each target.

For the THRU configuration, Figure 139 and Figure 140 show the magnitude and phase measurements. Figure 141 and Figure 142 compares the measurements to simulations. A basic percent-error plot is shown in Figure 143 and Figure 144 for these comparisons.

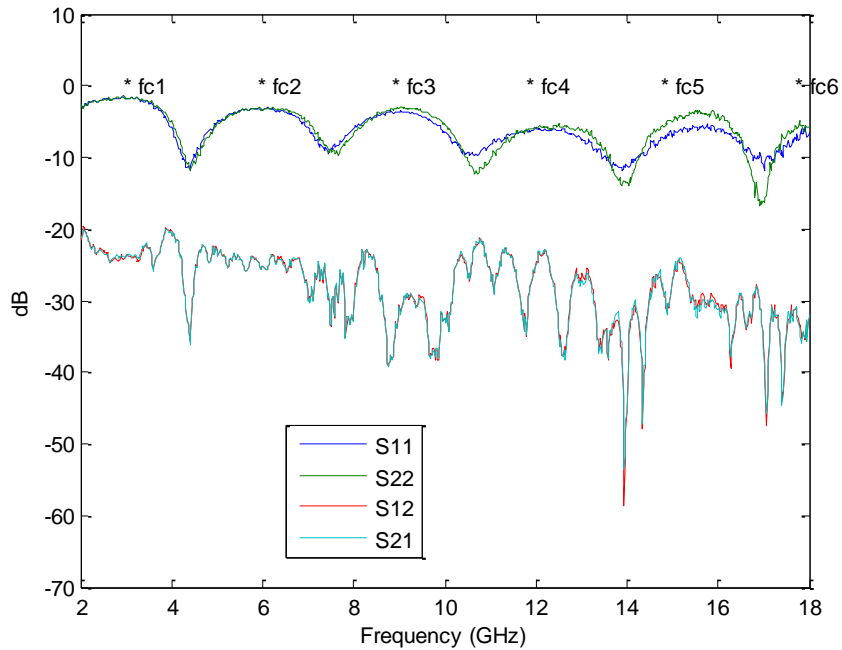


Figure 139: Measured Left-to-Right S-Parameters (THRU) (Mag.)

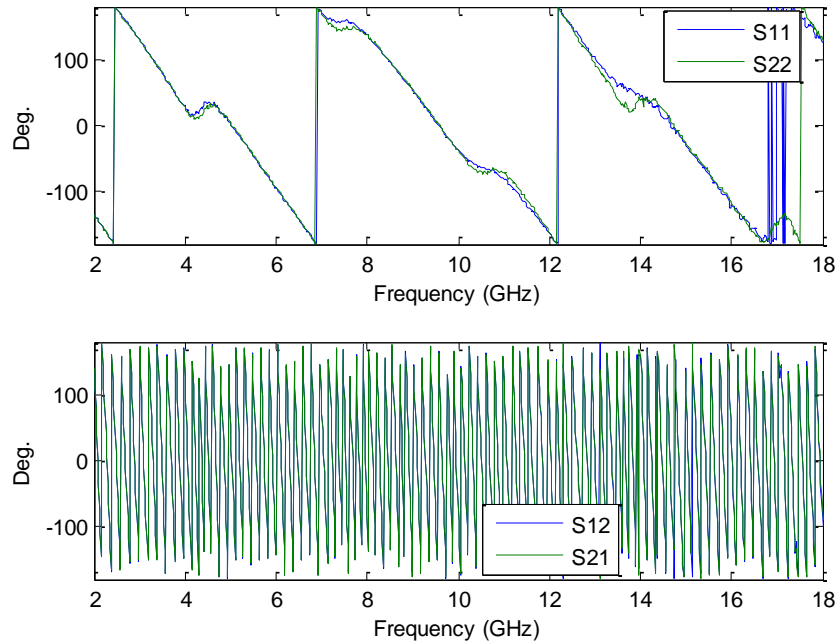


Figure 140: Measured Left-to-Right S-Parameters (THRU) (Phase)

Qualitatively, for these left-to-right magnitude plots, there is general agreement between S11 and S22. Compared to the baseline of the empty PPWG, the main difference is in the depth of the nulls. The presence of the large lenses seems to have softened the effects of prior interference, but it is unknown how this has occurred.

There is also general agreement between S12 and S21. When compared to the empty PPWG, the transmission responses with the lenses are not only unique but 10 dB higher in magnitude. The magnitude increase is assumed to be due to the focusing action of the lenses.

The left-to-right phase plots are in general agreement and as compared to those of the empty PPWG, there is no discernable change aside from the softened nulls throughout, especially at 14 GHz.

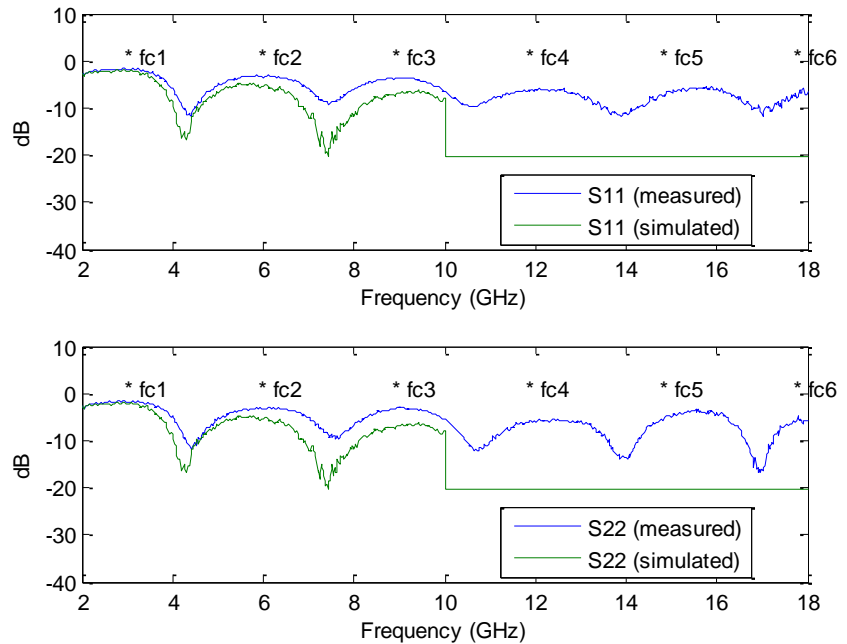


Figure 141: Measured vs. Simulated Left-to-Right Reflection (THRU)

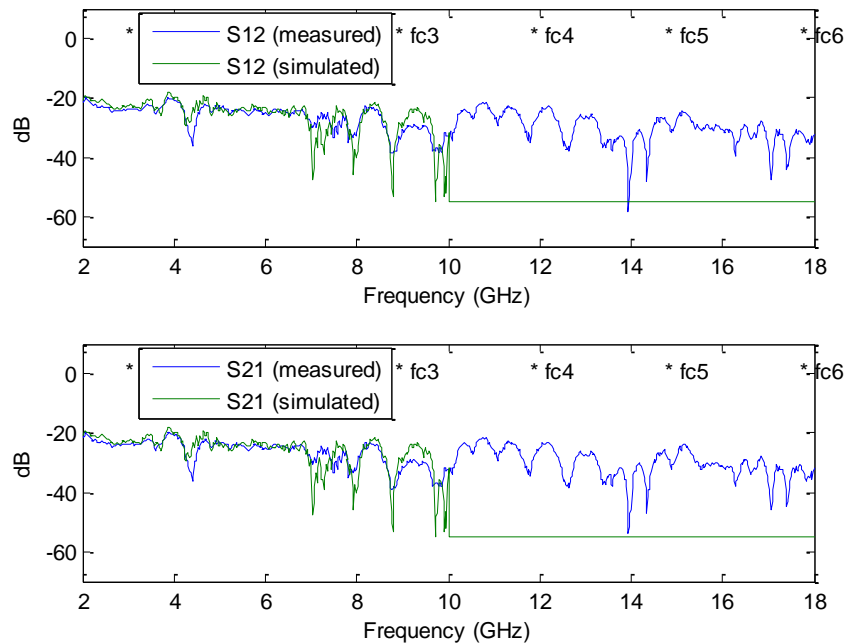


Figure 142: Measured vs. Simulated Left-to-Right Transmission (THRU)

In comparing measured S-parameters to simulated S-parameters, only 0-10 GHz can be reviewed. Qualitatively, there is general agreement between the measured and simulated S11 and S22. As was the case for the empty PPWG, the main difference with the lenses is still that the peaks and nulls of the reflection responses are shifted to higher frequencies relative to the simulations. It is not immediately discernable if there is a difference in the simulated reflection responses with or without the lenses.

There is very close agreement between the measured and simulated S12 and S21 with the large lenses. The very close agreement between the measured and simulated transmission responses with the large lenses is in sharp contrast to the less general agreement between the measured and simulated transmission responses of the empty PPWG. It was assumed previously that the lack of rolled edges in the empty PPWG simulation led to less agreement in those transmission responses. Based on the very close agreement just observed with the large lenses, it is assumed that the focusing action of the lenses has made the diffraction effects of the empty PPWG simulation negligible.

In these basic percent-error plots, the percent-error for the reflection responses follow the previous near-linear trends with error increasing from around 2 GHz (about 5%) to repeated maximums (about 50%-60%) at the positions of the magnitude nulls. The percent-error plots for the transmission responses follow the same general trend with the error peaks loosely corresponding to the positions of the nulls. As compared to the empty PPWG, the reflection response errors are similar, but with the lenses, there appears to be more point-to-point fluctuation in the error. As compared to the empty PPWG, the transmission response errors are also similar, but with the lenses, there appears to be less error overall as the measured and simulated responses are more closely aligned.

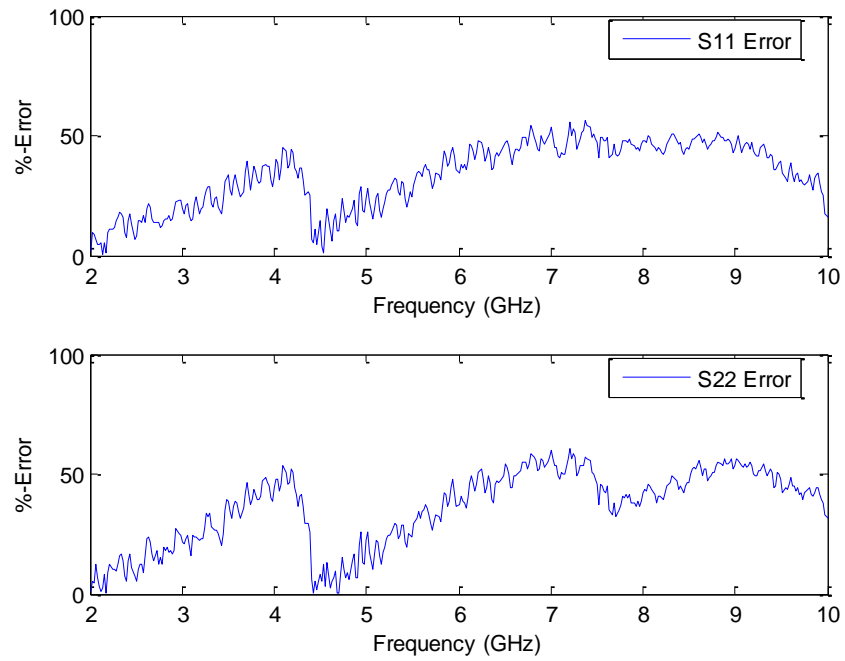


Figure 143: Left-to-Right Reflection Error (THRU)

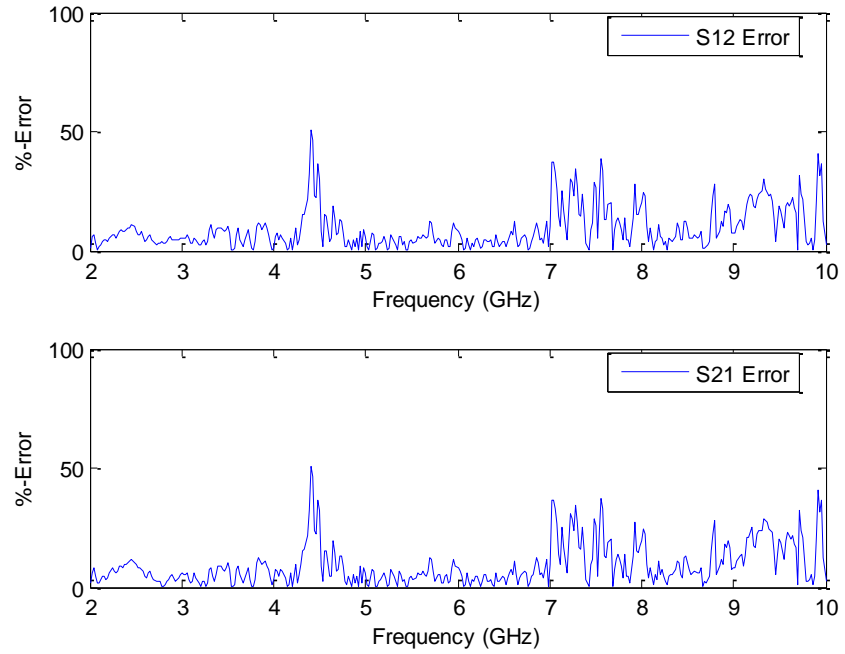


Figure 144: Left-to-Right Transmission Error (THRU)

For the SHORT measurement, Figure 145 and Figure 146 show the S-parameter magnitude and phase. Due to the untimely expiration of the CST license, these measurements could not be compared to simulations.

Qualitatively, for these left-to-right magnitude plots, there is very close agreement between S11 and S22. The nulls have deepened relative to the THRU measurement and a higher-frequency harmonic has been introduced throughout each response.

There is general agreement between S12 and S21 as well. Relative to the THRU measurement, the initial magnitude for the SHORT measurement is down 25 dB and there is a higher-frequency harmonic.

In the phase plots, the SHORT reflection responses exhibit sharpened discontinuities at the positions of the magnitude nulls and one very sharp discontinuity at 14 GHz.

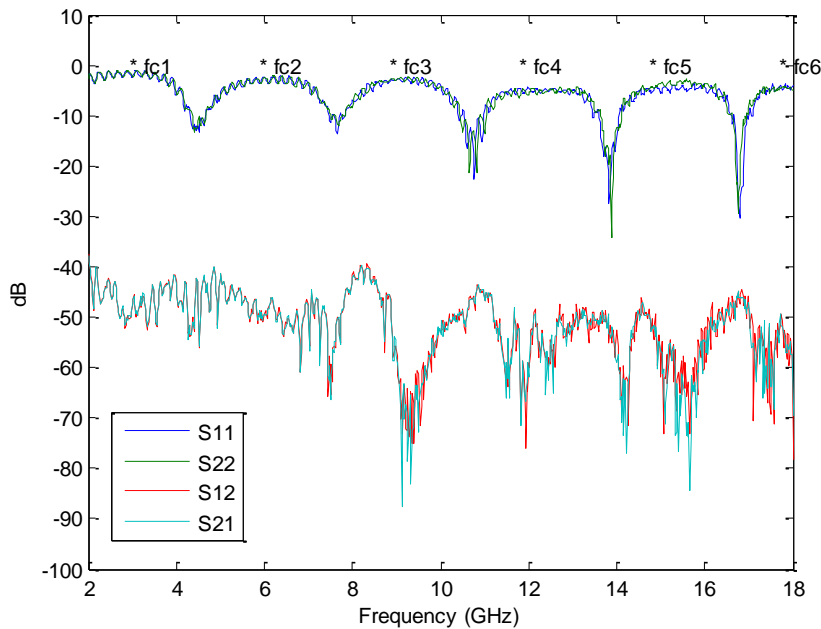


Figure 145: Measured Left-to-Right S-Parameters (SHORT) (Mag.)

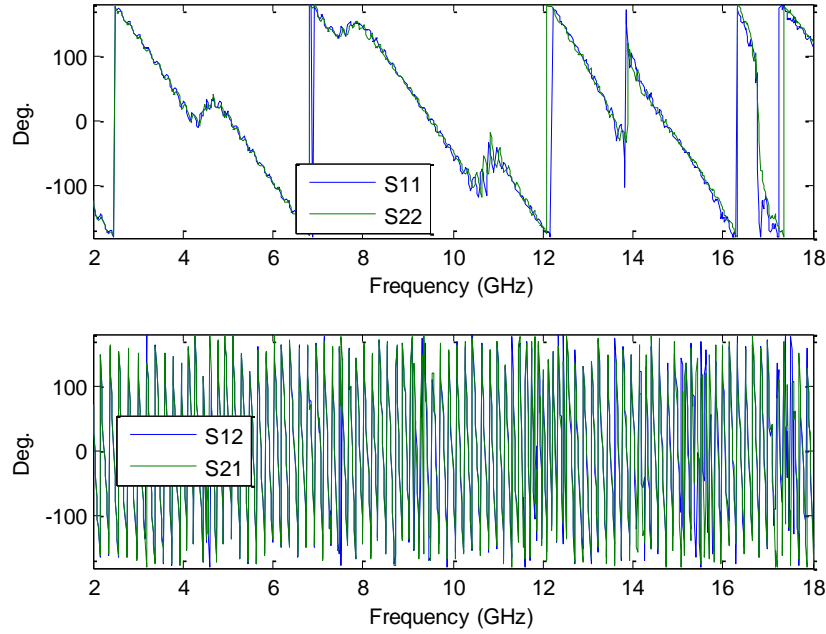


Figure 146: Measured Left-to-Right S-Parameters (SHORT) (Phase)

For the acrylic measurement, Figure 147 and Figure 148 show the S-parameter magnitude and phase. Due to the untimely expiration of the CST license, these measurements could not be compared to simulations either.

Qualitatively, for these left-to-right magnitude plots, there is general agreement between S11 and S22. The main difference between the acrylic and the THRU measurement is that the peaks of the acrylic measurement are higher, and that the higher-frequency nulls have deepened.

There is general agreement between S12 and S21 for acrylic. Relative to the THRU measurement, the initial magnitude for the acrylic measurement has not changed.

In the phase plots, the acrylic reflection responses behave similarly to the THRU reflection responses aside from the lack of S11 discontinuities between 16-18 GHz.

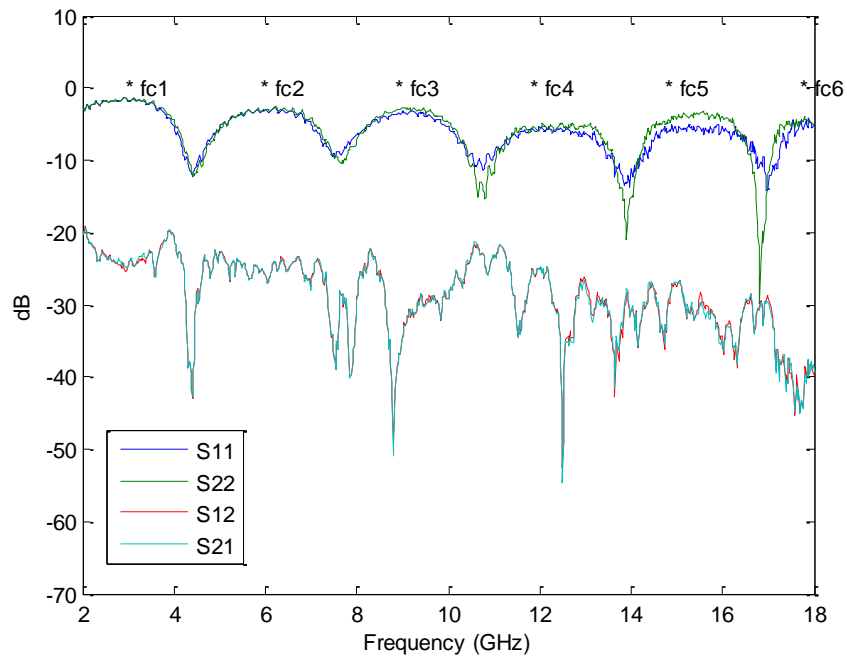


Figure 147: Measured Left-to-Right S-Parameters (Acrylic) (Mag.)

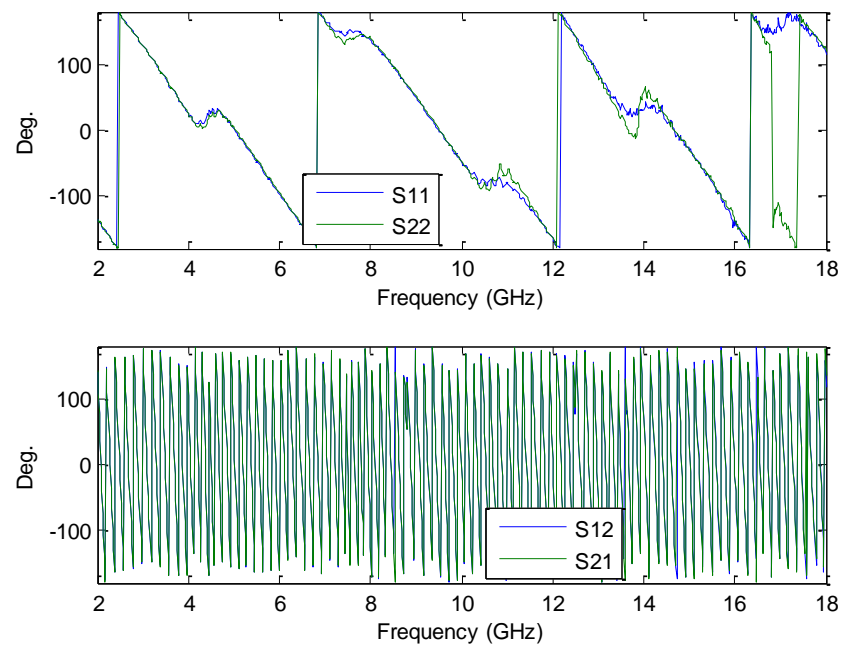


Figure 148: Measured Left-to-Right S-Parameters (Acrylic) (Phase)

For the D-ring measurement, Figure 149 and Figure 150 show the S-parameter magnitude and phase. Due to the untimely expiration of the CST license, these measurements could not be compared to simulations.

Qualitatively, for these left-to-right magnitude plots, there is general agreement between S11 and S22. The main difference between the D-Ring and the THRU measurement is that the higher-frequency nulls have deepened, especially at 14 GHz.

There is general agreement between S12 and S21 for the D-Rings. Relative to the THRU measurement, the initial magnitude for the D-ring measurement has dropped by nearly 20 dB, but has resumed to THRU magnitude levels after a narrow resonance band. Relative to the measurements using the small lenses, the large lens D-ring transmission response contains additional nulls at 4.5 GHz, 7.5 GHz and 9 GHz.

In the phase plots, the D-ring reflection responses behave similarly to the THRU reflection responses, varying only in sharpness at the positions of the magnitude nulls.

To conclude the basic analysis for the lenses in the PPWG, the highlighted measurement phenomena were 1) standing-wave beam established between the small lenses; 2) inverted cylindrical wavefronts converging to, then diverging from planar wavefronts at the beamwaist of the small lenses; 3) definable beam radius and normalized taper relative to the beamwaist of the small lenses; 4) magnitude and phase variations with an air gap above the small lenses; 5) distributed fields in the near-field region of a metamaterial; 6) effects on S-parameter magnitudes with lenses present; 7) softening effects on magnitude nulls with lenses present; 8) general agreement between S11 and S22 and between S12 and S21 for all lens and target configurations; 9) general agreement between all measurements and simulations (except for the exception of the SHORT).

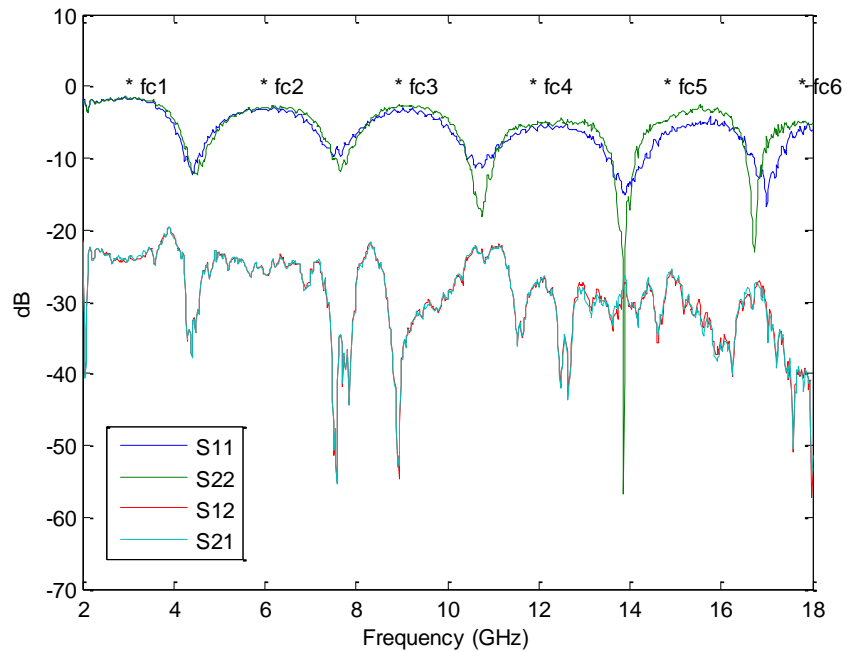


Figure 149: Measured Left-to-Right S-Parameters (D-Ring) (Mag.)

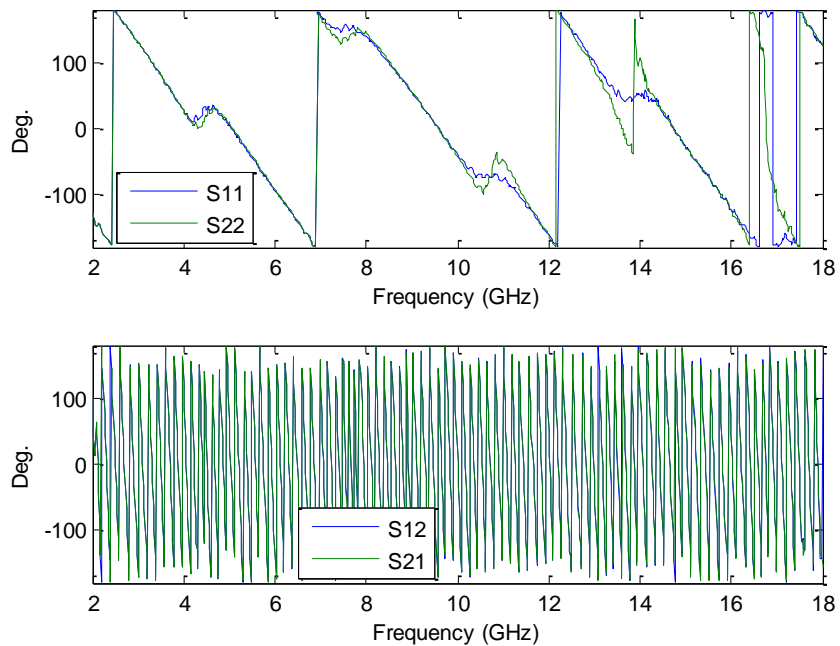


Figure 150: Measured Left-to-Right S-Parameters (D-Ring) (Phase)

V. Conclusions and Recommendations

Conclusions

Conclusions from Measurement Results and Analysis

The initial results and analysis presented throughout Chapter 4 have revealed that the BANTAM 2-D FBS is capable of yielding consistent measurements for both near-field scans and S-parameters, using both small lenses and large lenses, for a small selection of targets. The immediate intent of the analysis was to compare the performance of the newly-built system to an equivalent simulated system, and across these results, note the degree of agreement between the measurements and simulations. As it was pointed out in Chapter 4, the measurements were always (aside from one isolated case) in general agreement, if not very close agreement, with the simulations.

Logically, the next step beyond this analysis would be to apply these results to the derivation of the constituent parameters for the acrylic target. This next step has not been performed for this thesis, but all the necessary tools have been provided. The THRU, SHORT and acrylic S-parameters may be used to derive permittivity and permeability for acrylic for both the measured and simulated systems using either the small or the large lenses.

Likewise, the next logical step after deriving constituent parameters for a traditional radar-frequency material would be deriving [bulk] constituent parameters for a radar-frequency metamaterial (D-rings). Again, this step is not performed, but the

necessary tools are made available. Pairing the derived constituent parameters with the information found in the appropriate near-field scans should allow the basics of metamaterial taxonomy to begin.

Conclusions on Technical and Philosophical Significance

This thesis concludes with the understanding that use of the BANTAM 2-D FBS is far from being an accepted material measurement technique. However, in hybridizing designs from three other accepted techniques, the BANTAM 2-D FBS has a considerable technical significance. The primary significance is that it physically combines near-field measurement functions and focused-beam S-parameter measurement functions into a single apparatus. In secondary significance, the system operates two styles of focused-beams which can be used for targets of appreciable size over 2-18 GHz. Having been successful in developing this apparatus, this thesis should also be successful in the stated goal of furthering the technical development of radar-frequency metamaterials. It is anticipated that a patent will follow.

Based on the technical success, and in justifying the importance of systematic measurement and characterization of metamaterials, this thesis should also be successful in achieving the stated goal of shaping metamaterial definitions through a reliable and repeatable method of taxonomy.

Recommendations for Action and Research

Component Recommendations

Monopole (Action)

The monopole rods should be monitored for bending or replaced with a stiffer material. The current rods are soft and flexible and are prone to bending when inserting them into the coaxial adaptor. The coaxial adaptors should also be monitored or replaced due to their soft dielectric. At times of inserting or removing the monopole rods, the dielectric of the coaxial adaptor was noticed to be gouged enough to allow the collar of the inner conductor to spread open. The spreading results in a monopole that leans or a top probe that falls out.

The monopoles should be re-cut to a standard length of 1.9". They were previously tuned by iterative trimming to allow passage of the top plate over them, but the final height was not standardized throughout.

Monopole (Research)

The original monopole height optimization was performed considering far-field radiation of a monopole on a single ground plane. The optimization should be performed again to determine if there is a different optimum monopole height when introducing the top plate. Also, the optimum monopole heights per frequency octave should be sought out to determine if it would be practical to stage measurements over frequency octaves rather than the full 2-18 GHZ. If possible, radiation patterns should be used to estimate the relative strength of excitation for each of the PPWG modes.

Top Probe (Action)

The cabling to the top probe should be inspected to see if it is loose at any connecting point. There is one small length of cable attached to the coaxial adaptor in the top plate, but that small cable is joined to another long cable. It is assumed that the long cable runs through the conduits of the translation rails and directly to the network analyzer. It should be verified that this is the case. If this is not the case, any additional connecting points will have to be checked for tightness. Once the proper tightness is achieved in all the connecting points, the two-port network calibration must be run again before using the top probe for any measurements.

Top Probe (Research)

The design of the top plate allows for an open architecture with respect to installing various types of probes. In anticipation of a more-permanent probe, the design of the top plate, the linear translation system, and the cabling system must be reviewed to determine the degree of installation compatibility. Also, as was discussed in Chapter 1, any permanent probe should be characterized for its ability to take near-field measurements. Characterization should also include corrective measures for probe-target interactions.

Aluminum Sheets (Action)

Prior to each use, the aluminum sheets should be swept clean and wiped with alcohol. Routine cleaning will keep the surfaces free from small absorber debris and

conductive tape residue. It is recommended that the sheets be stripped bare of all components prior to cleaning. The painted surfaces should only be swept, but not cleaned with alcohol.

Aluminum Sheets (Research)

Fabrication techniques that result in precision sheet flatness should be researched. Also, fabrication techniques that warp sheet flatness should be researched and avoided. This recommendation is primarily directed at future PPWG designs.

Rolled Edges (Action)

The rolled edges, especially the front, should be continually monitored for scratching. Though very durable, the paint may become roughened or scratched by tools, watches, belts, targets, lenses, etc. The underside of the top plate near the tangents of the rolled edges should be monitored on both the front and back side for scratches made by the lenses or targets.

Rolled Edges (Research)

The rolled edges should be further characterized in CST simulations by evaluating the magnitude and phase distributions along a variety of evaluation lines. These lines would include not only straight lines in the propagation direction, but diagonal lines leading through specific tangent points on the rolled edge and circular lines leading around the rolled edge. This characterization could be performed on a small, square PPWG as presented in this document, or, time and simulation capabilities permitting, on

the actual size of the BANTAM PPWG. The advantage of using the size of the actual PPWG would be the ability to characterize the rolled edges at the furthest reaches of the scan.

Plate Frames (Action)

Rubber safety caps should be installed on the ends of all the short legs of the 80/20 plate frames. The sharp aluminum edges are a nuisance at best and a hazard at worst to a person's head when trying to maneuver tools and cables below the bottom plate. The sharp edges are also hazardous to a person's arm when trying to maneuver tools and cable above the top plate.

Plate Frames (Research)

At certain points along each rolled edge, the PVC pipes are fastened to the legs of the plate frames. The legs extend approximately 3" beyond the fastening point and may provide a reflection surface for waves traveling around the pipe. Experiments should be conducted to see how significantly reflections from these legs affect measurements. Measurements should be taken with the legs obscured by absorber and with the legs bare. The same experiment should be used to determine the effects of the large cavities formed by the rolled edges. The cavities are the areas immediately above the top plate and immediately below the bottom plate where the plate frames are fastened to the short axis and the scissor lift respectively.

Fiberglass Filler (Action)

The perimeter of the plates where the fiberglass filler was applied should be monitored for cracks. The likeliest cracks would form in the light-weight filler in the mitered corners. Cracks may form if the plates are put under enough twisting stress. Twisting stress can be avoided by sensibly operating the lift and translation axes and by not leaning on or otherwise unevenly loading the plates with weight. Cracks can also be avoided by not dropping objects onto the plates.

Paint (Action)

The paint should be monitored for roughened surfaces, scratches and blackened, yellowed or whitened areas. Blackened areas indicate that the metal in the paint has begun to oxidize. Blackened areas already exist on the painted PVC surfaces due to the handling of unpainted PVC pipe with bare hands – skin oils were absorbed into the PVC and could not be cleaned out. Blackened areas that are enlarging indicate that the top coat has become compromised and needs to be touched up. Blackened areas degrade the appearance of the PPWG but they should not adversely affect its performance.

Yellowed areas indicate that the paint has been removed from a region of aluminum. The yellowing is due to the exposure of the zinc-chromate primer. The primer is non-conductive and if it is exposed, it should be touched up. Whitened areas indicate that paint has been removed from a region of PVC.

Paint (Research)

Experiments should be conducted with the paint to determine a repeatable application process that achieves a consistent thickness and sheet resistance per coat. The process should be used to characterize the paint and verify its specified performance.

Scissor Lift (Action)

In general, the scissor lift should be maintained and used in accordance with the product manual. However, the RF cabling for the bottom plate is fed through the scissor lift so it should be monitored for consistent clearance, especially if the cabling has been moved. The scissor lift should not be moved from its position on the BANTAM floor.

The lift is capable of rising and lowering beyond what is apparent in the chamber. It is recommended that the lift be operated under constant observation and not allowed to travel to its design limits. The design limits are well below the tips of the floor absorber and above the lowest point of the top plate. It is also recommended that the foot pedal is operated by hand and stowed well removed from feet when idle.

Scissor Lift (Research)

Research should be conducted to determine if two lifts would be better suited for the PPWG than one. A second lift, positioned perpendicularly to the first, should help stabilize the PPWG and prevent rocking or swaying as the scanning function is performed. The advantages of a second lift should be weighed against the disadvantages of installing it and synchronizing it with the first lift.

Lenses (Action)

The lenses should be stored in a dedicated case surrounded by protective padding. The lenses are somewhat soft and can be scratched easily by rings, watches, belts and tools. Should significant scratches develop, the lenses should be re-polished. The lenses should be taped to the aluminum for every measurement to prevent inadvertent movement. Fresh tape should be applied every time the lenses are removed. The lenses may require some prying to remove them from the aluminum. The double-sided conductive tape can be removed from the lenses with warm water and a strong twisting action of a washcloth.

Lenses (Research)

The lens design spreadsheet should be used to look for other optimal lens designs. These designs should consider using thinner lenses and lenses made of a different material. One practical example would combine both parameters by designing a lens from 0.25" acrylic. Thin acrylic panels are readily available at Lowe's and acrylic has an index of refraction near that of Rexolite. The main advantage of designing a thin acrylic lens is that the PPWG can be brought to 0.25" spacing, eliminating all higher-order modes over 2-18 GHz. A secondary advantage is that the thin acrylic lens could be fabricated directly in the microwave laboratory rather than at the AFIT Model & Fabrication Shop.

It is recommended further that the beam profiles of the original lenses should be verified and published from CST simulations. Due to the untimely CST license expiration towards the end of this thesis, the simulated lens data could not be retrieved.

Mode-Matching Mesas and Cones (Research)

The concept of a mode-matching component should be fully researched for both a mesa and a cone structure. The cone structure should offer more to the preservation of cylindrical wavefronts as radiated from a monopole than the mesa, but the cone offers more challenges in fabrication. The research should include fabrication techniques as well as designs for frequency octave structures rather than designs for one broadband structure.

Targets (Action)

A precise, positionable target fixture is required almost immediately for successful material measurements. This fixture must be designed and built for targets 32" long, 2" tall and having a variety of thicknesses.

System Recommendations

Derive Constituent Parameters (Action)

A program for deriving the constituent parameters of the acrylic target should be developed based on the S-parameter measurements provided.

Calibration (Action)

Appropriate techniques for gating and windowing the signals of the BANTAM 2-D FBS should be developed. An isolation standard for the BANTAM PPWG should be fabricated and calibration using the standard should be performed similar to the GTRI system.

Right-Side Characterization (Action)

The right side of the BANTAM 2-D FBS system should be characterized as the left side has been. Measurements should be taken using the right side and compared to those taken using the left side.

Resolution (Research)

Spatial and frequency resolution should be optimized with the time to run a scan.

Transient Domain Characterization (Research)

The BANTAM 2-D FBS should be viewed in the transient domain and characterized as appropriate.

Hardware limit switches (Action)

The horizontal limit switches should be repositioned to the front of the chamber for easy access. Generally, the limits should be +/- 7.125" on both the long and short

axes. A vertical limit switch and a mechanical stop should be installed above the top plate to prevent it from inadvertently rising too far.

Simulations (Research)

Research should be conducted to determine how to properly simulate the BANTAM 2-D FBS in its full configuration over its full frequency band. This will require consultation with CST specialists at Sonnet Software.

A program for integrating the x-, y- and z- electric field components from CST simulations should be developed in order to make proper comparisons with measured data.

Simulations should be performed for the system with a small air gap introduced between the lenses and the top plate.

The lenses should be simulated with the appropriate mode-matching structure and the beam profiles should be compared to those without the mode-matching structure.

Field distributions in the near-field region of the metamaterial D-rings should be extracted from CST and compared to the measured data.

Documentation (Action)

The documents, specification sheets, drawings, etc. from the development of the BANTAM 2-D FBS should be compiled into a formal manual.

Camera System (Research)

A camera system should be considered for viewing the scan progress. An overhead camera within the chamber would be useful for monitoring the placement of lenses and targets.

Return to Original BANTAM (Research)

The procedures necessary to temporarily return the BANTAM 2-D FBS to the original BANTAM configuration for near-field antenna measurements should be researched.

Software Module (Research)

A software module similar to ALPINE should be developed in order to more easily process the BANTAM 2-D FBS measurement data.

Appendix: Lens Optimization Spreadsheet

Design Option: S-Parameters and Near-Field Scan											
Parameters	Symbol	Design To:									Actuals
Frequency (GHz)	f	2.534	2.000	4.000	6.000	8.000	10,000	12,000	14,000	16,000	18,000
Wavelength (in.)	λ	4.588	5.906	2.953	1.969	1.476	1.181	0.984	0.844	0.738	0.656
Propagation Constant (rad/in.)	k0	1.369	1.064	2.128	3.192	4.256	5.320	6.384	7.448	8.512	9.576
Focusing Factor (> π thresh, $>= 10$ obj)	kdw0	3.847	2.769	3.916	4.796	5.538	6.192	6.783	7.326	7.832	8.307
Desired BeamWaist Radius (in.)	w0	2.294	2.603	1.840	1.503	1.301	1.164	1.063	0.984	0.920	0.868
Desired Taper at Target Edge (dB)	Tt	-10.000	-15.538	-31.076	-46.614	-62.152	-77.690	-93.228	-108.766	-124.304	-139.842
Desired Target Radius (in.) ($>=$ indicated value)	rt	3.481	3.481	3.481	3.481	3.481	3.481	3.481	3.481	3.481	3.481
Desired Taper at Lens Edge (dB)	Tl	-20.000	-15.538	-31.076	-46.614	-62.152	-77.690	-93.228	-108.766	-124.304	-139.842
Lens Radius (in.) ($<=$ 7.5 in.)	rl										
Desired 1/e Radius at Lens Edge (in.)	wL	3.427	3.888	2.749	2.245	1.944	1.739	1.587	1.469	1.375	1.296
Refractive Index	n										
Collimating Lens											
Focal Length (in.) (position of monopole)	f1										
Thickness (in.)	t1										
Focusing Lens											
Focal Length (in.)	f2										
Thickness (in.)	t2										
Target Placement (in.)	z										
MonoMargin (λ at minimum focus)	Mm										
Scan Length											
Waveguide Length											14,492
Bottom Plate Length Constraint (in.)											12,762
Length of bottom plate (in.)	lbp	69.000									34,500
Width of bottom plate (in.)	wbp	45.000									
Length of top plate (in.)	ltp	54.508									
Width of top plate (in.) ($<=$ 30)	wtp	30.000									

Figure 151: Small Lens Optimization Sheet

Design Options: S-Parameters Only						
Parameters	Symbol	Design To:				Actuals
Frequency (GHz)	f	2,000	4,000	6,000	8,000	10,000
Wavelength (in.)	λ	4.588	5.906	2.953	1.969	1.476
Propagation Constant (rad/in.)	k_0	1.369	1.064	2.128	3.192	4.256
Focusing Factor ($> n_{\text{thresh}}$, ≥ -10 dB)	w0	2.294	2.769	3.916	4.796	5.538
Desired Beam/Waist Radius (in.)	Tl	-20.000	2.603	1.840	1.503	1.301
Desired Taper at Target Edge (dB)	Tr	3.481	-15.538	-31.076	-46.014	-62.152
Desired Target Radius (n_1) (\geq indicated value)	Tl	-20.000	-15.538	-31.076	-46.014	-62.152
Desired Taper at Lens Edge (dB)	rl	5.413	6.141	4.342	3.546	4.424
Lens Radius (in.) (≤ -7.5 in.)	wl	5.413	6.141	4.342	3.546	4.424
Desired 1/e Radius at Lens Edge (in.)	n					
Collimating Lens						
Focal Length (in.) (position of monopole)	f1					
Thickness (in.)	t1					
Focusing Lens						
Focal Length (in.)	f0					
Thickness (in.)	t0					
Target Placement (in.)	z^2					
MonoMargin (λ at minimum focus)	Mm					
Scan Length						
Waveguide Length						
Space constraint on S-param only						
Length of bottom plate (in.)	lbp	69,000				
Width of bottom plate (in.)	wbp	45,000				
Length of top plate (in.) (≤ 30)	ltip	54,508				
Width of top plate (in.)	wtip	30,000				

Figure 152: Large Lens Optimization Sheet

Bibliography

1. IEEE, "IEEE Standard Letter Designations for Radar-Frequency Bands," IEEE, NYC, Standard IEEE Std 521-2002, 2003.
2. Chen, L. F., and others, *Microwave Electronics*. West Sussex, England: John Wiley & Sons Ltd, 2004.
3. Wikipedia. (2011, August) Wikipedia: The Free Encyclopedia. [Online]. [http://en.wikipedia.org/wiki/Metaphysics_\(Aristotle\)#cite_note-3](http://en.wikipedia.org/wiki/Metaphysics_(Aristotle)#cite_note-3)
4. Collins, Peter J. and Charles McNeely, Technical discussions, BANTAM 2-D FBS Patent. Graduate School of Engineering and Management, Air Force Institute of Technology, Wright-Patterson AFB OH, August 2011.
5. C. M. Shafe, "Air Force Research Laboratory BANTAM," Air Force Research Laboratory, WPAFB, 2004.
6. Wikipedia. (2011, August) Wikipedia: The Free Encyclopedia. [Online]. http://en.wikipedia.org/wiki/File:field_regions_for_typical_antennas.gif.
7. Chi-Chih Chen, "Broadband Dielectric Probe Prototype Development for Near-Field Measurements," The Ohio State University ElectroScience Laboratory, Columbus, OH, Technical 2003.
8. GTRI, *Users Guide: Theory and Operation of the GTRI Focused Beam System*. Atlanta: Georgia Tech Research Corporation, 2007
9. Shelby, R. A., D. R. Smith and S. Schultz. "Experimental Verification of a Negative Index of Refraction," *SCIENCE*, 292: 77-79 (6 April 2001).
10. Metamaterials. (2011, August) Elsevier. [Online]. http://www.elsevier.com/wps/find/journaldescription.cws_home/710726/description#description
11. E. Shamonina and L. Solymar, "Metamaterials: How the subject started," *Metamaterials*, vol. I, no. 1, pp. 12-18, Feb 2007.

12. Ari Sihvola, "Metamaterials in Electromagnetics," *Metamaterials*, vol. I, no. 1, pp. 2-11, February 2007.
13. C-LEC Plastics Inc., "What is Rexolite?" Product Information. n. pag. <http://www.rexolite.com>. 2012.
14. Balanis, Constantine A. *Advanced Engineering Electromagnetics*. Hoboken, New Jersey: John Wiley & Sons, Inc., 1989.
15. McNamara, D. A. and others. *The Uniform Geometrical Theory of Diffraction*. Norwood, Massachusetts: Artech House, 1990.

REPORT DOCUMENTATION PAGE				<i>Form Approved OMB No. 074-0188</i>
<p>The public reporting burden for this collection of information is estimated to average 1 hour per response, including the time for reviewing instructions, searching existing data sources, gathering and maintaining the data needed, and completing and reviewing the collection of information. Send comments regarding this burden estimate or any other aspect of the collection of information, including suggestions for reducing this burden to Department of Defense, Washington Headquarters Services, Directorate for Information Operations and Reports (0704-0188), 1215 Jefferson Davis Highway, Suite 1204, Arlington, VA 22202-4302. Respondents should be aware that notwithstanding any other provision of law, no person shall be subject to any penalty for failing to comply with a collection of information if it does not display a currently valid OMB control number.</p> <p>PLEASE DO NOT RETURN YOUR FORM TO THE ABOVE ADDRESS.</p>				
1. REPORT DATE (DD-MM-YYYY) 22-03-2012	2. REPORT TYPE Master's Thesis	3. DATES COVERED (From – To) 11 Aug 2010 - 22 Mar 2012		
4. TITLE AND SUBTITLE Development of a Radar-Frequency Metamaterial Measurement and Characterization Apparatus		5a. CONTRACT NUMBER		
		5b. GRANT NUMBER		
		5c. PROGRAM ELEMENT NUMBER		
6. AUTHOR(S) Faris, Stephen I., Captain, USAF		5d. PROJECT NUMBER ENG 11G262		
		5e. TASK NUMBER		
		5f. WORK UNIT NUMBER		
7. PERFORMING ORGANIZATION NAMES(S) AND ADDRESS(S) Air Force Institute of Technology Graduate School of Engineering and Management (AFIT/ENG) 2950 Hobson Way, Building 640 WPAFB OH 45433-8865		8. PERFORMING ORGANIZATION REPORT NUMBER AFIT/GE/ENG/12-13		
9. SPONSORING/MONITORING AGENCY NAME(S) AND ADDRESS(ES) Air Force Research Laboratory, Materials Directorate Dr. Katie Thorp 2941 Hobson Way, Bldg 654 Wright-Patterson AFB, OH 45433-7739 (850) 882-8876, katie.thorp@wpafb.af.mil		10. SPONSOR/MONITOR'S ACRONYM(S) AFRL/RX		
		11. SPONSOR/MONITOR'S REPORT NUMBER(S)		
12. DISTRIBUTION/AVAILABILITY STATEMENT APPROVED FOR PUBLIC RELEASE; DISTRIBUTION IS UNLIMITED.				
13. SUPPLEMENTARY NOTES This material is declared a work of the U.S. Government and is not subject to copyright protection in the United States.				
14. ABSTRACT The purpose of this research was to design, build and test an apparatus for the measurement and characterization of radar-frequency metamaterials. Measurement and characterization is vital to metamaterial taxonomy and ultimately vital to metamaterial definitions. Thus, the current lack of clarity in metamaterial definitions has served as the primary motivation for pursuing a method for taxonomy and thus, this apparatus. The technical goal of this thesis was to aid understanding of a metamaterial's radar-frequency response by developing an apparatus that would take simple, yet significant measurements of a metamaterial's S-parameters and electric field distributions in near-field regions. The apparatus under design became a hybridized form of the designs of three existing measurement systems: a focused-beam system housed in a moveable-plate, parallel-plate transmission line. Some of the system components were borrowed directly from the existing designs, whereas some components were designed from the examples of existing designs and some components were designed altogether new. The culmination of this effort was a newly-built measurement device that upon inauguration provided the basic utility of measuring the radar-frequency responses of both traditional materials and metamaterials.				
15. SUBJECT TERMS Measurement, characterization, metamaterials, apparatus, radar-frequency				
16. SECURITY CLASSIFICATION OF:		17. LIMITATION OF ABSTRACT UU	18. NUMBER OF PAGES 215	19a. NAME OF RESPONSIBLE PERSON Collins, Peter J., Ph.D., USAF 19b. TELEPHONE NUMBER (Include area code) (937) 255-3636, x 7256 (peter.collins@afit.edu)
a. REPORT U	b. ABSTRACT U	c. THIS PAGE U		

Standard Form 298 (Rev. 8-98)
Prescribed by ANSI Std. Z39-18